

Anomalies in Tropical Methane Emissions: Using Isotopes to Characterise Source Variability

Submitted by

Rebecca Brownlow

for the degree of Doctor of Philosophy

Royal Holloway, University of London

2017

Abstract

In 2007 a sustained atmospheric global growth of methane began and was particularly strong in the tropics. The tropics are poorly understood with few measurements, despite being an important part of the global methane budget. Sources include natural wetlands, rice agriculture, biomass burning, ruminants, fossil fuels and waste.

This thesis focuses on sources sampled across the tropics using Tedlar bags, with Bachok, Malaysia and Ascension Island selected for more detailed sampling and studies. Samples were analysed for methane mole fractions using cavity ring-down spectroscopy and for isotopic source signatures, $\delta^{13}\text{C}$, using gas chromatography/isotope-ratio mass spectrometry. Using $\delta^{13}\text{C}$ and mole fraction measurements means both global and regional emissions can be constrained in models with better source apportionment improving the understanding of the sustained tropical methane growth. Keeling plots have been used to calculate the $\delta^{13}\text{C}$ source signature of each source type. Tropical wetlands have a signature between $-61.5 \pm 2.9 \text{ ‰}$ and $-53.0 \pm 0.4 \text{ ‰}$ and are generally more enriched than temperate and boreal wetlands.

Continuous monitoring of greenhouse gases and collection of air samples at Bachok research station, Malaysia showed the background CH_4 mole fraction is influenced by air masses arriving from over China and Southeast Asia. Local CH_4 peaks were not predominantly biomass burning as expected, but instead gave a signature of $-54.9 \pm 1.2 \text{ ‰}$, suggesting mixing with biogenic sources, showing the importance of monitoring CH_4 isotopes.

Ascension Island is a remote South Atlantic equatorial site, ideal for monitoring tropical background CH_4 . Octocopters were used to collect air samples

from different heights above and below the Trade Wind Inversion (TWI). This work has shown it is possible to retrieve air samples up to an altitude of 2700m above mean sea level. Both campaigns show a consistently higher mole fraction above the TWI, representative of air masses arriving from over Africa compared to below the TWI where air masses arrive from the remote south Atlantic.

Acknowledgements

I would like to thank my supervisors Dr. Dave Lowry, Dr. Rebecca Fisher, Dr. James France and Prof. Euan Nisbet for all their support and patience and allowing me the opportunity to do the PhD or 'extended holiday' in the words of Euan. Also thanks to my advisor Dr. Nathalie Grassineau. This work has been supported by a NERC studentship.

Thanks to Giulia Zazzeri, Aalia Al Shaalan, Mathias Lanoisellé and Babs White for help with lab work and general help. Everyone that helped me during the Bachok, Malaysia Campaign, especially Iq, Grant and Dave. Tom, Rick, Colin and Jim during the Ascension Island campaigns. The cows for being so patient with us during the Hong Kong campaign.

I would also like to acknowledge the support of the PhD community and all the tea breaks (especially Amy) 'ProcrasTEAnation'. Rehemat and Steph for completing both our undergrads and PhD's together and their support. Hannah and James for being understanding through out my PhD and eating pizza with me! The 'Party' House: Christof, Ben, Max and Kat for being amazing housemates and friends, as well as inspiring me to run more and teaching me some German. Steffen for being so supportive, teaching me LaTeX and teaching me better German!

Finally thanks to my Mum, Dad, Grandma and Thomas for all their support and Otto, Sootica, Felix and Floyd!

Contents

1	Introduction to Methane	13
1.1	General Background to Methane	13
1.2	Past Global Change	15
1.3	Methane Emissions	15
1.4	Natural Sources	16
1.4.1	Wetlands	16
1.4.2	Other Natural Sources	20
1.5	Anthropogenic Sources	21
1.5.1	Ruminants	21
1.5.2	Waste	22
1.5.3	Biomass Burning	23
1.5.4	Fossil Fuels	24
1.6	Atmospheric Chemistry and Sinks	24
1.7	Methane Isotopes	28
1.8	The recent global CH ₄ growth	32
1.9	Introduction to Tropical Methane	34
1.10	Aims	38
2	Methods	39

2.1	Sampling Locations	39
2.1.1	Ascension Island	39
2.1.2	Bachok, Malaysia	41
2.2	In Situ Sampling	41
2.3	Sample Analysis	43
2.3.1	Picarro CRDS	43
2.3.2	Los Gatos Research analyser	47
2.3.3	Continuous-flow gas chromatography/isotope-ratio mass spec- trometry	48
2.4	Analytical Methods	50
2.4.1	Keeling Plots	50
2.5	Trajectories	53
2.5.1	NOAA HYSPLIT	53
2.5.2	NAME	54
3	Isotopic ratios of tropical methane emissions by atmospheric measurement and continental-scale variability.	56
4	Influence of local methane emissions on a tropical monitoring site	55
5	Methane mole fraction and $\delta^{13}\text{C}$ above and below the trade wind inversion at Ascension Island in air sampled by aerial robotics	56
6	Discussions and Conclusions	57
6.1	Ascension Island	57
6.2	Possible reasons for Tropical Growth	59
6.3	Growth outside the Tropics	62

6.4	Isotope Source Signatures	62
6.5	Airborne and Mobile Measurements	69
6.6	Future locations for tropical measurements	70
6.7	Conclusions	73
	Bibliography	90
A	Atmospheric Sampling on Ascension Island Using Multirotor UAVs	91
B	Rising atmospheric methane: 2007-2014 growth and isotopic shift	90

List of Figures

1.1	CH ₄ over the past 1000 years from Antarctic ice cores (DE08, DE08-2 and DSS), firn air (DE08-2) and monitoring from Cape Grim (Etheridge et al., 1998)	16
1.2	Variation in $\delta^{13}\text{C}$ and δD with CH ₄ production and oxidation mechanisms(from: Chanton et al., 2005). δD , the stable isotopes of hydrogen, is is not studied in this thesis however its composition is also relative to the production pathway and oxidation.	30
1.3	a) The blue line shows the average global methane (in ppb) between 1983 and the end of 2015. The red line shows the deseasonalised trend. b) The growth rate from the time derivative of the deseasonalised trend in plot a (Dlugokencky, 2016).	32
1.4	Yearly mean NOAA station $\delta^{13}\text{C}$ methane trends, the right column of the NOAA station gives the latitude. (Nisbet et al., 2016). . . .	33
1.5	The global methane growth rate trends in ppb yr ⁻¹ between 2000 and 2015 plotted against sine of latitude. Growth is shown in red, yellow and green and decline in blue (Dlugokencky, 2016).	34
1.6	The GAW global network for CO ₂ over the last 10 years, CH ₄ is similar (WMO, 2016).	35

1.7	Regional methane emissions between 2000 and 2009. Top-down emissions are lighter coloured bars and bottom-up are darker coloured bars (Kirschke et al., 2013).	36
1.8	Methane emissions ($\text{CH}_4 \text{ m}^{-2} \text{ day}^{-1}$) from wetlands, fossil fuels, agriculture & waste and biomass burning between 2003 and 2012. The wetland emissions are the average emission per day of 11 models. The Fossil fuel, agriculture & waste and biomass burning are from mean values from EDGAR V4.2 and other models (Sauniois et al., 2016).	37
2.1	Map of tedlar bag sampling sites in this thesis (red). Ascension Island and Bachok, Malaysia (orange) have longer term monitoring as well as bag samples. The Hong Kong sites were also part of a mobile monitoring campaign undertaken by the RHUL GHG group.	40
2.2	Sampling method shown in Bachok, Malaysia.	42
2.3	schematic diagram showing how the gas samples are measured during CRDS (http://www.picarro.com).	44
2.4	Picarro 1301 CRDS in the RHUL lab.	46
2.5	Picarro 1301 CRDS at RHUL Target values for 2015 (Error bars give the standard deviation of the average target value). The mean value for 2015 is 1939 ppb and the precision is ± 0.2 ppb.	46
2.6	Continuous-flow gas chromatography/isotope-ratio mass spectrometry in the RHUL lab.	48
2.7	The Trace Gas CH_4 set up (Fisher et al., 2006).	49

2.8	Illustration of a Keeling plot for CH_4 showing the two end points of the source and background in black circles with sampled air shown by the crosses, adapted from Pataki et al., 2003.	51
2.9	An example of an offline HYSPLIT trajectory run for July 2015 arriving at ground level on Ascension Island. Hysplit was run offline with GDAS archive meteorological data four times per day at 00:00, 06:00, 12:00 and 18:00 UTC for 120 backwards (Rolph, 2017; Stein et al., 2015).	53
2.10	An example of a NAME plot run for 7 days back from the sample collection time and height on Ascension Island (this example is from 08 July 2015 09:38 75 masl) with particles being released at a rate of 100000 per hour for one hour, from a depth of 100 m centred on the sample height.	55
6.1	The top graph shows methane mole fractions from Ascension Island between 2000-2015. The red circles are NOAA flasks, the blue circles RHUL flasks and the black line is the RHUL continuous Picarro data. The bottom graph shows South Atlantic $\delta^{13}\text{C}$ data between 2000-2015. Red crosses show NOAA-INSTAAR flasks, Black show RHUL Ascension flasks and blue show Cape Point, South Africa. The RHUL $\delta^{13}\text{C}$ data also have error bars (Nisbet et al., 2016).	58
6.2	Conceptual model of the expected $\delta^{13}\text{C}$ and δH changes with organic carbon sources, methanogenic pathways and bacterial methane oxidation (Hamilton et al., 2014)	68

6.3	EDGAR V4.2 CH ₄ emissions (tons) for 2010 (European Commission, 2011) with all active NOAA carbon cycle gas measurement sites (purple diamonds) (from: www.esrl.noaa.gov/gmd/dv/iadv) and RHUL sample locations in this thesis (white circles). Note that $\delta^{13}\text{C}$ for methane is only measured at a small subset of these sites	71
6.4	Trends in Wetland CH ₄ emissions in Gg/yr between 1993 and 2014 from JULES (McNorton et al., 2016).	72

List of Tables

1.1	Global methane emissions estimates and sinks in Tg yr^{-1} for bottom-up and top-down methods with the range as [min-max]. Values between 2000-2009 from Kirchke et al. (2013) and 2003-2012 from Saunio et al. (2016). Note: Top down estimates are not able to separate individual processes.	17
1.2	2014 global CH_4 emissions from Ruminants (FAO, 2016).	22
1.3	General $\delta^{13}\text{C}_{\text{CH}_4}$ ‰ source signatures from Dlugokencky et al. (2011).	29
2.1	Internal secondary standards	49
6.1	Year on Year Ascension Island CH_4 mole fraction growth using hourly averaged RHUL picarro data, RHUL flasks and NOAA flasks, updated from Nisbet et al., 2014. The program HPspline was used to fit the curve using parameters suggested in Pickers and Manning, 2015.	59

6.2	Emission inventories and calculated regional yearly average source signatures for Tropical South America and Africa (methods are in Chapter 3 SI). The table compares yearly signatures calculated from using $\delta^{13}\text{C}$ values from this thesis (RHUL column) and $\delta^{13}\text{C}$ values used in $\delta^{13}\text{C}$ model studies. Errors are not given for $\delta^{13}\text{C}$ in these studies.	66
-----	--	----

Chapter 1

Introduction to Methane

1.1 General Background to Methane

Atmospheric greenhouse gases, water vapour (H_2O), carbon dioxide (CO_2), methane (CH_4) and nitrous oxide (N_2O) absorb outgoing infrared radiation and increase the temperature of the atmosphere. These greenhouse gases have significantly increased since the pre-industrial era due to anthropogenic emissions (Ciais et al., 2013).

CH_4 has a global warming potential (GWP) of 34 times that of CO_2 over 100 years (Ciais et al., 2013) therefore small changes will have important implications. Around 18% of human induced radiative forcing is from methane, making it one of the most important greenhouse gases (Bridgham et al., 2013). Changes in tropospheric ozone, enhanced stratospheric water vapour and CO_2 levels are caused by methane.

CH_4 has a lifetime of about 9 years (Saunio et al., 2016; Prather et al., 2012). This short lifetime, in comparison with CO_2 which has a variable lifetime of tens to thousands of years (Archer et al., 2009), means that reducing CH_4 emissions

would have a more rapid impact in reducing greenhouse gases in the atmosphere and is therefore attractive to policy makers.

Estimates of methane emissions vary depending on 'bottom-up' estimates (The sum of estimated fluxes of individual processes) which are usually greater than 'top-down' estimates (calculated from direct atmospheric measurements) (Table 1.1). More measurements are needed to close these discrepancies and uncertainties in methane sources (Nisbet and Weiss, 2010; Nisbet et al., 2014; Kirschke et al., 2013; Saunois et al., 2016).

Methane emissions may be biogenic, thermogenic or pyrogenic and may be from both anthropogenic and natural sources. CH_4 from biogenic sources is produced from methanogenic archaea (methanogens) in anaerobic environments which include wetlands, ruminants and landfill. Thermogenic sources of CH_4 are fossil fuels (coal, oil and gas) formed by geological processes over millions of years. CH_4 may be vented through natural seeps or through the fossil fuel extraction and use. Pyrogenic CH_4 is produced through incomplete combustion of biomass, for example peat fires and biomass burning (Kirschke et al., 2013).

Anthropogenic emissions are the major factor during the increase in the CH_4 burden and make up 54-72% of the global CH_4 flux total (Bridgham et al., 2013). The largest anthropogenic sources are fossil fuel extraction and distribution, industry, rice agriculture, livestock, biomass burning and waste. Natural sources include wetlands, forest fires and methane hydrates. Sources such as wetlands and hydrates have been shown to have strong positive feedbacks (Dlugokencky et al., 2011).

There is an inter-hemispheric gradient of CH_4 with higher concentrations in the northern hemisphere which results from more emissions from the northern hemisphere as there is more land and a higher population in this region. Seasonal

changes also occur as CH_4 decreases in summer due to photochemical oxidation (Reeburgh, 2003).

1.2 Past Global Change

The atmospheric methane burden has varied over the past 1000 years, as can be seen in Fig 1.1. Evidence from polar ice sheet cores show the atmospheric concentration of methane in the year 1750 was approximately 722 ± 25 ppb (Hartmann et al., 2013; Whiticar and Schaefer, 2007) showing CH_4 has more than doubled over the past 250 years since pre industrial time. Concentrations prior to 1750 fluctuated between 350 to 750 ppb and were closely correlated with temperature (Whiticar and Schaefer, 2007; Chappellaz et al., 1990).

The global average dry air mole fraction of CH_4 in 2015 was 1845 ± 2 ppb (WMO, 2016). The increase of CH_4 in the present day over natural background is due to anthropogenic emissions, this in turn creates a positive feedback loop, increasing the temperature and therefore increasing CH_4 emissions from wetlands through increased methanogenesis and retreating permafrost (Whiticar and Schaefer, 2007).

1.3 Methane Emissions

Global emissions for 2000 to 2009 are estimated by Kirsche et al. (2015) to be 526 - 569 Tg CH_4 yr^{-1} for top down-values and 542 - 852 Tg CH_4 yr^{-1} for bottom-up values. Global emissions for 2003 to 2012 are estimated by Saunois et al. (2016) to be 540 - 568 Tg CH_4 yr^{-1} for top-down values and 596 - 884 Tg CH_4 yr^{-1} for bottom-up values. Table 1.1 gives an overview of sources and their emissions

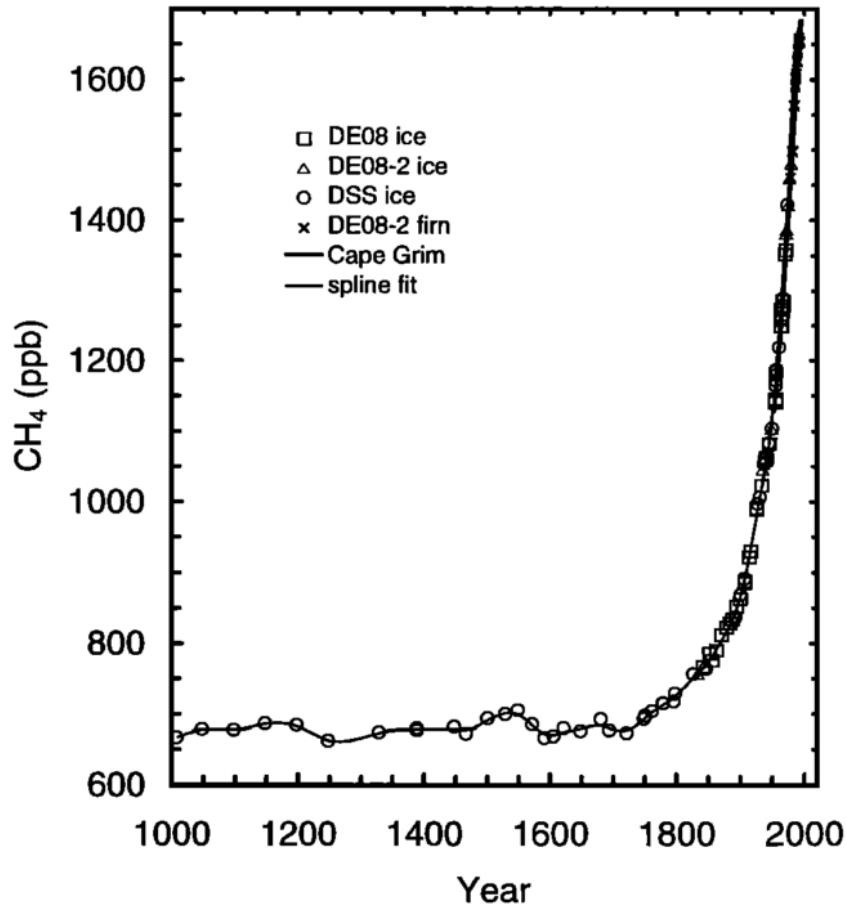


Figure 1.1: CH₄ over the past 1000 years from Antarctic ice cores (DE08, DE08-2 and DSS), firn air (DE08-2) and monitoring from Cape Grim (Etheridge et al., 1998)

input from Saunois et al. (2016) and Kirchke et al. (2013).

1.4 Natural Sources

1.4.1 Wetlands

The largest natural source of methane is wetlands, estimated to emit 153 – 227 Tg yr⁻¹ (Saunois et al., 2016). The term 'wetland' describes a range of CH₄

	Kirchke et al. (2013) 2000-2009		Saunois et al. (2016) 2003-2012	
Source	Bottom-up Tg yr ⁻¹	Top-down Tg yr ⁻¹	Bottom-up Tg yr ⁻¹	Top-down Tg yr ⁻¹
Natural Sources	347 [238-484]	218 [179-273]	384 [257-524]	231 [194-296]
<i>Wetlands</i>	217 [177-284]	175 [142-208]	185 [153-227]	167 [127-202]
<i>Other natural sources</i>	130 [45-232]	-	199 [104-297]	64 [21-132]
<i>Other land sources</i>	112 [43-192]	43 [37-65]	185 [99-272]	-
Fresh Waters	40 [8-73]	-	122 [60-180]	-
Geological (onshore)	54 [33-75]	-	40 [30-56]	-
Wild animals	15 [15-15]	-	10 [5-15]	-
Termites	11 [2-22]	-	9 [3-15]	-
Wild Fires	3 [1-5]	-	3 [1-5]	-
Permafrost soils (direct)	1 [0-1]	-	1 [0-1]	-
Oceanic Sources	18 [2-40]	-	14 [5-25]	-
Geological (offshore)	-	-	12 [5-20]	-
Other (including hydrates)	-	-	2 [0-5]	-
Anthropogenic Sources	331 [304-368]	335 [273-409]	352 [340-360]	328 [259-370]
<i>Agriculture & waste</i>	200 [187-224]	209 [180-241]	195 [178-206]	188 [115-243]
Enteric fermentation & manure	101 [98-105]	-	106 [97-111]	-
Landfills & waste	63 [56-79]	-	59 [52-63]	-
Rice cultivation	36 [33-40]	-	30 [24-36]	-
<i>Fossil Fuels</i>	96 [85-105]	96 [77-123]	121 [114-133]	105 [77-133]
Coal Mining	-	-	41 [26-50]	-
Gas, Oil & industry	-	-	79 [69-88]	-
<i>Biomass & biofuel burning</i>	35 [32-39]	30 [24-45]	30 [27-35]	34 [15-53]
Biomass burning	-	-	18 [15-21]	-
Biofuel burning	-	-	12 [10-14]	-
Sum of Sources	678 [542-852]	553 [526-569]	736 [596-884]	558 [540-568]
Sinks				
<i>Total Chemical Loss</i>	604 [438-738]	518 [510-538]	-	515
Tropospheric OH	528 [454-617]	-	-	-
Stratospheric loss	51 [16-84]	-	-	-
Tropospheric Cl	25 [13-37]	-	-	-
<i>Soil uptake</i>	28 [9-47]	32 [26-42]	-	33 [28-38]
Sum of Sinks	632 [592-785]	550 [514-560]	-	548

Table 1.1: Global methane emissions estimates and sinks in Tg yr⁻¹ for bottom-up and top-down methods with the range as [min-max]. Values between 2000-2009 from Kirchke et al. (2013) and 2003-2012 from Saunois et al. (2016). Note: Top down estimates are not able to separate individual processes.

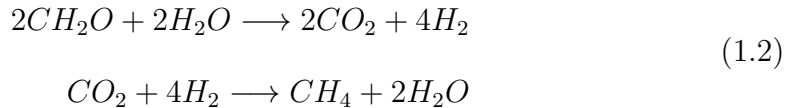
emitting ecosystems which include wet soils, swamps, bogs and peatlands (Ciais et al., 2013). Around 50% of the natural wetland area is situated in the boreal zone and up to 35% is found in the tropics (Saunois et al., 2016; Mitsch et al., 2010). Wetlands are sensitive to climate feedbacks. The CH_4 flux increases with temperature and precipitation with emissions likely to increase in a warming climate (Ciais et al., 2013). Rice fields are an anthropogenic source but share the same mechanisms and controls for CH_4 emissions as the natural wetlands.

CH_4 from wetlands is a biogenic source, produced from the breakdown of organic matter by the bacteria in anoxic conditions. Methanogenesis is influenced by temperature, vegetation type, the water table (which is linked to the anoxia level) and the availability of substrate (Saunois et al., 2016).

Hydrological processes are the predominant influence on tropical wetland methane emissions where as in higher latitudes temperature is the main factor (Ringeval et al., 2010; Bousquet et al., 2011). The two main pathways methanogenesis can occur through are: acetoclastic - the fermentation of acetate (Equation 1.1):



Or hydrogenotrophic - the reduction of CO_2 with hydrogen (Equation 1.2) (Chanton et al., 2005; Lai, 2009):



These two pathways vary depending on the environment. The fermentation of acetate occurs predominantly in freshwater sediments. In flooded basins

and sedimentary environments acetate production occurs more in the upper peat/sediment layers and is associated with the breakdown of organic carbon. In sulphate rich environments, for example marine sediments, the sulphate reducing bacteria out-compete methanogens for substrate. When the sulphate is exhausted the sulphate reducing bacteria become inactive and methanogenesis occurs using the substrate preferentially by CO_2 reduction (Whiticar, 1999).

Methane can leave wetlands via diffusion, ebullition or plant mediated transport. Ebullition is the formation of CH_4 bubbles and other gases (typically CO_2 and N related species) in sub-surface soils or sediments and their subsequent release through the water table directly to the atmosphere. It occurs as CH_4 is typically insoluble in water and may be the most significant pathway for methane loss in wetlands (Chanton et al., 2005; Green, 2013). The processes and conditions required for the formation and release of the bubbles are not clear. The bubbles may be formed when the dissolved gasses combined partial pressure exceed hydrostatic pressure (Green, 2013). Two types occur; steady ebullition and episodic ebullition. Steady ebullition is a constant release of the bubbles into the water. The CH_4 will then diffuse through the zone above the water table to the surface where methanotrophs may consume it. Episodic ebullition is short-lived and the bursts tend to be higher and more variable than background fluxes. Due to the buoyancy of the bubbles, they largely bypass the methanotrophic processing (Green, 2013). Episodic ebullition can be associated with changes in atmospheric pressure, turbulent shaking and buoyancy of the bubbles exceeding forces keeping them in place. The potential of wetland ebullition depends on the soil or sediment's ability to store methane in its gas phase. Ebullition is dependent on both the gaseous CH_4 pool and plant-mediated flux capacity (Green, 2013; Tokida et al., 2013).

Plant-mediated transport from vascular plants is driven by molecular diffusion. It varies between plant type and areas and can contribute between 30-100% of total CH_4 flux (Bridgham et al., 2013; Bhullar et al., 2013). A higher volume of bubbles may affect the rate by enhancing the transfer of CH_4 by the plant root (Tokida et al., 2013). Plants with less dense root tissues and larger root volumes also tend to enhance the CH_4 transport (Bhullar et al., 2013). Diffusion occurs due to the concentration gradient between the anaerobic layers that produce CH_4 and the atmosphere. Diffusion is slowest in the layers below the water table and overall the flux is slow compared to ebullition and plant-mediated transport. Diffusion can control the rate of microbial CH_4 consumption as it enables the interaction of CH_4 with methanotrophs in the aerobic layer, which oxidise CH_4 to CO_2 , when the water table is below the soil surface (Lai, 2009; Bridgham et al., 2013).

Tree mediated emissions have been shown to be an underestimated pathway in forested wetlands, as many process studies focus on ground surface fluxes. It has been estimated that tropical peatland environments tree-stems emit up to 87% of the total CH_4 flux (Pangala et al., 2013).

1.4.2 Other Natural Sources

Other natural sources such as termites (biogenic) or geological sources (such as oceanic seeps or mud volcanoes) contribute to a small part of the methane budget so are not discussed. Wild ruminants and wild fires make up a small amount of the total ruminant source and total biomass burning; processes relating to these will be discussed in 1.5.1 and 1.5.3 respectively.

It has also been suggested that CH_4 may be formed in situ in terrestrial plants

under oxic conditions by an unknown process (Keppler et al., 2006). However, plants do not have the necessary biochemical pathways to synthesize methane and therefore are not a major source of methane (Nisbet et al., 2009). Plants do have an important role in the transport of methane produced in wetlands to the atmosphere (Pangala et al., 2015).

1.5 Anthropogenic Sources

1.5.1 Ruminants

Ruminants may be both native and domesticated and include cattle, sheep and goats. They are a significant source of anthropogenic methane with 94% of animal emissions being from domesticated animals (Thorpe, 2009). Domesticated ruminants were estimated to produce around 99 Tg of methane in 2014 (FAO, 2016). Cattle (for beef and dairy production) are the main ruminant sources, in 2014 cattle contributed to 73% of the global ruminant CH_4 emissions (Table 1.2) (FAO, 2016). Livestock is used for 70% of global agricultural land. Deforestation for livestock land mainly occurs in the tropics and contributes to greenhouse gas emissions (Thorpe, 2009).

CH_4 is produced in their digestive systems (multi-chambered stomachs) by anaerobic microbial activity (enteric fermentation). In enteric fermentation hydrogen is released by microbes during the fermentation of plant based food. The hydrogen is used by the methanogens converting CO_2 to CH_4 . Around 87% of CH_4 is released through the mouth (eructation) of the rumen (Saunois et al., 2016; Aluwong et al., 2013). Factors influencing methane emissions vary with geographical location, the composition and quality of the feed, feed intake, pro-

Ruminant	CH ₄ emissions (Tg yr ⁻¹)	% of Total
	2014	2014
Cattle	72.5	73.0
Buffalo	10.7	10.8
Sheep	10.7	10.8
Goats	5.0	5.1
Camels	1.3	1.3
Swine	1.1	1.1
Horses	1.1	1.1
Mules & Asses	0.5	0.6
Llamas	0.3	0.3
Total	99.29	

Table 1.2: 2014 global CH₄ emissions from Ruminants (FAO, 2016).

cessing of feed and the breed of the animal (Hook et al., 2010).

1.5.2 Waste

Waste sources include the decomposition of biodegradable waste in landfills, waste waters, animal waste and human waste by microorganisms (Dlugokencky et al., 2011) due to anoxic conditions and an abundance of acetate, CO₂ and H₂ (Ciais et al., 2013). These sources are estimated to produce between 67 and 90 Tg yr⁻¹ (Ciais et al., 2013). Saunois et al. (2016) estimates these sources without including animal waste contribute to 52-63 Tg yr⁻¹ (bottom-up). Factors affecting the production of CH₄ from waste are the waste composition, moisture content, pH and temperature. pH and temperature influence the bacteria type for the rate of gas generation. In landfill different biodegradable waste components have different degradation rates; food and green waste is readily degradable whereas wood, paper, textiles and other materials degrade more slowly (Machado et al., 2009). In developed countries landfill sites tend to be managed through gas control (through gas collection or flaring), source separation and treatment of

separated biodegradable waste and the application of a cover material (for example soil and clay) to promote methanotrophs. In developing countries the gases produced from biodegradation in landfill receive no treatment and are directly released into the atmosphere (Saunois et al., 2016). Wastewater is treated in sewage or effluent treatment plants with the amount of organic degradable material determining the CH_4 emissions. Developed countries tend to use aerobic wastewater treatment so CH_4 emissions are small. In developing countries there is little collection of wastewater so anaerobic environments such as latrines, open sewers or lagoons are predominant (EPA, 2013).

1.5.3 Biomass Burning

Biomass burning includes forest fires from deforestation, shifting cultivation and wildfires (from lightning strikes) and fuel wood, for cooking, heating homes and industry (Chanton et al., 2000). The term biofuel burning may also be used as a term for burning in stoves, boilers, fireplaces etc. (Saunois et al., 2016). The CH_4 is emitted from incomplete combustion with the emissions depending on the amount of biomass, burning conditions and the composition of the biomass. It is estimated that biomass burning (including biofuel burning) emits between 27-35 Tg yr^{-1} (bottom-up) of global CH_4 emissions (EPA, 2013; Saunois et al., 2016). Most biomass burning occurs in the tropics and subtropics and up to 90% of this is thought to be anthropogenic (Crutzen and Andreae, 1990) with forests and savannahs burned for land clearance. It is difficult to estimate the amount of biomass burning due to the varied nature of burning in developing countries with many smaller fires being undetected (Saunois et al., 2016). Biomass burning occurs during the dry season. The seasonal changes between the wet and dry

seasons are dominated by the intertropical convergence zone (ITCZ) (Mitsch et al., 2010).

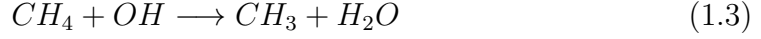
1.5.4 Fossil Fuels

Fossil fuel sources can range from extraction and use, for example coal extraction, crushing, processing and abandoned mines; oil extraction and gas flaring and natural gas extraction, processing and distribution (Dlugokencky et al., 2011). These are thermogenic sources and come from the transformation of organic matter into fossil fuels over a geological period of time (Ciais et al., 2013). In total these sources are estimated to produce 114-133 Tg yr⁻¹ (Saunois et al., 2016). Coal mining is estimated to emit 26-50 Tg yr⁻¹. CH₄ is stored in coal seams and is released from ventilation shafts during mining and during post-mining operations, processing and transport as well as waste piles (Saunois et al., 2016; EPA, 2013).

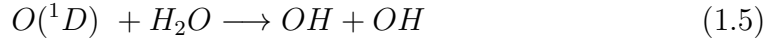
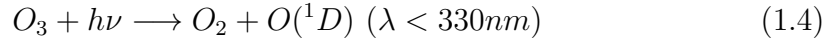
Oil and gas is estimated to emit 69-88 Tg yr⁻¹ of CH₄. CH₄ is the main component of natural gas and is emitted during its production. Oil production and processing also emits CH₄ as natural gas is commonly found with oil deposits. In both of these settings CH₄ is a fugitive emission through leaking equipment, flaring and venting (Saunois et al., 2016; EPA, 2013).

1.6 Atmospheric Chemistry and Sinks

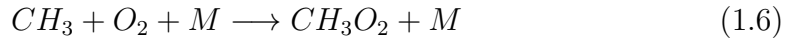
Oxidation by the hydroxyl radical (OH) is the main sink of CH₄ (Equation 1.3). This process predominantly occurs in the troposphere and contributes to 90% of the methane sink of surface emissions (Ciais et al., 2013). OH abundance is therefore related to CH₄ lifetime which is estimated to be 9.1 ± 0.9 years (Prather et al., 2012).



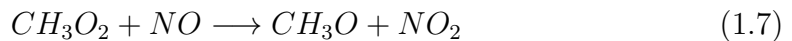
OH radicals are produced through the photolysis of ozone (O₃) (Equation 1.4) forming an excited oxygen atom (O(¹D)) which then combines with water vapour (Equation 1.5) (Voulgarakis et al., 2013):



High levels of ozone, shortwave radiation and humidity increase OH production decreasing the CH₄ lifetime, for example in the tropics (Voulgarakis et al., 2013; Dlugokencky et al., 2011). The methyl radical, CH₃, reacts rapidly with O₂ and forms the methyl peroxy radical, CH₃O₂ (M is a molecule such as N₂) (Seinfeld and Pandis, 2006) (Equation 1.6):



In the troposphere CH₃O₂ reactions with NO and HO₂ are the most important. These reactions are dependent on the concentration of NO and NO₂ (Seinfeld and Pandis, 2006). With sufficient NO the reaction (Equation 1.7) forms a methoxy radical and NO₂. The methoxy radical may then form formaldehyde (CH₂O) and the HO₂ radical (Equation 1.8):

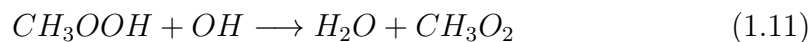
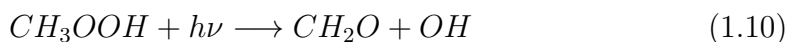




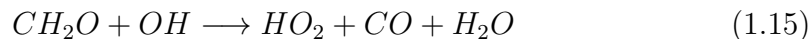
The HO_2 reaction with CH_3O_2 (Equation 1.9) forms methyl hydroperoxide:



Methyl hydroperoxide may photolyze (Equation 1.10) or react with OH (Equation 1.11, 1.12):

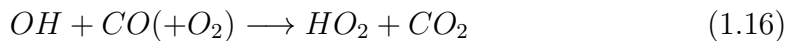


Formaldehyde may undergo photolysis forming HCO or CO (Equation 1.13 & 1.14) or react with OH forming CO (Equation 1.15):



CO is the principle product of methane oxidation. It reacts with OH to form

CO₂ (Equation 1.16) (Seinfeld and Pandis, 2006):



OH has a short lifetime of a few seconds as it reacts rapidly. It preferentially reacts with CO but also reacts with CH₄ and NMVOCs (Non-methane volatile organic carbon) to produce HO₂ (e.g. Equation 1.16) or an organic peroxy radical (e.g. Equation 1.11 & 1.12) (Naik et al., 2013). It is therefore not possible to directly estimate the concentration of OH in the atmosphere so modelling is essential to help constrain it. Methyl chloroform (CH₃CCl₃) is the main constraint on OH concentration as it has well known sources and there is very little of it. OH can therefore be estimated by the rate of methyl chloroform loss (Voulgarakis et al., 2013).

Around 454-617 Tg yr⁻¹ of CH₄ was lost through OH oxidation in the 2000s (Kirschke et al., 2013). The lifetime of CH₄ will increase from around 9-10 years to 12 years with more CH₄, or other greenhouse gases, as this will result in a decrease of OH (Voulgarakis et al., 2013). The short lifetime, in comparison with CO₂ which has a variable lifetime of tens to thousands of years (Archer et al., 2009), means that reducing these emissions would have a more rapid impact. Other smaller methane sinks include the reaction of chlorine atoms within the marine boundary layer (Equation 1.18) and reactions in the stratosphere with OH, Cl and O(¹D) (Cicerone and Oremland, 1988). These are estimated to remove between 13-37 Tg yr⁻¹ and 16-84 Tg yr⁻¹ of CH₄ in the 2000s respectively (Kirschke et al., 2013).



Methane oxidation also occurs by methanotrophic bacteria in aerobic soil or in freshwater at the anoxic-oxic boundary, following the sequence below (Cicerone and Oremland, 1988; Whiticar, 1999):



It may also occur through anaerobic oxidation, usually in marine or brackish sediments at the base of the sulphate reduction zone (Whiticar, 1999) by anaerobic methanotrophic archaea which gain energy from the oxidation of CH_4 , with sulphate being the final electron acceptor (Equation 1.20) (Knittel and Boetius, 2009).



The soil sink is estimated to remove between 9-47 Tg yr⁻¹ of CH_4 in the 2000s (Kirschke et al., 2013).

1.7 Methane Isotopes

It is difficult to quantify the emissions; wetlands and biomass burning are widely distributed, emissions change with season and sources are affected by climate and land use changes (Dlugokencky et al., 2009). The different sources of methane have different affinities for ^{13}C and ^{12}C isotopes, so $^{13}C/^{12}C$ ratios, which is expressed as $\delta^{13}C$, in per mil ‰ relative to the standard Vienna Peedee belemnite (VPDB) (Equation 1.21).

$$\delta^{13}C = \left(\frac{\left(\frac{^{13}C}{^{12}C} \right)_{\text{sample}}}{\left(\frac{^{13}C}{^{12}C} \right)_{\text{standard}}} - 1 \right) * 1000 \text{ ‰} \quad (1.20)$$

$\delta^{13}\text{C}$ signatures may be used to distinguish between sources of CH_4 . Relative to background ambient air which has a $\delta^{13}\text{C}$ of -47‰ , emissions can be either enriched or depleted in ^{13}C (Table 1.3) (Kirschke et al., 2013).

Source	$\delta^{13}\text{C} \text{ ‰}$
Coal and Industry	-35 ± 3
Gas North Sea	-34 ± 3
Gas Siberia	-50 ± 3
Ruminants C4 diet	-49 ± 4
Ruminants C3 diet	-70 ± 4
Biomass burning C4 vegetation	-17 ± 3
Biomass burning C3 vegetation	-26 ± 3
Landfills	-53 ± 2
Wetlands - swamps	-55 ± 3
Wetlands - bogs & tundra	-65 ± 5

Table 1.3: General $\delta^{13}\text{C}_{\text{CH}_4} \text{ ‰}$ source signatures from Dlugokencky et al. (2011).

Hydrogen isotopes, D/H (δD) may also be used to distinguish between sources of CH_4 , however are not analysed in this thesis as a larger sample volume would be needed and it is hard to analyse with good precision (Brass and Röckmann, 2010).

CH_4 from biological origins such as methanogens is depleted in ^{13}C as the bacteria have a preference for ^{12}C during production (Quay et al., 1991). The molecules with the lowest isotopic mass (e.g. acetate being $^{12}\text{CH}_3\text{COOH}$ rather than $^{13}\text{CH}_3\text{OOH}$) diffuse and react more rapidly than molecules with a higher isotopic mass (Whiticar, 1999). Different production pathways also result in different isotopic signatures. CH_4 in marine or other saline environments is usually more depleted than in freshwater as carbonate reduction is the main methanogenic pathway in marine environments and acetate fermentation is the main pathway in freshwater environments (Whiticar, 1999). The isotopic composition of the pre-cursor material affects CH_4 produced from decomposition,

digestion or burning. C3 plants (for example woody trees or temperate crops) and C4 plants (dominant in tropical grasslands) have different photosynthetic pathways. C4 vegetation pre-concentrates CO_2 leaving a more enriched $\delta^{13}\text{C}$. Therefore the decay of C3 plants produce a ^{13}C depleted signature compared to the decay of C4 plants (Whiticar, 1999; Dlugokencky et al., 2011).

Methanotrophs consume CH_4 through aerobic oxidation or anaerobic oxidation. ^{12}C is preferentially consumed by the methanotrophs leaving the residual CH_4 enriched in the heavier isotope ^{13}C (Chanton et al., 2005). Figure 1.2 shows the isotopic variations associated with CH_4 production and oxidation.

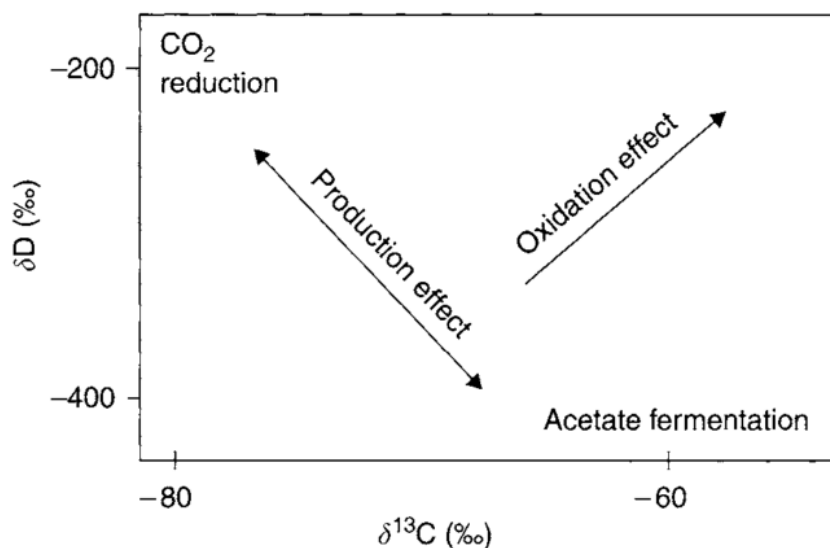


Figure 1.2: Variation in $\delta^{13}\text{C}$ and δD with CH_4 production and oxidation mechanisms (from: Chanton et al., 2005). δD , the stable isotopes of hydrogen, is not studied in this thesis however its composition is also relative to the production pathway and oxidation.

In general thermogenic sources (e.g. coal & gas), with isotopic values of -30‰ to -50‰ , are isotopically heavier than biogenic sources. This is due to factors such as precursor compounds and formation at higher temperatures (Whiticar, 1999)

There is little fractionation of $^{13}\text{C}/^{12}\text{C}$ during burning so the isotopic composition of the pre-cursor material (e.g. C3 or C4 plants) will be similar to that of the emitted methane (Quay et al., 1991). In relation to biogenic CH_4 , pyrogenic CH_4 , formed at higher temperatures, is enriched in the heavier isotope (Quay et al., 1991). Flaming fires are hotter than smouldering conditions so have a higher combustion efficiency and it has been suggested that CH_4 emitted from flaming fires is enriched in $\delta^{13}\text{C}$ by 2 - 3 ‰ (Chanton et al., 2000).

As well as variation in the quantities of different isotope sources, changes in $\delta^{13}\text{C}$ may also be from isotope dilution by a changing reservoir of total atmospheric CH_4 (Reeburgh, 2003). Sink processes have a kinetic isotope effect (KIE) which removes ^{12}C preferentially to ^{13}C (Platt et al., 2004). This is due to the lighter ^{12}C isotope reacting faster than the heavier ^{13}C isotope, therefore enriching the atmosphere in ^{13}C (Reeburgh, 2003).

The KIE effect for OH has been calculated to be 5.4 ‰ (Allan et al., 2001) and the KIE from the Cl sink enriches atmospheric CH_4 by $2.6 \pm 1.2\text{‰}$ (Allan et al., 2007). The global average $\delta^{13}\text{C}$ source signature is between -53.6 and -53.4 ‰, with the sink fractionation background ambient air at present has a $\delta^{13}\text{C}$ of -47.4 to -47.2 ‰ (Nisbet et al., 2014).

It is important to identify the isotopic composition for both natural and anthropogenic sources of methane to allow better constraints on the estimates of sources and sinks of the budget (Chanton et al., 2005). This will both increase our understanding of the global methane budget and improve understanding of the mechanisms of sudden growth events.

1.8 The recent global CH₄ growth

Global CH₄ is measured through the World Meteorological Organisation (WMO) Global Atmospheric Watch (GAW) programme. These CH₄ observations are reported on the WMO CH₄ scale or with a conversion factor to the World Data Centre for Greenhouse Gases (WDCGG) by laboratories participating in GAW (Dlugokencky et al., 2011).

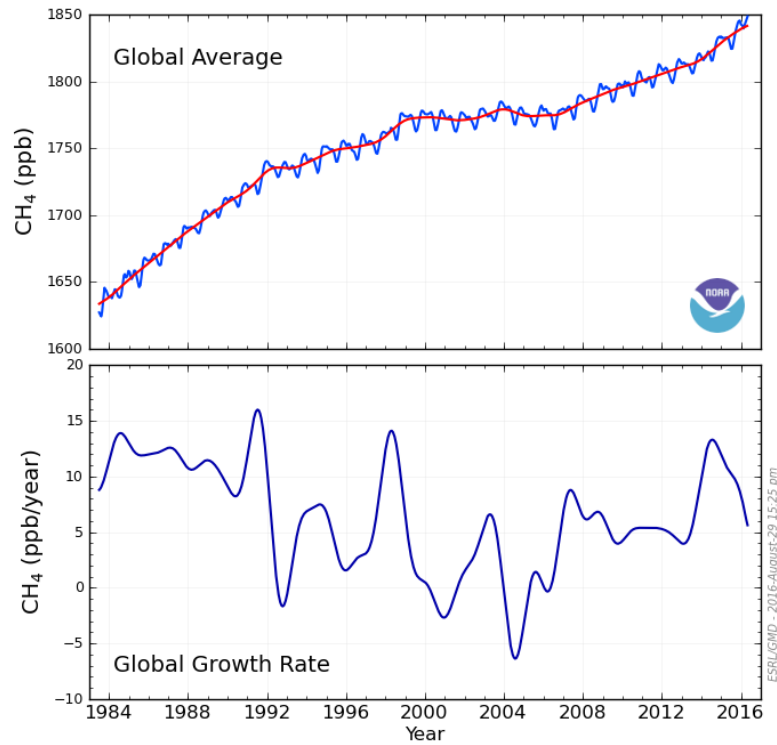


Figure 1.3: a) The blue line shows the average global methane (in ppb) between 1983 and the end of 2015. The red line shows the deseasonalised trend. b) The growth rate from the time derivative of the deseasonalised trend in plot a (Dlugokencky, 2016).

Figure 1.3 shows the global methane record and growth rate. From the early 1980s to 1992 global methane increased at around 12 ppb yr⁻¹, driven by anthro-

pogenic emissions. Between 1992 and 2007 the overall growth rate slowed with inter-annual events giving sharp changes. The 1991/1992 decline in the global growth rate relates to the eruption of Mt Pinatubo and the economic collapse of the former Soviet Union (including coal industry then after Russian investment cutting gas industry leaks). In 1997 - 1998, the growth rate increased relating to a strong El Nino (Dlugokencky et al., 2011).

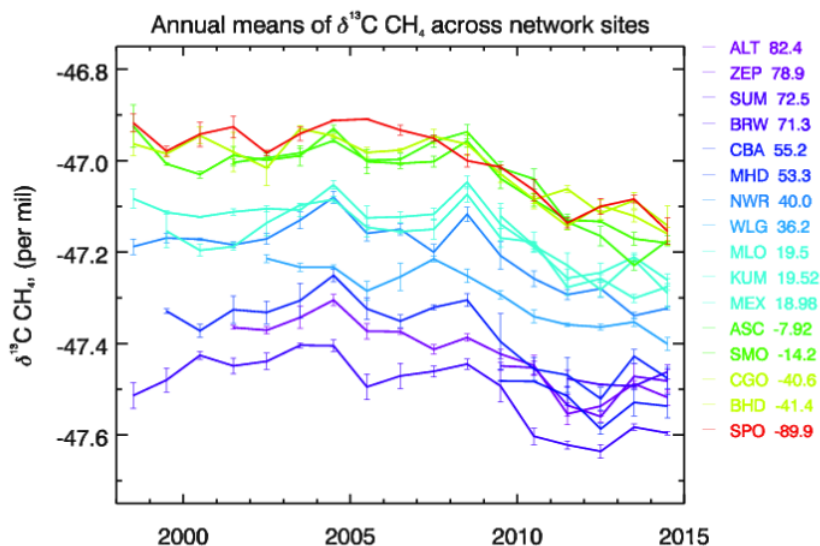


Figure 1.4: Yearly mean NOAA station $\delta^{13}\text{C}$ methane trends, the right column of the NOAA station gives the latitude. (Nisbet et al., 2016).

In early 2007 methane began to rise again (Fig 1.3). This rise shows one of the most sustained growth excursions on record (NOAA records began in 1983) however the cause of this is very poorly understood. Between 2007 and 2013 the global average CH_4 mole fraction increased by $5.7 \pm 1.2 \text{ ppb yr}^{-1}$ with a strong growth of $12.5 \pm 0.4 \text{ ppb}$ in 2014. During this global increase, globally, $\delta^{13}\text{C}$ has shifted to more negative values (Fig 1.4) (Nisbet et al., 2016).

This sustained atmospheric methane growth has occurred in many latitudinal zones (Fig 1.5). In early 2007 in the Arctic and boreal zone show a rapid methane

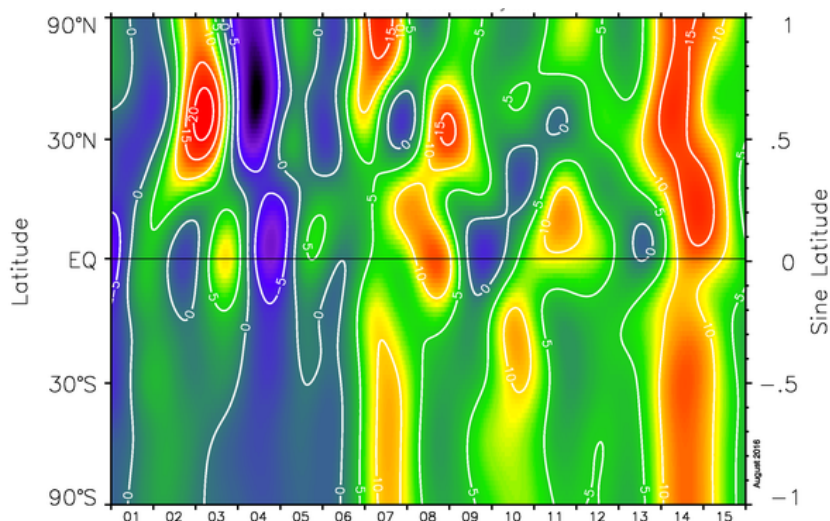


Figure 1.5: The global methane growth rate trends in ppb yr^{-1} between 2000 and 2015 plotted against sine of latitude. Growth is shown in red, yellow and green and decline in blue (Dlugokencky, 2016).

growth, after this period the rapid growth is dominated by latitudes south of this region, significantly in 2008 and 2010 to 2011. In 2014 the growth was especially strong at all latitudes (Nisbet et al., 2016).

1.9 Introduction to Tropical Methane

The tropics are thought of as a 'neglected' part of the methane budget. Measurements are generally made in more viable areas (Fig 1.6), despite evidence that natural tropical sources are responsible for some of the largest methane emissions (Dlugokencky et al., 2011; Nisbet et al., 2016). Emissions from the tropics produce around 200 Tg yr^{-1} of methane, about 40% of the global methane budget with the three largest methane emitting regions being South America, Africa and South East Asia. The variability in CH_4 removal through OH radicals is also dominated by the tropics as photochemistry is active throughout the year

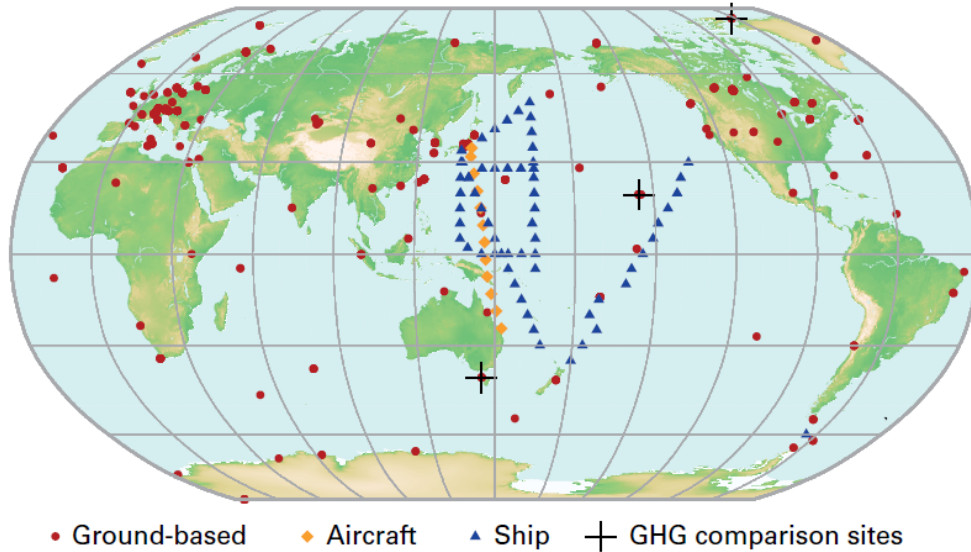


Figure 1.6: The GAW global network for CO₂ over the last 10 years, CH₄ is similar (WMO, 2016).

(Bousquet et al., 2006; Saunois et al., 2016).

Figure 1.7 shows top-down (direct atmospheric measurements) and bottom-up (the sum of estimated fluxes of individual processes) regional breakdowns of source emissions between 2000 and 2009. These bottom-up and top-down emissions differ and more measurements are needed to close these discrepancies in CH₄ sources (Nisbet et al., 2014; Kirschke et al., 2013; Saunois et al., 2016). Using $\delta^{13}\text{C}$ isotope source signatures means global and regional emissions may be constrained in models with better source apportionment giving a better understanding of tropical methane growth and also closing the gap between bottom-up and top-down emissions estimates (Fisher et al., 2017).

Emissions include wetlands, with up to 30% of the global wetlands located in the tropics (Mitsch et al., 2010) and biomass burning, significant in Africa and tropical South America with bottom-up estimates being less than top-down

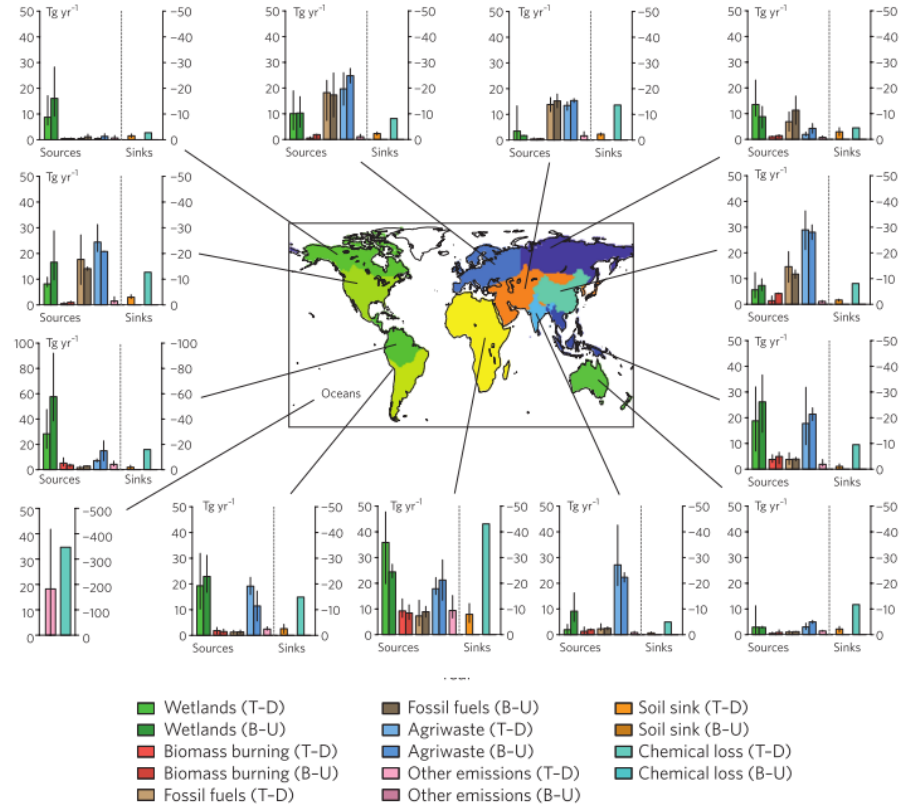


Figure 1.7: Regional methane emissions between 2000 and 2009. Top-down emissions are lighter coloured bars and bottom-up are darker coloured bars (Kirschke et al., 2013).

estimates due to satellites not detecting small fires. Other tropical sources include rice agriculture, termites, ruminants (domesticated and wild), fossil fuels and waste (Kirschke et al., 2013). Figure 1.8 shows the global spatial distribution of methane emissions from wetlands, fossil fuels, agriculture & waste and biomass burning highlighting these sources in the tropics.

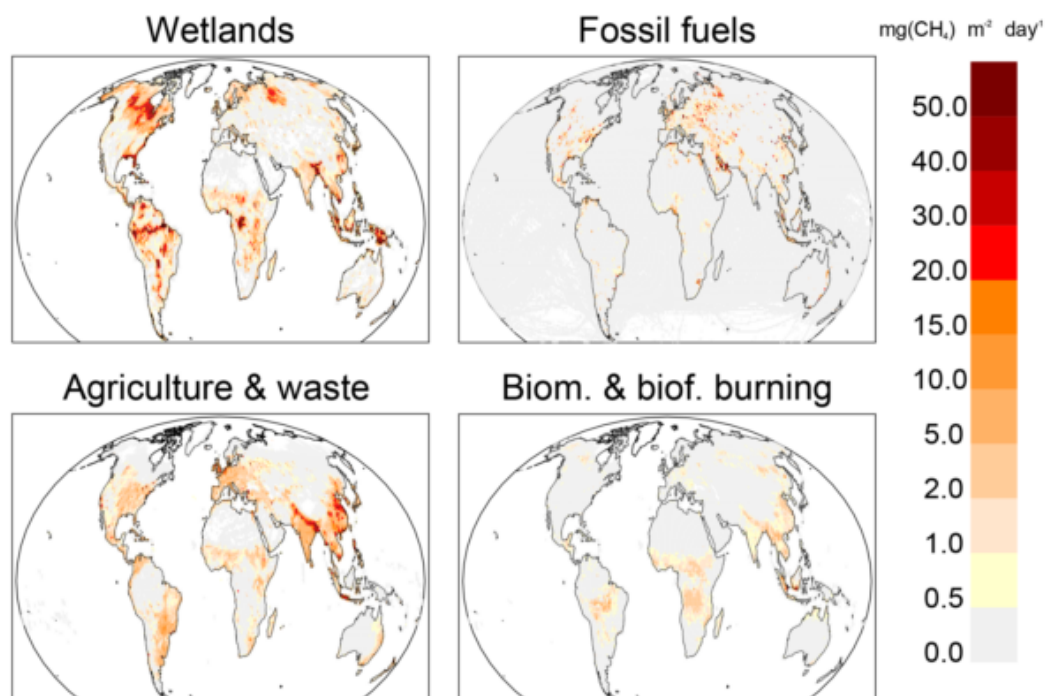


Figure 1.8: Methane emissions ($\text{CH}_4 \text{ m}^{-2} \text{ day}^{-1}$) from wetlands, fossil fuels, agriculture & waste and biomass burning between 2003 and 2012. The wetland emissions are the average emission per day of 11 models. The Fossil fuel, agriculture & waste and biomass burning are from mean values from EDGAR V4.2 and other models (Saunois et al., 2016).

A more detailed discussion on Tropical sources may be found in Chapter 3 ($\delta^{13}\text{C}$ Tropical Methane Source Signatures).

1.10 Aims

The aim of this research is to use methane mole fraction measurements and $\delta^{13}\text{C}$ isotopes to contribute to an increased understanding of the sustained tropical methane growth. The thesis has three sections:

- Contributing to the characterisation of tropical methane source signatures, providing narrower isotopic ranges for regional areas of the tropics, and therefore improve modelled regional source signatures.
- Measuring and interpreting methane measurements from the Institute of Ocean and Earth Sciences at Bachok, Malaysia.
- Using a new approach to sample air masses at different heights using Unmanned Aerial Systems (UASs) on Ascension Island.

Combining these studies will help to give an insight into the recent sustained methane growth in the tropics and how to further improve tropical methane monitoring.

Chapter 2

Methods

2.1 Sampling Locations

Atmospheric samples were taken from locations in the tropics and areas that influence the tropics to monitor the CH₄ mole fraction and identify the isotopic signatures of methane sources (Fig 2.1).

These sites were chosen to fill in tropical CH₄ source data gaps in wetlands, agriculture and biomass burning (see Chapter 3, $\delta^{13}\text{C}$ Tropical Methane Source Signatures). Samples were taken as an addition to other campaigns allowing for more data to be collected for this thesis. Samples at Ascension Island and Bachok, Malaysia were taken as part of field campaigns to complement continuous monitoring.

2.1.1 Ascension Island

Ascension Island (7°58'S, 14°24'W) is a South Atlantic background site. It experiences near constant South East Trade winds below the Trade wind inversion (TWI) bringing air from central South America and the Southern Ocean. Above

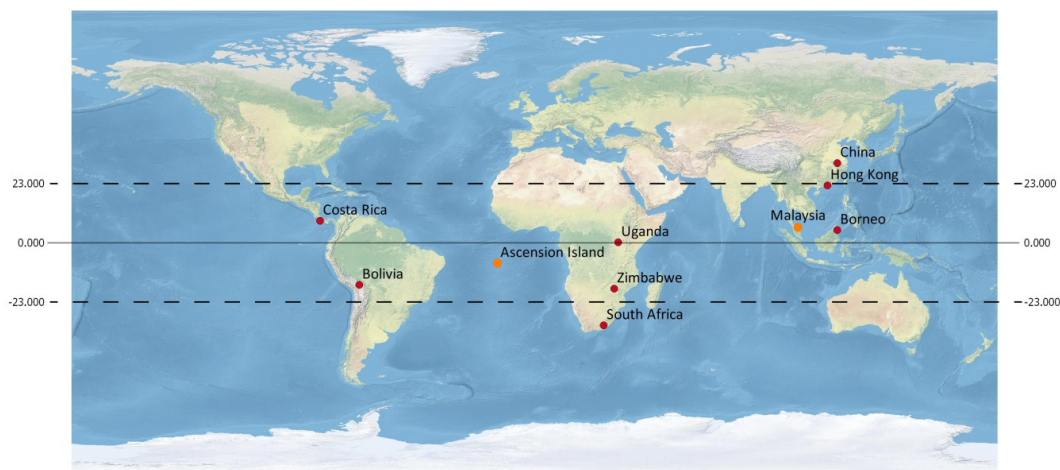


Figure 2.1: Map of tedlar bag sampling sites in this thesis (red). Ascension Island and Bachok, Malaysia (orange) have longer term monitoring as well as bag samples. The Hong Kong sites were also part of a mobile monitoring campaign undertaken by the RHUL GHG group.

the TWI the air mainly arrives from over tropical and southern Africa. Ascension Island is therefore ideally located to measure the tropical Atlantic background air in the boundary layer and to study African sources of CH_4 by sampling the mid-troposphere above the TWI.

Royal Holloway (hosted by the UK Met Office) have measured CH_4 mole fractions on Ascension Island (see section 3.3.1) and collected flask samples for CH_4 mole fractions and $\delta^{13}\text{C}$ (See section 3.2) since 2010.

Two field campaigns during September 2014 and July 2015 used Unmanned Aerial Systems (UASs) to collect air samples in Tedlar bags from different heights, up to 2700 m above mean sea level, above and below the TWI. This allowed for sampling of both remote air in the marine boundary layer below the TWI, and air masses above the TWI that had been lofted by convective systems in the African tropics. More information is given in Chapter 5 (Methane mole fraction and $\delta^{13}\text{C}$ above and below the trade wind inversion at Ascension Island in air

sampled by aerial robotics), see Greatwood et al. (2016) for details of the UAS setup in Appendix A.

2.1.2 Bachok, Malaysia

The Institute of Ocean and Earth Sciences (IOES) research station (6 °00'N, 102°25'E) has been built as part of the University of Malaya, located in the Kelantan province on the east coast of Peninsular Malaysia by the South China Sea. An observation tower built at the station aims to study long range transported pollution, air sea exchange, and coastal meteorology. Field work was undertaken from January to February 2014 during a campaign set up by the University of East Anglia (UEA), University of Cambridge and the University of Malaya. Continuous CH₄ and CO₂ mole fractions were measured using an LGR (Los Gatos Research) analyser (see section 2.3.2) and samples were collected to measure CH₄ and $\delta^{13}\text{C}_{\text{CH}_4}$ from both the coastal tower site, at an altitude of 19m, and local sources (see section 3.2). More information is given in Chapter 4 (Influence of local methane emissions on a tropical monitoring site).

2.2 In Situ Sampling

Tedlar bags (SKC Ltd) between 3 and 5 litres are used for sampling in situ as they are inert. They are filled using a battery operated micro diaphragm pump (KNF Neuberger Ltd.) (Fig 2.2). Before the bag is connected to the pump and opened the sample line was flushed for 10 seconds to remove contamination. The bag was then filled for about a minute until about 75% full and is then closed. Enough sample is taken to complete multiple analyses but the bag is not over filled due to risks of leaking or expansion during transport.

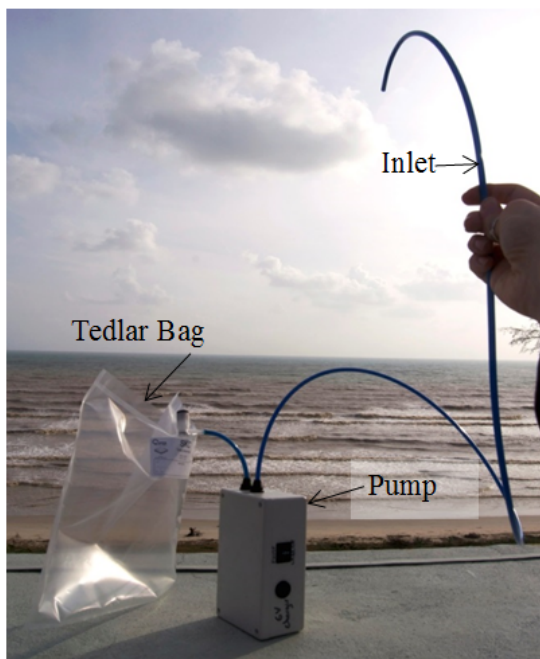


Figure 2.2: Sampling method shown in Bachok, Malaysia.

The sample name, location, height and meteorology are noted on the sample sheet and labelled on the sample bag. Care is taken to stand downwind during filling the bag to prevent contamination from the person taking the sample and the bags were filled at varying distances from the sources to allow for a range of concentrations.

Wetland and rice paddy samples were taken at heights between 5 cm and 3 meters above the source. For this thesis wetland and rice paddy sample locations include Hong Kong (samples taken by R. Brownlow, R. E. Fisher, D. Lowry and E. G. Nisbet), Uganda (samples taken by E. G. Nisbet), Bolivia (samples taken by E. G. Nisbet), Borneo (samples taken by N Harris), South Africa (samples taken by E. G. Nisbet) and Costa Rica (samples taken by A. Clarke). Ruminant samples were taken a few cm away from the mouth to 2-3 m away from the ruminants. Ruminant sample locations include Zimbabwe (samples taken by T.

Broderick) and Hong Kong (samples taken by R. Brownlow and R. E. Fisher). Biomass burning samples were taken between 30 cm and a few meters away from the fires. Both the China (samples taken by M. Wooster) and Zimbabwe fires (samples taken by D. Lowry and N. D. Rata) were controlled burns whereas the Bachok fires (samples taken by R. Brownlow) were for burning local waste. The China and Bachok fire samples were taken throughout flaming and smouldering stages. Background air samples were taken upwind of the sources.

The Tedlar bags were tested in the lab over periods of 3 months, and are able to store CH_4 . CO_2 leaks into the bags so the analysis is not reliable for CO_2 .

On Ascension Island stainless steel flasks are regularly sampled for longer term monitoring of CH_4 mole fractions and $\delta^{13}\text{C}_{\text{CH}_4}$. The flask samples are expensive and harder to transport so it is more practical to use Tedlar bags for a large number of samples. The method is simple and also allows further samples to be taken during separate field campaigns.

2.3 Sample Analysis

2.3.1 Picarro CRDS

CH_4 and CO_2 mole fractions and H_2O % are measured at RHUL using a Picarro 1301 CRDS (Cavity Ring-Down Spectroscopy). CRDS is a highly sensitive laser absorption technique which works by measuring infrared absorption lines of gaseous samples which absorb specific wavelengths of light. $^{12}\text{CO}_2$, $^{12}\text{CH}_4$ and water vapour each has a well-known unique near infrared absorption spectrum in their gas phase. The mole fraction is determined by the strength of absorption, measured in parts per million (ppm) for CH_4 and CO_2 . The air sample is intro-

duced into the optical cavity and the laser enters the cavity through one of the partially reflective mirrors until the photo-detector reaches threshold level. The light within the cavity bounces between the mirrors which have high reflectivity ($>99.995\%$). The photo detector measures the time it takes for the light intensity to decrease exponentially to zero (ring down time) (Fig 2.3). Ring down time is dependent on the reflectivity of the mirrors as well as the absorption and scattering of the sample. In the Picarro instrument, when the laser is shut off, the light remains in the cavity producing a path length of tens of kilometers allowing for high sensitivity. Gas species such as CO_2 , CH_4 and water vapour absorb laser light meaning the ring down time is faster with higher greenhouse gas mole fractions (<http://www.picarro.com>; Crosson, 2008).

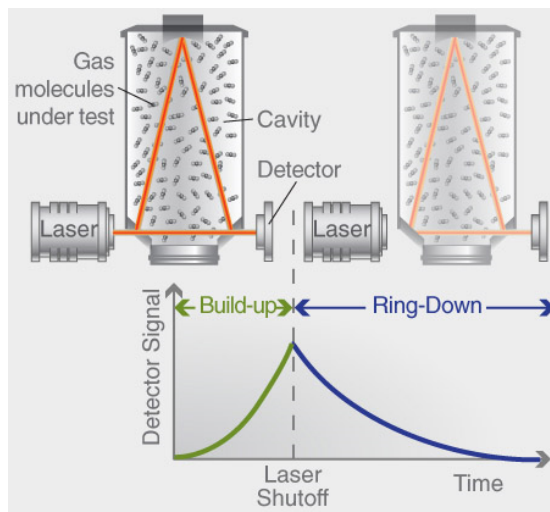


Figure 2.3: schematic diagram showing how the gas samples are measured during CRDS (<http://www.picarro.com>).

The Royal Holloway Picarro 1301 CRDS (Fig 2.4) is calibrated once weekly, as there is only a small drift from week to week, from three cylinders of air with methane mole fractions between 1.8085 to 2.0920 ppm on the NOAA04a scale (see: www.esrl.noaa.gov/gmd/cc1/ch4_scale.html, Dlugokencky, 2005). Each stan-

dard is run for 18 minutes with the last 10 minutes averaged. A target gas is measured during 2 days of the week for 18 minutes and the last 10 minutes being averaged with the standard deviation of this giving the repeatability for the methane mole fraction Fig(2.5). The Picarro CRDS measures linearly up to 20 ppm, so CH₄ samples with higher mole fractions must be diluted with nitrogen before analysis. 3 litre Tedlar bags were analysed for 240 seconds with the last 120 seconds of measurements being used for the mean mole fraction. If the bag samples had less air the bags were run for 120 seconds with 60 seconds being used for the mean mole fraction. Half a litre of air sample is kept in the bag for the $\delta^{13}\text{C}_{\text{CH}_4}$ isotope analysis (Fisher et al., 2017). The precision of the CRDS instrument for CH₄ mole fraction is ± 0.2 ppb for the standards and 0.4 ppb for the bag samples due to a shorter analysis time compared to the standards. The offset of the instrument can be calculated from a second target gas which has a known value of 2000.7 ppb, for 2015 the average value measured was 2000.6 ppb meaning there was an offset of 0.1 ppb.



Figure 2.4: Picarro 1301 CRDS in the RHUL lab.

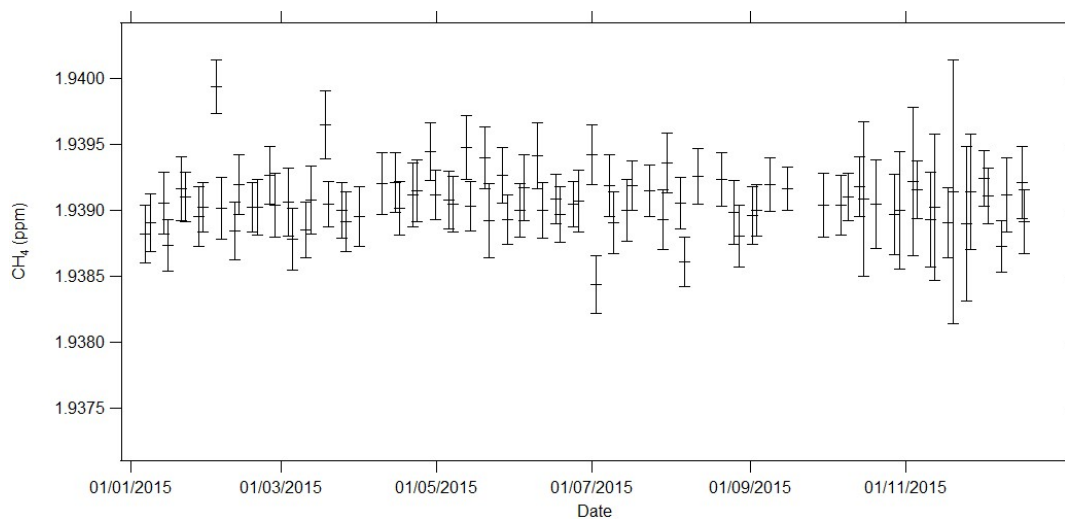


Figure 2.5: Picarro 1301 CRDS at RHUL Target values for 2015 (Error bars give the standard deviation of the average target value). The mean value for 2015 is 1939 ppb and the precision is ± 0.2 ppb.

Continuous high-precision greenhouse gas monitoring and flask sampling have been made by Royal Holloway, hosted by the Met Office, on Ascension Island since 2010. This Picarro 1301 CRDS system with a 6-gas calibration suit measures CH₄ and CO₂ from air taken through an inlet above the Met office station roof, 5 magl and 40 masl, with a precision of 0.5 ppb (Lowry et al., 2014).

2.3.2 Los Gatos Research analyser

The LGR (Los Gatos Research) analyser was used to take continuous CH₄, CO₂ and water vapour concentration measurements throughout the Bachok field campaign. The analyser uses off-axis integrated cavity output spectroscopy (OA-ICOS), a laser absorption technique which is similar to CRDS. It consists of a gas detection cavity with two high quality reflective end mirrors. The laser enters the cell at an off-axis angle which removes optical feedback from the cavity to the light source. The light is reflected multiple times filling the cavity and is lost through the mirrors, which are not 100% reflective. The light is measured by a photodetector and changes in intensity due to absorption (Nowakowski et al., 2009).

The instrument was installed on the Bachok tower in January 2014 sampling air at an altitude of 19m. It was calibrated before and after going to Bachok using the NOAA 09 and 10 cylinders in the RHUL laboratory and then the data was drift corrected.

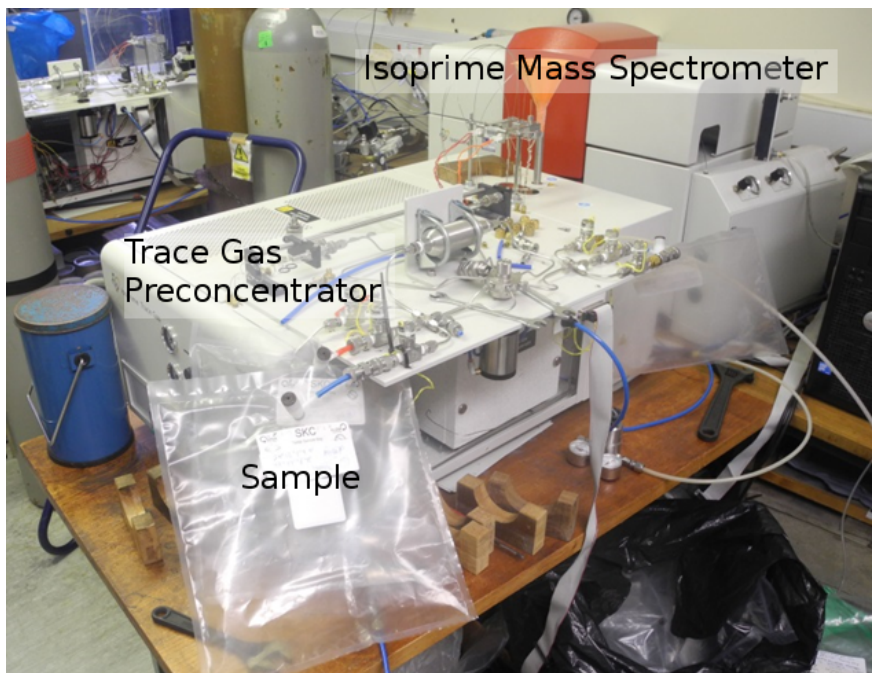


Figure 2.6: Continuous-flow gas chromatography/isotope-ratio mass spectrometry in the RHUL lab.

2.3.3 Continuous-flow gas chromatography/isotope-ratio mass spectrometry

Continuous-flow gas chromatography/isotope-ratio mass spectrometry (CF-GC/IRMS) allows for a highly precise $\delta^{13}\text{C}_{\text{CH}_4}$ isotopic analysis of methane with a repeatability of 0.05 ‰. The GV instruments Trace Gas preconcentrator and IsoPrime mass spectrometer are in a continuous-flow set up (Fig 2.6 & 2.7). Helium transports the air sample at around 20mL/min through magnesium perchlorate and carbosorb traps to remove water and CO_2 . CO in the air sample is then oxidised to CO_2 by Sofnocat catalyst and this is then trapped in a liquid nitrogen cryotrap at -196°C . CH_4 is oxidised to CO_2 in a combustion furnace and this resulting CO_2 is trapped and cryofocused in liquid nitrogen. The sample is passed through Nafion membrane to remove any water that may have been produced

during oxidation and is then separated from any residual gas. Part of the CO_2 is carried to the IsoPrime mass spectrometer at a flow rate of 0.3 mL/min and analysed (Fisher et al., 2006).

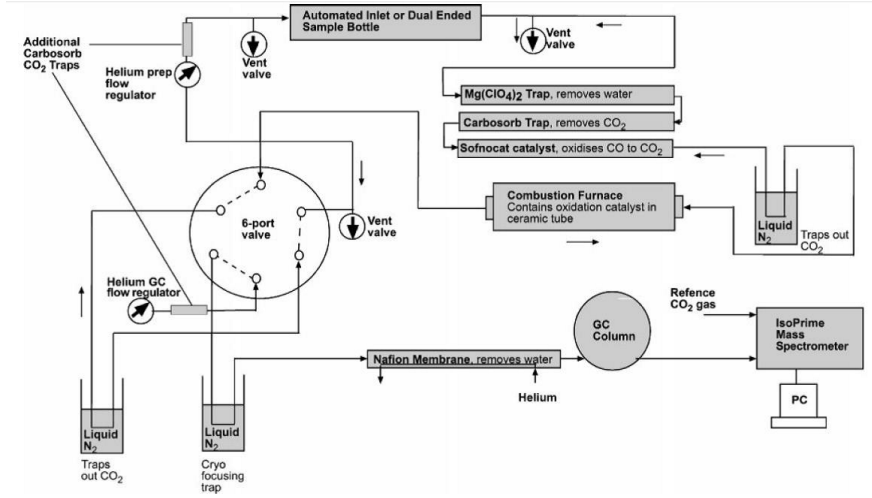


Figure 2.7: The Trace Gas CH_4 set up (Fisher et al., 2006).

An internal secondary standard (Table 2.1) is analysed at the beginning of each day at least four times until the measurements are stable and after every two samples to correct for drift. Sample measurements are made in triplicate with further measurements if results are not within 0.1 ‰ with each individual analysis taking around 20 minutes. Samples with a mole fraction of above 7 ppm are diluted with nitrogen. These results are then blank corrected and drift corrected against the difference of the mean of the secondary standard for that day and the true value of the secondary standard.

Standard	Value ‰	Dates
RHS669	-47.43	03/05/13 - 21/02/14
RHS673	-47.43	24/02/14 - 03/09/15
RHS676	-47.61	04/09/15 - 24/08/16
RHS677	-47.81	23/08/16 - Present

Table 2.1: Internal secondary standards

RHUL $\delta^{13}\text{C}$ measurements have been intercompared with labs at INSTAAR (The Institute of Arctic and Alpine Research, at the University of Colorado) who measure $\delta^{13}\text{C}$ in NOAA (National Oceanic and Atmospheric Administration) flasks and NIWA (National Institute of Water and Atmospheric Research, New Zealand). Before 04/09/15 an offset correction of 0.2 ‰ was removed from the data to bring measurements in line with those of INSTAAR, after this no correction was needed.

2.4 Analytical Methods

2.4.1 Keeling Plots

The Keeling plot method is used to identify the carbon isotope source signature for the excess CH_4 above background in the samples. The $\delta^{13}\text{C}$ is plotted against the inverse of the CH_4 mole fraction. Linear regression gives the isotopic source signature at the y-intercept (Fig 2.8). It is based on a mass conservation of carbon exchange between two reservoirs. (Pataki et al., 2003). C_a is the atmospheric mole fraction of a gas and C_b is the background atmospheric mole fraction and C_s is the mole fraction added by the source:

$$C_a = C_b + C_s \quad (2.1)$$

By assuming the conservation of mass:

$$\delta^{13}C_a C_a = \delta^{13}C_b C_b + \delta^{13}C_s C_s \quad (2.2)$$

Combining equations 2.1 and 2.2 the $\delta^{13}\text{C}$ source signature may be calculated:

$$\delta^{13}C_a = C_b(\delta^{13}C_b - \delta^{13}C_s) \times (1/C_a) + \delta^{13}C_s \quad (2.3)$$

$\delta^{13}C_a$ is the measured isotopic composition (the y values) and $1/C_a$ is $1/\text{CH}_4$ mole fraction (the x values) where the y axis intercept gives the isotopic signature of the excess CH_4 above background, $\delta^{13}C_s$. $\delta^{13}C_b$ is the background isotopic composition (Keeling, 1960; Pataki et al., 2003; Zazzeri et al., 2015).

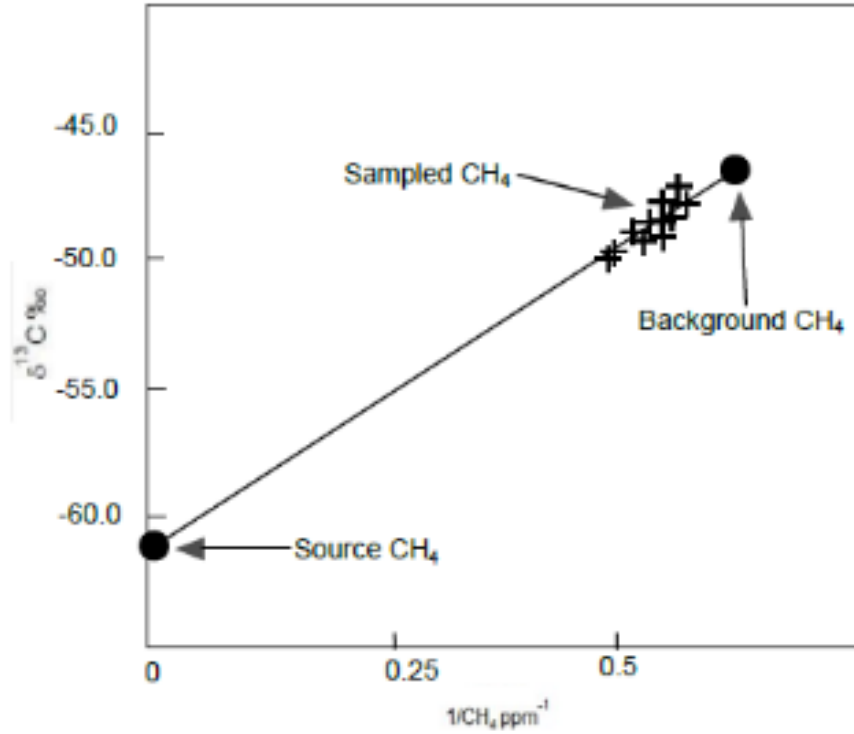


Figure 2.8: Illustration of a Keeling plot for CH_4 showing the two end points of the source and background in black circles with sampled air shown by the crosses, adapted from Pataki et al., 2003.

Linear regression is used to find the slope and intercept from the data. Ordinary least squares only takes into account one variable however Keeling plots have errors associated with both $\delta^{13}\text{C}$ and $1/\text{CH}_4$. For this reason orthogonal regression (also known as total least squares) is used. This method takes

into account both variables, minimising the square distance between the data points and the fitted line (Akritas and Bershad, 1996; Leng et al., 2007). The Bivariate Correlated Errors and intrinsic Scatter (BCES) program (available at: www.astro.wisc.edu/~mab/archive/stats/stats.html) accommodates the error changes across a variable (heteroscedastic measurement errors) with intrinsic scatter. BCES regression has been used to find the uncertainty of the Keeling plot intercept and therefore the $\delta^{13}\text{C}$ error (Akritas and Bershad, 1996; Zazzeri et al., 2015). The traditional Keeling plot method assumes the background value for both $\delta^{13}\text{C}$ and CH_4 does not change. A modified approach developed by Miller & Tans (2003) may be used to allow for a changing background, for example during a time series. From equations 2.1 and 2.2 a new set of equations allow the plotting of the data so that the background values may not be constant:

$$\delta^{13}C_a C_a = \delta^{13}C_b C_b + \delta^{13}C_s (C - C_b) \quad (2.4)$$

$$\delta^{13}C_a C_a = \delta^{13}C_s C_a - C_b (\delta^{13}C_b - \delta^{13}C_s) \quad (2.5)$$

Equation 2.5 is of the linear form $y = mx + c$ where the $\delta^{13}\text{C}$ source ($\delta^{13}C_s$) is m . This technique is used for background changes during the Bachok, Malaysia campaign.

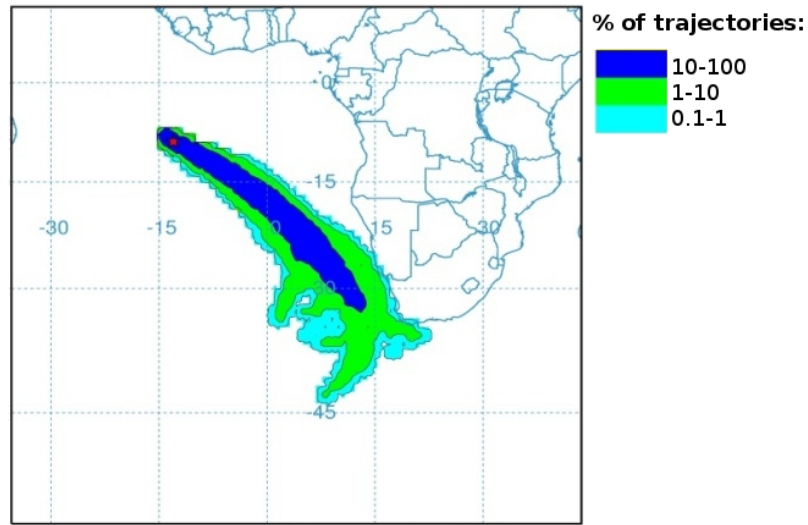


Figure 2.9: An example of an offline HYSPLIT trajectory run for July 2015 arriving at ground level on Ascension Island. Hysplit was run offline with GDAS archive meteorological data four times per day at 00:00, 06:00, 12:00 and 18:00 UTC for 120 backwards (Rolph, 2017; Stein et al., 2015).

2.5 Trajectories

2.5.1 NOAA HYSPLIT

Back-trajectory analysis is used to identify the origin of air masses using the HYSPLIT model (Hybrid Single Particle Lagrangian Integrated Trajectory Model) developed by NOAA’s Air Resources Laboratory (Rolph, 2017; Stein et al., 2015). HYSPLIT is based on a combination of Lagrangian and Eulerian methods (Stein et al., 2015). The Lagrangian method uses a moving frame of reference as the trajectory of air moves for calculating advection and diffusion and Eulerian method calculates the air pollutant concentrations using a fixed 3D grid as a frame of reference. The online trajectories are run backwards in time for either 240 or 120 hours to show where the arriving air mass had come from using the sample height. These are estimated by using observed wind fields backwards in time. The height

of the planetary boundary layer in the tropics is 1000 km or above so we can assume that in this region the air masses will pick up signatures from below. HYSPLIT was also used offline to run monthly multiple simulations which show the probability of the air masses being in a specified place. Figure 2.9 shows an offline HYSPLIT example run 120 hours back for air masses arriving at ground level on Ascension Island during July 2015. HYSPLIT was used in Chapter 4 and Chapter 5.

2.5.2 NAME

The UK Met Office Numerical Atmospheric dispersion Modelling Environment (NAME) was used for some publications in this thesis to identify potential CH₄ source regions for individual samples and daily ground monitoring and was run by a collaborator at the University of Cambridge. The current model is a Lagrangian particle-trajectory model. Particles are released from the source and tracked in the model atmosphere driven by the met data. It has modelling capabilities from meters to global scale (Jones et al., 2007). Figure 2.10 shows an example of a NAME plot run 7 days back arriving at Ascension Island during July 2015. NAME was used in Chapter 4 and Chapter 5.

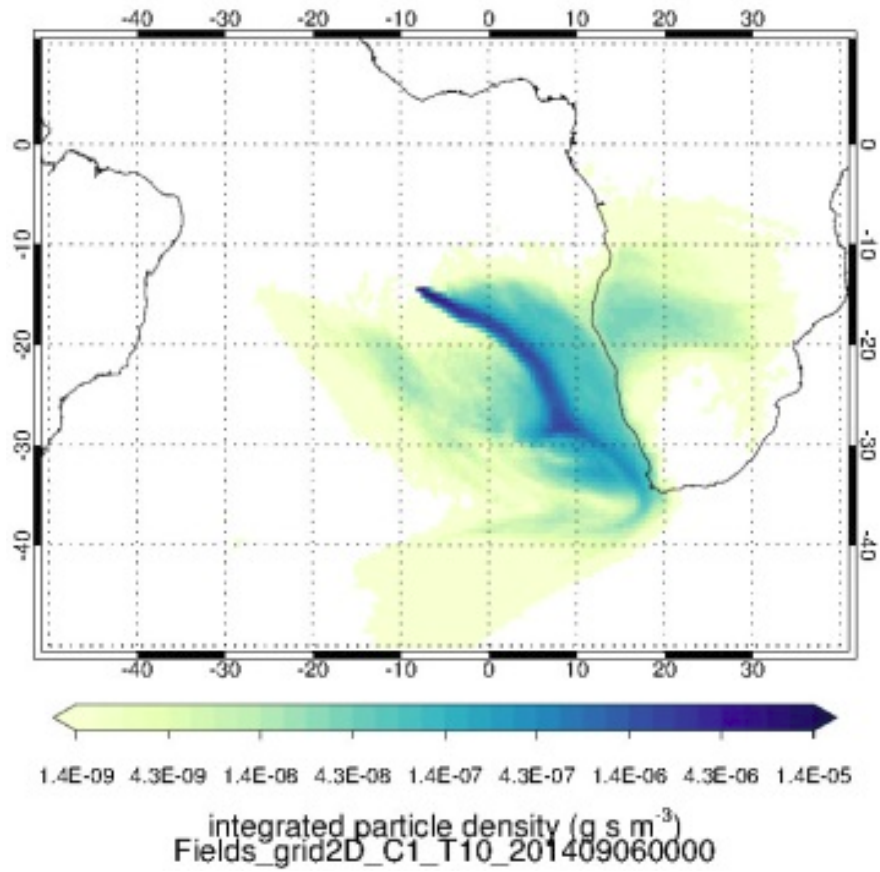


Figure 2.10: An example of a NAME plot run for 7 days back from the sample collection time and height on Ascension Island (this example is from 08 July 2015 09:38 75 masl) with particles being released at a rate of 100000 per hour for one hour, from a depth of 100 m centred on the sample height.

Chapter 3

Isotopic ratios of tropical methane emissions by atmospheric measurement and continental-scale variability.

This chapter is presented in paper format and has been submitted to Global Biogeochemical Cycles. R. Brownlow wrote the manuscript, plotted and interpreted the data. R. Brownlow, D. Lowry, R. E. Fisher, B. White & M. Lanoisellé analysed the samples at RHUL. M. J. Wooster and T. Zhang contributed to the Chinese biomass burning work. All the authors made suggestions and comments on the manuscript. R. Brownlow, R. E. Fisher, D. Lowry & E. G. Nisbet collected samples from Hong Kong. The acknowledgement section lists other sample collection contributions.

Isotopic ratios of tropical methane emissions by atmospheric measurement and continental-scale variability.

R. Brownlow¹, D. Lowry¹, R. E. Fisher¹, J. L. France², M. Lanoisellé¹, B. White¹, M. J. Wooster^{3,4}, T. Zhang^{3,4} and E. G. Nisbet¹

¹ Department of Earth Sciences, Royal Holloway, University of London, Egham, TW20 0EX, UK.

² Centre for Oceanic and Atmospheric Sciences, School of Environmental Sciences, University of East Anglia, Norwich, NR4 7TJ, UK

³ King's College London, Dept. of Geography, Strand, London WC2R 2LS

⁴ NERC National Center for Earth Observation, UK

Corresponding authors: Rebecca Brownlow (Rebecca.Brownlow.2009@live.rhul.ac.uk) and Euan Nisbet (e.nisbet@es.rhul.ac.uk)

Key Points:

- Methane $\delta^{13}\text{C}$ isotopic signatures have been measured in the tropics for wetland, rice, ruminant and biomass burning.
- Wetlands, rice and ruminants are depleted in ^{13}C but it is difficult to distinguish between them, biomass burning values are enriched in ^{13}C .
- An expected average annual isotopic signature has been calculated for Tropical South America and Africa.

Abstract

Tropical methane sources are an important part of the global methane budget and include natural wetlands, rice agriculture, biomass burning, ruminants, fossil fuels and waste. $\delta^{13}\text{C}_{\text{CH}_4}$ can provide strong constraints on methane source apportionment. For example, tropical wetlands give $\delta^{13}\text{C}_{\text{CH}_4}$ values between $-61.5 \pm 2.9 \text{ ‰}$ and $-53.0 \pm 0.4 \text{ ‰}$ and in general are more enriched in ^{13}C than temperate and boreal wetlands. However, thus far relatively few measurements of $\delta^{13}\text{C}_{\text{CH}_4}$ in methane-enriched air have been made in the tropics. In this study samples have been collected from tropical wetland, rice, ruminant, and biomass burning emissions to atmosphere. Regional isotopic signatures vary greatly as different processes and source material affect methane signatures. Measurements were made to determine bulk source inputs to the atmosphere, rather than to study individual processes, to provide inputs for regional methane budget models, to constrain emissions with better source apportionment. An expected inferred annual isotopic signature has been estimated for tropical South America and Africa as these regions have the largest tropical methane sources. We find tropical South America to have an expected annual isotopic signature of $-57 \pm 3 \text{ ‰}$ and Africa an inferred annual isotopic signature of $-52 \pm 2 \text{ ‰}$.

1. Introduction

In 2007 a sustained growth of atmospheric CH_4 began, with the global methane mole fraction increasing by $5.7 \pm 1.2 \text{ ppb yr}^{-1}$ from 2007 to 2013. Growth was remarkable in 2014, at $12.5 \pm 0.4 \text{ ppb}$ and in 2015 at $9.5 \pm 0.7 \text{ ppb}$. The growth was particularly strong in the tropics (Nisbet et al., 2016), which satellite based estimates indicate produce around 200 Tg/year of methane, approximately 40% of global methane emissions (Bousquet et al., 2006; Saunois et al., 2016; Frankenberg et al., 2008). The largest natural source is tropical wetlands (Mitsch et al., 2009; Saunois et al., 2016) with other tropical sources including rice agriculture, natural and anthropogenic biomass burning, ruminants (such as cattle, water buffalo and sheep), fossil fuels and waste. However the cause of this methane growth remains poorly understood (Nisbet et al., 2016; Schaefer et al., 2016).

Here we provide isotopic measurements of methane coming from these different sources, and use these to provide constraints on methane source apportionment. To resolve the causes of the rise in methane, detailed modelling of the methane isotopic budget can place strong

64 constraints on sources and sinks, however, modelling is hampered by the lack of detailed
65 knowledge of isotopic ratios of tropical sources.

66 Emissions estimates of CH₄ from ‘bottom-up’ (the sum of estimated fluxes of individual
67 processes) and ‘top-down’ (direct atmospheric measurements) differ greatly. Bottom-up
68 approaches tend to give higher global estimates due to larger individual emissions from
69 natural sources (Nisbet et al., 2014; Kirschke et al., 2013; Saunio et al., 2016). In-situ
70 isotopic measurements can bring further accuracy to these budgets, but more such
71 measurements are required, especially from tropical regions. CH₄ flux and isotopic
72 measurements are predominantly made in developed countries, and there are far fewer
73 measurements in tropical areas (Dlugokencky et al, 2011; Bousquet et al., 2006).

74 Different processes of methane production have characteristic ¹³C/¹²C ratios ($\delta^{13}\text{C}_{\text{CH}_4}$) (e.g.
75 Dlugokencky et al., 2011), and so this ratio is useful in helping identify changing sources.
76 Relative to background ambient air, which has a $\delta^{13}\text{C}_{\text{CH}_4}$ of -47‰ (Nisbet et al., 2016),
77 emissions can be either enriched or depleted in ¹³C. Atmospheric sinks impose a kinetic
78 isotope effect of about 4 to 6‰ on isotopic ratios with the global isotopic bulk source
79 averaging around -53 ‰ (Nisbet et al., 2016). Biogenic sources are depleted in the heavier
80 isotope (e.g. an Arctic wetland may give a signature of -71 ‰ (Fisher et al., 2017)), whilst
81 thermogenic/pyrogenic sources are enriched in ¹³C (e.g. biomass burning of C₄ plants at -10
82 to -20 ‰ (Dlugokencky et al, 2011)). Schwietzke et al., (2016) compiled a database of
83 isotopic methane source signatures, but very few tropical non-fossil fuel sources were
84 included.

85 Since the sustained CH₄ growth began in 2007, $\delta^{13}\text{C}_{\text{CH}_4}$ has shifted globally to more negative
86 values suggesting an increased biogenic source either from increased agricultural emissions
87 (Schaefer et al., 2016) or increased emissions from wetlands as a result of meteorological

88 variations and/or changing climate (Nisbet et al., 2016). Models tend to focus on methane
89 mole fraction measurements, and either do not take into account the source types, or use a
90 very general isotopic number for each source type (e.g. Rigby et al., 2012) without taking
91 into account zonal variation of the sources, for example boreal vs. tropical latitudinal
92 variation in emissions from wetlands (Zazzeri et al., 2016; Fisher et al., 2017; Schwietzke et
93 al., 2016). Global and regional models that include methane isotopes should therefore include
94 regional isotope signatures for better source apportionment, as regional variations (e.g.
95 latitudinal) may be overlooked when using a single value (Kirschke et al., 2013; Fisher et al.,
96 2017). Using isotopic source signatures together with mole fraction measurements to
97 constrain global and regional emissions provides models with better source apportionment.
98 This should permit better understanding of the sustained tropical methane growth, and help
99 close the gap between bottom-up and top-down emission estimates.

100 The new measurements of methane isotope signatures provided in the current work (Section
101 3) have been made directly on air collected above tropical sources, as well as directly from
102 individual ruminants or ruminant herds. Plumes also have been sampled downwind of larger
103 sources. The aim is to improve the characterisation of tropical methane source signatures,
104 providing narrower ranges for specific regions of the tropics and therefore allowing a
105 calculation of modelled regional source signatures with these values. Most previous studies
106 of wetland and rice emissions have used chamber sampling (Whiticar et al., 1986; Fisher et
107 al., 2017), which only sample isolated points in the wetland. Methanotrophy may also occur
108 in the chambers which may further fractionate the methane emissions released to the
109 atmosphere. Localised vegetation and microbes within the chamber, and disturbance to the
110 natural local microenvironment mean that the chambers may not fully represent the wider
111 wetland emissions entering the atmosphere (Sriskantharajah et al., 2012). Ambient air
112 sampled in this study is taken from above wetlands and therefore represents the mixed

methane inputs to the atmosphere and provides average wetland isotopic signatures for a local regional source (Fisher et al., 2017).

1.2 Wetlands

It is estimated that tropical wetlands between 30° N and 30° S emit $126 \pm 31 \text{ Tg yr}^{-1}$ of methane (Melton et al., 2013). The term ‘wetland’ describes a range of CH_4 emitting ecosystems, including wet soils, swamps, bogs and peatlands. Rice fields are an anthropogenic source but share the same mechanisms and controls for CH_4 emissions as natural wetlands.

In wetlands methanogenesis can occur through two main pathways that vary with specific environments and affect the isotopic signature: Fermentation of acetate (acetotrophic methanogenesis) and reduction of CO_2 with hydrogen (hydrogenotrophic methanogenesis). Hydrogenotrophic methanogenesis produces methane with a $\delta^{13}\text{C}$ of -110‰ to -60‰ which is more negative than acetotrophic methanogenesis, which produces CH_4 with a $\delta^{13}\text{C}$ of -60‰ to -50‰ (Whiticar et al., 1986). Partial oxidation of methane by methanotrophs may cause significant enrichment in ^{13}C in the sediment column before it is emitted to the atmosphere (Schaefer & Whiticar, 2008). Methane can exit wetland surfaces and enter the atmosphere via diffusion, ebullition and/or plant mediated channelling. The degree of oxidation and therefore the isotopic signature depends on the pathway that the methane follows to the atmosphere. Mixing then occurs in the atmosphere, giving a more general source signature (Chanton, 2005; Chanton et al., 2005; Whiticar et al., 1986).

These different production pathways in wetlands may be influenced by temperature, vegetation type and the water table, which is linked to the anoxia level and the availability of

substrate (Saunois et al., 2016). Hydrological processes are a major control on tropical wetland methane emissions and may play a larger role than in higher latitudes where temperature and seasonality may be a more important factor (Ringeval et al., 2010; Bousquet et al., 2011). In the rice paddies, water management and rice type affect methane production along with significant in-situ methanotrophy (Conrad, 2002). Methane is predominantly released by diffusive transport through the rice plant (Saunois et al., 2016).

1.3 Biomass Burning

Intense seasonal dry season anthropogenic biomass burning occurs throughout much of the tropics and subtropics, resulting in significant methane emissions (Saunois et al., 2016). Contributing sources include seasonal C4 grassland burning, especially in African savannahs, C3 forest fires, including those related to deforestation, shifting cultivation and, wildfires (anthropogenic or naturally ignited), and use of fuel wood, for cooking, heating and industry (Crutzen & Andreae, 1990; Chanton et. al., 2000). Tropical biomass burning typically shows very strong seasonality, and in some areas strong inter-annual variations due to meteorological shifts and/or climate anomalies (e.g. Wooster et el. 2012). Tropical biomass burning emissions of methane are estimated by models to be 13.6-34.5 Tg yr⁻¹ (Kirschke at al., 2013), though there are significant increases in some years/locations e.g. El Niño related droughts increasing the availability of combustible fuel (e.g. Huijnen et al., 2016).

Factors affecting the amount of methane emitted by tropical burning includes the amount of fuel burned and its type, the latter affecting the CH₄ emissions factor (the amount of CH₄ released per kg of fuel burned (Andreae and Merlet, 2001)). The photosynthetic pathway of carbon capture is important. C3 plants (e.g. woody trees or most temperate crops) and C4 plants (dominating many tropical grasslands) have different $\delta^{13}\text{C}$ signatures, reflected in the

isotopic signatures of the methane emitted. C4 vegetation pre-concentrates CO₂ and thus is ¹³C enriched compared to C3 plants. In contrast CH₄ from burning C3 vegetation is more depleted in ¹³C by up to ~24%. Isotopic ratios also appear to depend on fire conditions: for example fires in a particular ecosystem that are flaming involve per unit area rates of heat release and fuel consumption typically far higher than when smouldering, with significantly lower CH₄ emissions factors (e.g. Wooster et al., 2011), but with smoke appearing generally more enriched in ¹³C (Chanton et. al., 2000). However, the different fuels preferentially accessed by the fires during natural flaming and smouldering activity, and the amount of moisture present can complicate interpretations of in situ collected smoke samples in relation to the controls on isotopic signatures.

1.4 Ruminants

Agricultural emissions (rice and ruminants) may have increased in the tropics (Schaefer et al., 2016). However, few ruminant isotopic signatures have been measured, especially in the tropics (Schwietzke et al., 2016) so expanding the methane isotope dataset for ruminant emissions is highly valuable.

Around 26% of global land area is dedicated to grazing (Ripple et al., 2013), and livestock accounts for 35-40% of anthropogenic global emissions through enteric fermentation and manure (Aluwong et al., 2011). The African and South American tropics host large populations of domesticated cattle, water buffalo, some sheep, goats and a few wild ruminants, while deforestation occurs widely in part in the tropics to make way for livestock, helping to drive fire emissions (Ripple et al., 2013).

Ruminants may be either native or domesticated, and consume plants that are digested through enteric fermentation. They are a significant source of anthropogenic methane with ~94% of animal emissions being from domesticated animals (Thorpe, 2008; Ripple et al., 2013). In less economically developed countries, many of which are in the tropics, livestock populations have increased in response to human population growth. Greenhouse gas emissions from livestock are estimated to have risen by 117% in less economically developed countries from 1961 to 2010 (Caro et al., 2014).

Nearly all of the methane emitted from ruminants is produced in the rumen then exhaled (Hook et al., 2010). Domesticated ruminants were estimated (bottom-up) to produce around 99 Tg of methane in 2014 (FAO, 2016). Factors influencing methane emissions vary with geographical location, C3 or C4 plant composition and quality of the feed, processing of feed and the breed of the animal (Hook et al., 2010). Tropical ruminants may graze on C4 savannah grasslands or consume feed including C4 maize, sugar cane tops, millet, sorghum crop waste or C3 trees and bushes (Nisbet et al., 2016).

1.5 Other anthropogenic sources

Fossil fuel emissions of methane occur in coal, oil and gas extraction and use. Coal emits methane during extraction, crushing, processing and burning, and from abandoned mines. Methane is flared in oil extraction. Major emissions come from natural gas extraction, flaring, processing, distribution and use (Dlugokencky et al., 2011). Fossil methane is mainly thermogenic and comes from the transformation of organic matter into fossil fuels over a geological period of time (Ciais et al., 2013). Globally fossil fuel emissions contribute between 114 and 133 Tg CH₄ yr⁻¹ to the atmosphere (Saunio et al., 2016). Tropical gas source

regions include Southeast Asia, Bolivia, Qatar and Algeria and tropical coal source regions include India.

Waste sources include the decomposition of biodegradable municipal solid waste in landfills, animal waste and human waste (Dlugokencky et al., 2011). These combined sources produce between 67 and 90 Tg CH₄ yr⁻¹ (Ciais et al., 2013). In many tropical countries the gases produced from biodegradation in landfill receive no treatment and are directly released into the atmosphere (Wangyao et al., 2010).

1.6 Sinks

Oxidation by OH radicals predominantly in the troposphere is the main sink of atmospheric methane (90% of the global sink), particularly in the tropics where there is bright sunlight (Kirschke et al., 2013). Removal of CH₄ by OH has a kinetic isotope shift of 5.4‰ on the residual CH₄ (Allan et al., 2007). Oxidation by methanotrophic bacteria in soils also enriches δ¹³C_{CH₄} and contribute to a CH₄ loss of about 30 Tg yr⁻¹ (Dlugokencky et al., 2011; Ciais et al., 2013). Karst systems also may act as a net sink of atmospheric methane through microbial oxidation (Matthey et al., 2013). Other sinks include Cl and Br radicals in the marine boundary layer, Cl and oxygen radicals in the stratosphere. The KIE from the Cl sink enriches atmospheric CH₄ by 2.6 ± 1.2 ‰. Global δ¹³C sources of methane averages around -53.6 ‰ to -53.4 ‰, with the sink fractionation, background ambient air at present has a signature between -47.4 and -47.2 ‰ (Allan et al., 2001; Nisbet et al., 2016).

1.7 Tropical source values

Table 1 shows literature-derived values for tropical sources. Fossil fuel sources, including in the tropics, are well defined in the literature (Sherwood et al., 2016; Schwietzke et al., 2016)

228 however wetlands, agriculture (rice & ruminants), waste and biomass burning are less well
 229 studied.

Source		$\delta^{13}\text{C}_{\text{CH}_4}(\text{‰})$	Reference
Tropical Wetlands		<i>Sampling method</i>	
Mangroves: Florida Everglades	Glass dome or Plexiglas pyramid	-70.1 ± 1.8	Chanton et al., 1988
Swamps: Southern Thailand	Inverted funnel	-66.1 ± 5.1	Nakagawa et al., 2002
Floodplain: Amazon	Flask samples at ground level	-63.7 ± 6	Tyler et al., 1987
Swamps: Nyahururu, Kenya	Stainless steel ring - Bag enclosure	-61.7 ± 0.5	Tyler et al., 1988
Florida Everglades	Flask Surface air samples	-55 ± 3	Stevens & Engelkemeir, 1988
Floodplain: Amazon	Inverted funnel & flux chamber	-53 ± 8	Quay et al., 1988
Swamp: North Florida	Chamber	-52.7 ± 6.1	Happel et al., 1994
Rice agriculture		<i>Sampling method</i>	
Rice Paddies: Japan	Chamber	-70 to -57	Tyler et al., 1994
Rice paddy: Kenya	Stainless steel ring - Bag enclosure	-63 to -57	Tyler et al 1988
Rice Paddies, India	Chamber	-57.2 to -54.3	Rao et al., 2008
Rice paddies: Peat soils Southern Thailand	Gas bubbles trapped in inverted funnel	-56.5 ± 4.6	Nakagawa et al., 2002
Rice paddies: mineral soils Southern Thailand	Gas bubbles trapped in inverted funnel	-51.5 ± 7.1	Nakagawa et al., 2002
Termites			
Kenya		-61.6 ± 8	Tyler et al., 1988
Ruminants			
C3 diet, Germany		-74 to -60	Stevens, 1988; Levin et al., 1993; Klevenhusen et al., 2010
C4 diet, Germany		-55 to -50	
Biomass burning		<i>Fire type</i>	
C3 plants: Primary forest slash fires, Brazil	Smouldering	-26.87 ± 0.2 & -30.61 ± 0.2	Snover et al. 2000
C3 plants: African woodland	Flaming	-29.1 ± 0.2	Chanton et al., 2000
	Smouldering	-30.4 ± 1.3	
C3 plants: Agricultural grass field	Flaming	-30.1 ± 1	Stevens and Engelkemeir, 1988
		-24 to -32	
C4 plants: Zambian savanna	Smouldering	-26.1 ± 6	Chanton et al., 2000
C4 plants: Brown grass, Brazil	Flaming	-16.6 ± 2	
		-12.45 ± 0.2	Snover et al. 2000
Waste (Europe)		-55 ± 5	Levin et al., 1993; Bergamaschi et al., 1998
Fossil Fuels			
Coal: Brazil		-53.2 ± 1.4	Levandowski, 2009
Coal: Sub-Saharan Africa		-52.2 ± 3.8	Ward et al., 2004
Conventional Gas: India		-54.2 ± 12.6	Pande et al., 2011
Conventional Gas: Indonesia		-44.3 ± 11.6	Satjana et al 2007
Conventional Gas: Brazil		-42.2 ± 6.2	Prinzhofer et al 2010; Prinzhofer et al 2000
Conventional Gas: Thailand		-40.6 ± 4.2	Giggenbach 1997; Jenden 1988

Table 1: summary of methane sources from literature, focussing on the tropics if the data is available. Note a lack of ruminant & waste tropical studies so more general values are used.

2. Methodology

2.1 Sampling methods

Air samples were collected in 3 litre Tedlar bags (SKC Ltd) using a battery operated pump at each of the sites (Fig. 1 & Table S1). The bags were filled at varying distances downwind and upwind from the sources to allow for a range of methane mole fractions. Wetland and rice paddy samples were taken at heights between 5cm and 3m above the source. Ruminant samples were taken between a few cm to 2-3m away from the head of the animal. Biomass burning samples were mostly taken between 30cm and a few meters away from the fires, with some further afield in downwind plumes. The sampled Chinese fires were burning agricultural wastes, the Malaysian fires were burning local waste and the Chisipite Vlei, Zimbabwean fire was uncontrolled. Some sampled Zimbabwean fires were controlled burns. The Chinese and Malaysian samples were taken throughout flaming and smouldering stages. The air-line was flushed before the bag was attached and opened to remove any residual air from the previous sample.

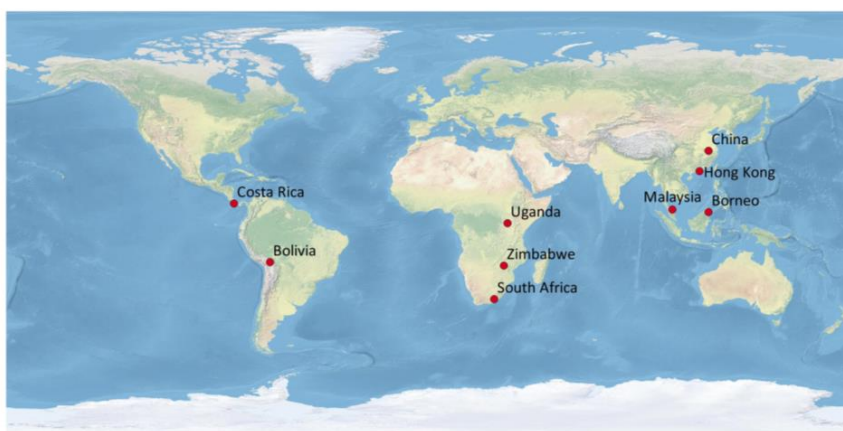


Figure 1: Sampling sites showing a wide coverage of the tropics.

2.2 Laboratory Analysis

The Tedlar bag samples were analysed in the Greenhouse Gas Laboratory at Royal Holloway University of London (RHUL). A Picarro 1301 cavity ring down spectrometer (CRDS) measured the mole fraction of methane calibrated to the NOAA 2004A scale. The Picarro CRDS measures linearly up to 20 ppm so CH₄ samples with higher mole fractions must be diluted with nitrogen before analysis. The 3 litre Tedlar bags were analysed for 240 seconds with the last 120 seconds of measurements being used to calculate the mean mole fraction. If the bags had less air they were analysed for 120 seconds with the final 60 seconds being used for the mean mole fraction calculation. The precision of the instrument for CH₄ is ± 0.2 ppb (600 seconds) for the standards and ± 0.4 ppb for the bag samples due to the much shorter averaging time.

Continuous-flow gas chromatography / isotope-ratio mass spectrometry (CF-GC/IRMS) using a modified Trace Gas – Isoprime system (Fisher et al., 2006) allows for precise $\delta^{13}\text{C}$ analysis of methane with repeatability of 0.05‰. A minimum of 0.5 litres of air sample is retained for the $\delta^{13}\text{C}_{\text{CH}_4}$ isotopic analysis (Fisher et al., 2017). The isotope ratios are given in δ -notation on the VPDB (Vienna Pee Dee Belemnite) scale. An internal secondary standard is analysed at least three times the beginning of each day, or until the measurements are stable, and after every two samples to allow correction for instrumental drift throughout the day. Samples are measured in triplicate with an additional measurement analysis if the first 3 are not within 0.1‰. If the recorded mole fraction in the sample was above 7 ppm it was diluted to be in the linear and dynamic range of the mass spectrometer for isotopic analysis (Fisher et al., 2006).

2.3 Isotopic Source Signatures

Keeling plot regression (Keeling, 1958; Pataki et al., 2003; Zazzeri et al., 2015) is used to identify the isotopic source signature of the methane in the samples. The $\delta^{13}\text{C}_{\text{CH}_4}$ is plotted against the inverse of the CH_4 mole fraction then linear regression is used to calculate the isotopic source signature responsible for the excess over background (the y-intercept - Equation 1). Orthogonal regression is used to take into account both errors on the x and y axes (Akritas & Bershadsky, 1996).

$$\delta^{13}\text{C}_a = c_b (\delta^{13}\text{C}_b - \delta^{13}\text{C}_s) \times (1/c_a) + \delta^{13}\text{C}_s \quad (\text{Equation 1})$$

C_a is the atmospheric mole fraction of a gas and C_b is the background atmospheric mole fraction. $\delta^{13}\text{C}_a$ is the measured isotopic composition, $\delta^{13}\text{C}_b$ is the background isotopic composition and $\delta^{13}\text{C}_s$ is the source isotopic composition.

The Bivariate Correlated Errors and intrinsic Scatter (BCES) program (available at: <http://www.astro.wisc.edu/~mab/archive/stats/stats.html>) accommodates for the error changes in each sample. BCES regression has been used to find the uncertainty of the Keeling plot intercept and therefore the $\delta^{13}\text{C}$ error (Akritas & Bershadsky, 1996; Zazzeri et al., 2015).

296 **2. Results**

297 Results are given in Table 2 with corresponding Keeling plots in the SI

Source	Sample Site	Description	Source signature ‰	No. Samples
Wetland				
	Pui O, Hong Kong	Marsh (C3 & C4)	-52.3 ±0.7	6
	Papyrus swamp, Uganda	Papyrus swamp (C4)	-53.0 ±0.4	9
	Palo Verde National Park, Costa Rica	Coastal floodplain freshwater marsh (C3 & C4)	-53.3 ±1.7	5
	Edge of Lake Victoria, Uganda	Freshwater Wetland: Papyrus (mostly C4)	-58.7 ±4.1	6
	Lake Titicaca, Bolivia	Freshwater Wetland (C3)	-59.7 ±1.0	11
	Yi O, Hong Kong	Marsh (C3 & C4)	-60.2 ±0.4	12
	Danum Valley Borneo	Forest wetland (C3)	-61.5 ±2.9	11
	Tor Doone, South Africa	Freshwater Wetland (C3)	-61.5 ±0.1	11
<i>Mangroves</i>	Mai Po, Hong Kong	Reed (C4), Mangroves (C3) & marshes	-54.6 ±0.7	9
	Costa Rica Mangroves, Sierpe & Puerto Jimenez	Mangroves (C3)	-70.1 ±2.4 to -77.7 ±0.2	4 & 4
Rice paddies				
	Hong Kong Rice, Yi O	Rice (C3)	-58.7 ±0.4	16
	Hong Kong Rice, Hok Tau	Rice wetland (C3)	-58.9 ±0.4	11
Enteric fermentation				
<i>C4</i>	Zimbabwe Lobels cows	Eating C4	-52.5 ±0.6	9
	Zimbabwe Dom cows	Eating mostly C4	-56.8 ±0.5	11
	Zimbabwe Tavistock cows	Eating C4 & C3	-56.9 ±0.4	9
<i>C3</i>	Hong Kong Water Buffalo	Eating mostly C3	-63.3 ±0.4	5
	Hong Kong cows	Eating C3	-70.5 ±0.7	12
Biomass Burning				
<i>C3</i>	China	Wheat & oil plant crop residue	-28.5 ±0.4 to -33.4 ±0.6	5 & 5
	Bachok, Malaysia	Mango wood	-32.8 ±0.2 to -30.3 ±0.2	3 & 3
<i>C4</i>	Zimbabwe	Grass	-16.3 ±0.1 to -18.8 ±0.3	3 & 3
	Chisipite Vlei, Zimbabwe	Grass	-15.9 ±1.3	6

Table 2: Methane $\delta^{13}\text{C}$ source signature results from this study. The Keeling plots for these are given in SI (supplementary information) S1- 4. The uncertainties (1σ) given take into account both variables ($\delta^{13}\text{C}$ & CH_4 mole fraction) (described in the methods section)

3.1 Wetland & Rice Sources

The newly studied tropical wetland sources give methane emissions with $\delta^{13}\text{C}$ between $-61.5 \pm 2.9 \text{ ‰}$ and $-53.0 \pm 0.4 \text{ ‰}$. This is within or near the range of other tropical wetland or swamp studies. Table 1 shows sources from tropical wetland sources between -66 to -52 ‰ . Schaefer et al., (2016) give values of -60 to -52 ‰ for more general tropical wetlands.

Tropical wetlands are in general more enriched in ^{13}C than temperate and boreal wetlands, for example, Fisher et al., (2017) give a value of $-71 \pm 1 \text{ ‰}$ for European Arctic wetland emissions. The enrichment of ^{13}C in tropical wetlands may be due to thicker oxic zones in the sediments or water column compared to northern wetlands. Oxidation effects leave the methane more enriched in ^{13}C . The difference of northern and tropical wetlands may also be due to differences in methanogenic communities, temperature differences and precursor plant material in the northern wetlands being C3 compared to the tropics where C4 plants are more abundant (Chanton, 2005; Nakagawa et al., 2002; Fisher et al., 2017).

The Hong Kong rice values are $-58.7 \pm 0.4 \text{ ‰}$ and $-58.9 \pm 0.4 \text{ ‰}$ taken during rice growth in July. Literature values given in Table 1 show rice paddies in tropical areas to range between -70 to -51 ‰ . The more depleted values of -70 ‰ for Japanese rice paddies were found to be seasonal (Tyler et al., 1994) however other studies have found little variation between the growth stages of the rice (Tyler 1988). Nakagawa et al., (2002) gives a value of $-63 \pm 5 \text{ ‰}$ for temperate rice paddies. More general rice paddy signatures are given by Dlugokencky et al. (2011) with a value of $-62 \pm 3 \text{ ‰}$ and Schaefer et al., (2016) with values of -59 to -65 ‰ . The new results are at the upper end of the range from previous studies and are representative of ambient air rather than chamber measurements.

The literature values for wetlands and rice agriculture are predominantly chamber studies or using an inverted funnel and are more variable than atmospheric samples that have been

322 mixed (Fisher et al., 2017). These new results show that simple atmospheric grab sampling
323 gives results consistent with averages from chamber studies and are more representative
324 values for regional modelling.

325 The Costa Rican mangrove samples, from a saline environment, are more depleted in ^{13}C
326 than the other sites between $-77.7 \pm 0.2 \text{ ‰}$ to $-70.1 \pm 2.4 \text{ ‰}$. This is comparable to mangroves
327 in the Florida Everglades with a signature of $-70 \pm 2 \text{ ‰}$ (Chanton et al., 1988). These
328 differences may be due to more acetoclastic methanogenesis occurring in the freshwater
329 tropics whilst hydrogenotrophic methanogenesis is the more dominant process in marine
330 sediment environments such as the Costa Rican mangroves (Whiticar et al., 1986). In
331 comparison the Hong Kong reed, mangrove & marshes at Mai Po, an environment with both
332 freshwater and brackish marine components, give $-54.6 \pm 0.7 \text{ ‰}$. This is comparable to the
333 Florida everglades, Stevens & Engelkemeir (1988) with a value of $-55 \pm 3 \text{ ‰}$ and Happell et
334 al., (1994) with a value of $-52.7 \pm 6.1 \text{ ‰}$.

336 **3.2 Ruminant sources**

337 Cattle and water buffalo are the main tropical ruminant sources. In 2014 cattle contributed to
338 73.0% of global ruminant CH_4 emissions and water buffalo contributed 10.8% (Table 3) as
339 assessed in inventory studies (FAO, 2016). Water buffalo are found mainly in Southern Asia,
340 with the majority of the population located in India, Pakistan and China so they are a
341 significant methane contributor in these regions (FAO, 2016).

342 Feral water buffalo from Hong Kong with a predominantly C3 diet give a $\delta^{13}\text{C}_{\text{CH}_4}$ emission
343 value of $-63.3 \pm 0.4 \text{ ‰}$ and domesticated Hong Kong cows gave $-70.5 \pm 0.7 \text{ ‰}$. Farmed cattle
344 in Zimbabwe emitted methane between $-56.9 \pm 0.4 \text{ ‰}$ and $-52.5 \pm 0.6 \text{ ‰}$ for a predominantly

C4 diet (See Table S2). Ruminants which digest C3 plants shown in Table 1 have signatures between -74 to -60% (Dlugokencky et al. 2011; Schaefer et al., 2016). Values of ruminants which digest C4 plants (Table 1) have signatures between -55 and -50% . (Schaefer & Whiticar, 2008; Dlugokencky et al. 2011).

Ruminant	CH₄ emissions (Tg yr⁻¹) 2014	% of Total 2014
Cattle	72.5	73.0
Buffalo	10.7	10.8
Sheep	6.8	6.8
Goats	5.0	5.1
Camels	1.3	1.3
Swine	1.1	1.1
Horses	1.1	1.1
Mules and Asses	0.5	0.6
Llamas	0.3	0.3

Table 3: 2014 global CH₄ emissions from Ruminants (FAO, 2016).

Biomass Burning

The C3 plant biomass burning methane $\delta^{13}\text{C}$ signatures from China and Malaysia lie between $-33.4 \pm 0.6 \%$ and $-28.5 \pm 0.4 \%$. These are similar to African woodlands that gave a value of -30% (Chanton et al., 2000) and an agricultural grass field and dried tree branches with values of -24 to -32% (Stevens and Engelkemeir, 1998). The C4 plant results of $-18.7 \pm 0.3 \%$ and $-15.9 \pm 1.3 \%$ from Zimbabwe are comparable to Zambian savanna burns which give a mean value of -16.6% at a flaming stage of burning (Chanton et al., 2000).

There is little $\delta^{13}\text{C}_{\text{CH}_4}$ fractionation during biomass burning due to the high combustion temperature however if the biomass is damp the combustion temperature may decrease. The main factor affecting the source signature is the plant type being C3 or C4 (Quay et al., 1991;

Bréas et al., 2001) and these results confirm the need to separate these values in models. The limited data sets show no difference between flaming and smouldering stages of the burning in terms of isotopic signatures.

3. Summary

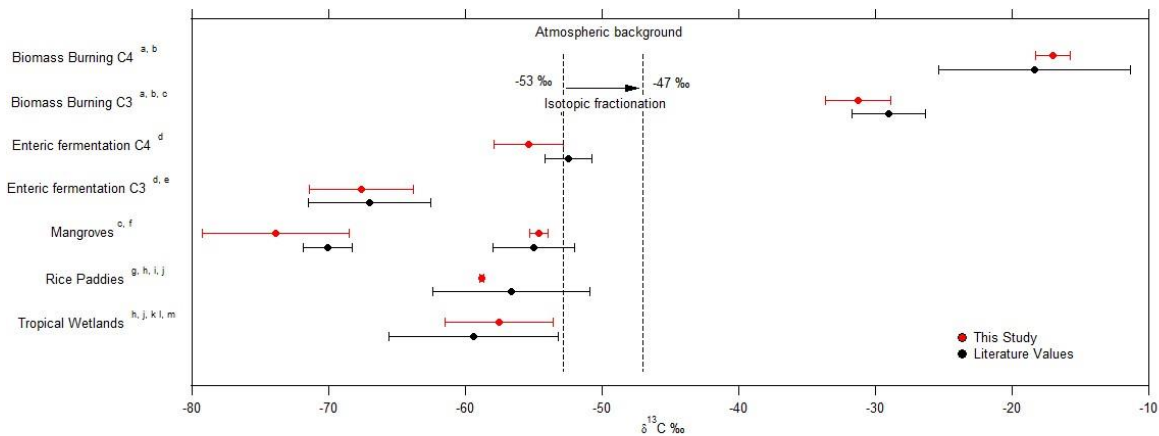


Fig 2: Tropical $\delta^{13}\text{C}$ source value ranges taken from both this study only (red) and literature values (black): a) Chanton et al., (2000), b) Snover et al. (2000), c) Stevens and Engelkemeir (1998), d) Dlugokencky et al. (2011), e) Schaefer et al. (2016), f) Chanton et al. (1988), g) Tyler et al. (1994), h) Tyler et al. (1988), i) Rao et al. (2008), j) Nakagawa et al. (2002), k) Tyler et al. (1987), l) Quay et al. (1988) & m) Happel et al. (1994). The errors show standard deviations of the average signatures. The dashed lines show the global average $\delta^{13}\text{C}$ source signature, between -53.6 and -53.4‰ with the sink fractionation ‰ leaving the residual ambient background air with a signature close to -47 ‰ (Allan et al., 2001; Nisbet et al., 2016).

The wetlands, mangroves, rice sources and ruminants are depleted in ^{13}C but it is difficult to distinguish between them. The biomass burning values are enriched in ^{13}C (Fig. 2).

In the equatorial and wet savannah tropics of South America, Africa and South East Asia emissions are likely to be from primarily wetland sources, in contrast emissions from China, India and Northern Africa are likely to be predominantly from agricultural sources as well as fossil fuel emissions. Agriculture is also an important source for South East Asia (Saunois et

al., 2016). Both agricultural and wetland sources in the different regions will contribute to the sustained growth and $\delta^{13}\text{C}_{\text{CH}_4}$ shifting to more negative (biogenic) values (Nisbet et al., 2016; Schaefer et al., 2016).

An expected average annual isotopic signature may be calculated for anthropogenic sources in regions by using the EDGAR v4.2 emission inventory (Table 4). This is useful to see if a region contributes strongly via biogenic, thermogenic or pyrogenic pathways and to test the confidence in inventories by comparing the calculated value to measured regional plumes. Natural wetland and termite emissions must also be taken into consideration, and the papers of Kirschke et al. (2013) and Sanderson (1996) are used to estimate these.

Tropical South America and Africa are given as examples as these regions have the largest tropical sources. This is calculated with an average $\delta^{13}\text{C}_{\text{CH}_4}$ source signature value weighted by the percentage contribution of each source to the regional total CH_4 emission. Tropical South America has an expected annual isotopic signature of $-57 \pm 3\text{‰}$ and Africa has an expected annual isotopic signature of $-52 \pm 2\text{‰}$. The uncertainties (1σ) on the isotopic signatures are calculated using a Monte Carlo error analysis. The difference is largely caused by the predominance of wetlands in South America, and much higher biomass burning in Africa (Table 4).

Source	Tropical South America	Africa	Reference	$\delta^{13}\text{C}_{\text{CH}_4} \text{‰}$	Reference
	Tg yr ⁻¹	Tg yr ⁻¹			
Wetlands	58 [39 – 92]	24 [22-27]	Kirschke et al., 2013	-57.5 ± 3.9	This study.
Rice	0.71 ± 0.01	1.04 ± 0.04	EDGAR V4.2	-58.8 ± 0.2	This study.
Ruminants C3	6.58 ± 0.53	2.44 ± 0.10	EDGAR V4.2 ; Osborne et al., 2014	-67.6 ± 3.8	This study.
Ruminants C4	9.87 ± 0.80	9.75 ± 0.42	EDGAR V4.2; Osborne et al., 2014	-55.4 ± 2.5	This study.
Manure	0.39 ± 0.03	0.45 ± 0.02	EDGAR V4.2	-55.0 ± 1.2	See table 1 waste section.
Termites	7.20 ± 0.55	8.06 ± 0.61	Sanderson, 1996	-61.6 ± 8	Tyler et al., 1988.

Biomass Burning C3	2.07 ±1.39	6.09 ±2.42	EDGAR V4.2;Randerson et al., 2005	-31.2 ±2.4	This study.
Biomass Burning C4	0.69 ±0.46	4.98 ±1.98	EDGAR V4.2; Randerson et al., 2005	-17.0 ±1.2	This study.
Waste	3.68 ±0.18	5.07 ±0.26	EDGAR V4.2	-55.0 ±1.2	See table 1 waste section.
Fossil Fuels	3.95 ±0.26	11.53 ±0.52	EDGAR V4.2	-47.8 ±6.1	See table 1 Fossil Fuel section.
Total emissions	93.1 ± 34	73.4 ± 4			
Average Annual $\delta^{13}\text{C}_{\text{CH}_4}$	-57.0 ±3 ‰	-51.5 ±2 ‰			

Table 4: Emissions inventories and average source signatures used to calculate an average regional tropical source signature for Tropical South America and Africa.

Biogenic wetland and rice emissions and pyrogenic biomass burning emissions have strong seasonality. This seasonality is especially strong in the African savannah. For example, northern hemisphere African burning primarily occurs between December and March, shifting the average continental signal in this region towards less negative isotopic values. This period coincides with the most negative (biogenic) values in the Southern hemisphere Africa region during the wet season (Roberts et al., 2009). For this reason seasonal bulk isotopic sources and emissions inventories would be useful to further constrain methane sources especially in regions such as tropical Africa and South America.

Biogenic sources (wetlands, ruminants, waste etc.) have comparable $\delta^{13}\text{C}_{\text{CH}_4}$ signatures in the tropical regions. Waste $\delta^{13}\text{C}_{\text{CH}_4}$ values in the tropics may also be different from managed landfill sites in Europe that many studies are based on. More detailed land use maps in the tropics may help in quantifying the inputs of different sources. The calculated values may be tested from regional measurements, for example from flight campaigns (e.g. Fisher et al., 2017).

Isotope measurements provide strong constraints on methane source apportionment however it is important to take into account variation of isotopic signatures such as the latitudinal variation of wetlands and the regional biogenic sources. The measurements in this study are

more representative of source emissions as a whole, rather than individual processes and can be included in regional models to constrain the methane emissions with better source apportionment. Schaefer et al. (2016) and Nisbet et al. (2016) show the sustained CH₄ growth is from biogenic sources, however, more measurements, particularly in areas with seasonal source emissions, are needed to constrain tropical sources further and therefore help to explain the sustained methane growth in the tropics.

Acknowledgements

This work was funded by the UK Natural Environment Research Council (NERC) projects: Investigation of the Southern Methane Anomaly: causes, implications, and relevance to past global events (grant NE/K006045/1), MOYA; The Global Methane Budget (grant NE/N016211/1), Methane at the edge; jointly developing state-of-the-art high-precision methods to understand atmospheric methane emissions (grant NE/M005836/1); International Collaboration on Measurement of Globally-important Gases in the Atmosphere of the Tropical Maritime Continent (grant NE/J016012/1); and a NERC studentship to RB. Thank you to Tim, Trish & Lucy Broderick, Alex Clarke, Neil Harris, Steve Forsyth and The Laboratory for Atmospheric Physics, Institute for Physics Research, Universidad Mayor de San Andres for collecting samples. Thanks to Cecily Law, Jerry Morris, Martin Williams, Gray Williams and the Swire Institute of Marine Science for all their help and logistical planning during the Hong Kong field campaign. Thanks to Prof. Siew Moi Phang and Prof. Datu Azizan Abu Samah at the University of Malaya, Institute of Ocean and Earth Sciences and their staff at the Bachok Marine Research Station. Data will be deposited in the UK Centre for Environmental Data Analysis on completion of Rebecca Brownlow's PhD thesis.

References

- Akritas, M.G., Bershad, M.A., (1996), Linear Regression for Astronomical Data with Measurement Errors and Intrinsic Scatter. *Astrophys. J.* 470, 706.
- Allan, W., Manning, M.R., Lassey, K.R., Lowe, D.C., Gomez, A.J., (2001), Modeling the variation of $\delta^{13}\text{C}$ in atmospheric methane: Phase ellipses and the kinetic isotope effect. *Global Biogeochem. Cycles* 15, 467–481.
- Allan, W., Struthers, H., Lowe, D.C., (2007), Methane carbon isotope effects caused by atomic chlorine in the marine boundary layer: Global model results compared with Southern Hemisphere measurements. *J. Geophys. Res.* 112, D04306.
- Andreae, M.O. and Merlet, P., (2001), Emission of trace gases and aerosols from biomass burning. *Global biogeochemical cycles*, 15(4), pp.955-966.

- 457 Aluwong T, Wuyep P, Allam L (2011), Livestock–environment interac- tions: methane
458 emissions from ruminants. *Afr J Biotechnol* 10: 1265–1269
- 459 Bergamaschi, P., Lubina, C., Königstedt, R., Fischer, H., Veltkamp, A.C., Zwaagstra, O.,
460 (1998), Stable isotopic signatures ($\delta^{13}\text{C}$, δD) of methane from European landfill sites. *J.*
461 *Geophys. Res. Atmos.* 103, 8251–8265.
- 462 Bousquet, P., Ringeval, B., Pison, I., Dlugokencky, E. J., Brunke, E.- G., Carouge, C.,
463 Chevallier, F., Fortems-Cheiney, A., Franken- berg, C., Hauglustaine, D. A., Krummel, P. B.,
464 Langenfelds, R. L., Ramonet, M., Schmidt, M., Steele, L. P., Szopa, S., Yver, C., Viovy, N.,
465 and Ciais, P. (2011), Source attribution of the changes in atmospheric methane for 2006–
466 2008, *Atmos. Chem. Phys.*, 11, 3689–3700, doi:10.5194/acp-11-3689-2011
- 467 Bousquet, P., Ciais, P., Miller, J. B., Dlugokencky, E. J., Hauglustaine, D. A, Prigent, C., Van
468 der Werf, G. R., Peylin, P., Brunke, E. G., Carouge, C., Langenfelds, R. L., Lathière, J., Papa,
469 F., Ramonet, M., Schmidt, M., Steele, L. P., Tyler, S. C., and White, J. (2006), Contribution
470 of anthropogenic and natural sources to atmospheric methane variability. *Nature*, 443(7110),
471 439–43. doi:10.1038/nature05132
- 472 Bréas, O., Guillou, C., Reniero, F. & Wada, E. (2001), The Global Methane Cycle: Isotopes
473 and Mixing Ratios, Sources and Sinks, *Isotopes in Environmental and Health Studies*, 37:4,
474 257-379, DOI: 10.1080/10256010108033302
- 475 Caro, D., Davis, S.J., Bastianoni, S., Caldeira, K., (2014), Global and regional trends in
476 greenhouse gas emissions from livestock. *Clim. Change* 126, 203–216.
- 477 Ciais, P., Sabine, C., Bala, G., Bopp, L., Brovkin, V., Canadell, J., Chhabra, A., DeFries, R.,
478 Gal- loway, J., Heimann, M., Jones, C., Le Queirèi, C., Myneni, R. B., Piao, S., and
479 Thornton, P. (2013), Carbon and other biogeochemical cycles, in: *Climate Change 2013: The*
480 *Physical Science Basis. Contribution of Working Group I to the Fifth Assessment Report of*
481 *the Intergovernmental Panel on Climate Change*, edited by: Stocker, T. F., Qin, D., Plattner,
482 G.-K., Tignor, M., Allen, S. K., Boschung, J., Nauels, A., Xia, Y., Bex, V., and Midgley, P.
483 M., Cambridge University Press, Cambridge, UK and New York, NY, USA, 465–570
- 484 Chanton, J.P. (2005), The effect of gas transport on the isotope signature of methane in
485 wetlands. *Org. Geochem.* 36, 753–768.
- 486 Chanton, J., Liptay, K., (2000), Seasonal variation in methane oxidation in a landfill cover
487 soil as determined by an in situ stable isotope technique. *Global Biogeochem. Cycles* 14, 51–
488 60.
- 489 Chanton, J., Chaser, L., Glasser, P., & Siegel, D. (2005), Carbon and Hydrogen Isotopic
490 Effects in Microbial Methane from Terrestrial Environments. In: Flanagan, L.B., Ehleringer
491 J.R. and Pataki D.E. eds., *Stable Isotopes and Biosphere Atmosphere Interactions*, Elsevier,
492 Oxford

- 493 Chanton, J. P., Rutkowski, C. M., Schwartz, C. C., Ward, D. E., & Boring, L. (2000), Factors
494 influencing the stable carbon isotopic signature of methane from combustion and biomass
495 burning. *Journal of Geophysical Research*, 105(D2), 1867. doi:10.1029/1999JD90090
- 496 Chanton, J.P., Pauly, G.G., Martens, C.S., Blair, N.E., Dacey, J.W.H., (1988), Carbon
497 isotopic composition of methane in Florida Everglades soils and fractionation during its
498 transport to the troposphere. *Global Biogeochem. Cycles* 2, 245–252.
- 499 Conrad, R., (2002), Control of microbial methane production in wetland rice fields. *Nutr.*
500 *Cycl. Agroecosystems* 64, 59–69.
- 501 Crutzen, P.J. & Andreae, M.O. (1990), Biomass burning in the tropics: impact on
502 atmospheric chemistry and biogeochemical cycles. *Science*, 250, 1669–78
- 503 Dlugokencky, E. J., Nisbet, E. G., Fisher, R., & Lowry, D. (2011), Global atmospheric
504 methane: budget, changes and dangers. *Philosophical Transactions. Series A, Mathematical,*
505 *Physical, and Engineering Sciences*, 369(1643), 2058–72. doi:10.1098/rsta.2010.0341
- 506 European Commission, Joint Research Centre (JRC)/Netherlands Environmental Assessment
507 Agency (PBL), (2011), Emission Database for Global Atmospheric Research (EDGAR),
508 release version 4.2. <http://edgar.jrc.ec.europa.eu>
- 509 Food and agricultural organisation of the United Nations (FAO), (2016), FAOSTAT
510 Emissions Database, Agriculture, Enteric Fermentation,
511 <http://faostat3.fao.org/download/G1/GE/E> (Accessed 15 Oct 2016).
- 512 Fisher R. E, France J. L., Lowry, D., Lanoisellé M., Brownlow R., Pyle J.A., Cain M.,
513 Warwick N., O'Shea S., Bauguitte S.J.-B., Wellpott A., Skiba U., Drewer J., Dinsmore K.,
514 George C., Hayman G.D., Allen G., Gallagher M.W., Bower K., Aalto T., Lohila A., Crill P.,
515 and Nisbet E.G. (2017), Measurement of the ¹³C isotopic signature of methane emissions
516 from Northern European wetlands, *Global Biogeochem. Cycles*, 31,
517 doi:10.1002/2016GB005504.
- 518 Fisher, R. E., Lowry, D., Wilkin, O., Sriskantharajah, S., & Nisbet, E. G. (2006), High
519 precision, automated stable isotope analysis of atmospheric methane and carbon dioxide
520 using continuous-flow isotope-ratio mass spectrometry. *Rapid Communications in Mass*
521 *Spectrometry* : 20(2), 200–8. doi:10.1002/rcm.2300
- 522 Frankenberg, C., Bergamaschi, P., Butz, A., Houweling, S., Meirink, J.F., Notholt, J.,
523 Petersen, A.K., Schrijver, H., Warneke, T., Aben, I., (2008), Tropical methane emissions: A
524 revised view from SCIAMACHY onboard ENVISAT. *Geophys. Res. Lett.* 35, 1–5.
- 525 Giggenbach WF (1997), Relative importance of thermodynamic and kinetic processes in
526 governing the chemical and isotopic composition of carbon gases in high-heatflow
527 sedimentary basins. *Geochim Cosmochim Acta* 61:3763-3785.

- 528 Happell JD, Chanton, JP & Showers W (1994), The influence of methane oxidation on the
529 stable isotopic composition of methane emitted from Florida Swamp forests. *Geochim.*
530 *Cosmochim. Acta.* 58: 4377–4388
- 531 Hook, S.E., Wright, A.-D.G., McBride, B.W. (2010), Methanogens: methane producers of the
532 rumen and mitigation strategies. *Archaea*. doi:10.1155/2010/94578
- 533 Huijnen, V., Wooster, M.J., Kaiser, J.W., Gaveau, D.L.A., Flemming, J., Parrington, M.,
534 Inness, A., Murdiyarso, D., Main, B. and van Weele, M., (2016) Fire carbon emissions over
535 maritime southeast Asia in 2015 largest since 1997. Scientific reports, 6.
- 536 Jenden PD (1988), Analysis of Gases in the Earth's Crust. Gas Research Institute, Chicago,
537 571pp.
- 538 Keeling, C. D. (1958), The concentration and isotopic abundances of atmospheric carbon
539 dioxide in rural areas, *Geochimica et Cosmochimica Acta*, 13, 322-334
- 540 Kirschke, S., Bousquet, P., Ciais, P., Saunois, M., Canadell, J. G., Dlugokencky, E. J., ...
541 Zeng, G. (2013), Three decades of global methane sources and sinks. *Nature Geoscience*,
542 6(10), 813–823. doi:10.1038/ngeo1955
- 543 Klevenhusen, F., Bernasconi, S. M., Kreuzer, M., & Soliva, C. R. (2010), Experimental
544 validation of the Intergovernmental Panel on Climate Change default values for ruminant-
545 derived methane and its carbon-isotope signature. *Animal Production Science*, 50(3), 159.
546 <http://doi.org/10.1071/AN09112>
- 547 Levandowski J. H. (2009), Petrologia e Geoquimica Das Camadas De Carvao E Sua Relacao
548 Com Gas Natural Determinado No Poco. Dissertation, Universidade Federal do Rio Grande
549 do Sul, Porto Alegre, Brazil, 92 pp.
- 550 Levin, I., Bergamaschi, P., Dörr, H., & Trapp, D. (1993), Stable isotopic signature of
551 methane from major sources in Germany. *Chemosphere*, 26(1–4), 161 – 177.
552 [http://doi.org/http://dx.doi.org/10.1016/0045-6535\(93\)90419-6](http://doi.org/http://dx.doi.org/10.1016/0045-6535(93)90419-6)
- 553 Matthey, D.P., Fisher, R., Atkinson, T.C., Latin, J.-P., Durrell, R., Ainsworth, M., Lowry, D.,
554 Fairchild, I.J., (2013), Methane in underground air in Gibraltar karst. *Earth Planet. Sci. Lett.*
555 374, 71–80.
- 556 Melton, J. R., R. Wania, E.L. Hodson, B. Poulter, B. Ringeval, R. Spahni, T. Bohn, C.A.
557 Avis, D.J. Beerling, G. Chen, A.V. Eliseev, S.N. Denisov, P.O. Hopcroft, D.P. Lettenmaier,
558 W.J. Riley, J.S. Singarayer, Z.M. Subin, H. Tian, S. Zurcher, V. Brovkin, P.M. van
559 Bodegom, T. Kleinen, Z.C. Yu and J.O. Kaplan (2013), Present state of global wetland extent
560 and wetland methane modelling: conclusions from a model inter-comparison project
561 (WETCHIMP), *Biogeosciences*, 10(2), 753-788, doi: 10.5194/bg-10-753-2013.
- 562 Mitsch, W.J., Nahlik, A., Wolski, P., Bernal, B., Zhang, L., Ramberg, L. (2009), Tropical
563 wetlands: seasonal hydrologic pulsing, carbon sequestration, and methane emissions. *Wetl.*
564 *Ecol. Manag.* 18, 573–586

- 565 Nakagawa, F., Yoshida, N., Sugimoto, A., Wada, E., Yoshioka, T., Ueda, S., Vijarnsorn, P.,
566 (2002), Stable isotope and radiocarbon compositions of methane emitted from tropical rice
567 paddies and swamps in Southern Thailand. *Biogeochemistry* 61, 1–19
- 568 Nisbet E.G., Dlugokencky E.J., Manning M.R., Lowry D., Fisher R. E., France J. L., Michel
569 S. E., Miller J.B., White J.W.C., Vaughn B., Bousquet P. Pyle J.A., Warwick N.J., Cain M.,
570 Brownlow R., Zazzeri G., Lanoisellé M., Manning A.C., Gloor E., Worthy D.E.J., Brunke E.-
571 G., Labuschagne C., Wolff E.W. and Ganesan A.L. (2016), Rising atmospheric methane:
572 2007-14 growth and isotopic shift,. *Global Biogeochem. Cycles*, 30, doi:10.1002/
573 2016GB005406.
- 574 Nisbet, E. G., Dlugokencky, E. J., & Bousquet, P. (2014), Atmospheric science. Methane on
575 the rise--again. *Science (New York, N.Y.)*, 343(6170), 493–5. doi:10.1126/science.1247828
- 576 Osborne, C.P., Salomaa, A., Kluyver, T.A., Visser, V., Kellogg, E.A., Morrone, O.,
577 Vorontsova, M.S., Clayton, W.D., Simpson, D.A., (2014). A global database of C 4
578 photosynthesis in grasses. *New Phytol.* 204, 441–446.
- 579 Pande HC, Raina A, Roy V, Saxena RK, Singh H, Singh RR (2011) Origin of Biogenic
580 Gases in East Coast Basins of India. Geo-India 2011 Conference, Available at:
581 <http://www.apgindia.org/pdf/649.pdf>
- 582 Pataki, D.E., Ehleringer, J.R., Flanagan, L.B., Yakir, D., Bowling, D.R., Still, C.J.,
583 Buchmann, N., Kaplan, J.O., Berry, J. a., (2003), The application and interpretation of
584 Keeling plots in terrestrial carbon cycle research. *Global Biogeochemical. Cycles* 17.
- 585 Prinzhofer A, Santos Neto EV, Battani A (2010), Coupled use of carbon isotopes and noble
586 gas isotopes in the Potiguar basin (Brazil): Fluids migration and mantle influence. *Mar Petrol*
587 *Geol* 27:1273-1284.
- 588 Prinzhofer AA, Mello MR, Takaki T (2000), Geochemical characterization of natural gas: A
589 physical multivariable approach and its applications in maturity and migration estimates.
590 *AAPG Bull* 84:1152-1172.
- 591 Quay, P.D., King, S.L., Stutsman, J., Wilbur, D.O., Steele, L.P., Fung, I., Gammon, R.H.,
592 Brown, T.A., Farwell, G.W., Grootes, P.M., Schmidt, F.H., (1991), Carbon Isotopic
593 Composition of Atmospheric CH₄: Fossil and biomass burning source strengths. *Global*
594 *Biogeochem. Cycles* 5, 25–47.
- 595 Quay, P.D., King, S.L., Lansdown, J.M., Wilbur, O. D, (1988), Isotopic composition of
596 methane released from wetlands: implications for the increase in atmospheric methane.
597 *Global Biogeochem. Cycles* 2, 385–397.
- 598 Randerson, J.T., van der Werf, G.R., Collatz, G.J., Giglio, L., Still, C.J., Kasibhatla, P.,
599 Miller, J.B., White, J.W.C., DeFries, R.S., Kasischke, E.S., (2005), Fire emissions from C3
600 and C4 vegetation and their influence on interannual variability of atmospheric CO₂ and
601 δ¹³CO₂. *Global Biogeochem. Cycles* 19, 1–13.

- 602 Rao, D.K., Bhattacharya, S.K. and Jani, R.A., (2008), Seasonal variations of carbon isotopic
603 composition of methane from Indian paddy fields. *Global Biogeochem. Cycles* 22, 1–5.
- 604 Rigby, M., Manning, A.J. and Prinn, R.G., (2012), The value of high-frequency, high-
605 precision methane isotopologue measurements for source and sink estimation. *J. Geophys.*
606 *Res. Atmos.* 117.
- 607 Ringeval, B., de Noblet-Ducoudre, N., Ciais, P., Bousquet, P., Prigent, C., Papa, F., and
608 Rossow, W. B. (2010), An attempt to quantify the impact of changes in wetland extent on
609 methane emissions on the seasonal and interannual time scales, *Global Biogeochem. Cy.*, 24,
610 GB2003, doi:10.1029/2008GB003354
- 611 Ripple W. J., Smith P., Haberl H., Montzka S. A., McAlpine C. & Boucher D. H. (2013),
612 Ruminants, climate change and climate policy. *Nature Climate Change*, 4, 2–5
- 613 Roberts, G., M. J. Wooster, and E. Lagoudakis (2009), Annual and diurnal African biomass
614 burning temporal dynamics, *Biogeosciences*, 6, 849–866, doi:10.5194/bg-6-849-2009.
- 615 Rust, F. E. (1981), Ruminant Methane d(13C/12C) Values: Relation to Atmospheric
616 Methane. *Science*. Vol. 211, Issue. 4486. Pp. 1044-1046.
- 617 Sanderson, M.G., (1996), Biomass of termites and their emissions of methane and carbon
618 dioxide: a global database. *Glob. Biogeochem. Cycles* 10, 543–557.
- 619 Satyana AH, Marpaung LP, Purwaningsih ME, Utama MK (2007), Regional gas
620 geochemistry of Indonesia: Genetic characterization and habitat of natural gases. Proc
621 *Indonesian Petrol Assoc*, Available at:
622 http://archives.datapages.com/data/ipa_pdf/078/078001/pdfs/IPA07-G-050.pdf
- 623 Saunois, M., Bousquet, P., Poulter, B., Peregon, A., Ciais, P., Canadell, J.G., Dlugokencky,
624 E.J., Etiope, G., Bastviken, D., Houweling, S., Janssens-Maenhout, G., Tubiello, F.N.,
625 Castaldi, S., Jackson, R.B., Alexe, M., Arora, V.K., Beerling, D.J., Bergamaschi, P., Blake,
626 D.R., Brailsford, G., Brovkin, V., Bruhwiler, L., Crevoisier, C., Crill, P., Curry, C.,
627 Frankenberg, C., Gedney, N., Höglund-Isaksson, L., Ishizawa, M., Ito, A., Joos, F., Kim, H.-
628 S., Kleinen, T., Krummel, P., Lamarque, J.-F., Langenfelds, R., Locatelli, R., Machida, T.,
629 Maksyutov, S., McDonald, K.C., Marshall, J., Melton, J.R., Morino, I., O’Doherty, S.,
630 Parmentier, F.-J.W., Patra, P.K., Peng, C., Peng, S., Peters, G.P., Pison, I., Prigent, C., Prinn,
631 R., Ramonet, M., Riley, W.J., Saito, M., Schroder, R., Simpson, I.J., Spahni, R., Steele, P.,
632 Takizawa, A., Thorton, B.F., Tian, H., Tohjima, Y., Viovy, N., Voulgarakis, A., van Weele,
633 M., van der Werf, G., Weiss, R., Wiedinmyer, C., Wilton, D.J., Wiltshire, A., Worthy, D.,
634 Wunch, D.B., Xu, X., Yoshida, Y., Zhang, B., Zhang, Z., Zhu, Q., (2016), The Global
635 Methane Budget: 2000-2012. *Earth Syst. Sci. Data Discuss.* 1–79.
- 636 Schaefer, H., Mikaloff Fletcher, S. E., Veidt, C., Lassey, K. R., Brailsford, G. W., Bromley,
637 T. M., Dlugokencky, E. J., Michel, S. E., Miller, J. B., Levin, I., Lowe, D. C., Martin, R. J.,
638 Vaughn, B. H. and White, J. W. C. (2016), A 21st century shift from fossil-fuel to biogenic
639 methane emissions indicated by 13CH₄. *Science*, 351(6278). doi:10.1126/science.aad2705

- 640 Schaefer, H., & Whiticar, M. J. (2008), Potential glacial-interglacial changes in stable carbon
641 isotope ratios of methane sources and sink fractionation. *Global Biogeochemical Cycles*,
642 22(1), 1–18. doi:10.1029/2006GB002889
- 643 Schwietzke, S., Sherwood, O.A., Bruhwiler, L.M.P., Miller, J.B., Etiope, G., Dlugokencky,
644 E.J., Michel, S.E., Arling, V.A., Vaughn, B.H., White, J.W.C., Tans, P.P., (2016), Upward
645 revision of global fossil fuel methane emissions based on isotope database. *Nature* 538, 88–
646 91.
- 647 Sherwood, O., Schwietzke, S., Arling, V. & Etiope, G. (2016), Global Inventory of Fossil and
648 Non-fossil Methane $\delta^{13}\text{C}$ Source Signature Measurements for Improved Atmospheric
649 Modeling. <http://doi.org/10.15138/G37P4D>.
- 650 Snover, A.K., Quay, P.D. & Hao, W.M., (2000), The D / H content of methane emitted from
651 biomass burning ponderosa. *Global Biogeochem. Cycles* 14, 11–24.
- 652 Sriskantharajah, S., Fisher, R.E., Lowry, D., Aalto, T., Hatakka, J., Aurela, M., Laurila, T.,
653 Lohila, A., Kuitunen, E., Nisbet, E.G., (2012), Stable carbon isotope signatures of methane
654 from a Finnish subarctic wetland. *Tellus B* 64, 1–8.
- 655 Stevens, C.M., & Engelkemeir, A. (1988), Stable carbon isotopic composition of methane
656 from some natural and anthropogenic sources. *J. Geophys. Res. Atmos.* 93, 725–733.
- 657 Thorpe, A. (2008), Enteric fermentation and ruminant eructation: the role (and control?) of
658 methane in the climate change debate. *Clim. Change*, 93, 407–431
- 659 Tyler, S. C. (1986), Stable carbon isotope ratios in atmospheric methane and some of its
660 sources. *Journal of Geophysical Research: Atmospheres*, 91(D12), 13232–13238.
661 <http://doi.org/10.1029/JD091iD12p13232>
- 662 Tyler, S.C., Brailsford, G.W., Yagi, K., Minami, K. & Cicerone, R.J., (1994), Seasonal
663 variations in methane flux and $\delta^{13}\text{C}$ values for rice paddies in Japan and their
664 implications. *Global Biogeochem. Cycles* 8, 1–12.
- 665 Tyler, S.C., Zimmerman, P.R., Greenberg, J.P., Westberg, C., Darlington, J.P.E.C., (1988),
666 Measurements and interpretation of $\delta^{13}\text{C}$ of methane from termites, rice paddies, and wetlands
667 in Kenya. *Global Biogeochem. Cycles* 2, 341–355.
- 668 Tyler, S.C., Blake, D.R. & Rowland, F.S., (1987), $\delta^{13}\text{C} / \delta^{12}\text{C}$ Ratio in Methane From the
669 Flooded Amazon Forest. *J. Geol. Res.* 92, 1044–1048.
- 670 Wangyao, K., Yamada, M., Endo, K., Ishigaki, T., Naruoka, T., Towprayoon, S.,
671 Chiemchaisri, C., Sutthasil, N., (2010), Methane generation rate constant in tropical landfill.
672 *J. Sustain. Energy Environ.* 1, 181–184.

- 673 Ward J, Slater G, Moser D, Lin LH, Lacrampe-Couloume G, Bobin AS, et al (2004),
674 Microbial hydrocarbon gases in the Witwatersrand Basin, South Africa: Implications for the
675 deep biosphere. *Geochim Cosmochim Acta* 68: 3239–3250.
- 676 Whiticar, M. J., E. Faber and M. Schoell (1986), Biogenic Methane Formation in Marine and
677 Fresh-Water Environments - CO₂ Reduction Vs Acetate Fermentation Isotope Evidence,
678 *Geochimica Et Cosmochimica Acta*, 50(5), 693-709, doi: 10.1016/0016-7037(86)90346-7
- 679 Wooster, M.J., Perry, G.L.W. and Zoumas, A., (2012), Fire, drought and El Niño
680 relationships on Borneo (Southeast Asia) in the pre-MODIS era (1980–2000).
681 *Biogeosciences*, 9(1), pp.317-340.
- 682 Wooster, M.J., Freeborn, P.H., Archibald, S., Oppenheimer, C., Roberts, G.J., Smith, T.E.L.,
683 Govender, N., Burton, M. and Palumbo, I., (2011), Field determination of biomass burning
684 emission ratios and factors via open-path FTIR spectroscopy and fire radiative power
685 assessment: headfire, backfire and residual smouldering combustion in African savannahs.
686 *Atmospheric Chemistry and Physics*, 11(22), pp.11591-11615.
- 687 Zazzeri, G., Lowry, D., Fisher, R.E., France, J.L., Lanoisellé, M., Kelly, B.F.J., Necki, J.M.,
688 Iverach, C.P., Ginty, E., Zimnoch, M., Jasek, A., Nisbet, E.G., (2016), Carbon isotopic
689 signature of coal-derived methane emissions to the atmosphere: from coalification to
690 alteration. *Atmos. Chem. Phys.* 16, 13669–13680.
- 691 Zazzeri, G., D. Lowry, R.E. Fisher, J.L. France, M. Lanoisellé and E.G. Nisbet (2015), Plume
692 mapping and isotopic characterisation of anthropogenic methane sources, *Atmospheric*
693 *Environment*, 110, 151-162, doi: 10.1016/j.atmosenv.2015.03.029

Isotopic ratios of tropical methane emissions by atmospheric measurement and continental-scale variability.

R. Brownlow¹, D. Lowry¹, R. E. Fisher¹, J. L. France², M. Lanoisellé¹, B. White¹, M. J. Wooster^{3,4}, T. Zhang^{3,4} and E. G. Nisbet¹

¹ Department of Earth Sciences, Royal Holloway, University of London, Egham, TW20 0EX, UK.

² Centre for Oceanic and Atmospheric Sciences, School of Environmental Sciences, University of East Anglia, Norwich, NR4 7TJ, UK

³ King's College London, Dept. of Geography, Strand, London WC2R 2LS

⁴ NERC National Center for Earth Observation, UK

Contents of this file

Figures S1 to S4

Tables S1 to S2

Introduction

The supporting information gives keeling plots for all the wetland samples (Fig. S1), rice sources (Fig S2), enteric fermentation sources (Fig. S3) and biomass burning sources (Fig. S4). The sample types, locations and dates are listed in Table S1. Table S2 gives a description of the Zimbabwe cow diets.

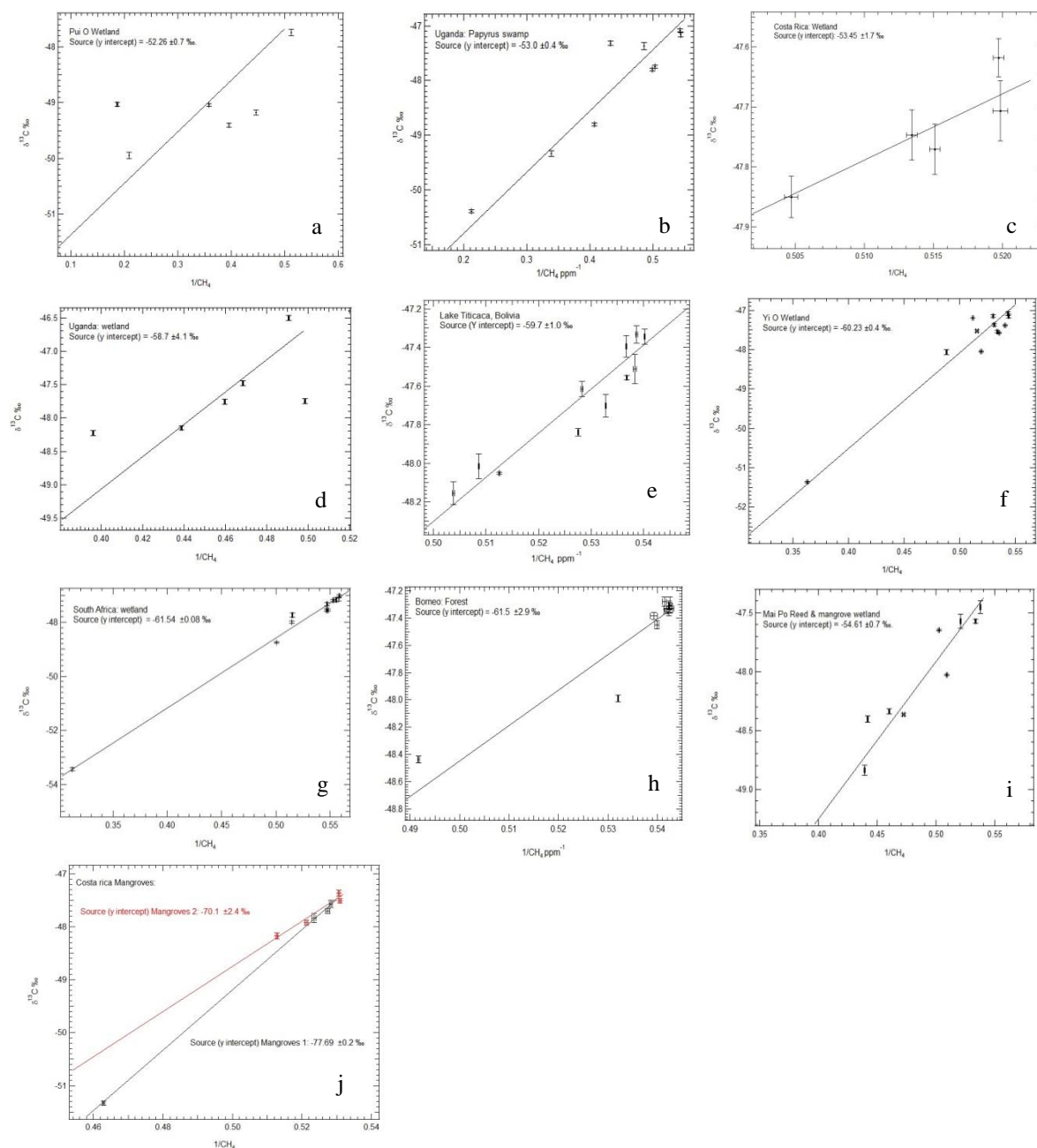


Figure S1: Keeling plots for wetland sites:

- a) Pui O, Hong Kong: wetland. Source signature is $-52.3 \pm 0.7 \text{ ‰}$.
- b) Kajjansi airstrip, Kampala, Uganda: Papyrus swamp. Source signature is $-53.0 \pm 0.4 \text{ ‰}$.
- c) Palo Verde National Park, Costa Rica: Wetland. Source signature is $-53.5 \pm 1.7 \text{ ‰}$.
- d) Edge of Lake Victoria, Uganda: wetland. Source signature is $-58.7 \pm 4.1 \text{ ‰}$.
- e) Lake Titicaca, Bolivia: samples taken at distances between 1m and 200m from water giving a source signature of $-59.7 \pm 1.0 \text{ ‰}$.
- f) Yi O, Hong Kong: wetland. Source signature is $-60.2 \pm 0.4 \text{ ‰}$.
- g) Tor Doone, South Africa: wetland. Source signature is $-61.5 \pm 0.1 \text{ ‰}$.
- h) Danum valley, Borneo: Forest, decaying leaves and streams and Forest background. Source signature is $-61.5 \pm 2.9 \text{ ‰}$.
- i) Mai Po, Hong Kong: Mangrove wetland. Source signature is $-54.6 \pm 0.7 \text{ ‰}$.
- j) Sierpe Mangroves (1) and Mangroves in Puerto Jimenez (2) Costa Rica. Source signatures are $-77.7 \pm 0.2 \text{ ‰}$ and $-70.1 \pm 2.4 \text{ ‰}$.

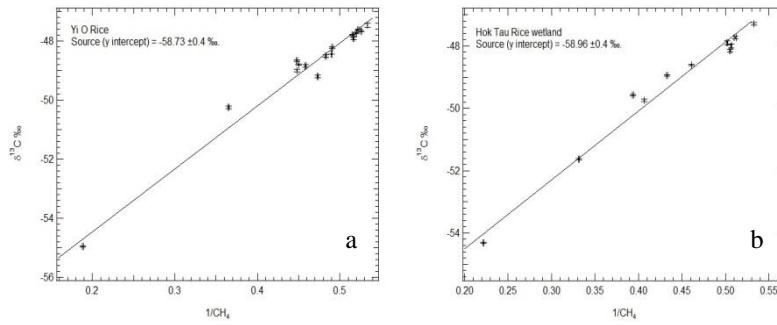


Figure S2: Keeling plots for rice sources:

a) Yi O, Hong Kong: Rice paddy -58.7 ± 0.4 ‰.

b) Hok Tau, Hong Kong: Rice wetland -58.9 ± 0.4 ‰.

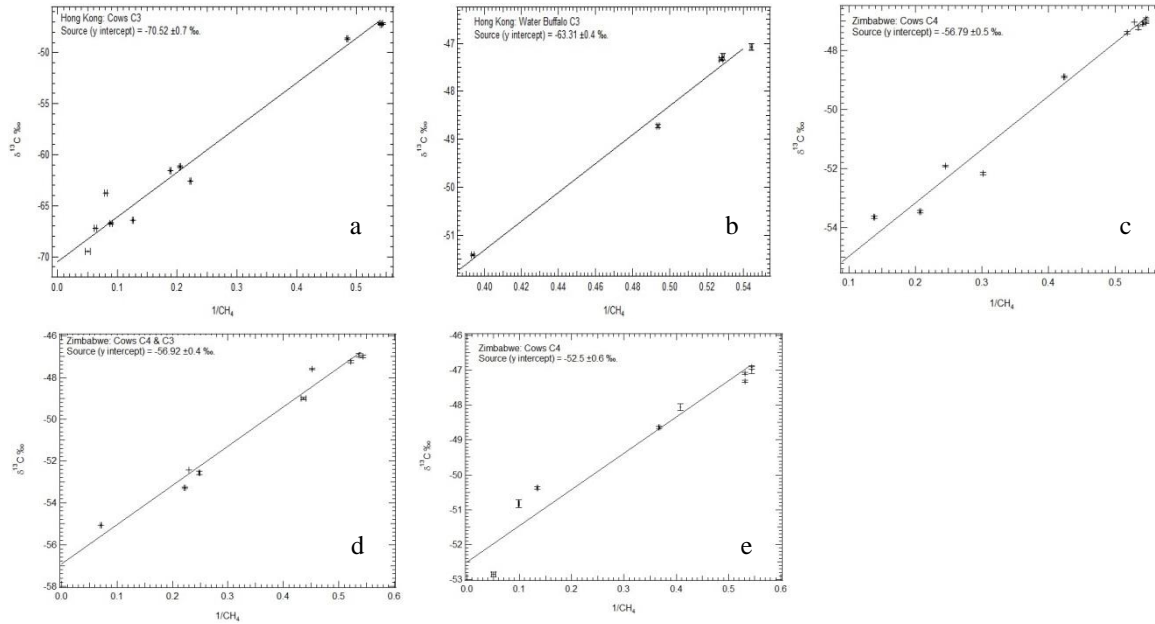


Figure S3: Keeling plots for enteric fermentation:

a) Tai O, Hong Kong cows. Source signature: -70.5 ± 0.7 ‰. C3

b) Pui O, Hong Kong Water Buffalo. Source signature: -63.3 ± 0.4 ‰. C3

c) Zimbabwe Dom cows. Source signature: -56.8 ± 0.5 ‰. C4

d) Zimbabwe Tavistock Farm cows. Source signature: -56.9 ± 0.4 ‰. C3 & C4

e) Zimbabwe Lobels Farm cows. Source signature: -52.5 ± 0.6 ‰. C4

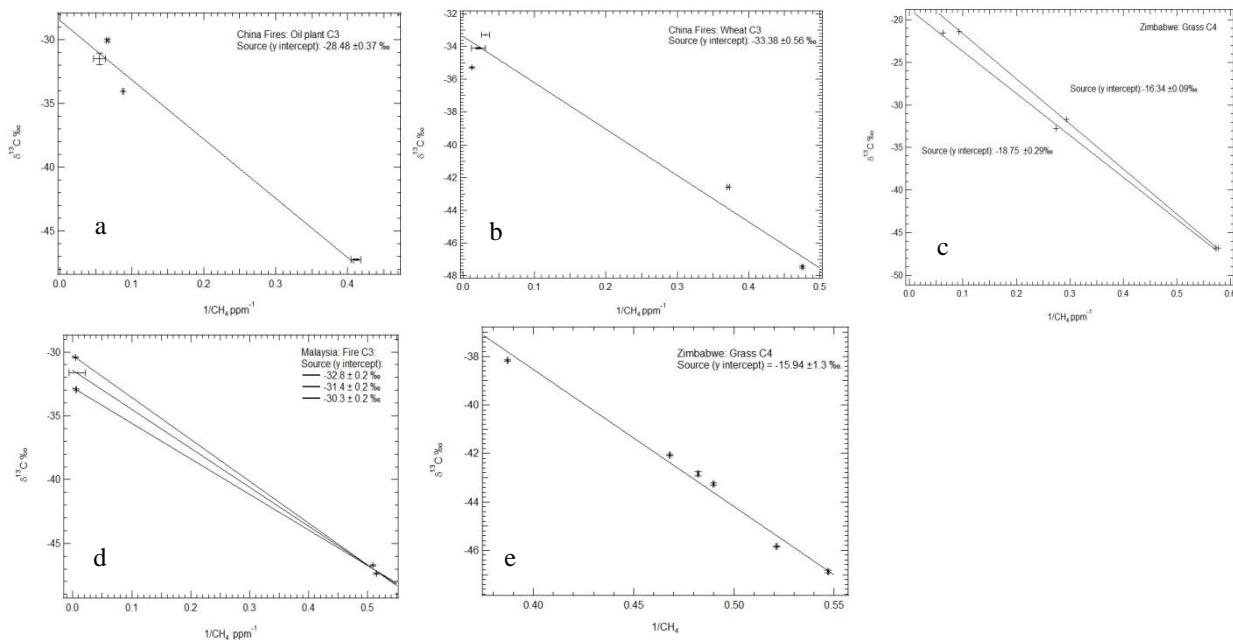


Figure S4: Keeling Plots for Biomass Burning:

- a) China oil plant, C3, burn giving a source signature of -28.5 ± 0.4 ‰.
- b) China wheat, C3, burn giving a source signature of -33.4 ± 0.6 ‰.
- c) Zimbabwe C4 grass burning gives source signatures of -16.3 ± 0.1 ‰ and -18.8 ± 0.3 ‰.
- d) Bachok Fire Keeling plots Mango wood (C3) burning: larger plume with waste mixed = -30.3 ± 0.2 . Small plume = -32.8 ± 0.2 ‰. Bottom of the large plume = -31.4 ± 0.2 ‰.
- e) Chisipite Vlei, Zimbabwe C4 grass burning -15.9 ± 1.3 ‰.

Table S1: Sample type, location and date.

Sample Site	Site type	Latitude	Longitude	Sample dates
Tongling, China	Biomass burning	30°56' N	117°46' E	14/06/14 – 16/06/14
Hok Tau, Hong Kong	Rice wetland	22°29' N	114°10' E	28/06/16
Mai Po, Hong Kong	Reed, mangroves & marshes	22°28' N	114° 2' E	28/06/16
Pui O, Hong Kong	Water Buffalo & marsh	22°14' N	113°58' E	25/06/16
Tai O, Hong Kong	Cows & Mangroves	22°14' N	113°51' E	26/06/16
Yi O, Hong Kong	Marsh & rice	22°13' N	113°50' E	25/06/16
Palo Verde National Park, Costa Rica	Coastal floodplain freshwater marsh	10° 20' N	85° 20' W	06/02/16
Puerto Jimenez, Costa Rica Mangroves	Mangroves	8°32' N	83° 18' W	31/01/16
Sierpe, Costa Rica Mangroves	Mangroves	8°32' N	83°18' W	11/01/16
Bachok, Malaysia	Biomass burning	6° 0' N	102°25' E	22/01/14
Danum Valley, Borneo	Forest wetland	4° 54' N	117° 42' E	18/08/15- 19/08/15
Lake Victoria, Uganda	Freshwater wetland	0°15' N	32°38' E	10/15/14
Papyrus swamp, Uganda	Papyrus swamp	0°11' N	32°33' E	12/05/14
Lake Titicaca, Bolivia	Freshwater wetland	16°14' S	68°34' W	19/02/14
Zimbabwe	Cows	17° 48' S	31° 0' E	07/06/16
Chisipite Vlei, Zimbabwe	Biomass burning	17° 48' S	31° 0' E	26/08/16
Zimbabwe	Biomass burning	20°11' S	28°37' E	July 1998
Tor Doone, South Africa	Freshwater wetland	32°35' S	26° 56' E	24/12/14-28/12/14

Table S2: Diet description for the Zimbabwe cows sampled.

Zimbabwe cows	Description
Dom cows	The samples were collected from rural cattle in a pen near Domboshawa north of Harare. The cattle are mainly herded in the rural area and are grass fed (C4) with little or no supplementary feed.
Lobels cows	Cattle are rotated on pasture and a tractor-drawn mobile dairy comes to them at milking time when supplementary feed in the form of hay and pellets is given to them. Mostly C4.
Tavistock cows	Cows occupy pasture blocks, which due to the density of dairy animals is generally overgrazed. C4/C3 - no bushes etc., but possibly cotton seed plus hay and balanced vitamins.

Chapter 4

Influence of local methane emissions on a tropical monitoring site

This chapter is presented in paper format and will be submitted to a journal. R. Brownlow carried out sampling in Bachok, wrote the manuscript, plotted and interpreted the data. R. Brownlow, D. Lowry & R. E. Fisher analysed the Tedlar bag samples at RHUL. G. Forster set up and ran the LGR in Bachok. M. J. Ashfold and Z. L. Fleming ran the NAME plots. All the authors made suggestions and comments on the manuscript.

Influence of local methane emissions on a tropical monitoring site

R. Brownlow¹, D. Lowry¹, R. E. Fisher¹, J. L. France², E. G. Nisbet¹, G. Forster^{2,3}, D. Oram^{2,3}, W. Sturges², M. I. Mead⁴, N. Harris⁴, Z. L. Fleming⁵, M. J. Ashfold⁶, A. A. Samah⁷ and S. M. Phang⁷

1. Department of Earth Sciences, Royal Holloway, University of London, Egham, TW20 0EX, UK

2. Centre for Oceanic and Atmospheric Sciences, School of Environmental Sciences, University of East Anglia, Norwich, NR4 7TJ, UK

3. NCAS, UK

4. Centre for Atmospheric Informatics and Emissions Technology, Cranfield University, Cranfield MK43 0A, UK

5. National Centre for Atmospheric Science (NCAS), Department of Chemistry, University of Leicester, Leicester, LE1 7RH, UK

6. School of Biosciences, University of Nottingham Malaysia Campus, Jalan Broga, 43500 Semenyih, Selangor, Malaysia

7. Institute of Ocean and Earth Sciences, University of Malaya, 50603 Kuala Lumpur, Malaysia

Corresponding author: Rebecca Brownlow (Rebecca.Brownlow.2009@live.rhul.ac.uk)

Abstract

The tropics are an important part of the global methane budget but are understudied. In south east Asia increasing industry, biomass burning from tropical forests and agriculture influence the CH₄ emissions. During January and February 2014 CH₄, $\delta^{13}\text{C}_{\text{CH}_4}$ and other species were measured from a coastal site in Bachok, Malaysia. Background mole fraction at the site is determined by longer range transport with higher mole fractions when air masses arrive from over land, during the cold surge event however, long range transport of CH₄ may be hard to monitor at this site due to significant local emissions. The local isotopic signature from the tower is $-54.9 \pm 1.2\text{‰}$ and the local peaks are likely to be caused by diurnal cycles with mixed CH₄ emissions from local wetlands and biomass burning.

1. Introduction

Methane is an important greenhouse gas with emissions from both anthropogenic and natural sources. The mole fraction of CH₄ has increased by a factor of 2.5 since pre-industrial times, rising from 722 ppb to 1845 ±2 ppb in 2015 (WMO, 2016). Tropical CH₄ emissions are thought to contribute to around 200 Tg/year which is about 40% of the global methane (CH₄) budget (Bousquet et al., 2006; Nisbet et al., 2014; Schaefer et al., 2016). Measurements in the tropics are sparse as they are usually made in more accessible areas (Dlugokencky et al., 2011).

Isotopic measurements are useful in helping to identify CH₄ emissions as the varying sources have different affinities for ¹³C and ¹²C. The δ¹³C (¹³C/¹²C ratios) signature, expressed in permil (‰), can be used to help determine the sources. Relative to the background air (-47‰) the emissions may be either enriched or depleted in ¹³C (Kirschke et al., 2013). These ratios are related to temperature. CH₄ formed at a higher temperature is enriched in the heavier isotope compared to biogenic sources which are depleted as less energy is needed to incorporate the lighter isotope (Chanton et al., 2005). Examples of expected tropical isotopic signatures for different sources are shown in Table 1.

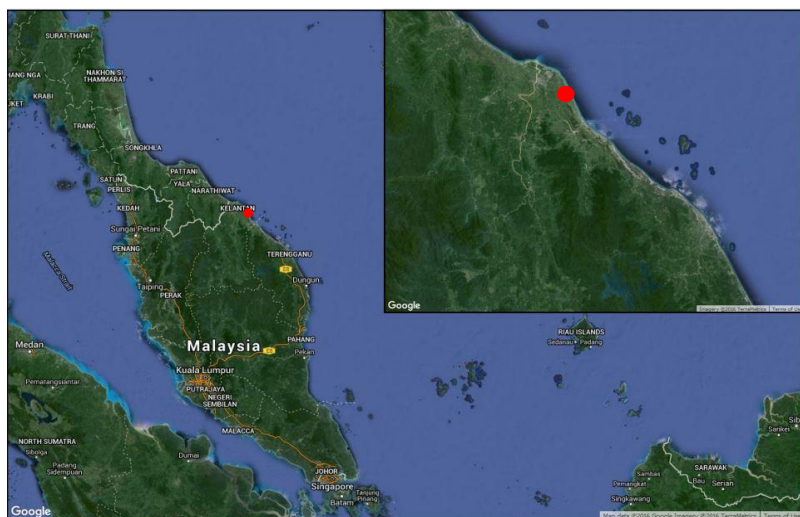
Site	δ ¹³ C (‰)	References
Energy		
Fossil Fuels	-47.8 ±6.1	Levandowski, 2009; Ward et al., 2004; Pande et al., 2011; Satyana et al 2007; Prinzhofer et al 2010; Prinzhofer et al 2000 Giggenbach 1997; Jenden 1988
Wetlands		
Tropical wetlands	-58.2 ±3.9	Brownlow et al., 2017
Rice agriculture	-51 to -65	Tyler et al., 1994; Tyler et al 1988; Rao et al., 2008; Nakagawa et al., 2002; Brownlow et al., 2017
Biomass Burning		
C4 plants	-12 to -17	Chanton et al., 2000; Snover et al. 2000; Brownlow et al., 2017
C3 plants	-24 to -33	Chanton et al., 2000; Snover et al. 2000; Brownlow et al., 2017

Table 1: Tropical δ¹³C Isotopic Source Signatures

1.2 Bachok, Malaysia

In Southeast Asia increasing industry, biomass burning from tropical forests and agriculture influence the CH₄ emissions (Saunois et al., 2016; Nisbet et al., 2016). The most significant anthropogenic emission sources in this region are from China, where fossil fuels, waste and agriculture dominate (Saunois et al., 2016) (see Table 2).

The Institute of Ocean and Earth Sciences (IOES) (6.009°N, 102.425°E) is located in the South China Sea region. It is part of the University of Malaya, located in the Kelantan province on the east coast of Peninsular



Malaysia (Fig. 1). A 19m high observation tower at the site aims to study long range transported pollution, air sea exchange, and coastal meteorology. This study focuses on a field campaign undertaken from January to February 2014. In this region there is a transition from the winter monsoon period into the dry season during this period.

During the winter monsoon period, air masses in the region are influenced by the large anticyclones over Siberia and so arrive from the north east (Zhang et al., 1997) (See Supplementary Information (SI) 1), allowing Chinese and South East Asia source regions to be monitored. Cold-surge events also occur regularly in this region. They are caused by a southeasterly movement of the Siberian High pressure system. The cold air flowing south from the Siberian highs intensifies low-level north-easterly winds in the South China Sea.

70 Within a few days the cold surge spreads towards the tropics and often dominates the low-
71 level circulation patterns over the South China Sea (Ashfold et al., 2015). The cold surge is
72 identified by a quick rise in surface pressure, strong northerly winds and a decrease in
73 temperature (Zhang et al., 1997; Garreaud, 2001). These cold surge events, which last up to
74 several days, may cause rapid mass transport of air masses with anthropogenic influence from
75 China and South East Asia to this region (Ashfold et al., 2015).

76 The EDGAR emissions (European Commission, 2011) inventory may be used to identify
77 likely anthropogenic sources that are expected to be influencing the air masses travelling
78 from the North East over South East Asian regions (Table 2). The EDGAR V4.2 inventory
79 also shows there are significant anthropogenic biogenic emissions in Cambodia and Vietnam
80 from agriculture (rice and ruminants). In Cambodia and Vietnam rice emissions contribute to
81 39.6% and 42.5% and ruminant emissions contribute to 16.5% and 11.7%, respectively.
82 Fossil fuel emissions are important in Vietnam and Malaysia and Biomass burning is
83 important in Cambodia. In South East Asia biomass burning peaks in March so it is expected
84 to be increasing during the campaign period (Streets et al., 2003). The EDGAR inventory
85 does not give natural wetland emissions which may also be a significant biogenic source
86 influencing the air masses (Saunio et al., 2016).

CH₄ Source	Cambodia		Vietnam		Malaysia		China	
	Tg yr⁻¹	%	Tg yr⁻¹	%	Tg yr⁻¹	%	Tg yr⁻¹	%
Rice	0.43	39.6	1.81	42.5	0.16	10.6	13.3	22.2
Ruminants	0.18	16.5	0.50	11.7	0.05	3.0	9.6	16.1
Manure	0.03	2.3	0.17	3.9	0.02	1.3	1.5	2.5
Biomass Burning	0.33	29.9	0.11	2.6	0.08	5.5	0.05	0.1
Waste	0.07	6.6	0.51	11.9	0.26	16.9	9.4	15.7
Fossil Fuels	0.05	5.0	1.17	27.5	0.98	62.8	25.8	43.3
Other					0.002	0.1	0.04	0.1
Total	1.09		4.26		1.55		59.7	

87 Table 2: Anthropogenic emissions inventories from EDGAR V4.2, (European
88 Commission, 2011) the yearly data is averaged between 2000 to 2008.

89 Monthly HYSPLIT back trajectories show the paths of air masses for 120 hours before
 90 arriving at Bachok during January and February 2014. These back trajectories have been
 91 overlain over MODIS fire maps (Fig. 2). The trajectories show the air masses coming from
 92 the NE during January (Fig. 2a) and February (Fig. 2b) may be influenced by both long range
 93 and local biomass burning. During February the air masses were more dispersed and interact
 94 with less land. Individual NAME trajectories are plotted for specific data values.

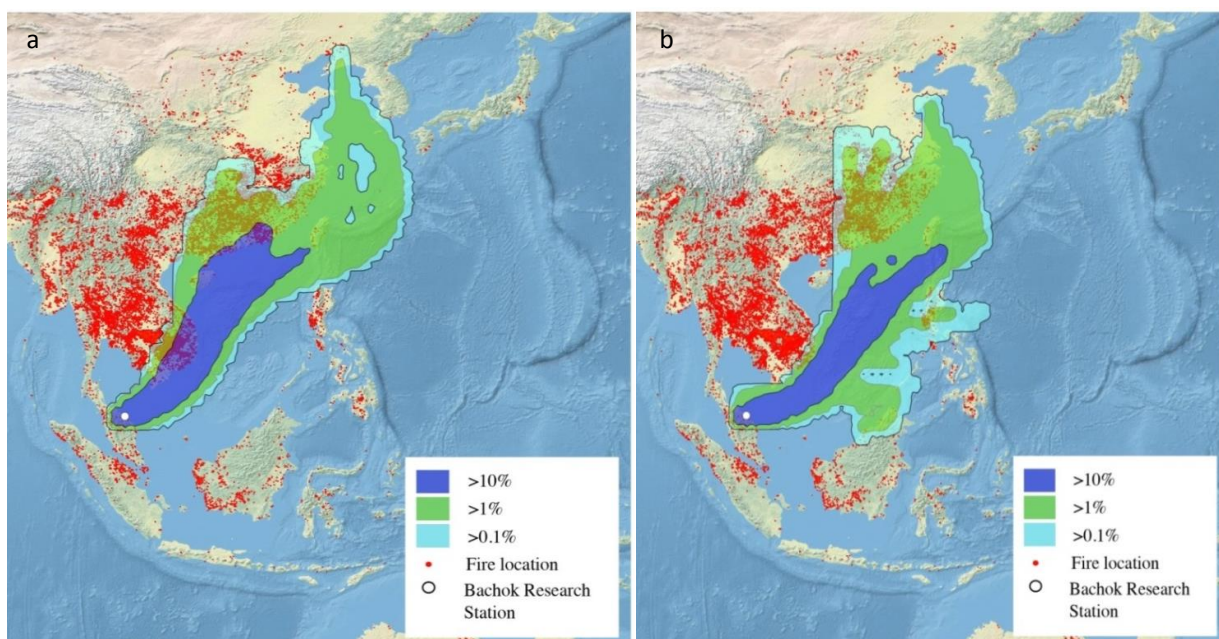


Figure 2: MODIS fire maps (Giglio et al., 2003; Davies et al., 2004) for the campaign period (01 January to 09 February 2014) and monthly trajectories plotted on QGIS (QGIS, 2014).

Trajectories show air mass origins up to 1000m, 120 hours back for a = January 2014 and b= February 2014: blue >10%, green >1% and turquoise >0.1% (Draxler & Hess, 1997; Draxler & Hess, 1998; Draxler, 1999).

2. Methods

2.1 Instrumentation for continuous measurement

A number of instruments were set up at the IOES tower with inlet lines on the roof at 19.2 meters. Various species were measured including CO₂, CH₄, CO, H₂, O₃, NO_x, VOCs, OVOCs, HCHO, SO₂, halocarbons and $\delta^{13}\text{C}_{\text{CH}_4}$. During the campaign a Los Gatos Research

110 greenhouse gas analyser (LGR) took continuous CH₄, CO₂ mole fraction and water vapour
111 measurements throughout the duration of the campaign from the tower.

112 **2.2 Sample collection and analysis**

113 Throughout the campaign bag samples were taken from the top of the tower at 19.2 meters
114 above ground level (agl) using a battery operated pump to fill a 3 litre Tedlar bag (SKC Ltd)
115 bag. Before the bag was connected to the pump and opened the sample line was flushed for
116 10 seconds to remove contamination.

117 During the campaign, starting on the 14 January 2014 continuing to the end of the campaign
118 on 7 February 2014, 3 samples were taken daily at 9am, 12pm and 5pm Local time
119 (Malaysian time, MYT, UTC +8). Diel samples were also taken from the tower; beginning 30
120 January 2014 9:00 continuing every 4 hours until 1 January 2014 20:00.

121 Biomass burning samples were taken on 22 January 2014 just outside the research station.
122 Samples were taken in and out the plumes as well as a background sample by the tower.
123 Mango wood with domestic waste was being burnt. These samples may help identify local
124 biomass signatures from longer range sources.

125 The CH₄ mole fractions from the bag samples were analysed at RHUL using a Picarro 1301
126 CRDS (cavity ring-down spectrometer). Bag samples were analysed for 240 seconds with the
127 mean of the last 120 seconds taken as the mole fraction. The Picarro CRDS is calibrated once
128 weekly using 3 NOAA 04 scale cylinders with CH₄ mole fractions between 1.8085 to 2.0920
129 ppm (Dlugokencky et al., 2005). A target gas is measured twice a week with the standard
130 deviation of this giving the repeatability for the CH₄ mole fraction. Half a litre of air sample
131 is kept in the bag for the $\delta^{13}\text{C}_{\text{CH}_4}$ isotope analysis.

$\delta^{13}\text{C}_{\text{CH}_4}$ is measured by continuous-flow gas chromatography/isotope-ratio mass spectrometry (CF-GC/IRMS) to a precision on triplicate analysis averaging $\pm 0.05\text{‰}$ (Fisher et al., 2006). An internal secondary standard is analysed at the beginning of each day at least four times until the measurements are stable and after every two samples to correct for drift. Biomass samples were diluted with nitrogen as the mass spectrometer can only analyse samples containing up to 7ppm CH_4 .

The $\delta^{13}\text{C}_{\text{CH}_4}$ source signatures are calculated using the Keeling plot approach (Keeling, 1958; Pataki et al., 2003; Zazzeri et al., 2015) The $\delta^{13}\text{C}$ is plotted against the inverse of the CH_4 mole fraction and linear regression (orthogonal) is used to give the source signature at the y-axis intercept (Pataki et al., 2003):

$$\delta^{13}\text{C}_a = C_b (\delta^{13}\text{C}_b - \delta^{13}\text{C}_s) \times (1/C_a) + \delta^{13}\text{C}_s \quad (\text{Equation 1})$$

C_a is the atmospheric mole fraction of a gas and C_b is the background atmospheric mole fraction. $\delta^{13}\text{C}_a$ is the measured isotopic composition, $\delta^{13}\text{C}_b$ is the background isotopic composition and $\delta^{13}\text{C}_s$ is the source isotopic composition:

The Miller-Tans plot is a modified approach to the Keeling plot, taking into account background changes in CH_4 . It is used to identify the $\delta^{13}\text{C}$ source signature when the background is not constant through time (Miller & Tans, 2003):

$$\delta^{13}\text{C}_a C_a = \delta^{13}\text{C}_s C_a - C_b (\delta^{13}\text{C}_b - \delta^{13}\text{C}_s) \quad (\text{Equation 2})$$

Equation 2 is of the linear form $y = mx + c$ where the ^{13}C source ($^{13}\text{C}_s$) is m .

2.3 Back Trajectories and Particle Dispersion Modelling

The Met Offices Numerical Atmospheric dispersion Modelling Environment (NAME) (Jones et al., 2007) was used to identify the origins of the air masses arriving at the Bachok tower. The offline NOAA Hybrid Single-Particle Lagrangian Integrated Trajectory (HYSPLIT) model (Rolph 2016; Stein et al., 2015) was also used to run monthly multiple simulations for January and February 2014. These show the probability of the air masses being in each place between ground level and 1000m, 120 hours back by using observed wind fields back in time. For each month HYSPLIT used GDAS archive meteorological data and was run offline four times per day at 00:00, 06:00, 12:00 and 18:00 UTC.

MODIS fire maps have been plotted covering the demonstration activity period. Each active fire location represents the center of a 1 km pixel that is flagged by the algorithm as containing one or more fires within the pixel (Giglio et al., 2003; Davies et al., 2004).

2.4 Meteorological data

Daily meteorological data has been downloaded from the weather underground website (www.wunderground.com). The nearest recordings are at Kota Bharu airport which is ~30km away from the research station. The study could be improved if meteorological data measurements were taken onsite however during the campaign this was not possible.

3. Results

3.2 LGR and Bag sample mole fractions

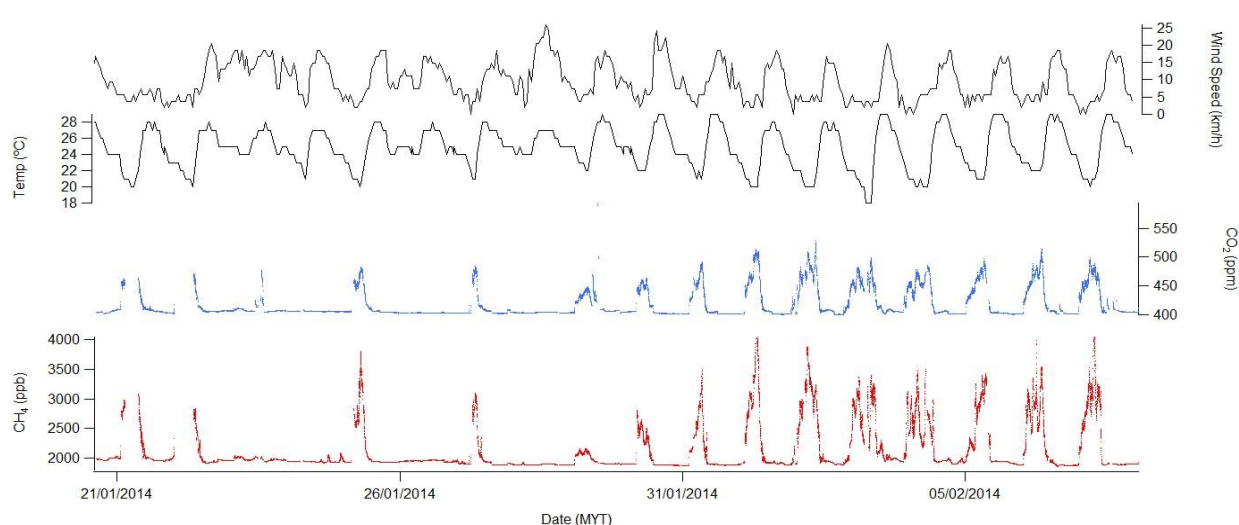
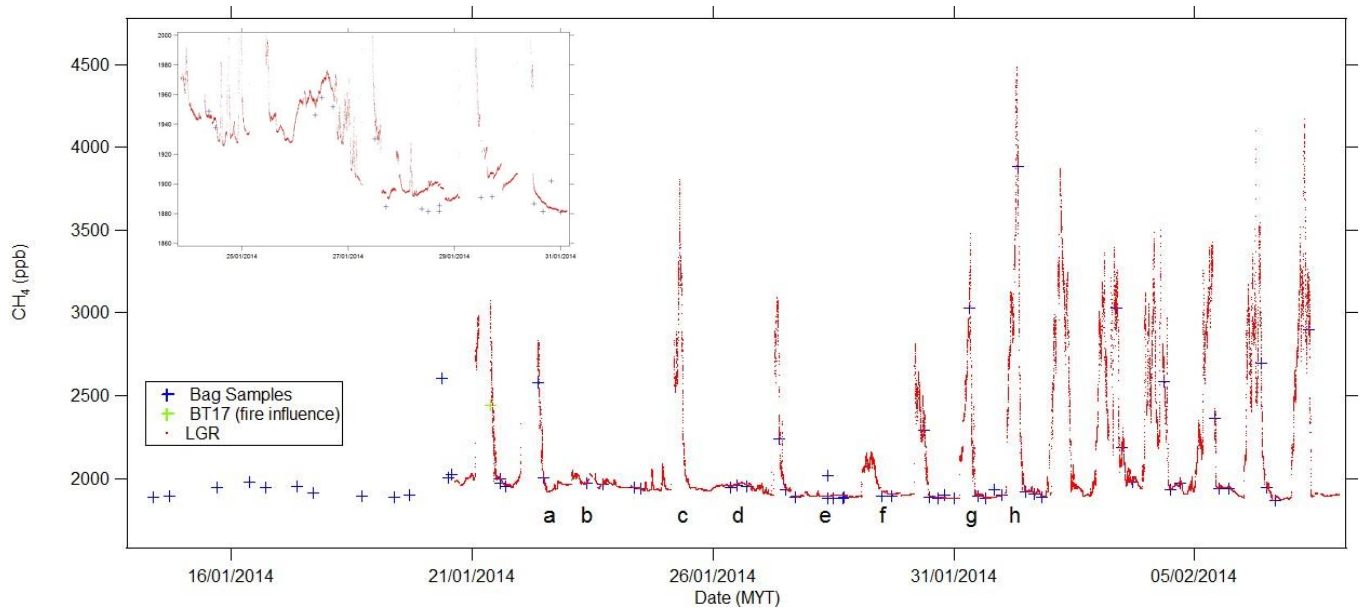


Figure 3: CH₄ and CO₂ mole fractions from the LGR from 20/01/14 to 07/02/14 (MYT) compared with wind speed and temperature (from: www.wunderground.com). The CH₄ and CO₂ peaks are correlated $r = 0.94$ where critical $r = 0.087$ at 0.05 significance.

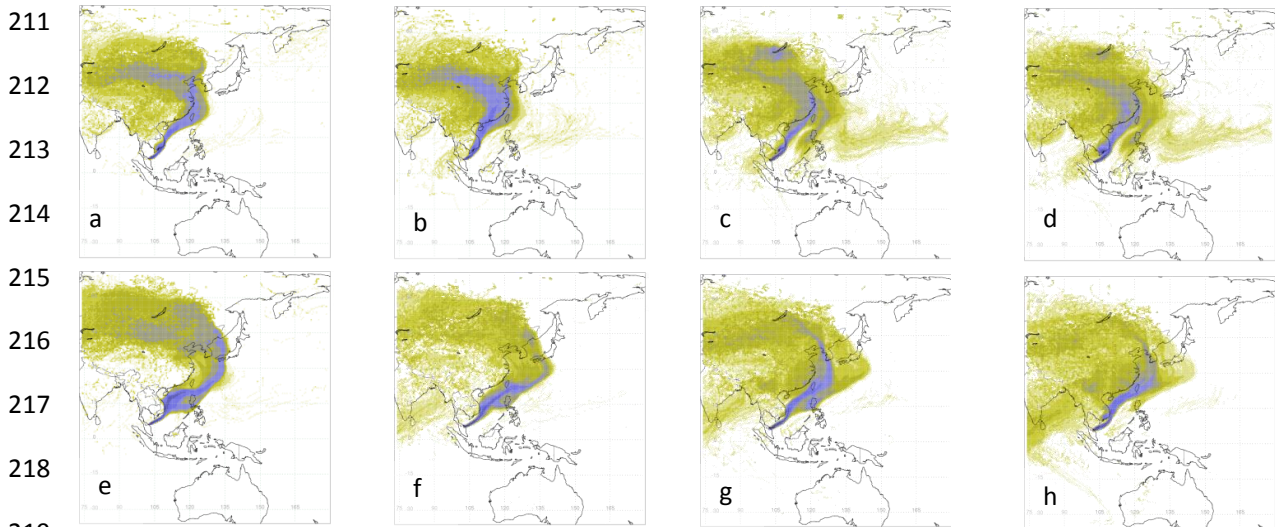
Large peaks in both CH₄ and CO₂ occurred throughout the duration of the 2014 campaign (Fig. 3). These tended to start between 00:00 and 05:00 MYT with many peaking between 6:00 to 08:00 MYT and returning to the background mole fraction around 10:00 to 11:30 MYT. These peaks occurred when there is an overnight decrease in temperature and wind speed (Fig. 3) and become more frequent as the wind speed drops more regularly after 31/01/14. Thus the peaks are likely to be from local emissions building up under the boundary layer.

NAME plots (Fig. 4) plotted 12 days back starting between 08-11 MYT on each day show CH₄ mole fractions are higher, all above 1900 ppb, when the air mass goes over land between 20th January to 27th January. Air masses after this period tend to come from over the sea, this correlates with a drop in background CH₄ mole fractions below 1900 ppb. The larger peaks

200 are likely to be more local as trajectories do not change from during background mole
 201 fractions.



210



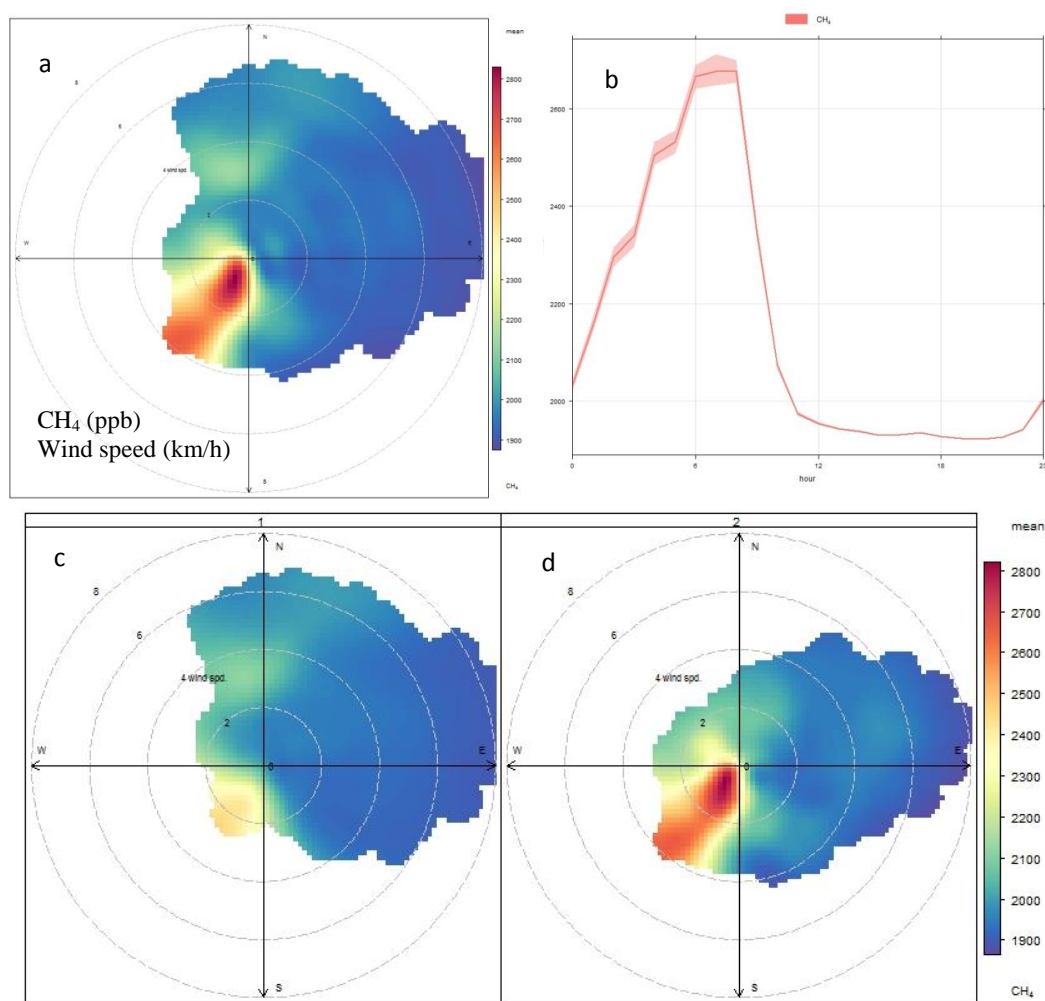
219

Figure 4: CH₄ mole fraction from the LGR (20/01/14 to 07/02/14) and bag samples (14/01/14 to 07/02/14). Error bars on the bag samples are too small to be seen on this plot. The top left graph shows the change in background mole fractions on 27/01/14 in more detail. There are significant correlations (95% confidence) between the bag samples and the continuous LGR CH₄ mole fractions ($r^2 = 0.948$ where critical $r^2 = 0.122$ at 0.05 significance).

223 NAME plots The models are run for 12 days back for each 3 hour period starting between 08-11 MYT (00-03UTC) on each day at the tower: a) 22/01/14, b) 23/01/14, c) 25/01/14, d) 26/01/14, e) 28/01/14, f) 29/01/14, g) 31/01/14 and h) 01/02/14. NAME plots for campaign period not shown here are in SI 2.

224

225
226
227
228
229
230
231
232
233
234
235
236
237
238
239



240 Figure 5a) polar plot of all CH₄ data during January & February 2014. b) Plot showing LGR CH₄ variation
by time (MYT) for the demonstration period. The shading shows the 95 % confidence intervals of the mean.
241 The CH₄ polar plots are split up into 12 hour periods based on the peak and background levels during 24
hours c) background between 12:00 – 00:00 MYT d) - Peak between 00:00-12:00 MYT (Carslaw &
Ropkins, 2012; Carslaw & Ropkins, 2014; R Core Team, 2014).

242

243 Openair (Carslaw & Ropkins, 2014) , an R package, has been used for polar plots which show
244 how CH₄ and CO₂ mole fraction varies with wind speed and direction at a point. Over the
245 whole campaign period higher mole fractions of CH₄ (Fig. 5a) and CO₂ (Fig. 6a) came from
246 the south west at low wind speed suggesting input from local sources from land. Figure 5b
247 and 6b show the average diel variation for CH₄ and CO₂ respectively, both peaks were
248 between 00:00 to ~11:30 MYT.

The CH₄ and CO₂ data were separated into 12 hour periods to give polar plots for the background between 12:00 to 00:00 MYT (Fig. 5c & 6c) and the peak between 00:00-12:00 MYT (Fig. 5d & 6d). Figure 5c and 6c show the background mole fractions of CH₄ and CO₂ between 12:00 to 00:00 MYT are mostly from the north east, over the sea. Figure 5d and 6d show more variable wind directions but higher mole fractions from the south west (inland) for CH₄ and higher mole fractions from the south and south west for CO₂.

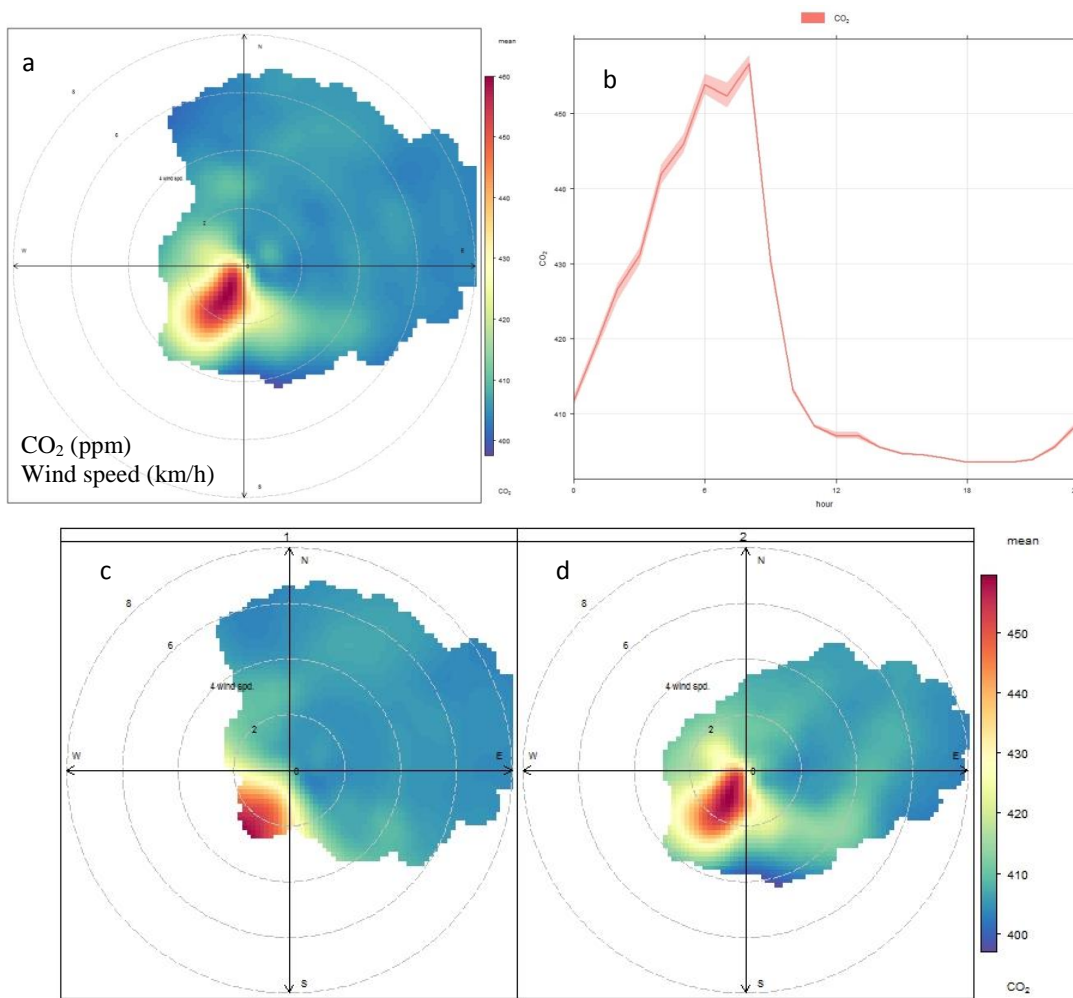


Figure 6a: polar plot of all CO₂ data during January & February 2014 b) Plot showing LGR CO₂ variation by time (MYT) for the demonstration period. The shading shows the 95 % confidence intervals of the mean

c) The CO₂ polar plots are split up into 12 hour periods based on the peak and background levels during 24 hours. c) background between 12:00 – 00:00 MYT d) Peak between 00:00-12:00 MYT (Carslaw & Ropkins, 2012; Carslaw & Ropkins, 2014; R Core Team, 2014).

3.3 Source signatures

The bag samples shown in Fig. 4 can be separated into 3 periods: 1) lower CH₄ background mole fractions between 14th and 19th January, 2) an increase in CH₄ background with air masses tending to arrive from over the land between 20th and 27th January, 3) a return to lower CH₄ background with air masses arriving from over the sea between 27th January and 6th February. The samples can be separated further through wind direction; background samples can be identified with the wind coming from the east or north east and local sources may be identified with wind coming from the south west and have wind speeds below 10 km/h.

The isotopic source signature of the background values for period 2 is $-64.6 \pm 2.7\text{‰}$ and period 3 is $-60.3 \pm 2.2 \text{‰}$ (Fig. 7).

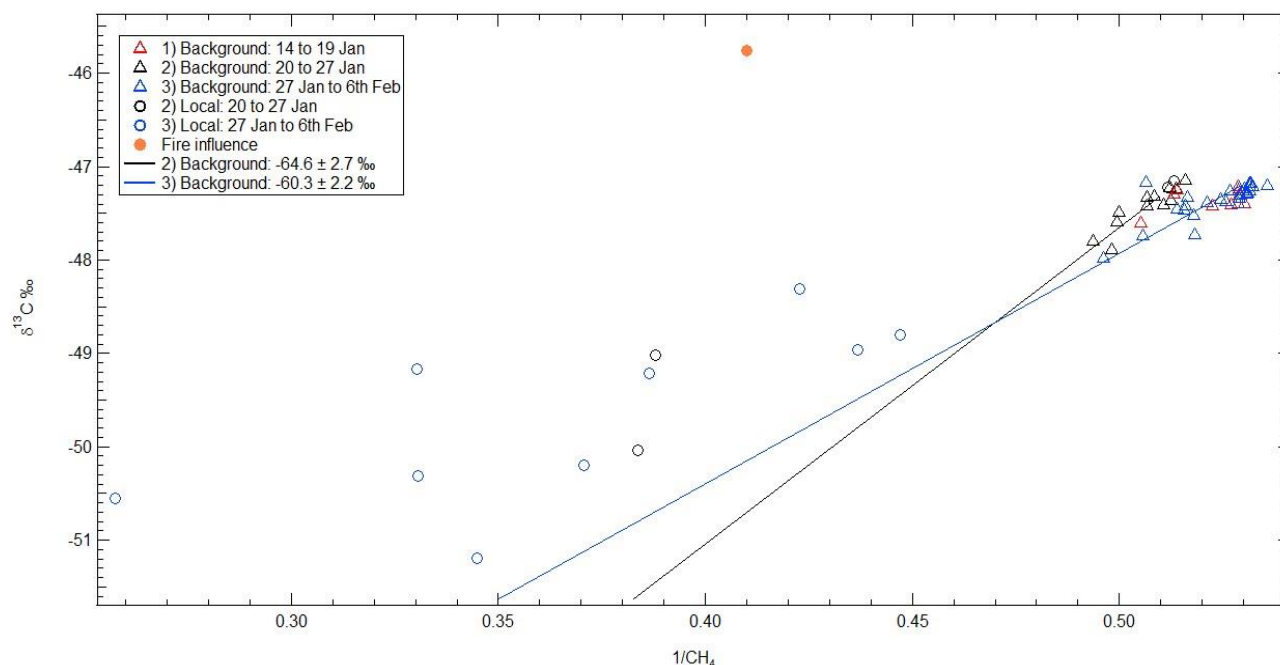


Figure 7: Plot of all the samples taken from the tower during January and February 2014. Keeling plot regression has been done for background values during period 2 giving a signature of $-64.6 \pm 2.7\text{‰}$ and period 3 giving a signature of $-60.3 \pm 2.2 \text{‰}$. It should be noted only one sample taken during this period has a strong fire signature.

All local sources during the sampling period have been plotted using a Miller-Tans plot (Fig. 8) allowing for the changing background to be taken into account. The plot shows an isotopic signature of $-54.9 \pm 1.2 \text{ ‰}$.

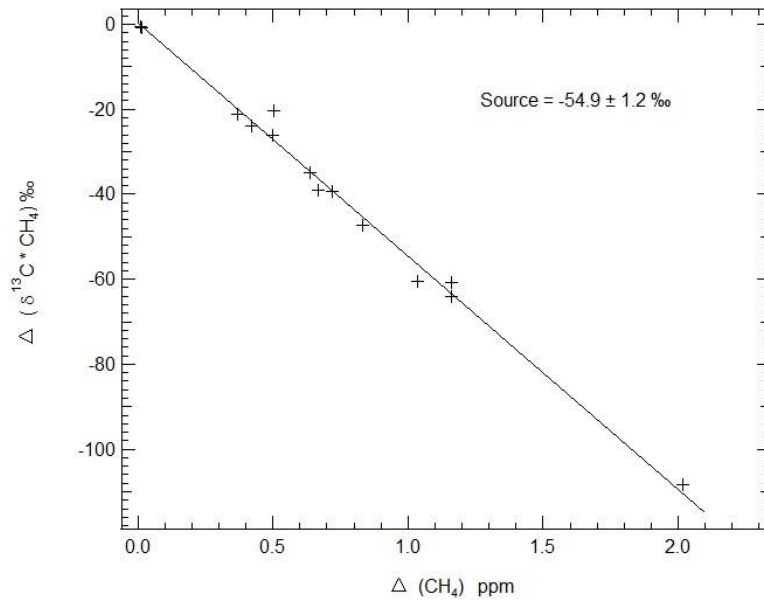


Figure 8: Miller-Tans plot for all local sources during January and February 2014. The plot shows an isotopic signature of $-54.9 \pm 1.2 \text{ ‰}$.

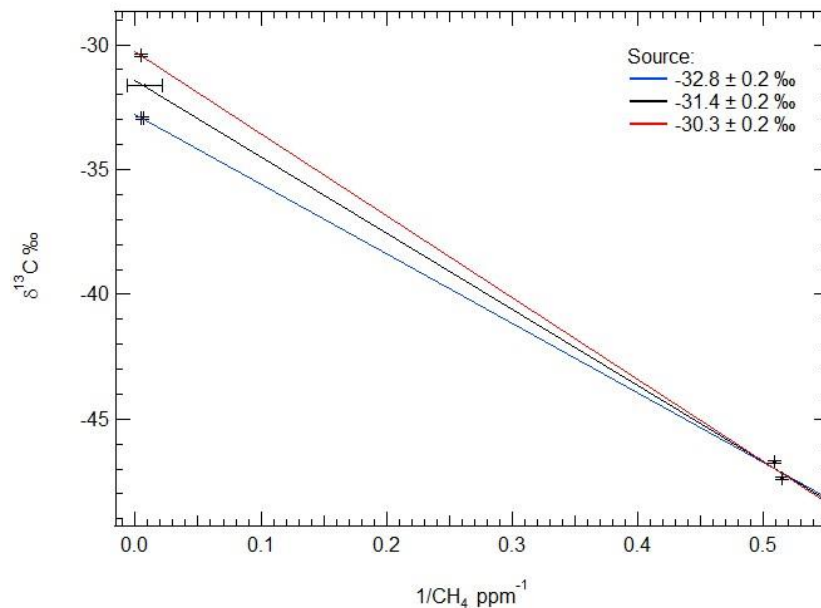


Figure 9: Keeling plot for fire sources giving source signatures of:

- a) $-32.8 \pm 0.2 \text{ ‰}$ (fire sample taken higher in the large plume with waste mixed in)
- b) $-31.4 \pm 0.2 \text{ ‰}$ (fire sample taken at bottom of the large plume)
- c) $-30.3 \pm 0.2 \text{ ‰}$ (fire sample taken in the small plume)

The fire samples give source signatures of between $-32.8 \pm 0.2 \text{ ‰}$ to $-30.3 \pm 0.2 \text{ ‰}$ (Fig. 9).

The fire Keeling plots consists of the two background samples, one taken out of the plume by the fire and one taken at the base of the tower and a sample at each source.

Discussion

CH_4 mole fraction increases with a decline in temperature and wind speed, as there is less mixing in the atmosphere, indicating a stronger boundary layer. These peak events take place during 00:00-12:00 MYT (Fig. 6b). NAME plot back trajectories do not show change between the peak events and background (Fig. 4) indicating CH_4 and CO_2 peaks are from local sources with a diurnal influence. Polar plots show the local influence with higher CH_4 and CO_2 mole fraction at low wind speeds from south west of the tower, over land (Fig. 5 & 6). During still mornings and evenings there is influence from local biomass burning as it is common for local waste burning as a means of disposal.

Biomass burning samples taken outside the tower give signatures of $-32.8 \pm 0.2 \text{ ‰}$, $-31.4 \pm 0.2 \text{ ‰}$ and $-30.3 \pm 0.2 \text{ ‰}$. These may vary slightly due to the different materials and the temperature of burning. These results compare well with results of -30 ‰ in Zambian woodland from Chanton et al. (2000) and C_3 vegetation values of $-26 \pm 3 \text{ ‰}$ given by Dlugokencky et al. (2011). Fig 7 shows a sample taken on 21/01/14 1:00 UTC (labelled: fire influence) trending towards a more enriched ^{13}C suggesting this point had a biomass burning influence.

The local isotopic signature from the tower is $-54.9 \pm 1.2 \text{ ‰}$; this is likely to be from a mixture of sources. This value is more enriched in ^{13}C compared to the background and the CO_2 increase with visible fires around the station suggests a local biomass burning influence.

However, $-54.9 \pm 1.2\text{‰}$ is significantly more depleted in ^{13}C than the biomass burning signatures, which would be expected to be more enriched. Biogenic inputs for example from local wetlands, agriculture or landfill are therefore also likely to be influencing this source signature but further work is needed to identify it. The wetlands of the Kelantan region consist of mangroves, swamps and marshes. Rice fields are also major wetlands throughout Malaysia however there is no total area data available in this region (UNEP, 2008). Examples of tropical wetland source signatures include rice paddies in Thailand: $-51.5 \pm 7.1 \text{‰}$ and $-56.5 \pm 4.6 \text{‰}$ (Nakagawa et al., 2002), swamps in southern Thailand: -61.7 ± 0.5 (Nakagawa et al., 2002) and swamps in Kenya: $-61.7 \pm 0.5 \text{‰}$ (Tyler et al., 1988). Ruminants are unlikely to be a major local biogenic input as cattle are kept individually rather than in large herds.

Background CH_4 mole fraction is dominated by longer range transport. CH_4 background decreases after 27th January when air masses tend to move from over land (the NAME plots show air masses arriving from over Cambodia and Vietnam) to over sea (Fig. 4). The period between 20th and 27th January 2014 has been identified as a cold surge event (Oram et al., 2017). This cold surge event can be seen as an increase in the background CH_4 mole fraction ratios however it is not seen in the isotopic values. The isotope source signatures for the background give values of $-64.6 \pm 2.7\text{‰}$ during the cold surge period and $-60.3 \pm 2.2 \text{‰}$ after the cold surge period, suggesting biogenic signatures have an influence on both these background values with the cold surge period being more depleted in ^{13}C . These signatures may be explained from a local biogenic source and being picked up in the background signature through the recycling of the air mass, through an on-shore off-shore breeze. However, NAME and HYSPLIT back trajectories do not account for local meteorology.

Local sources mean the small isotopic changes in the background methane needed to identify between cold surge events are not seen and therefore the isotopes are not useful on a regional scale at this site. Sites such as Bachok allow for measurements of local tropical methane

sources, which are sparse (Dlugokencky et al, 2011; Bousquet et al., 2006). A bulk rural tropical isotopic source signature input of -54.9 ± 1.2 ‰ may be attributed to this area which may be input into models allowing for a better understanding of the tropical methane budget.

An expected annual isotopic source signature may be estimated for South East Asia. Anthropogenic emissions are from EDGAR v4.2 emissions inventory (Table 3). Natural wetland emissions are estimated from Kirschke et al. (2013). This is calculated with an average $\delta^{13}\text{C}_{\text{CH}_4}$ source signature value weighted by the percentage contribution of each CH_4 source in the South East Asia region.

Source	Tg yr ⁻¹	Reference	$\delta^{13}\text{C}_{\text{CH}_4}$ ‰
Wetlands	26 [14-37]	Kirschke et al., 2013	-57.5 ± 3.9
Rice	7.10 ± 0.83	EDGAR V4.2	-58.8 ± 0.2
Ruminants C3	1.11 ± 0.12	EDGAR V4.2 ; Osborne et al., 2014	-67.6 ± 3.8
Ruminants C4	1.36 ± 0.03	EDGAR V4.2; Osborne et al., 2014	-55.4 ± 2.5
Manure	0.47 ± 0.05	EDGAR V4.2	-55.0 ± 1.2
Biomass Burning C3	1.32 ± 0.17	EDGAR V4.2; Randerson et al., 2005	-31.2 ± 2.4
Biomass Burning C4	0.18 ± 0.02	EDGAR V4.2; Randerson et al., 2005	-17.0 ± 1.2
Waste	2.51 ± 0.20	EDGAR V4.2	-55.0 ± 1.2
Fossil Fuels	4.05 ± 0.38	EDGAR V4.2	-47.8 ± 6.1
Total emissions	44 ± 12		
Average Annual $\delta^{13}\text{C}_{\text{CH}_4}$	-55.97 ± 3 ‰		

Table 3: Emissions inventories and average source signatures used to calculate an average regional tropical source signature for South East Asia (Brownlow et al., 2017).

South East Asia has an expected annual isotopic signature of -56 ± 3 ‰. The uncertainties (1σ) on the isotopic signatures are calculated using a Monte Carlo error analysis. The bulk isotopic signature from the tower of -54.9 ± 1.2 ‰ is within error of this value suggesting Bachok is a

representative South East Asia site. Local sources seen at Bachok are representative of SE Asia source mix over the wider region.

Conclusions

The background mole fraction at Bachok tower is determined by longer range transport with a higher mole fraction when air masses arrive from over land, during the cold surge event, compared with only over sea. The source signatures given for the background CH₄ arriving at the tower are $-64.6 \pm 2.7\%$ during the cold surge period and $-60.3 \pm 2.2 \%$ after the cold surge period, suggesting a biogenic source. Longer range transport of CH₄ may be hard to monitor at this site due to significant local emissions.

The local isotopic signature from the tower is $-54.9 \pm 1.2\%$, which fits with the calculated south east Asia signature. The local biomass burning signatures are $-32.8 \pm 0.2 \%$, $-31.4 \pm 0.2\%$ and $-30.3 \pm 0.2\%$. The CH₄ peaks are likely to be caused by diurnal cycles with mixed CH₄ emissions from local wetlands and biomass burning. It would be useful in future campaigns to look at the different wetlands types in the local area to characterise the source signatures.

416 **References**

- 417 Ashfold, M.J., Pyle, J.A., Robinson, A.D., Meneguz, E., Nadzir, M.S.M., Phang, S.M., Samah, A.A.,
418 Ong, S., Ung, H.E., Peng, L.K., Yong, S.E., Harris, N.R.P., (2015), Rapid transport of East Asian
419 pollution to the deep tropics. *Atmos. Chem. Phys.* 15, 3565–3573.
- 420 Bousquet, P., Ciais, P., Miller, J. B., Dlugokencky, E. J., Hauglustaine, D. A, Prigent, C., Van der
421 Werf, G. R., Peylin, P., Brunke, E. G., Carouge, C., Langenfelds, R. L., Lathière, J., Papa, F.,
422 Ramonet, M., Schmidt, M., Steele, L. P., Tyler, S. C., and White, J. (2006). Contribution of
423 anthropogenic and natural sources to atmospheric methane variability. *Nature*, 443(7110), 439–43.
424 doi:10.1038/nature05132
- 425 Brownlow R., Lowry D., Fisher R E., France J. L., M. Lanoisellé, B. White, M. J. Wooster, T. Zhang
426 and Nisbet E. G. (2017), Isotopic ratios of tropical methane emissions by atmospheric measurement
427 and continental-scale variability, Submitted to *Global Biogeochem. Cycles*.
- 428 Carslaw, D.C. & Ropkins, K. (2012). openair --- an R package for air quality data analysis.
429 *Environmental Modelling & Software*. Volume 27-28, 52-61.
- 430 Carslaw, D.C. & Ropkins, K. (2014). openair: Open-source tools for the analysis of air pollution data.
431 R package version 0.9-2.
- 432 Chanton, J., Chaser, L., Glasser, P., & Siegel, D. (2005). Carbon and Hydrogen Isotopic Effects in
433 Microbial Methane from Terrestrial Environments. In: Flanagan, L.B., Ehleringer J.R. and Pataki D.E.
434 eds., *Stable Isotopes and Biosphere Atmosphere Interactions*, Elsevier, Oxford
- 435 Chanton, J.P., Rutkowski, C.M., Schwartz, C.C., Ward, D.E., Boring, L. (2000). Factors influencing
436 the stable carbon isotopic signature of methane from combustion and biomass burning. *J. Geophys.*
437 *Res.* 105, 1867.
- 438 Crutzen, P.J., Andreae, M.O., (1990). Biomass burning in the tropics: impact on atmospheric
439 chemistry and biogeochemical cycles. *Science* 250, 1669–78.
- 440 Davies, D., Kumar, S., and Descloitres, J. (2004). Global fire monitoring using MODIS near-real-time
441 satellite data. *GIM International*, 18(4):41-43
- 442 Dlugokencky, E. J., Nisbet, E. G., Fisher, R., & Lowry, D. (2011). Global atmospheric methane:
443 budget, changes and dangers. *Philosophical Transactions. Series A, Mathematical, Physical, and*
444 *Engineering Sciences*, 369(1943), 2058–72. doi:10.1098/rsta.2010.0341
- 445 Dlugokencky, E. J., Myers R. C., Lang, P. M., Masarie. K. A., Crotwell, A. M., Thoning K. W., Hall,
446 B. D., Elkins, J. W. and Steele L. P., (2005). Conversion of NOAA atmospheric dry air CH₄ mole

447 fractions to a gravimetrically prepared standard scale. *Journal of Geophysical Research*, 110(D18),
448 doi:10.1029/2005JD006035

449 Draxler, R.R. (1999). HYSPLIT4 user's guide. NOAA Tech. Memo. ERL ARL-230, NOAA Air
450 Resources Laboratory, Silver Spring, MD.

451 Draxler, R.R., and G.D. Hess, (1997). Description of the HYSPLIT_4 modeling system. NOAA Tech.
452 Memo. ERL ARL-224, NOAA Air Resources Laboratory, Silver Spring, MD, 24 pp.

453 Draxler, R.R., and Hess G.D. (1998). An overview of the HYSPLIT_4 modeling system of
454 trajectories, dispersion, and deposition. *Aust. Meteor. Mag.*, **47**, 295-308.

455 European Commission, Joint Research Centre (JRC)/Netherlands Environmental Assessment Agency
456 (PBL), (2011), Emission Database for Global Atmospheric Research (EDGAR), release version 4.2.
457 <http://edgar.jrc.ec.europa.eu>

458 Fisher, R., Lowry, D., Wilkin, O., Sriskantharajah, S., & Nisbet, E. G. (2006). High precision,
459 automated stable isotope analysis of atmospheric methane and carbon dioxide using continuous-flow
460 isotope-ratio mass spectrometry. *Rapid Communications in Mass Spectrometry* : 20(2), 200–8.
461 doi:10.1002/rcm.2300.

462 Garreaud, R.D., (2001), Subtropical cold surges: regional aspects and global distribution. *Int. J.*
463 *Climatol.* 21, 1181–1197.

464 Giggenbach WF (1997) Relative importance of thermodynamic and kinetic processes in governing the
465 chemical and isotopic composition of carbon gases in high-heatflow sedimentary basins. *Geochim*
466 *Cosmochim Acta* 61:3763-3785.

467 Giglio, L., Descloitres, J., Justice, C. O. & Kaufman Y. J. (2003). An enhanced contextual fire
468 detection algorithm for MODIS. *Remote Sensing of Environment*, 87:273-282.

469 Jenden PD (1988) *Analysis of Gases in the Earth's Crust*. Gas Research Institute, Chicago, 571pp.

470 Jones A.R., Thomson D.J., Hort M. and Devenish B., (2007), The U.K. Met Office's next-generation
471 atmospheric dispersion model, NAME III, in Borrego C. and Norman A.-L. (Eds) *Air Pollution*
472 *Modeling and its Application XVII* (Proceedings of the 27th NATO/CCMS International Technical
473 Meeting on Air Pollution Modelling and its Application), Springer, pp. 580-589

474 Keeling, C. D. (1958), The concentration and isotopic abundances of atmospheric carbon dioxide in
475 rural areas, *Geochimica et Cosmochimica Acta*, 13, 322-334

476 Kirschke, S., Bousquet, P., Ciais, P., Saunois, M., Canadell, J. G., Dlugokencky, E. J., Bergamaschi,
477 P., Bergmann, D., Blake, D. R., Bruhwiler, L., Cameron-Smith, P., Castaldi, S., Chevallier, F., Feng,
478 L., Fraser, A., Heimann, M., Hodson, E. L., Houweling, S., Josse, B., Fraser, P. J., Krummel, P. B.,
479 Lamarque, J., Langenfelds, R. L., Le Quééré, C., Naik, V., O'Doherty, S., Palmer, P. I., Pison, I.,
480 Plummer, D., Poulter, B., Prinn, R. G., Rigby, M., Ringeval, B., Santini, M., Schmidt, M., Shindell,

481 D. T., Simpson, I. J., Spahni, R., Steele, L. P., Strode, S. A., Sudo, K., Szopa, S., van der Werf, G. R.,
482 Voulgarakis, A., van Weele, M., Weiss, R. F., Williams, J. E. and Zeng, G., (2013). Three decades of
483 global methane sources and sinks. *Nature Geoscience*, 6(10), 813–823. doi:10.1038/ngeo1955

484 Levandowski JH (2009) *Petrologia e Geoquímica Das Camadas De Carvão E Sua Relação Com Gás*
485 *Natural Determinado No Póco*. Dissertation, Universidade Federal do Rio Grande do Sul, Porto
486 Alegre, Brazil, 92 pp.

487 Miller, J.B., Tans, P.P., 2003. Calculating isotopic fractionation from atmospheric measurements at
488 various scales. *Tellus B* 55, 207–214

489 Nakagawa, F., Yoshida, N., Sugimoto, A., Wada, E., Yoshioka, T., Ueda, S., Vijarnsorn, P., (2002).
490 Stable isotope and radiocarbon compositions of methane emitted from tropical rice paddies and
491 swamps in Southern Thailand. *Biogeochemistry* 61, 1–19.

492 Nisbet E.G., Dlugokencky E.J., Manning M.R., Lowry D., Fisher R. E., France J. L., Michel S. E.,
493 Miller J.B., White J.W.C., Vaughn B., Bousquet P. Pyle J.A., Warwick N.J., Cain M., Brownlow R.,
494 Zazzeri G., Lanoisellé M., Manning A.C., Gloor E., Worthy D.E.J., Brunke E.-G., Labuschagne C.,
495 Wolff E.W. and Ganesan A.L. (2016) Rising atmospheric methane: 2007-14 growth and isotopic
496 shift,. *Global Biogeochem. Cycles*, 30, doi:10.1002/ 2016GB005406.

497 Nisbet, E. G., Dlugokencky, E. J., & Bousquet, P. (2014). Atmospheric science. Methane on the rise--
498 again. *Science (New York, N.Y.)*, 343(6170), 493–5. doi:10.1126/science.1247828

499 Oram D. E., Ashfold, M. J., Laube, J. C., Gooch, L. J., Humphrey, S., Sturges, W. T., Leedham-
500 Elvidge, E., Forster, G. L., Harris, N. R. P., Mead, M. I., Samah, A. A., Phang, S. M., Ou-Yang, C. F.,
501 Lin, N. H., Wang, J. L., Baker, A. K., Brenninkmeijer, C. A. M. and Sherry, D., (2017), A growing
502 threat to the ozone layer from short-lived anthropogenic chlorocarbons., In Prep.

503 Osborne, C.P., Salomaa, A., Kluyver, T.A., Visser, V., Kellogg, E.A., Morrone, O., Vorontsova,
504 M.S., Clayton, W.D., Simpson, D.A., (2014). A global database of C 4 photosynthesis in grasses.
505 *New Phytol.* 204, 441–446.

506 Pande HC, Raina A, Roy V, Saxena RK, Singh H, Singh RR (2011) Origin of Biogenic Gases in East
507 Coast Basins of India. *Geo-India 2011 Conference*, Available at: <http://www.apgindia.org/pdf/649.pdf>

508 Pataki, D.E., Ehleringer, J.R., Flanagan, L.B., Yakir, D., Bowling, D.R., Still, C.J., Buchmann, N.,
509 Kaplan, J.O., Berry, J. a., (2003). The application and interpretation of Keeling plots in terrestrial
510 carbon cycle research. *Global Biogeochemical. Cycles* 17.

511 Prinzhofer A, Santos Neto EV, Battani A (2010) Coupled use of carbon isotopes and noble gas
512 isotopes in the Potiguar basin (Brazil): Fluids migration and mantle influence. *Mar Petrol Geol*
513 27:1273-1284.

514 Prinzhofer AA, Mello MR, Takaki T (2000) Geochemical characterization of natural gas: A physical
515 multivariable approach and its applications in maturity and migration estimates. *AAPG Bull* 84:1152-
516 1172.

517 R Core Team (2014). *R: A language and environment for statistical computing*. R Foundation for
518 Statistical Computing, Vienna, Austria. URL <http://www.R-project.org/>.

519 Randerson, J.T., van der Werf, G.R., Collatz, G.J., Giglio, L., Still, C.J., Kasibhatla, P., Miller, J.B.,
 520 White, J.W.C., DeFries, R.S., Kasischke, E.S., (2005), Fire emissions from C3 and C4 vegetation and
 521 their influence on interannual variability of atmospheric CO₂ and $\delta^{13}\text{C}_{\text{CO}_2}$. *Global Biogeochem.*
 522 *Cycles* 19, 1–13.

523 Rao, D.K., Bhattacharya, S.K., Jani, R.A., (2008) Seasonal variations of carbon isotopic composition
 524 of methane from Indian paddy fields. *Global Biogeochem. Cycles* 22, 1–5.

525 Rolph, G.D. (2016). *Real-time Environmental Applications and Display sYstem (READY) Website*
 526 (<http://www.ready.noaa.gov>). NOAA Air Resources Laboratory, College Park, MD.

527 Satyana AH, Marpaung LP, Purwaningsih ME, Utama MK (2007) Regional gas geochemistry of
 528 Indonesia: Genetic characterization and habitat of natural gases. Proc Indonesian Petrol Assoc,
 529 Available at: http://archives.datapages.com/data/ipa_pdf/078/078001/pdfs/IPA07-G-050.pdf

530 Saunois, M., Bousquet, P., Poulter, B., Peregon, A., Ciais, P., Canadell, J.G., Dlugokencky, E.J.,
 531 Etiope, G., Bastviken, D., Houweling, S., Janssens-Maenhout, G., Tubiello, F.N., Castaldi, S.,
 532 Jackson, R.B., Alexe, M., Arora, V.K., Beerling, D.J., Bergamaschi, P., Blake, D.R., Brailsford, G.,
 533 Brovkin, V., Bruhwiler, L., Crevoisier, C., Crill, P., Curry, C., Frankenberg, C., Gedney, N., Höglund-
 534 Isaksson, L., Ishizawa, M., Ito, A., Joos, F., Kim, H.-S., Kleinen, T., Krummel, P., Lamarque, J.-F.,
 535 Langenfelds, R., Locatelli, R., Machida, T., Maksyutov, S., McDonald, K.C., Marshall, J., Melton,
 536 J.R., Morino, I., O’Doherty, S., Parmentier, F.-J.W., Patra, P.K., Peng, C., Peng, S., Peters,
 537 G.P., Pison, I., Prigent, C., Prinn, R., Ramonet, M., Riley, W.J., Saito, M., Schroder, R., Simpson, I.J.,
 538 Spahni, R., Steele, P., Takizawa, A., Thornton, B.F., Tian, H., Tohjima, Y., Viovy, N., Voulgarakis, A.,
 539 van Weele, M., van der Werf, G., Weiss, R., Wiedinmyer, C., Wilton, D.J., Wiltshire, A., Worthy, D.,
 540 Wunch, D.B., Xu, X., Yoshida, Y., Zhang, B., Zhang, Z., Zhu, Q., (2016) The Global Methane
 541 Budget: 2000-2012. *Earth Syst. Sci. Data Discuss.* 1–79.

542 Schaefer, H., Mikaloff Fletcher, S. E., Veidt, C., Lassey, K. R., Brailsford, G. W., Bromley, T. M.,
 543 Dlugokencky, E. J., Michel, S. E., Miller, J. B., Levin, I., Lowe, D. C., Martin, R. J., Vaughn, B. H.
 544 and White, J. W. C. (2016). A 21st century shift from fossil-fuel to biogenic methane emissions
 545 indicated by $^{13}\text{CH}_4$. *Science*, 351(6278). doi:10.1126/science.aad2705

546 Snover, A.K., Quay, P.D. & Hao, W.M., (2000) The D / H content of methane emitted from biomass
 547 burning ponderosa. *Global Biogeochem. Cycles* 14, 11–24.

548 Stein, A.F., Draxler, R.R, Rolph, G.D., Stunder, B.J.B., Cohen, M.D., and Ngan, F., (2015). NOAA’s
 549 HYSPLIT atmospheric transport and dispersion modeling system, *Bull. Amer. Meteor. Soc.*, **96**, 2059-
 550 2077, <http://dx.doi.org/10.1175/BAMS-D-14-00110.1>

551 Streets, D.G., Yarber, K.F., Woo, J.-H., Carmichael, G.R., (2003), Biomass burning in Asia: Annual
 552 and seasonal estimates and atmospheric emissions. *Global Biogeochem. Cycles* 17,

553 Tyler, S.C., Brailsford, G.W., Yagi, K., Minami, K. & Cicerone, R.J., (1994) Seasonal variations in
 554 methane flux and $\delta^{13}\text{C}_{\text{CH}_4}$ values for rice paddies in Japan and their implications. *Global*
 555 *Biogeochem. Cycles* 8, 1–12.

Tyler, S.C., Zimmerman, P.R., Greenberg, J.P., Westberg, C., Darlington, J.P.E.C., (1988)
Measurements and interpretation of ^{13}C of methane from termites, rice paddies, and wetlands in
Kenya. *Global Biogeochem. Cycles* 2, 341–355.

UNEP (2008). National Reports on Wetlands in the South China Sea. UNEP/GEF/SCS Technical
Publication No. 13.

Ward J, Slater G, Moser D, Lin LH, Lacrampe-Couloume G, Bobin AS, et al (2004) Microbial
hydrocarbon gases in the Witwatersrand Basin, South Africa: Implications for the deep biosphere.
Geochim Cosmochim Acta 68: 3239–3250.

WMO (2016), The State of Greenhouse Gases in the Atmosphere Based on Global Observations
through 2015, 12. <http://library.wmo.int/opac/doc num.php?explnum id=3084>

Zhang, Y., Sperber, K.R., Boyle, J.S., (1997), Climatology and Interannual Variation of the East
Asian Winter Monsoon: Results from the 1979–95 NCEP/NCAR Reanalysis. *Mon. Weather Rev.*
125, 2605–2619.

Zazzeri, G., D. Lowry, R.E. Fisher, J.L. France, M. Lanoisellé and E.G. Nisbet (2015) Plume mapping
and isotopic characterisation of anthropogenic methane sources, *Atmospheric Environment*, 110, 151-
162, doi: 10.1016/j.atmosenv.2015.03.029

586 **Supporting Information**

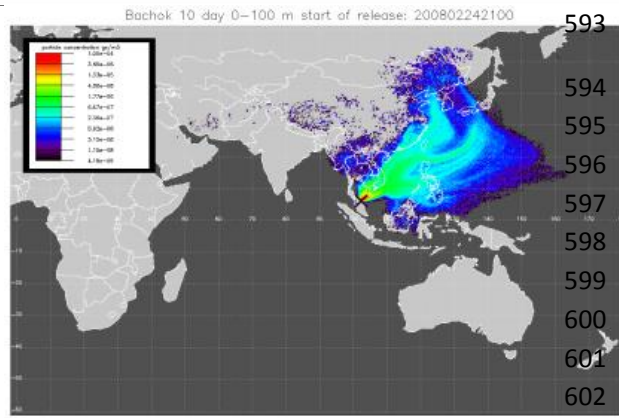
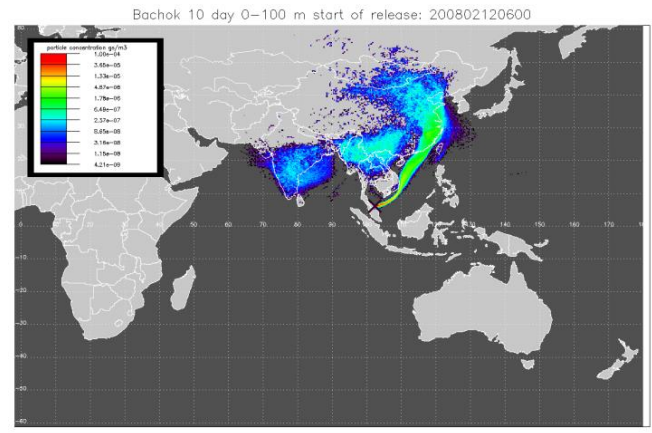
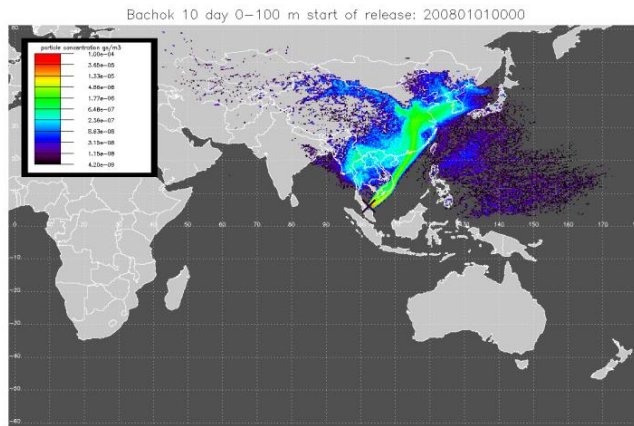
587 **S1. NAME Plots**

588

589 Each footprint shows the where the air arriving at the Bachok tower has been at the surface
590 (0-100 m elevation) in the last 10 days

591

592 **January/February: North Easterlies and Asian continent**



603

604

605

606

607

608

609

610

611

612

613

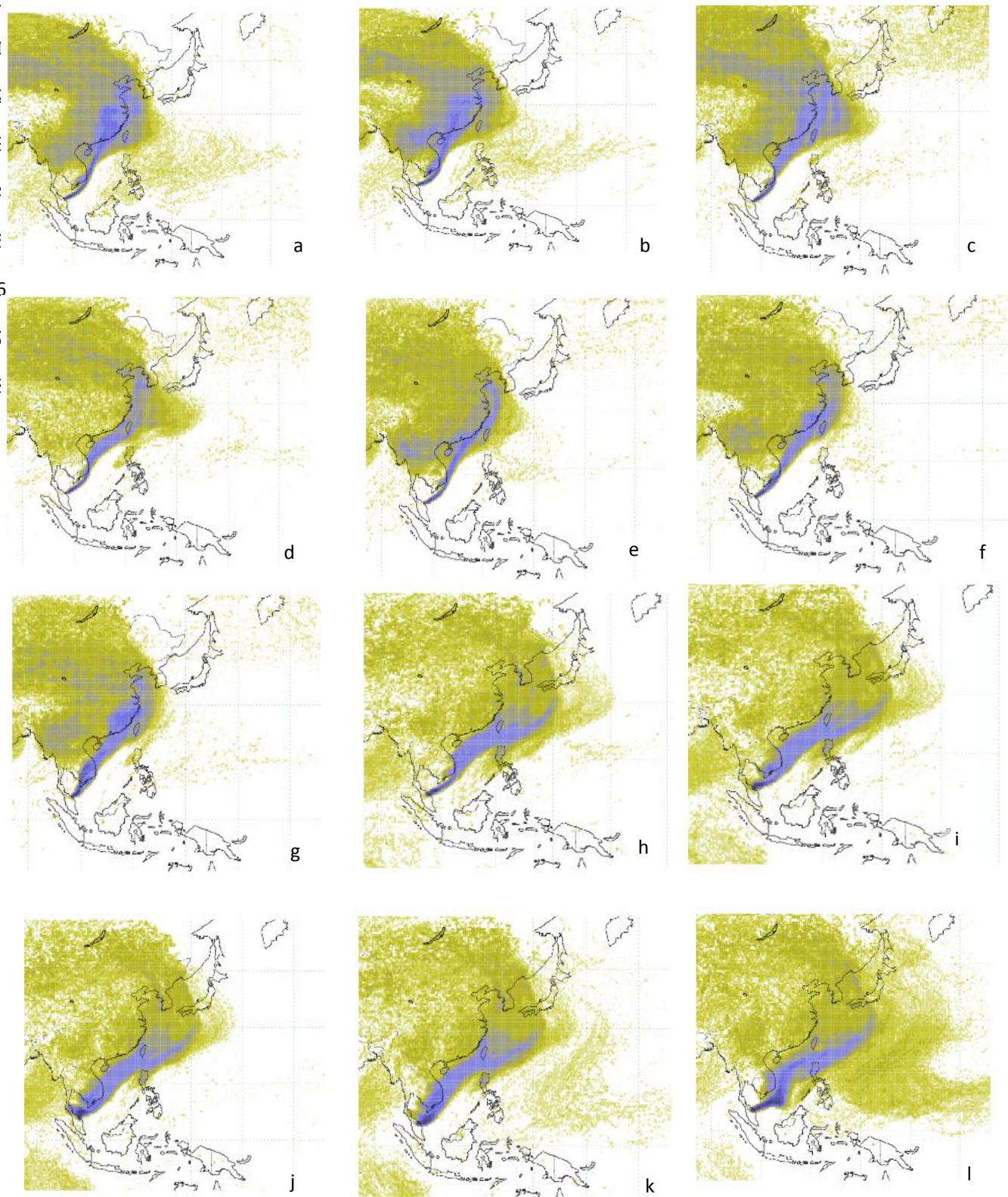
614

615

616

617

S2. NAME Plots The models are run for 12 days back for each 3 hour period starting between 08-11 MYT (00-03UTC) on each day at the tower.



a) 15/01/14, b) 16/01/14, c) 17/01/14, d) 18/01/14, e) 19/01/14, f) 20/01/14, g) 21/01/14, h) 02/02/14, i) 03/02/14, j) 04/02/14, k) 05/02/14 & l) 06/02/14

Chapter 5

Methane mole fraction and $\delta^{13}\text{C}$ above and below the trade wind inversion at Ascension Island in air sampled by aerial robotics

This Chapter has been published in Geophysical Research Letters. R. Brownlow wrote the manuscript, plotted & interpreted the CH_4 data. T. S. Richardson & C. Greatwood developed the UAS. R. M. Thomas designed the payload for sample collection. R. Brownlow & D. Lowry planned the sampling strategy and analysed the samples. M. Cain ran the NAME plots. All the authors made comments on the manuscript.

Brownlow, R., Lowry, D., Thomas, R. M., Fisher, R. E., France, J. L., Cain, M., Richardson, T. S., Greatwood, C. and Nisbet, E. G. (2016). Methane mole fraction and $\delta^{13}\text{C}$ above and below the trade wind inversion at Ascension Island in air sampled by aerial robotics. *Geophysical Research Letters*, 43(22), 11,893-11,902. <https://doi.org/10.1002/2016GL071155>

RESEARCH LETTER

10.1002/2016GL071155

Key Points:

- Methane mole fraction and $\delta^{13}\text{C}$ have been measured from samples collected by UASs on Ascension Island over two campaigns
- CH_4 mole fraction increases above the TWI, but isotopes have no consistent signal indicating input from Africa is close to background
- The campaigns illustrate the usefulness of UAS sampling and Ascension's value for atmospheric measurement in an understudied region

Supporting Information:

- Supporting Information S1

Correspondence to:

R. Brownlow,
Rebecca.Brownlow.2009@live.rhul.ac.uk

Citation:

Brownlow, R., et al. (2016), Methane mole fraction and $\delta^{13}\text{C}$ above and below the trade wind inversion at Ascension Island in air sampled by aerial robotics, *Geophys. Res. Lett.*, 43, doi:10.1002/2016GL071155.

Received 13 SEP 2016

Accepted 3 NOV 2016

Accepted article online 5 NOV 2016

©2016. The Authors.

This is an open access article under the terms of the Creative Commons Attribution License, which permits use, distribution and reproduction in any medium, provided the original work is properly cited.

Methane mole fraction and $\delta^{13}\text{C}$ above and below the trade wind inversion at Ascension Island in air sampled by aerial robotics

R. Brownlow¹, D. Lowry¹, R. M. Thomas^{2,3}, R. E. Fisher¹, J. L. France⁴, M. Cain⁵, T. S. Richardson⁶, C. Greatwood⁶, J. Freer⁷, J. A. Pyle⁵, A. R. MacKenzie^{2,3}, and E. G. Nisbet¹
¹Department of Earth Sciences, Royal Holloway, University of London, Egham, UK, ²School of Geography, Earth and Environmental Sciences, University of Birmingham, Birmingham, UK, ³Birmingham Institute of Forest Research, University of Birmingham, Birmingham, UK, ⁴Centre for Oceanic and Atmospheric Sciences, School of Environmental Sciences, University of East Anglia, Norwich, UK, ⁵Centre for Atmospheric Science, University of Cambridge, Cambridge, UK, ⁶Department of Aerospace Engineering, University of Bristol, Bristol, UK, ⁷School of Geographical Sciences, University of Bristol, Bristol, UK

Abstract Ascension Island is a remote South Atlantic equatorial site, ideal for monitoring tropical background CH_4 . In September 2014 and July 2015, octocopters were used to collect air samples in Tedlar bags from different heights above and below the well-defined Trade Wind Inversion (TWI), sampling a maximum altitude of 2700 m above mean sea level. Sampling captured both remote air in the marine boundary layer below the TWI and also air masses above the TWI that had been lofted by convective systems in the African tropics. Air above the TWI was characterized by higher CH_4 , but no distinct shift in $\delta^{13}\text{C}$ was observed compared to the air below. Back trajectories indicate that lofted CH_4 emissions from Southern Hemisphere Africa have bulk $\delta^{13}\text{C}_{\text{CH}_4}$ signatures similar to background, suggesting mixed emissions from wetlands, agriculture, and biomass burning. The campaigns illustrate the usefulness of unmanned aerial system sampling and Ascension's value for atmospheric measurement in an understudied region.

1. Introduction

Global atmospheric methane (CH_4) is increasing rapidly. Between 2007 and 2013 CH_4 increased globally by $5.7 \pm 1.7 \text{ ppb yr}^{-1}$ with a more rapid increase in the equatorial tropics in 2010–2011. In 2014 the yearly growth increased to $12.5 \pm 0.4 \text{ ppb}$ [Nisbet et al., 2016]. Tropical emissions are thought to be a major contributor to this growth [Nisbet et al., 2014; Schaefer et al., 2016]. Natural tropical sources include wetlands and other freshwater systems, lightning-lit fires, geological leaks, termites, and wild ruminants [Dlugokencky et al., 2011]. CH_4 emissions from the tropics produce around $\sim 200 \text{ Tg/yr}$ which is thought to be about 40% of the global CH_4 budget [Frankenberg et al., 2008; Bousquet et al., 2006]. Variability in CH_4 removal through reaction with OH radicals is also dominated by the tropics as photochemistry is active throughout the year [Bousquet et al., 2006].

$\delta^{13}\text{C}_{\text{CH}_4}$ isotope ratios can be used to help apportion emission sources, because the different sources of CH_4 have different ratios of ^{13}C and ^{12}C isotopes. Background ambient air at present approximately has a $\delta^{13}\text{C}_{\text{CH}_4}$ of -47.4 to -47.2‰ [Nisbet et al., 2016]. CH_4 emissions from biological sources are depleted in comparison to background ambient air, for example, swamps give a signature of $-55 \pm 3\text{‰}$ [Dlugokencky et al., 2011], because methanogenic archaea preferentially use the lighter ^{12}C isotope. CH_4 formed at higher temperatures is relatively enriched in the heavier isotope, for example, biomass burning of savannah grassland (C_4 plants) gives a signature of -20 to -15‰ [Kirschke et al., 2013; Dlugokencky et al., 2011; Chanton et al., 2005]. See supporting information (S) Table S1 [Teh et al., 2005; Dlugokencky et al., 2011; Chanton et al., 2000] for isotopic CH_4 source values for tropical wetlands and biomass burning.

In situ sampling of carbon isotopes in CH_4 can be used to distinguish sources [Dlugokencky et al., 2011]. Apart from short airborne campaigns, such measurements have, however, usually been confined to within the planetary boundary layer. Unmanned aerial systems (UASs) offer a practical option for regular sampling at higher level. Aircraft measurements and flask sampling [Schuck et al., 2012] are not practical for regular (daily or subdaily) sampling and are also limited by their rate of vertical and horizontal movement and hovering

abilities [Chang *et al.*, 2016]. Balloon flights lack maneuverability compared to UASs [Karion *et al.*, 2010; Chang *et al.*, 2016]. AirCore-like systems [Karion *et al.*, 2010] are impractical for routine monitoring of $\delta^{13}\text{C}_{\text{CH}_4}$ and mole fraction as it is difficult to achieve sufficient isotopic precision to observe small changes.

In this study, a new approach to sampling air masses at different heights using bespoke octocopters (UAS) was developed during two field campaigns on Ascension Island in September 2014 and July 2015. The target was to sample above the Trade Wind Inversion (TWI), a strong and persistent temperature inversion capping the marine boundary layer at altitudes between 1200 and 1800 m above sea level (asl) [Barry and Chorley, 2009]. There is strong wind shear across the TWI with air trajectories indicating different origins for air above and below the inversion, as discussed in section 1.1 below.

Air masses were sampled at various heights above and below the TWI, using a remotely controlled pump and valve system to fill Tedlar bags, probing air from different origins. Ascension Island's location is ideal for these experiments. The work has proved the ability of using UASs to collect and maintain the integrity of air samples using real time sensors for targeting specific air profile characteristics.

1.1. Ascension Island

Ascension Island (7°58'S, 14°24'W) (supporting information Text S1 and Figure S1), in the South Atlantic, experiences near constant South East Trade winds below the TWI (Figure S1a) [Rolph, 2016; Stein *et al.*, 2015] with little diurnal variation, bringing air from central South America and the Southern Ocean. From Ascension the air crosses the Atlantic to become background into Amazonia. Above the TWI, air trajectories are quite different, and the air comes predominantly from tropical and southern Africa (Figure S1b). Ascension Island is therefore ideally located to measure the tropical Atlantic background air in the boundary layer and to study African sources of CH_4 by sampling the midtroposphere above the TWI.

Cumulative 240 h monthly backtrajectories were simulated for both the September and July campaign period using the NOAA Hybrid Single-Particle Lagrangian Integrated Trajectory (HYSPLIT) trajectory tool [Stein *et al.*, 2015]. Air masses at ground level in September and July are from the remote South Atlantic, and above the TWI are from central and West Africa (Figures S1e–S1h) [Rolph, 2016; Stein *et al.*, 2015].

Royal Holloway, University of London (RHUL), hosted by the UK Met Office, has measured CH_4 mole fractions (in situ) and $\delta^{13}\text{C}_{\text{CH}_4}$ (in flasks) on Ascension Island from 2010 [Nisbet *et al.*, 2016]. NOAA and the University of Colorado's Institute of Arctic and Alpine Research have measured both CH_4 mole fractions and $\delta^{13}\text{C}_{\text{CH}_4}$ in flasks collected on the island since 2000 (Figure S2) [Nisbet *et al.*, 2016; Dlugokencky *et al.*, 2016; White *et al.*, 2015].

2. Methods/Experimental Design

Three 8-rotor multirotor (octocopter) (Figure S3a) platforms were built from off the shelf components at the University of Bristol. The platforms were custom designed to carry gas sampling equipment and temperature and humidity response sensors to an altitude of 2700 m within 20 min, with 20% battery capacity remaining on landing. The meteorological sensors sent data to the ground control station in real time to allow targeted gas sampling during descent. Flight and avionic specifications of the platform [Greatwood *et al.*, 2016] are detailed in Table S2 and key elements of the operational manual in Text S1 [Thomas *et al.*, 2012].

Octocopters were flown from a site at 340 m asl (Figure S1c) with a maximum climb rate of 5 m/s. The system retrieved an in situ air sample using an on board diaphragm pump with a flow rate of 4.5 L/min to fill either 3 L or 5 L Tedlar bags (SKC Ltd) as the octocopter hovered for between 45 and 60 s, dependent on atmospheric pressure at the sampling altitude. It was possible to fill two samples per flight at different altitudes. A longer sampling time with a single bag was used at higher altitude ensuring enough sample mass was drawn into the bag for measurement.

High temporal resolution atmospheric profiles of temperature and humidity were telemetered to ground station computers during ascent. The TWI is characterized by temperature increase and relative humidity decrease above the cloud layer. This informed in-flight targeting decisions by the ground observer with remote communication to the UAS for the desired sampling altitude around the unexpectedly tightly defined TWI during the descent leg of the flight. Heights were accurate to within a few meters and allowed samples to be taken above, below, and within the TWI each day, avoiding the use of more uncertain model predictions of

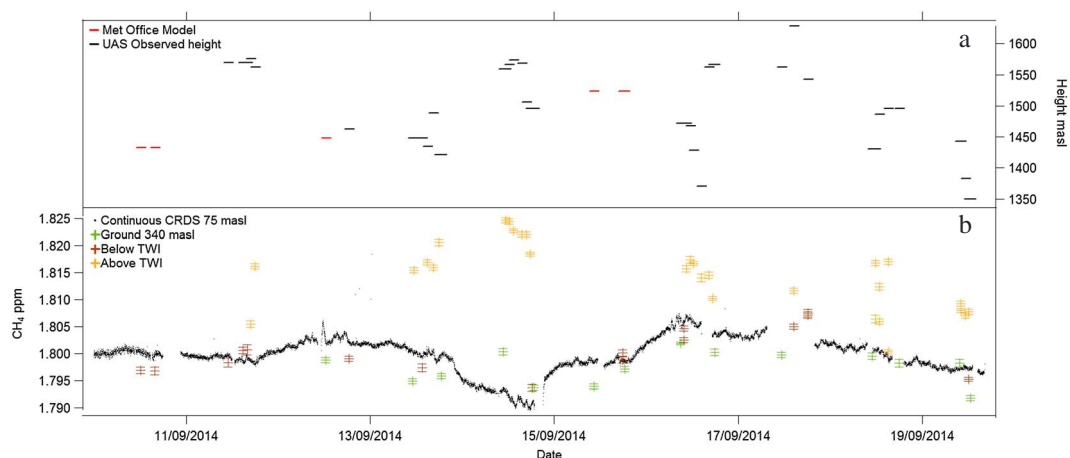


Figure 1. (a) The boundary layer heights per day calculated from either the temperature and humidity sensors on the UAS (black) or from the Met Office model (red). (b) Continuous CRDS CH₄ ground level (75 m asl) compared with bag samples taken during the September 2014 campaign, date markers denote 00 Coordinated Universal Time (UTC). The correlation between CRDS values and ground bag samples $r^2 = 0.558$ where critical $r^2 = 0.247$ at 0.05 significance. The bag samples have a negative bias of 2 ppb compared to the continuous CRDS values perhaps due to the sampling height difference. Using the difference between the median and the 95th percentile of the ground, below TWI, and above the TWI samples as a benchmark; ground level values give a difference of 3 ppb, below the TWI gives a difference of 7 ppb, and above the TWI mixing ratios gives a difference of 8 ppb. The difference of the median mixing ratios below and above the TWI is 16 ppb.

the TWI boundary (Figure S3b). Additional 3 L Tedlar bags were filled with air from approximately 1 m above site ground level (340 m asl) and Met Office ground level (75 m asl) each day to compliment the UAS samples. Samples from the flights and ground sampling were subsequently analyzed together, (see Text S2 [Lowry et al., 2014; Fisher et al., 2006; Jones et al., 2007; Cullen, 1993] for methods).

3. Results

NOAA and RHUL measurements show that the CH₄ mole fraction at Ascension has been increasing sharply since 2007 [Nisbet et al., 2016]. A parametric curve fitting program, HPspline, was used to assess the longer-term trends of the RHUL data using the parameters suggested in Pickers and Manning [2015]. Yearly deseasonalized trends show an increase in 2011–2012 of 4.36 ± 0.6 ppb, a slower increase of 3.91 ± 0.4 ppb in 2012–2013, a renewed larger increase of 6.68 ± 1.3 ppb in 2013–2014, and an increase of 12.67 ± 2.3 ppb in 2014–2015 (Figures S2 and S4) [Nisbet et al., 2016]. Continuous cavity ring-down spectroscopy (CRDS) monitoring of CH₄ shows regular dip and peak events (Figure S5). Peak events occur intermittently, with an increase of around 10 ppb and may last for a period of hours or days. A number of dip and peak events in CH₄ mole fraction occur even though the trajectories below the TWI are steady. The field campaigns were in September 2014 and July 2015. July was chosen as a comparison to the September campaign as July is normally the peak biomass burning season in Southern Hemisphere Africa [Roberts et al., 2009], when smoke plumes inject upward into the free troposphere [Chatfield et al., 1998].

3.1. Campaign 1—September 2014

The September 2014 campaign period overlaps with one of the numerous dip and peak events with a decline in the average mole fraction measured by the CRDS of 8 ppb on 14 September 2014 then a 6 ppb increase on 15 September 2014 of followed by a further 7 ppb increase on 16 September 2014 (Figures 1b and S9a). There are significant correlations (95% confidence) between the bag sample ground values collected at the UAS site, 340 m asl, and in situ measurements at 75 m asl showing no significant difference between the two sites.

Samples taken above the TWI have a higher CH₄ mole fraction than samples taken below (Figures 1b and 2). The samples retrieved from above the TWI contain higher CH₄ mixing ratios than ground level; however, during periods of lower mixing ratio of CH₄ at ground level there is an increased change in concentration across the TWI. The spread of CH₄ mixing ratios when compared over the whole campaign increases with altitude. No distinct isotope ratio change was seen between samples taken above or below the TWI. Ground values

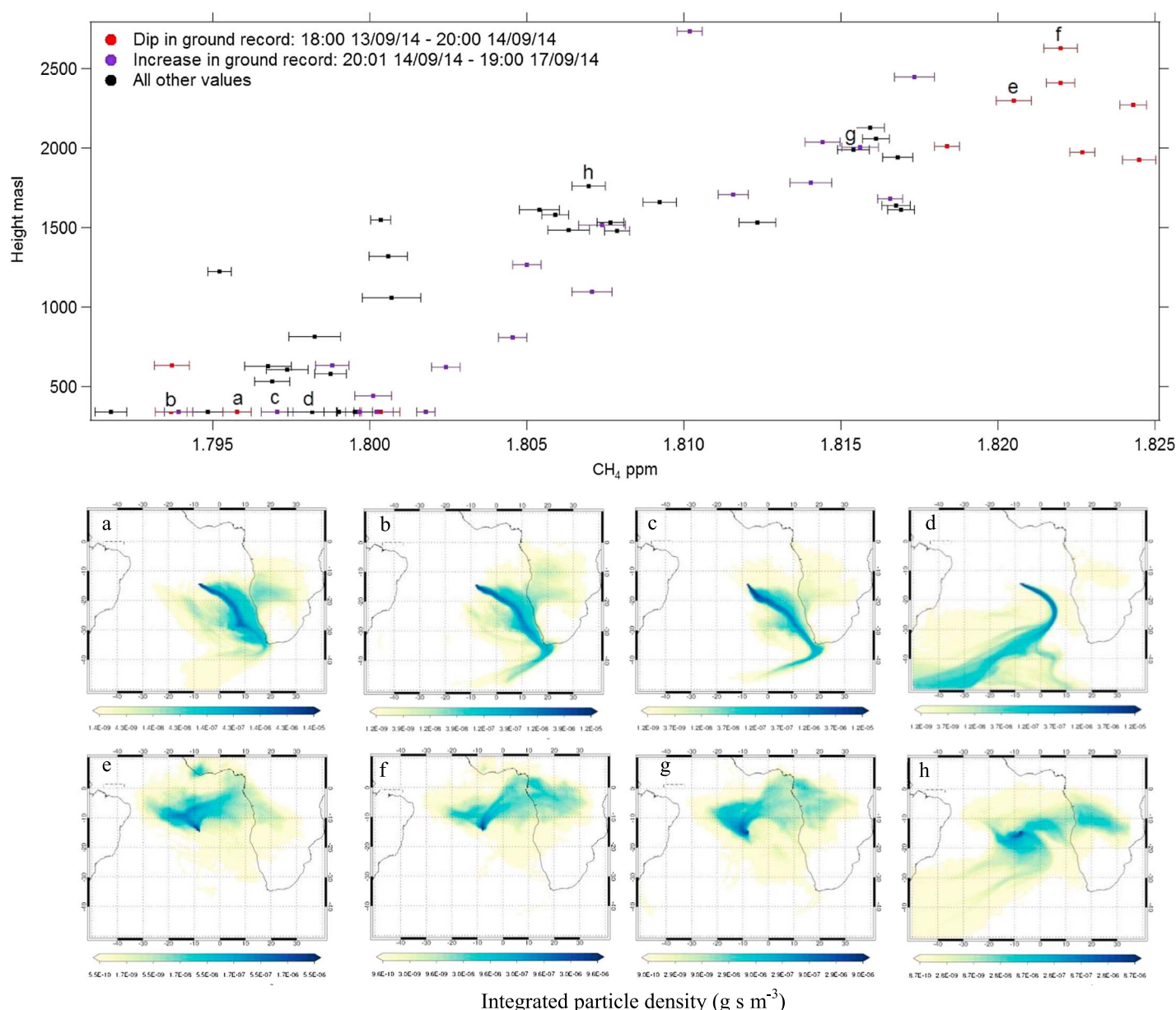


Figure 2. September 2014 bag samples plotted with height meters above sea level compared to typical NAME plots for each period. The NAME models are run for 7 days back from the sample collection time and height. Letters a–h on the graphs compare to the NAME plots. (a) The 13 September 2014 18:34 340 m asl, (b) 14 September 2014 18:40 340 m asl, (c) 15 September 2014 18:20 340 m asl, (d) 19 September 2014 09:45 340 m asl, (e) 13 September 2014 18:01 2298 m asl, (f) 14 September 2014 16:42 2629 m asl, (g) 16 September 2014 10:31 2008 m asl, and (h) 19 September 2014 11:07 1761 m asl.

ranged between -47.41 and -47.17‰ with samples taken from the UAS ranging between -47.60 and -47.00‰ (see Figure 5). Boundary layer heights (Figure 1) vary between 1350 and 1628 m asl with no correlation between boundary layer height and changes in the CH_4 mole fraction at ground level.

Daily NAME modeled footprint plots (Figure S6) have been generated from particles released from a height of 0 to 100 m above ground level with time integrated particle density in the boundary layer over the 11 days up to the release time. These plots show air arriving from the remote South Atlantic, and to a lesser extent from southern Africa as indicated in the cumulative trajectories.

NAME was run backward for 7 days for individual samples. Particles were released from the sample location (from a depth of 100 m centered on the sample height) in order to model where the measured air had come from. Figure S7 shows all the 7 day integrated particle density plots for each sample, for three different height

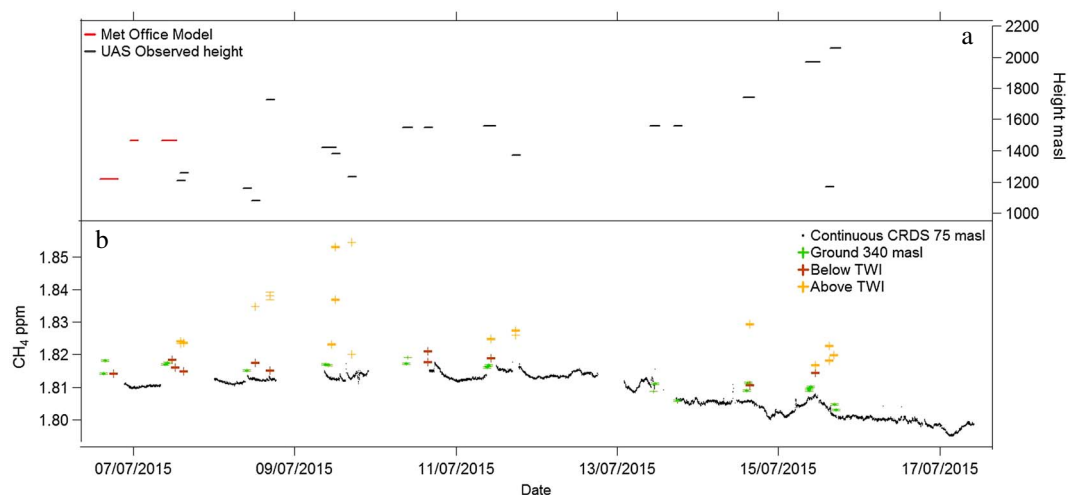


Figure 3. (a) The boundary layer heights calculated either from the temperature and humidity sensors on the UAS (black) or from the Met Office model (red). (b) Continuous CRDS CH₄ ground level (75 m asl) compared with bag samples taken during the July 2015 campaign. The correlation between CRDS values and ground bag samples $r^2 = 0.77$ where critical $r^2 = 0.171$ at a 0.05 significance. The bag samples have a negative bias of 1 ppb compared to the continuous CRDS values perhaps due to the sampling height difference. Using the difference between the median and the 95th percentile of the ground, below TWI, and above the TWI samples as a benchmark; ground level values give a difference of 4 ppb, below the TWI gives a difference of 5 ppb, and above the TWI mixing ratios gives a difference of 28 ppb. The difference of the median mixing ratios below and above the TWI is 8 ppb and the 95th percentile mixing ratios is 31 ppb.

bands (0.1–1 km, 1–3 km, and 3–9 km). Each plot shows the density of particles that passed through that grid box and height band over the last week. Clear differences can be seen in the air mass histories of different samples with variable influence from the different height layers. Some samples are mainly influenced by the remote South Atlantic, whereas others include air masses coming from the north or central Africa. Figure 2 shows typical NAME plots during each sampling period. Ground samples (Figures 2a to 2d) in general arrive from the remote South Atlantic. Above the TWI samples with influence from the east and northeast with air coming from over Africa (Figures 2e–2g and S7) tend to have higher mole fractions than those with South Atlantic influence (Figure 2h).

3.2. Campaign 2—July 2015

Continuous CRDS ground level measurements (Figure 3b) were on average 8 ppb higher in July 2015 than in September 2014. July 2015 ground samples have a larger range from 1800 to 1820 ppb before the drop of mole fraction on 13 July 2015 after which they range from 1795 to 1810 ppb, whereas the September 2014 campaign mole fractions were between 1790 and 1805 ppb (Figure S9). In contrast to the September campaign the samples taken above the TWI have a higher CH₄ mole fraction during the period when CH₄ is high at ground level (Figure 3). There is significant correlation between samples taken from the ground at both the UAS (340 m asl) and Met Office (75 m asl) sites and the Picarro CRDS values.

Boundary layer heights (Figure 3a) range from 1000 to 1500 masl between 7 July 2015 and 11 July 2015. During the decrease in the ground level mole fraction beginning on 13 July 2015 the boundary layer height increases from ~1500 to ~2050 m asl.

Ground level mole fraction measurements can be separated into three periods in the July campaign (Figure 4ii); 6–12 July has the highest ground mole fractions and more enriched $\delta^{13}\text{C}_{\text{CH}_4}$, 13–14 July is an intermediate period, and 15 July has lowest ground mole fraction and depleted $\delta^{13}\text{C}_{\text{CH}_4}$ values (Figures 3b and 4). During the 6–12 July back trajectories on the ground show the air masses have a higher possibility of arrival from over Africa (Figures 4a and 4b) or from the remote South Atlantic (Figures 4 and S8).

4. Campaign Comparisons

Both campaigns show consistently higher CH₄ mole fractions above the TWI with increments up to 31 ppb. NAME modeling indicates these air masses may be influenced by source emissions north of the intertropical

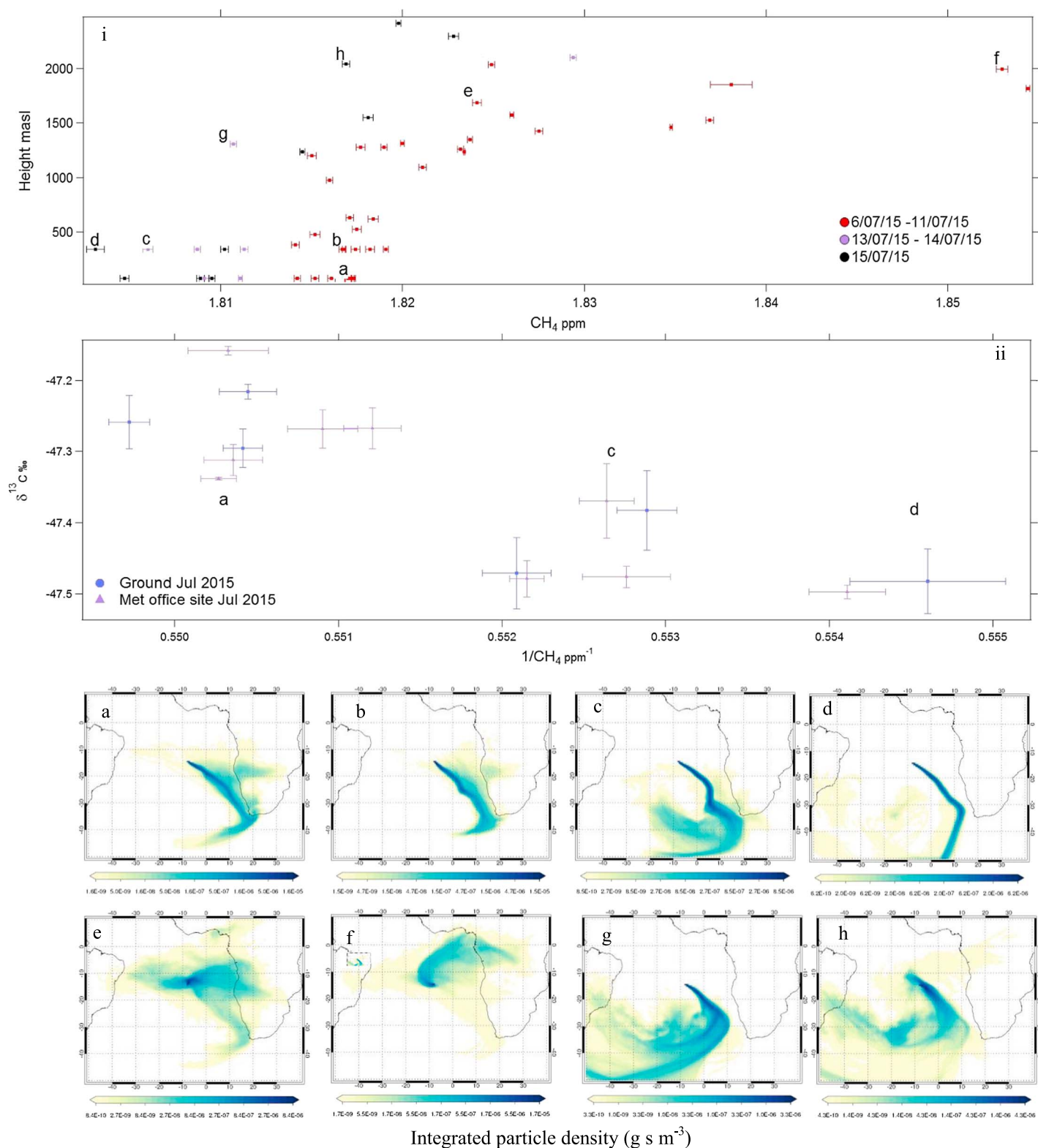


Figure 4. i: July 2015 bag samples plotted with height meters above sea level compared to typical NAME plots for each period. Letters a–h on the graphs compare to the NAME models. The NAME models are run for 7 days back from the sample collection time and height: (a) 08 July 2015 09:38 75 m asl, (b) 09 July 2015 09:55 340 m asl, (c) 13 July 2015 17:50 340 m asl, (d) 15 July 2015 17:00 340 m asl, (e) 07 July 2015 14:00 1686 m asl, (f) 09 July 2015 12:00 1996 m asl, (g) 14 July 2015 15:30 1309 m asl, and (h) 15 July 2015 11:00 2044 m asl. ii. Plot showing the isotopic ground level values taken during July 2015. The $\delta^{13}C_{CH_4}$ is plotted against the inverse of the concentration [Pataki et al., 2003]. These periods are compared to the NAME plots.

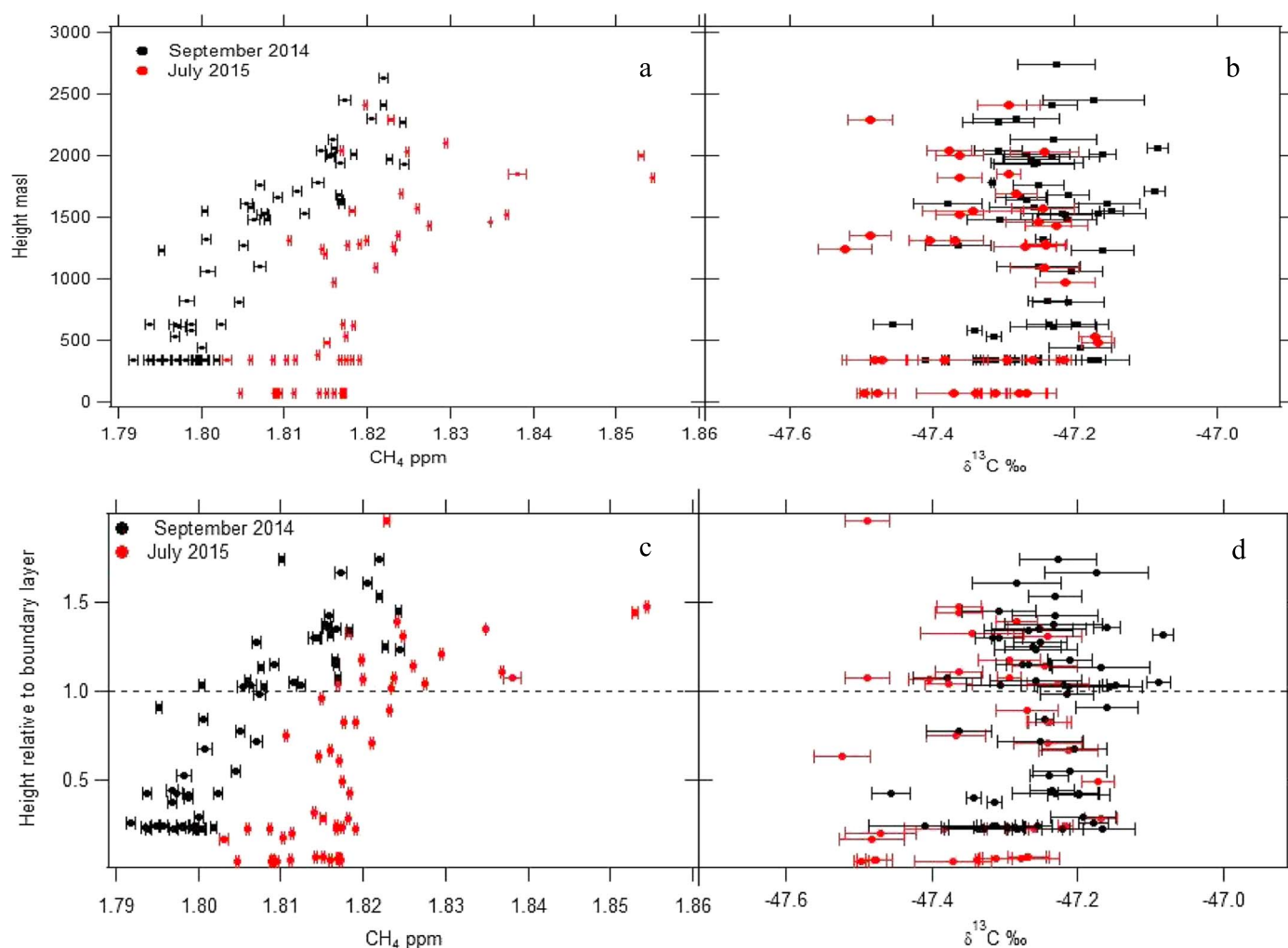


Figure 5. (a) Comparison of CH₄ mole fraction variation with altitude for two field campaigns in September 2014 and July 2015. (b) Comparison of $\delta^{13}\text{C}_{\text{CH}_4}$ variation with altitude between the two field campaigns in September 2014 and July 2015. Errors bars denote 1 standard deviation of the CRDS measurements for each sample (Text S2). (c) Comparison of CH₄ mole fraction with the sample height relative to the boundary layer. (d) Comparison of $\delta^{13}\text{C}_{\text{CH}_4}$ variation with the sample height relative to the boundary layer. Each error bar denotes 1 standard deviation of triplicate measurements (Text S2).

convergence zone and air lofted above Africa by large-scale convection [e.g., Schuck *et al.*, 2012]. Samples from July 2015 have higher mole fractions and ranges compared to samples from September 2014 (Figure 5). This may reflect year-on-year growth and seasonality. There is expected to be more biomass burning ($\delta^{13}\text{C}$ heavy), as shown in the ground level samples (Figure 4ii) and wetland ($\delta^{13}\text{C}$ light) influence from southern Africa in July [Roberts *et al.*, 2009].

Different mixing rates across the TWI are suggested by the increase in mole fraction above the TWI during periods with lower ground values and a decrease in mole fraction above the TWI when higher ground values occurred in the September campaign. Trajectories above the TWI also show a NE component during the dip in ground level mole fraction compared to before and after the dip event. The three ground mole fraction periods shown in Figure 4ii during the July campaign shows that the mole fractions measured above the TWI were higher when higher ground values occurred suggesting the ground mole fraction was influenced by increments along the air mass trajectory.

During the July campaign there was a greater TWI height range (1030 to 2057 m asl). When the inversion is higher, the inversion strength is weaker with more mixing across the boundary layer [Cao *et al.*, 2007]. The 7–11 July campaign showed a larger CH₄ contrast above and below the TWI, indicating a stronger capping of the TWI with less mixing with the free troposphere. On the 15 July, the TWI height was higher, and there was less CH₄ mole fraction contrast across the TWI. The September campaign had more constant TWI height,

suggesting mixing above and below the TWI occurred before the air reached Ascension during the periods where there is a lower mole fraction separation above and below the TWI.

Isotopic data give an average of $\delta^{13}\text{C} -47.25 \pm 0.09\text{‰}$ during the September campaign and an average of $-47.33 \pm 0.09\text{‰}$ during the July campaign (Figure 5). The shift to more depleted values in July corresponds to the long-term trend both on Ascension Island and globally. Overall, no distinct isotopic ratio change was seen above the TWI during either of the campaigns (Figures 5 and S10) [Pataki *et al.*, 2003]. Figures 5i, 5f, and 5h show two samples at a similar height above the TWI with air masses arriving from different source regions. Sample f has a trajectory with a higher possibility of inputs from African emissions and has a CH_4 mole fraction of 1853 ppb and $\delta^{13}\text{C} -47.36\text{‰}$. Sample h has a trajectory predominately from over the South Atlantic and a CH_4 mole fraction of 1817 ppb and $\delta^{13}\text{C} -47.38\text{‰}$. There is an input of 36.1 ppb CH_4 from African sources but an isotopic shift of only 0.02‰ suggesting the sources (Table S1) have a combined isotopic signature close to the bulk atmospheric value. A mixture of tropical wetland emissions ($-55 \pm 3\text{‰}$), agriculture ($-62 \pm 3\text{‰}$), and biomass burning of savannah grassland (-20 to -15‰) [Dlugokencky *et al.*, 2011] would fit. Destruction by OH is the main CH_4 sink; this has a kinetic isotope shift of 4 to 6‰ [Allan *et al.*, 2001, 2007; Nisbet *et al.*, 2016]. However, the lifetime of CH_4 is ~ 9 years [Dlugokencky *et al.*, 2011] so even in the intense OH of the tropical mid-troposphere the effect of OH destruction between the African sources and Ascension Island is small. A more local influence may be from the marine CI sink in the marine boundary layer [Allan *et al.*, 2001, 2007].

5. Conclusions

Ground values, taken more frequently during the campaigns, show a wider spread of isotopic signatures than the long-term bimonthly RHUL samples [Nisbet *et al.*, 2016], making it more difficult to identify a distinct isotopic change above the TWI. The September ground values have a range of 10 ppb and 0.33‰, and the July ground values have a range of 17 ppb and 0.24‰. This may suggest an influence from possible local factors such as the little studied CI sink or varied OH loss. Sink processes preferentially remove $^{12}\text{C}_{\text{CH}_4}$ [Schaefer *et al.*, 2016]. The air mass footprints have varying influences from Africa as well as the remote South Atlantic likely contributing to the isotopic changes.

NAME modeling has shown that the air mass origin above the TWI can vary daily. Both the origin of air masses and mixing events above and below the TWI influence the mole fractions of the ground samples. The isotopes have no consistent signal above or below the TWI, despite the significant CH_4 increment measured indicating the input from Africa is close to background $\delta^{13}\text{C}$. This input is likely to be a mixture of emissions from tropical wetlands, agriculture, and biomass burning. The samples taken higher up may be more influenced by these diverse sources over Africa.

Longer-term regular monitoring above the TWI would be useful for identifying isotopic signatures of the mixed tropical sources from Africa, determining seasonality and long-term trends. During such monitoring, replacing Tedlar bags with aluminum flask samples would allow CO/CO_2 to be monitored, which perhaps along with absorbing aerosol measurements would help characterize air masses according to biomass burning history. Other measurements such as water vapor mixing ratios and $^{18}\text{O}/^{16}\text{O}$ [Bailey *et al.*, 2013], or O_3/CO_2 ratios [Berkes *et al.*, 2016], could allow quantification of vertical mixing over the TWI and aid interpretation of CH_4 isotopic composition. If a UAS were to be used, an increase of approximately 30% in the mass should allow these changes to be realized.

Relatively lightweight sensors (1–2 kg) may be placed on a UAS to measure the CH_4 concentration although the precision of $\sim 1\%$ is not sufficient to detect small changes in ambient air [Kahn *et al.*, 2012]. A precision of at least 5 ppb would be needed to distinguish differences across the TWI and a higher precision for smaller mole fraction changes associated with meteorological factors. It is likely that such instrumentation will be developed in the next few years.

Overall, the campaigns have shown that it is possible to use inexpensive UASs to access the midtroposphere above Ascension Island and retrieve air samples. Sampling at Ascension is able to measure both remote South Atlantic air from below the trade wind inversion and also air from above that has been lofted by convective systems in a wide region of the equatorial and southern savannah tropics. Thus, the technique extends Ascension's access from sea level up to 2700 masl, making it a superb location for long-term global monitoring.

Acknowledgments

This work was part of the investigation of the southern methane anomaly: causes, implications, and relevance to past global events funded by the UK Natural Environment Research Council (NERC) (grant NE/K006045/1) and NERC studentship. Thanks to support from the Met Office, RAF, and USAF on Ascension Island. The authors gratefully acknowledge the NOAA Air Resources Laboratory (ARL) for the provision of the HYSPLIT transport and dispersion model and/or READY website (<http://www.ready.noaa.gov>) used in this publication. Data will be deposited in the UK Centre for Environmental Data Analysis on completion of Rebecca Brownlow's PhD thesis. We acknowledge use of the NAME atmospheric dispersion model and associated NWP meteorological data sets made available to us by the Met Office. We acknowledge the significant storage resources and analysis facilities made available to us on JASMIN by STFC CEDA along with the corresponding support teams.

References

- Allan, W., H. Struthers, and D. C. Lowe (2007), Methane carbon isotope effects caused by atomic chlorine in the marine boundary layer: Global model results compared with Southern Hemisphere measurements, *J. Geophys. Res.*, **112**, D04306, doi:10.1029/2006JD007369.
- Allan, W., M. R. Manning, K. R. Lassey, D. C. Lowe, and A. J. Gomez (2001), Modeling the variation of $\delta^{13}\text{C}$ in atmospheric methane: Phase ellipses and the kinetic isotope effect, *Global Biogeochem. Cycles*, **15**(2), 467–481, doi:10.1029/2000GB001282.
- Bailey, A., D. Toohey, and D. Noone (2013), Characterizing moisture exchange between the Hawaiian convective boundary layer and free troposphere using stable isotopes in water, *J. Geophys. Res. Atmos.*, **118**, 8208–8221, doi:10.1002/jgrd.50639.
- Barry, R. G., and R. J. Chorley (2009), *Atmosphere, Weather and Climate*, Routledge, New York.
- Bousquet, P., et al. (2006), Contribution of anthropogenic and natural sources to atmospheric methane variability, *Nature*, **443**(7110), 439–443, doi:10.1038/nature05132.
- Berkes, F., P. Hoor, H. Bozem, D. Kunkel, M. Sprenger, and S. Henne (2016), Airborne observation of mixing across the entrainment zone during PARADE 2011, *Atmos. Chem. Phys.*, **16**, 6011–6025.
- Cao, G., T. W. Giambelluca, D. E. Stevens, and T. a. Schroeder (2007), Inversion variability in the Hawaiian trade wind regime, *J. Clim.*, **20**(7), 1145–1160, doi:10.1175/JCLI4033.1.
- Chang, C. C., J. L. Wang, C. Y. Chang, M. C. Liang, and M. R. Lin (2016), Development of a multicopter-carried whole air sampling apparatus and its applications in environmental studies, *Chemosphere*, **144**, 484–492, doi:10.1016/j.chemosphere.2015.08.028.
- Chanton, J., L. Chaser, P. Glasser, and D. Siegel (2005), Carbon and hydrogen isotopic effects in microbial methane from terrestrial environments, in *Stable Isotopes and Biosphere Atmosphere Interactions*, edited by L. B. Flanagan, J. R. Ehleringer, and D. E. Pataki, Elsevier, Oxford.
- Chanton, J. P., C. M. Rutkowski, C. C. Schwartz, D. E. Ward, and L. Boring (2000), Factors influencing the stable carbon isotopic signature of methane from combustion and biomass burning, *J. Geophys. Res.*, **105**, 1867, doi:10.1029/1999JD900909.
- Chatfield, R. B., J. A. Vastano, L. Li, G. W. Sachse, and V. S. Connors (1998), The Great African Plume from biomass burning: Generalizations from a three-dimensional study of TRACE A carbon monoxide, *J. Geophys. Res.*, **103**, 28,059–28,077, doi:10.1029/97JD03363.
- Cullen, M. J. P. (1993), The unified forecast climate model, *Meteorol. Mag.*, **122**(1449), 81–94.
- Dlugokencky, E. J., P. M. Lang, A. M. Crowell, J. W. Mund, M. J. Crowell, and K. W. Thoning (2016), Atmospheric methane dry air mole fractions from the NOAA ESRL carbon cycle cooperative global air sampling network, 1983–2015, Version: 2016-07-07. [Available at ftp://aftp.cmdl.noaa.gov/data/trace_gases/ch4/flask/surface/]
- Dlugokencky, E. J., E. G. Nisbet, R. Fisher, and D. Lowry (2011), Global atmospheric methane: Budget, changes and dangers, *Phil. Trans. R. Soc. A*, **369**(1943), 2058–72, doi:10.1098/rsta.2010.0341.
- Fisher, R. E., D. Lowry, O. Wilkin, S. Sriskantharajah, and E. G. Nisbet (2006), High precision, automated stable isotope analysis of atmospheric methane and carbon dioxide using continuous-flow isotope-ratio mass spectrometry, *Rapid Commun. Mass Spectrom.*, **20**(2), 200–8, doi:10.1002/rcm.2300.
- Frankenberg, C., P. Bergamaschi, A. Butz, S. Houweling, J. F. Meirink, J. Notholt, A. K. Petersen, H. Schrijver, T. Warneke, and I. Aben (2008), Tropical methane emissions: A revised view from SCIAMACHY onboard ENVISAT, *Geophys. Res. Lett.*, **35**, L15811, doi:10.1029/2008GL034300.
- Greatwood, C., Richardson, T., J. Freer, R. Thomas, R. Brownlow, D. Lowry, R. E. Fisher, and E. G. Nisbet (2016), Automatic path generation for multirotor descents through varying air masses above Ascension Island, *AIAA Atmospheric Flight Mechanics Conference*, (January 2016), 1–12, doi:10.2514/6.2016-1532.
- Jones, A. R., D. J. Thomson, M. Hort, and B. Devenish (2007), The U.K. Met Office's next-generation atmospheric dispersion model, NAME III, in *Air Pollution Modeling and Its Application XVII* (Proceedings of the 27th NATO/CCMS International Technical Meeting on Air Pollution Modelling and its Application), edited by C. Borrego and A.-L. Norman, pp. 580–589, Springer.
- Kahn, A., D. Schaefer, L. Tao, D. J. Miller, K. Sun, M. A. Zondlo, W. A. Harrison, B. Roscoe, and D. J. Lary (2012), Low power greenhouse gas sensors for unmanned aerial vehicles, *Remote Sens.*, **4**(5), 1355–1368, doi:10.3390/rs4051355.
- Karion, A., C. Sweeney, P. Tans, and T. Newberger (2010), AirCore: An innovative atmospheric sampling system, *J. Atmos. Oceanic Technol.*, **27**(11), 1839–1853, doi:10.1175/2010JTECHA1448.1.
- Kirschke, S., P. Bousquet, P. Ciais, M. Saunio, J. G. Canadell, E. J. Dlugokencky, and G. Zeng (2013), Three decades of global methane sources and sinks, *Nat. Geosci.*, **6**(10), 813–823, doi:10.1038/ngeo1955.
- Lowry, D., R. E. Fisher, J. L. France, M. Lanoisellé, E. G. Nisbet, E. Brunke, E. Dlugokencky, N. Brough and A. Jones (2014), Continuous monitoring of greenhouse gases in the South Atlantic And Southern Ocean: Contributions from the equianos network. 17th WMO/IAEA Meeting of Experts on Carbon Dioxide, Other Greenhouse Gases and related Tracers Measurement Techniques, GAW Report 213, Geneva, 109–112.
- Nisbet, E. G., et al. (2016), Rising atmospheric methane: 2007–14 growth and isotopic shift, *Global Biogeochem. Cycles*, **30**, 1356–1370, doi:10.1002/2016GB005406.
- Nisbet, E. G., E. J. Dlugokencky, and P. Bousquet (2014), Atmospheric science. Methane on the rise-again, *Science*, **343**(6170), 493–5, doi:10.1126/science.1247828.
- Pataki, D. E., J. R. Ehleringer, L. B. Flanagan, D. Yakir, D. R. Bowling, C. J. Still, N. Buchmann, J. O. Kaplan, and J. A. Berry, (2003), The application and interpretation of Keeling plots in terrestrial carbon cycle research, *Global Biogeochem. Cycles*, **17**(1), 1022, doi: 10.1029/2001GB001850.
- Pickers, P. A., and A. C. Manning (2015), Investigating bias in the application of curve fitting programs to atmospheric time series, *Atmos. Meas. Tech.*, **8**(3), 1469–1489, doi:10.5194/amt-8-1469-2015.
- Roberts, G., M. J. Wooster, and E. Lagoudakis (2009), Annual and diurnal African biomass burning temporal dynamics, *Biogeosciences*, **6**, 849–866, doi:10.5194/bg-6-849-2009.
- Rolph, G. D. (2016), Real-time Environmental Applications and Display sYstem (READY), NOAA Air Resources Laboratory, College Park, Md. [Available at <http://www.ready.noaa.gov>]
- Schaefer, H., et al. (2016), A 21st century shift from fossil-fuel to biogenic methane emissions indicated by $^{13}\text{CH}_4$, *Science*, **351**(6278), doi:10.1126/science.aad2705.
- Schuck, T. J., K. Ishijima, P. K. Patra, A. K. Baker, T. Machida, H. Matsueda, Y. Sawa, T. Umezawa, C. A. M. Brenninkmeijer, and J. Lelieveld (2012), Distribution of methane in the tropical upper troposphere measured by CARIBIC and CONTRAIL aircraft, *J. Geophys. Res.*, **117**, D19304, doi:10.1029/2012JD018199.
- Stein, A. F., R. R. Draxler, G. D. Rolph, B. J. B. Stunder, M. D. Cohen, and F. Ngan (2015), NOAA's HYSPLIT atmospheric transport and dispersion modeling system, *Bull. Am. Meteorol. Soc.*, **96**, 2059–2077, doi:10.1175/BAMS-D-14-00110.1.

- Teh, Y. A., W. L. Silver, and M. E. Conrad (2005), Oxygen effects on methane production and oxidation in humid tropical forest soils, *Glob. Change Biol.*, *11*(8), 1283–1297, doi:10.1111/j.1365-2486.2005.00983.x.
- Thomas, R. M., K. Lehmann, H. Nguyen, D. L. Jackson, D. Wolfe, and V. Ramanathan (2012), Measurement of turbulent water vapor fluxes using a lightweight unmanned aerial vehicle system, *Atmos. Meas. Tech.*, *5*, 243–257.
- White, J. W. C., B. H. Vaughn, and S. E. Michel (2015), University of Colorado, Institute of Arctic and Alpine Research (INSTAAR), Stable Isotopic Composition of Atmospheric Methane (^{13}C) from the NOAA ESRL Carbon Cycle Cooperative Global Air Sampling Network, 1998–2014, Version: 2016-04-26. [Available at ftp://aftp.cmdl.noaa.gov/data/trace_gases/ch4c13/flask/.]

Methane mole fraction and $\delta^{13}\text{C}$ above and below the Trade Wind Inversion at Ascension Island in air sampled by aerial robotics

R. Brownlow¹, D. Lowry¹, R. M. Thomas^{2,3}, R. E. Fisher¹, J. L. France⁴, M. Cain⁵, T. S. Richardson⁶, C. Greatwood⁶, J. Freer⁷, J. A. Pyle⁵, A. R. MacKenzie^{2,3} & E. G. Nisbet¹

¹ Department of Earth Sciences, Royal Holloway, University of London, Egham, TW20 0EX, UK

² School of Geography, Earth and Environmental Sciences, University of Birmingham, Birmingham, B15 2TT, UK.

³ Birmingham Institute of Forest Research, University of Birmingham, Edgbaston, Birmingham, B15 2TT, UK.

⁴ Centre for Oceanic and Atmospheric Sciences, School of Environmental Sciences, University of East Anglia, Norwich, NR4 7TJ, UK.

⁵ Centre for Atmospheric Science, University of Cambridge, Cambridge CB2 1EW, UK.

⁶ Department of Aerospace Engineering University of Bristol, Bristol, UK.

⁷ School of Geographical Sciences, University of Bristol, Bristol, UK.

Contents of this file

Tables S1 & S2

Text S1 & S2

Figures S1 to S10

Introduction

The supporting information gives a table of general tropical wetland and biomass burning $\delta^{13}\text{C}$ signatures (Table S1). Multirotor Specifications (Table S2). Key elements of the operational manual (Text S1). Methods for bag analysis (Text S2) Hysplit back trajectories for the September 2014 and July 2015 campaigns (Fig. S1). $\delta^{13}\text{C}$ and Methane mole fraction plots from the Ascension site (Figs: S2, S4 & S5). An example plot of a high resolution temperature and humidity profile from the UAV sensors compared with the Met office model (Fig. S3). NAME plots showing air mass back trajectories (Fig. S6, S7 & S8). Graphs showing the variation (ppb) in the mean ground level mixing ratios for bag samples and equivalent Picarro CRDS values (Fig. S9). A graph showing the isotopic values above the TWI during both campaigns (Fig. S10).

Site	$\delta^{13}\text{C}$ (‰)	Reference
Wetlands		
Tropical humid forests	-84 and -98	Teh et al., 2005
Swamps	-55±3	Dlugokencky et al., 2011
Rice agriculture	-62±3	Dlugokencky et al., 2011
Biomass Burning		
Savannah grassland (C4)	-20 to -15	Dlugokencky et al., 2011
C4 plants	-13 to -17	Chanton et al., 2000
C3 plants	-26 to -29	Chanton et al., 2000

Table S1: General wetland and biomass burning tropical methane sources.

Maximum Take Off Weight (inc. batteries)	10kg
Diagonal rotor-rotor distance	1.07m
Maximum battery capacity	32,000mAh 6 cell Lithium Polymer
Motors	T-Motor MN3515 400KV
Propellers	T-Motor 16x5.4"
Electronic Speed Controllers	RCTimer NFS ESC 45A (OPTO)
Autopilot	Pixhawk by 3DRobotics
Autopilot software	ArduCopter v3.1.5
Safety pilot control link	FrSky L9R 2.4GHz
Ground Control Station link	Ubiquiti 5GHz directional
Onboard computing	BeagleBone Black
Sampling pump	KNF Diaphragm Pump (NMP 850 KNDC)

Table S2: Multirotor Specifications (from Greatwood et al. 2016).

Text S1: key elements of the operational manual

As with all field trials, the key to success in Ascension was the preparation and flight trials that took place in the UK. Two development vehicles were used to test each individual part of the system and the overall mission development prior to each trip. All flight trials were carried out at low altitude, i.e. beneath the 400ft limit in the UK, with a staged approach in Ascension up to the full sample height. Because Ascension is so remote and isolated, it is an ideal place to test this approach to air sampling due to the restricted airspace that surrounds the island.

Ascension Island airspace and airfield are jointly managed by the US Air Force (USAF) and UK Royal Air Force (RAF). Planning of the UAS campaign centred on our operations procedures have been developed over several years in a variety of environmental (Thomas et al., 2012) contexts. Key operations procedures included: i) roles and experience of the flight team; ii) operational logistics; iii) physical and electrical components of the airframe; iv) frequencies used by the UAS and ground communications; v) maintenance of communications with local Air Traffic Control before, during and after flights; vi) access management of land beneath the flight zone. Excellent communications with the RAF/USAF, Ascension Island Government and other stakeholders allowed the operations plan to evolve and be agreed well in advance of the flight campaigns.

Text S2: Methods

Mole fractions of CH₄ in the Tedlar bag samples were measured within 1-2 days of collection using Royal Holloway's Picarro 1301 CRDS (cavity ring-down spectrometer) with a NOAA traceable 6-gas calibration suite (on Ascension Island) giving a precision of ± 0.5 ppb (Lowry et al., 2014). The samples are measured for 240 seconds with the last 120 seconds of measurements being used for the mean mole fraction. If the bag samples had less air the bags were run for 120 seconds with 60 seconds being used for the mean mole fraction. The CRDS on Ascension measures CH₄ and CO₂ in air taken through an inlet above the Met Office station roof, 5 magl and 75 masl.

The Tedlar bag samples were then air freighted to RHUL and the remaining gas analysed for $\delta^{13}\text{C}_{\text{CH}_4}$ by continuous-flow gas chromatography isotope-ratio mass spectrometry (CF-GC-IRMS) (Fisher et al., 2006) to a precision on triplicate analysis averaging $\pm 0.04\%$.

NAME (Numerical Atmospheric-dispersion Modelling Environment) was used to model air mass histories (Jones et al., 2007). It is a 3-D Lagrangian particle dispersion model, and was used here with the UK Meteorological Office's Unified Model meteorological fields (Cullen, 1993).

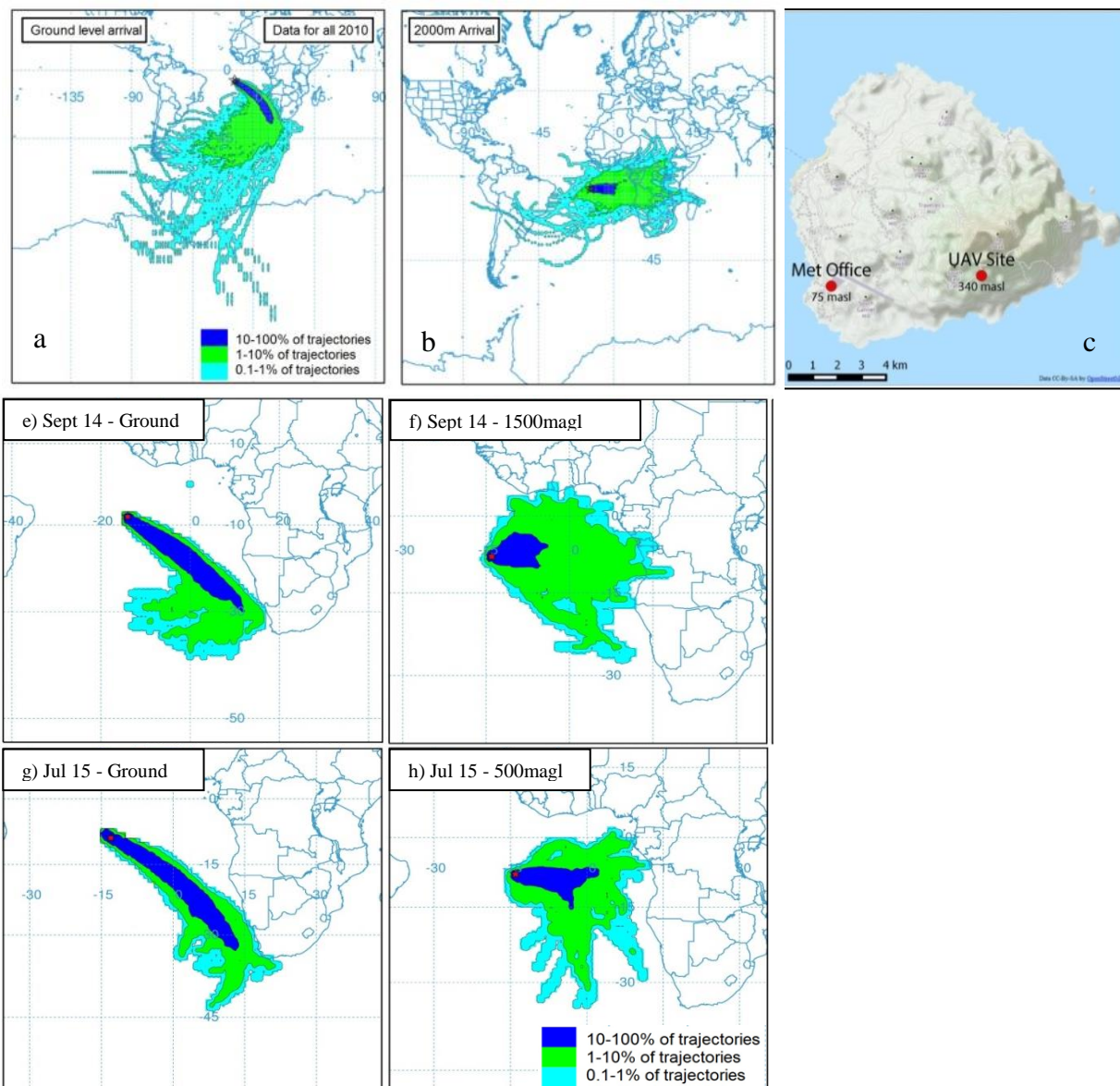


Figure S1:

Offline NOAA Hybrid Single-Particle Lagrangian Integrated Trajectory (HYSPLIT) modelled Trajectories (Yearly) for a & b: 2010 240 hours back arriving at a) ground level and b) 2000magl representative of above the TWI (Rolph 2016; Stein et al., 2015).

c: Map showing the location of the sampling points on Ascension Island ($7^{\circ}58'S$, $14^{\circ}24'W$). Mapped using QGIS 2.2.0 with base map layer from OpenStreetMap.

HYSPLIT trajectories (Monthly) for e, f, g & h: September 2014 and July 2015 run 120 hours back arriving at e & g) ground level and f & h) 1500magl representative of above the TWI (Rolph 2016; Stein et al., 2015).

For each month Hysplit was run offline with GDAS archive meteorological data four times per day at 00:00, 06:00, 12:00 and 18:00 UTC. The yearly plots are an accumulation of each month in the year. Note: map areas are sized to fit each individual trajectory scale.

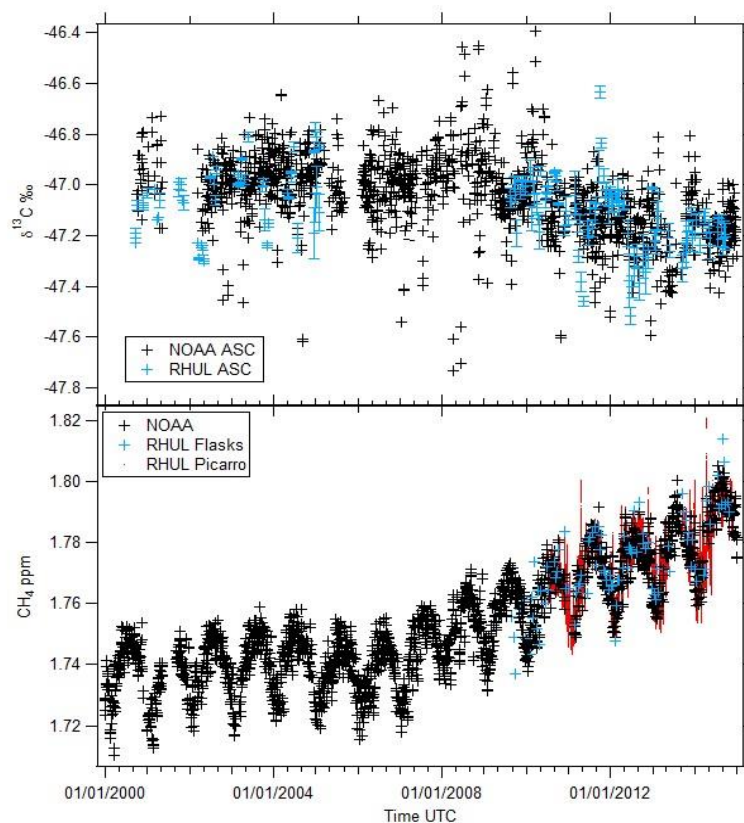


Figure S2 (Reproduced from Nisbet et al., 2016): (Top) Ascension Island $\delta^{13}\text{C}_{\text{CH}_4}$ record for 2000-2014 showing NOAA-INSTAAR (black crosses) and RHUL measurements (blue crosses with error bars) from the Airhead, Ascension. (Bottom) Methane mole fraction on Ascension Island 2000-2014 showing NOAA discrete air samples (black crosses), continuous RHUL Picarro measurements (red line) and RHUL flask samples (blue crosses) from the Airhead, Ascension.

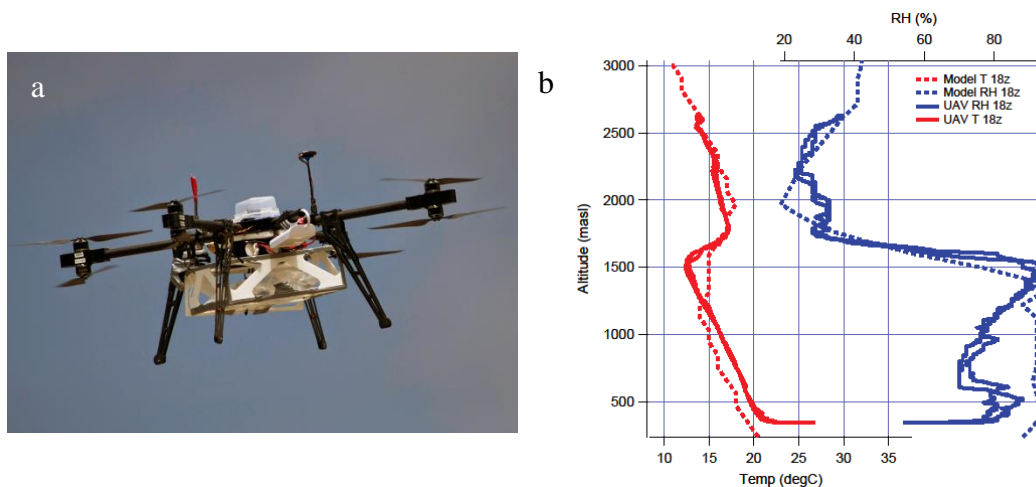


Figure S3: a) A photo of the UAS in flight. b) An example of a high resolution temperature and humidity profile with the Met office model shown for comparison.

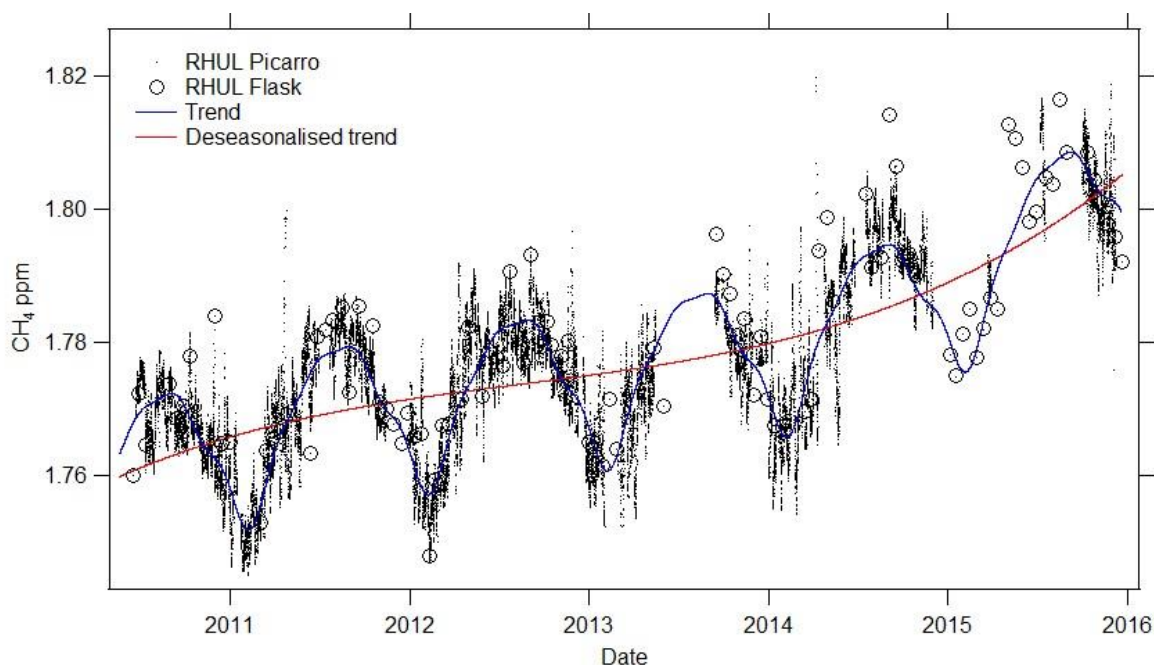


Figure S4: Continuous Picarro measurements and Flask sampling at Ascension Island and the trends given using the curve fitting program HPspline.

Growth rates: 2011-2012: 4.36 ± 0.6 ppb, 2012-2013: 3.91 ± 0.4 ppb, 2013-2014: 6.68 ± 1.3 ppb & 2014-2015: 12.67 ± 2.3 .

The errors on the yearly growth rates are the standard deviation of each monthly year on year growth rates.

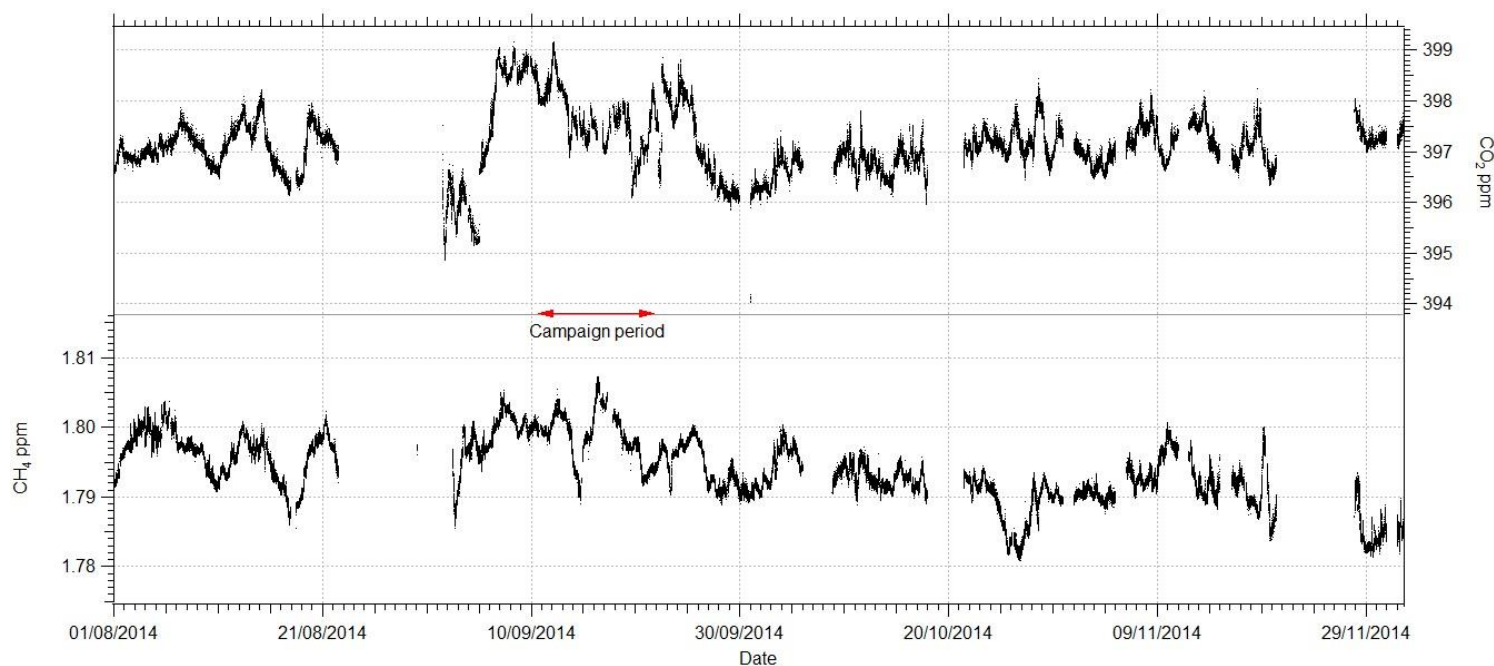


Figure S5: Continuous Picarro CH₄ and CO₂ ground values before & during the September campaign.

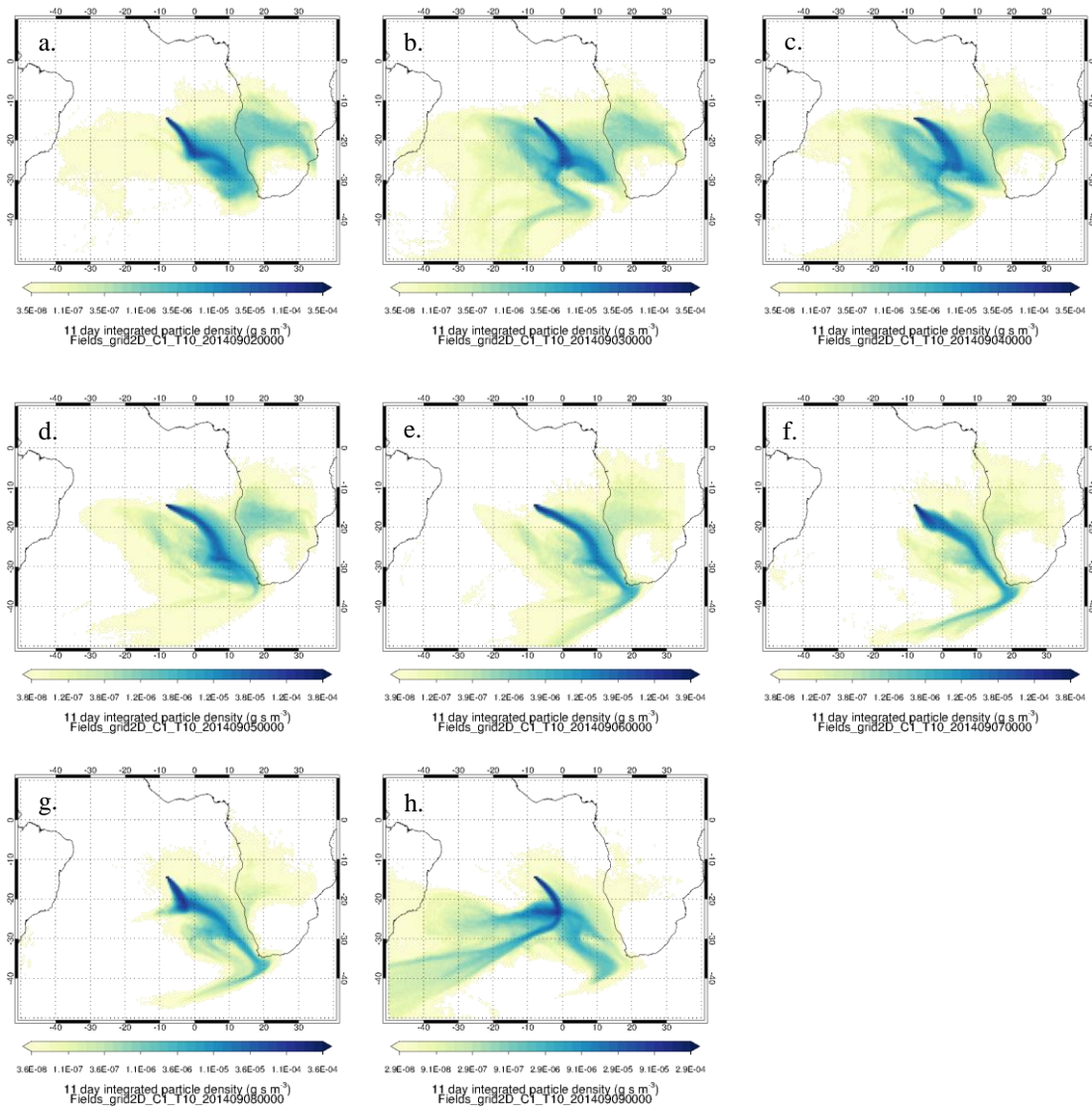
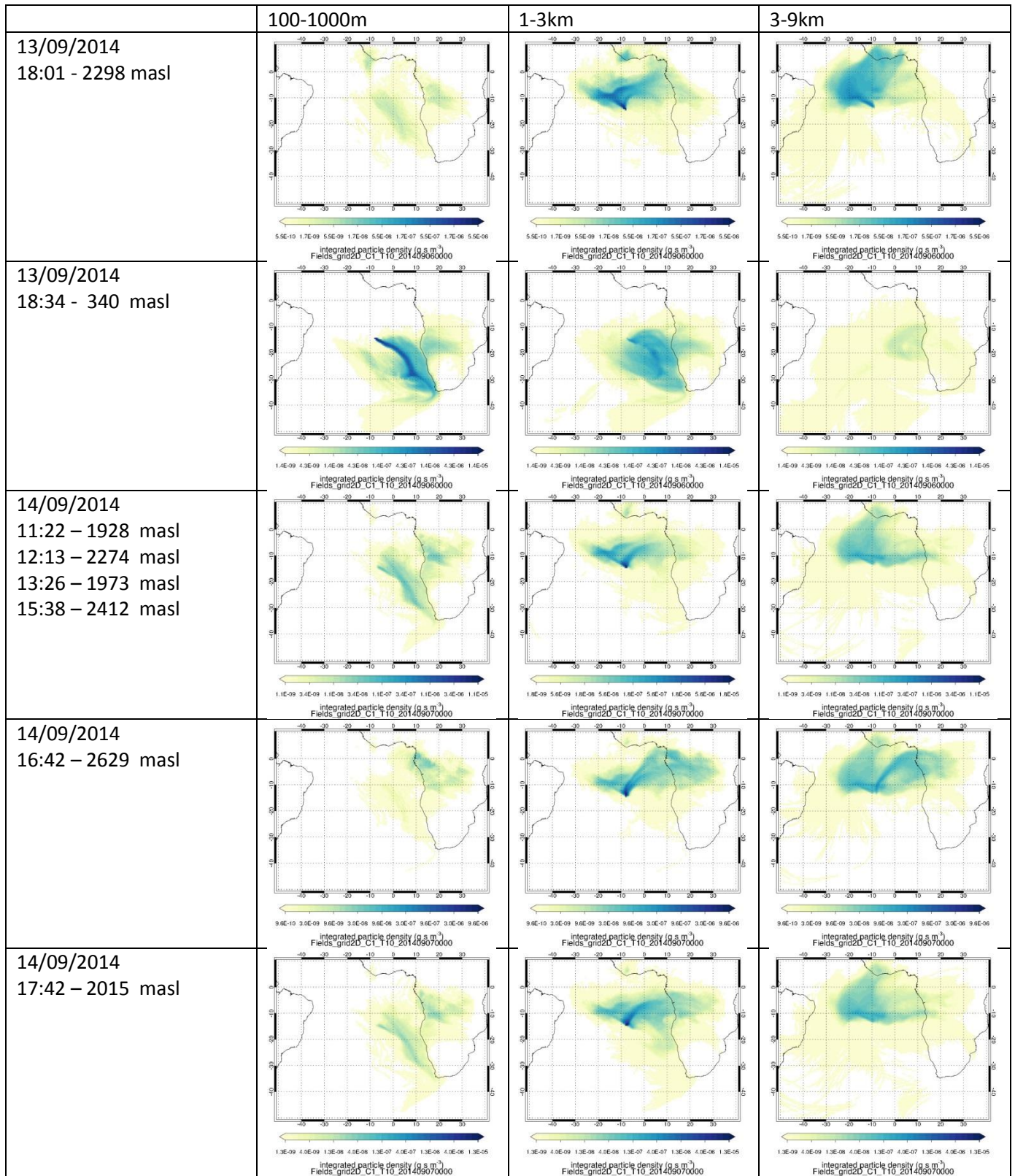
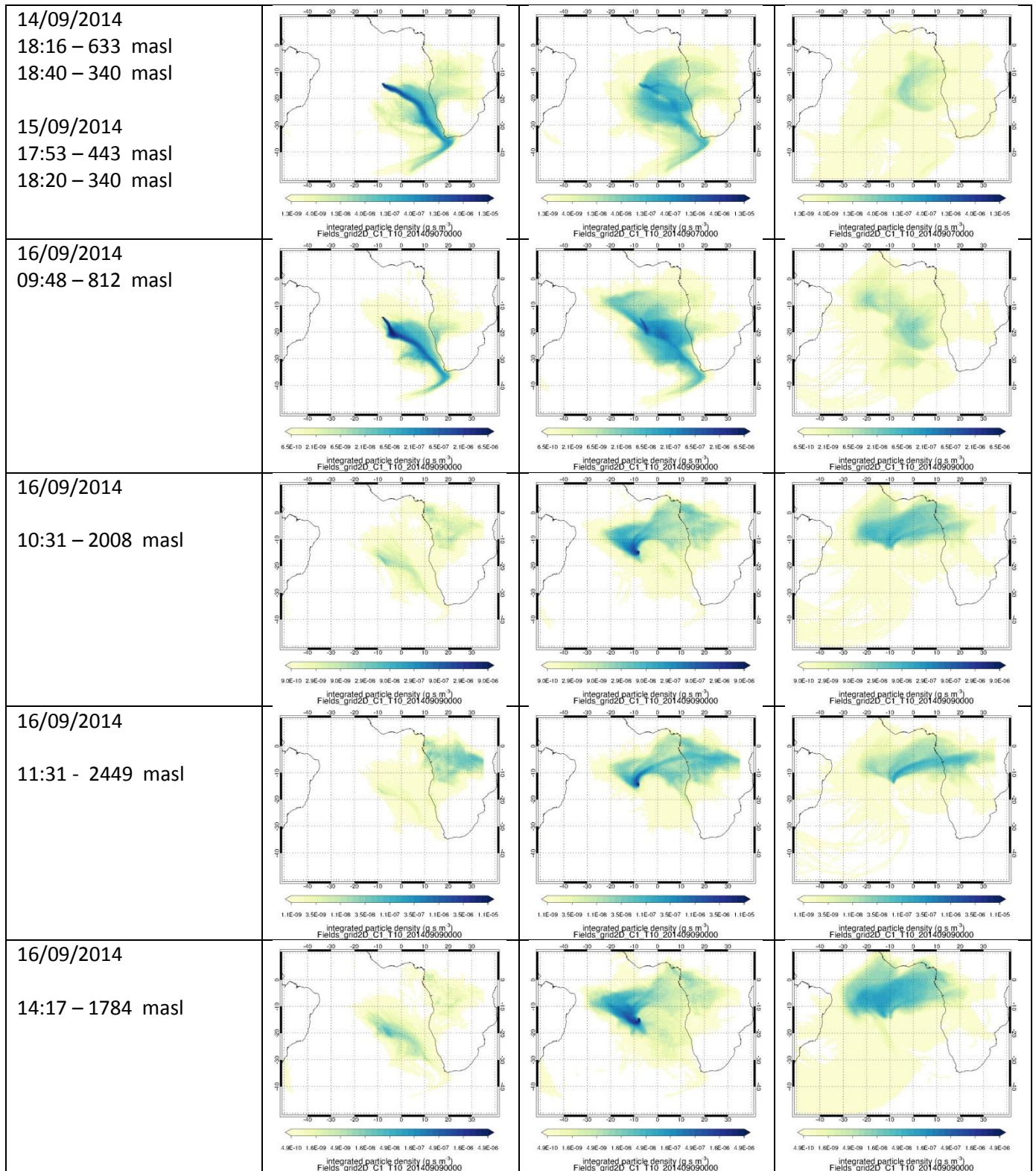


Fig. S6: NAME plots for the September 2014 campaign on Ascension Island. Particles are released for 24 hours at a rate of 20000 per hour from our site on Ascension Island, from a height of 0-100m above ground level. Shown are the footprint maps for 11 days back for air masses arriving at Ascension Island on the following 24 hour periods (midnight to midnight):

a) 10-11/09/2014, b) 11-12/09/2014, c) 12-13/09/2014, d) 13-14/09/2014, e) 14-15/09/2014, f) 15-16/09/2014, g) 16-17/09/2014 and h) 17-18/09/2014





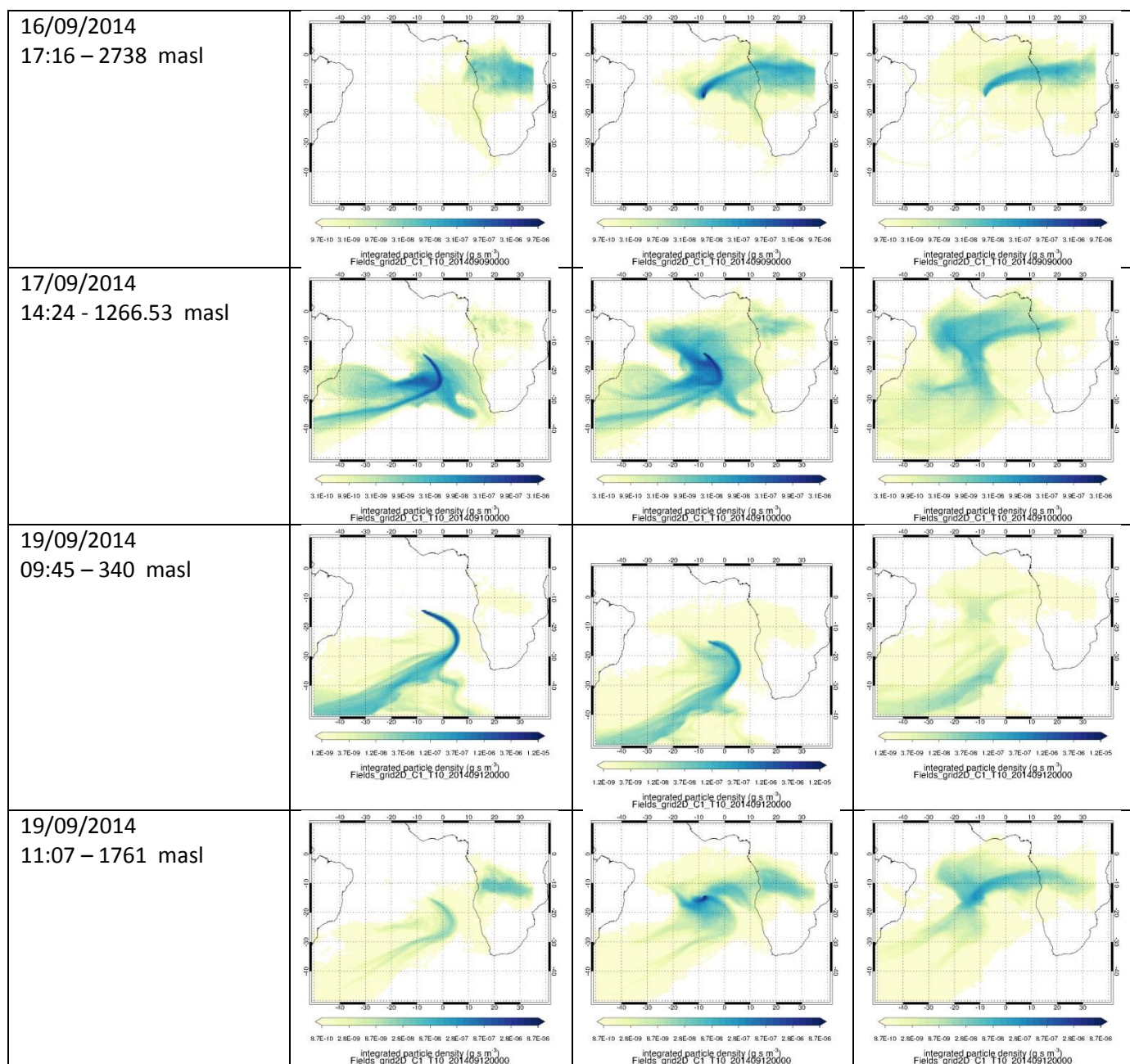
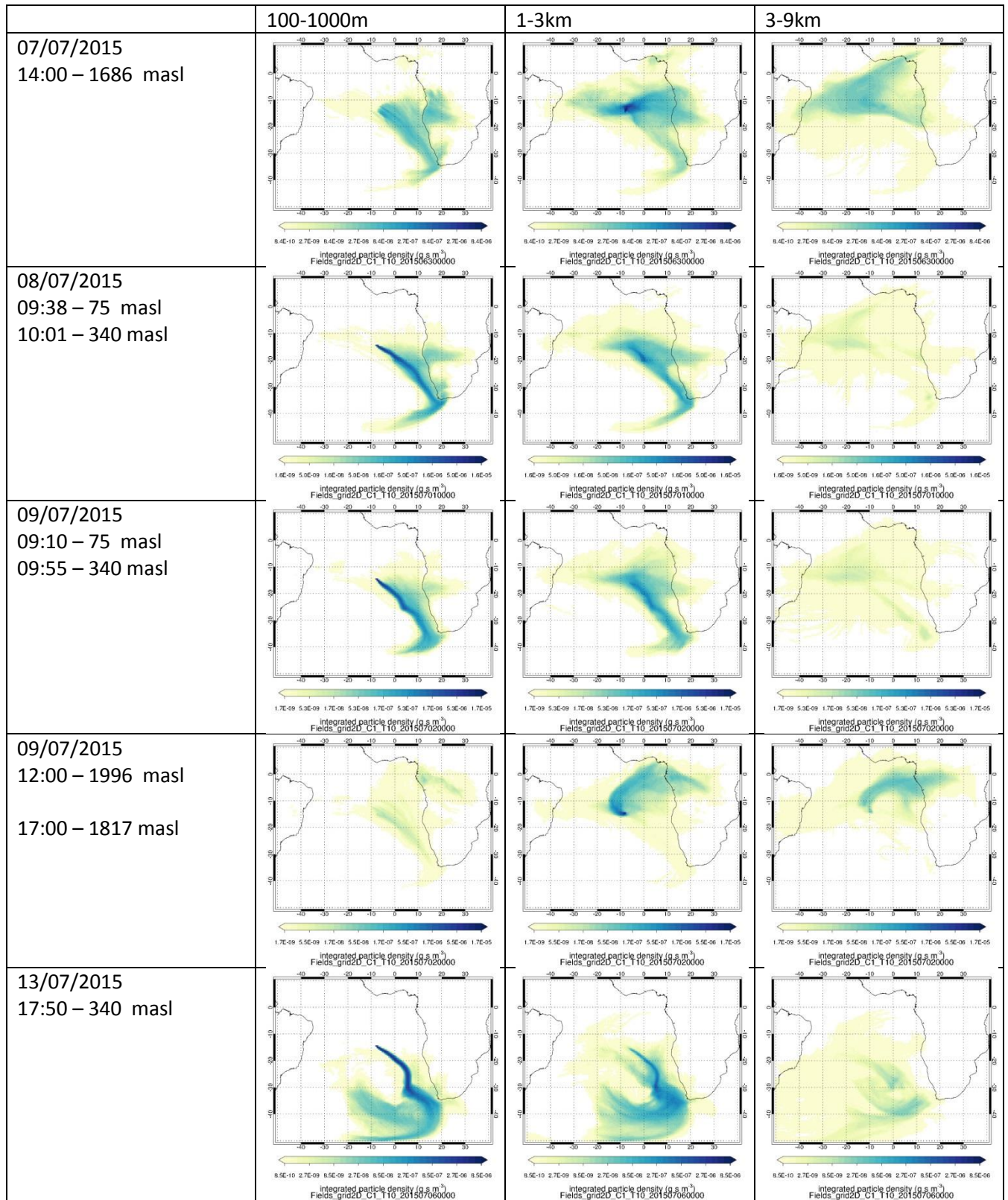


Fig. S7: NAME plots 7 day back for September 2014 samples. The sample details: date, time and height taken, are in the far left column. NAME was run backwards from the sample locations, with particles being released at a rate of 100000 per hour for one hour, from a depth of 100 m centered on the sample height. The other 3 columns show the air masses passing through the height bands 100-1000m, 1-3km and 3-9km in the 7 days prior to the sample.



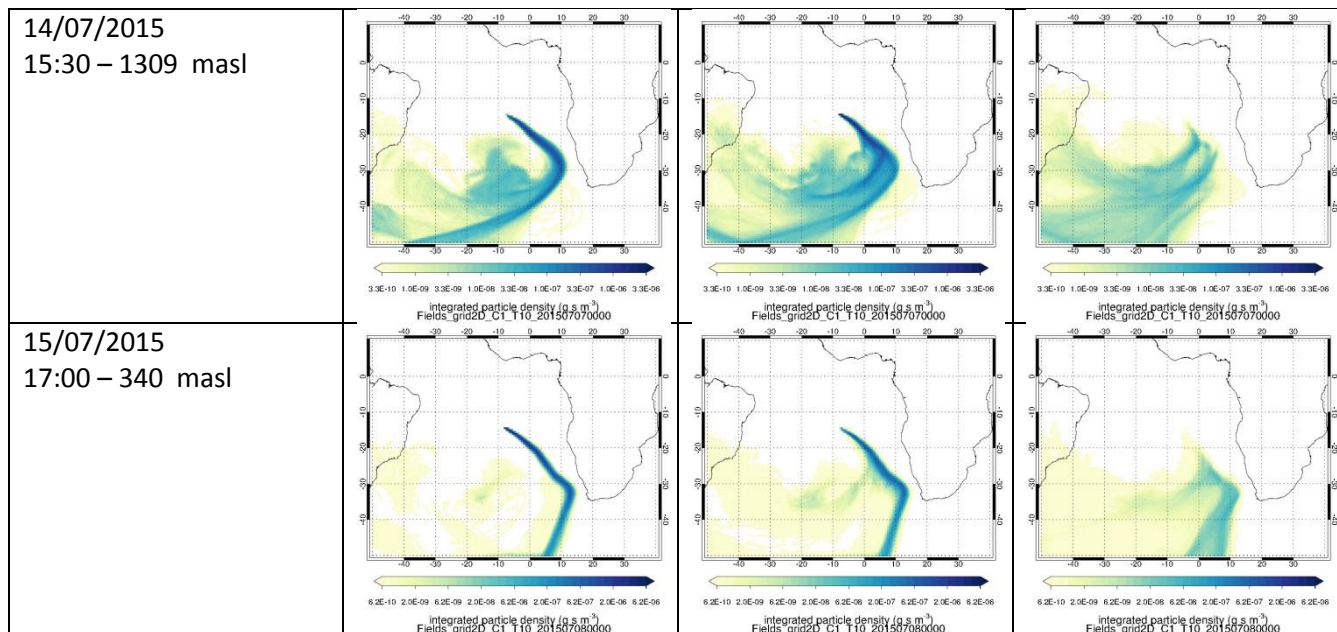


Fig. S8: NAME plots 7 day back for July 2015 samples. The sample details: date, time and height taken, are in the far left column. NAME was run backwards from the sample locations, with particles being released at a rate of 100000 per hour for one hour, from a depth of 100 m centered on the sample height. The other 3 columns show the air masses passing through the height bands 100-1000m, 1-3km and 3-9km in the 7 days prior to the sample.

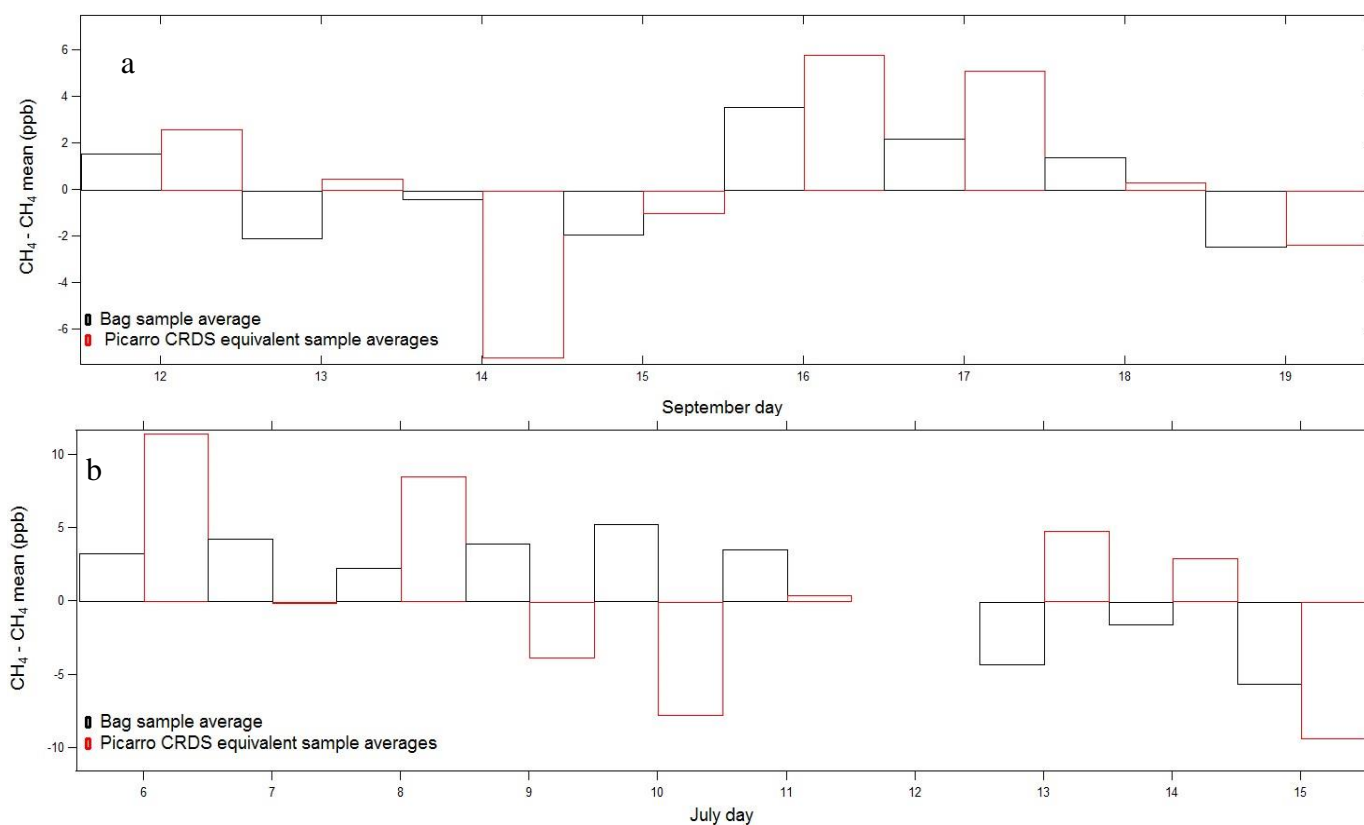


Fig. S9: Bar graphs showing the variation (ppb) in the mean ground level mixing ratios for bag samples (black) and equivalent Picarro CRDS values (red) against the mean ground level mixing ratio a) September campaign b) July campaign. The mean is taken from the bags and CRDS during the campaign period.

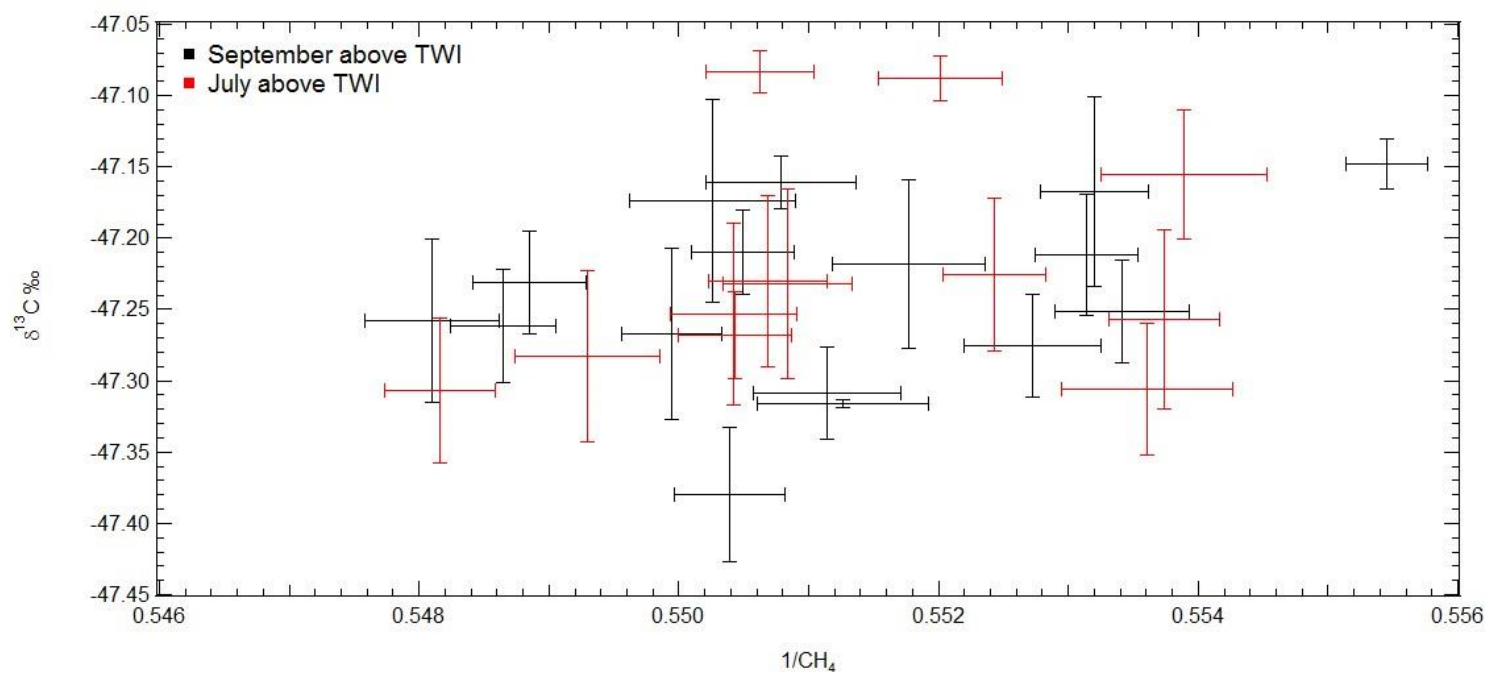


Fig. S10: Plot showing the isotopic values above the TWI taken during both campaigns. The $\delta^{13}\text{C}_{\text{CH}_4}$ is plotted against the inverse of the concentration (Pataki et al., 2003)

Chapter 6

Discussions and Conclusions

This Chapter uses content from Nisbet et al., 2016, Rising atmospheric methane: 2007-2014 growth and isotopic shift which I co-authored. This paper is given as Appendix B.

Global methane began to rise in 2007 after a slow down in growth. This growth has been predominantly driven by sources in the tropics, north and south of the equator in 2008 and the southern tropics in 2010-2011 (Nisbet et al., 2016). This growth is shown in the Ascension Island record discussed in section 6.1. Reasons for the methane growth and isotopic characterisation of the sources are discussed in sections 6.2, 6.3 and 6.4. Future work is discussed in sections 6.5 and 6.6.

6.1 Ascension Island

As discussed in Chapter 5, Ascension Island gives a background South Atlantic CH₄ overview below the trade wind inversion. Continuous monitoring at ground level shows an increased sustained growth in CH₄ mole fraction between 2007 and 2014 and isotopic change beginning in 2009 (Fig 6.1). The CH₄ year on year

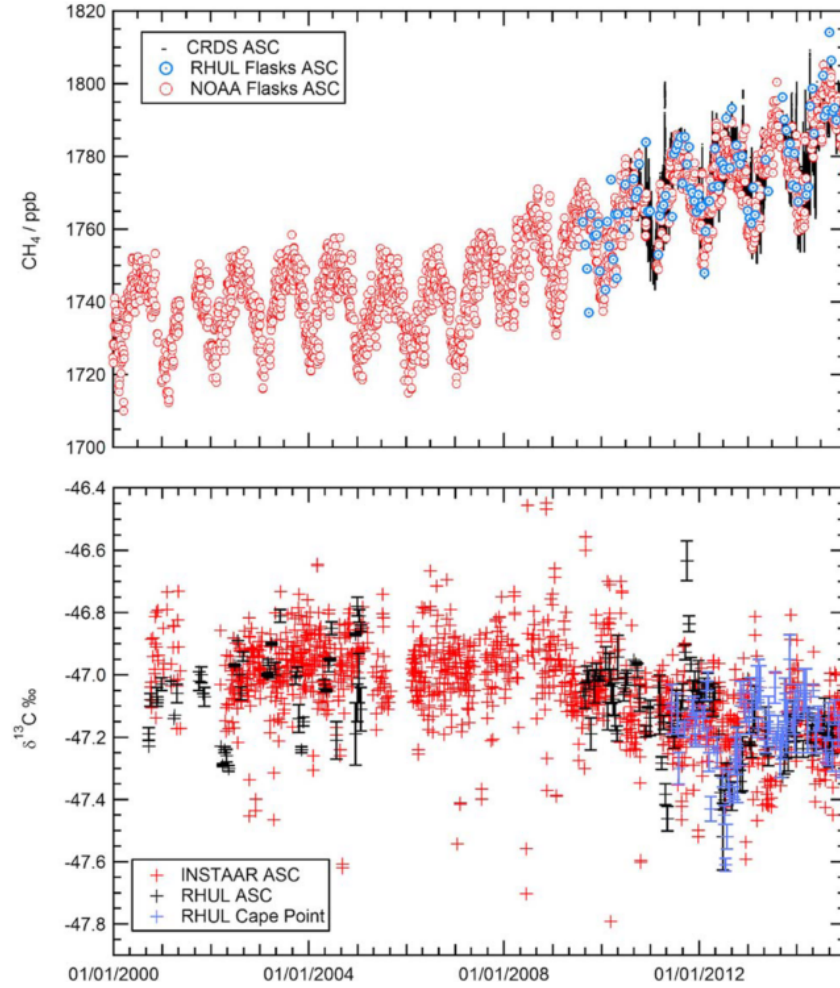


Figure 6.1: The top graph shows methane mole fractions from Ascension Island between 2000-2015. The red circles are NOAA flasks, the blue circles RHUL flasks and the black line is the RHUL continuous Picarro data. The bottom graph shows South Atlantic $\delta^{13}\text{C}$ data between 2000-2015. Red crosses show NOAA-INSTAAR flasks, Black show RHUL Ascension flasks and blue show Cape Point, South Africa. The RHUL $\delta^{13}\text{C}$ data also have error bars (Nisbet et al., 2016).

growth was calculated from RHUL and NOAA measurements, shown in Table: 6.1 using a smoothed spline (in the program HPspline). For the annual growth the deseasonalised monthly averages were subtracted from the previous years monthly average giving the growth rate for each month. The monthly averages were then averaged to give the yearly growth rate and standard deviation of this

applies to the yearly growth rates.

Year	Ascension growth (ppb)
2010 - 2011	7.7 ± 1.5
2011 - 2012	4.4 ± 0.6
2012 - 2013	4.0 ± 0.4
2013 - 2014	6.6 ± 1.2
2014 - 2015	12.3 ± 2.1

Table 6.1: Year on Year Ascension Island CH₄ mole fraction growth using hourly averaged RHUL picarro data, RHUL flasks and NOAA flasks, updated from Nisbet et al., 2014. The program HPspline was used to fit the curve using parameters suggested in Pickers and Manning, 2015.

Air masses in the southern hemisphere pass through the brightly lit, moist, OH-rich region in the mid-troposphere around the inter-tropical convergence zone (ITCZ), where CH₄ destruction is at its peak. The CH₄ background is therefore more enriched in ¹³C than North of the Equator (as shown in Fig 1.4) due to the OH KIE. On Ascension Island in 2009 $\delta^{13}\text{C}$ shifted to depleted values by more than 0.2 ‰ and in 2011 and 2012 the $\delta^{13}\text{C}$ values became even more depleted. By the end of 2014 values become more enriched and values through 2015 stabilised, but were still around 0.2 ‰ more depleted than in 2007-2008. The Cape Point record is also similar to the record shown at Ascension Island. The shift to more depleted $\delta^{13}\text{C}$ was also seen between the two Ascension Island campaigns in September and July; further details are given in Chapter 5.

6.2 Possible reasons for Tropical Growth

In South America, Africa and South East Asia the main biogenic sources of CH₄ are wetlands, however agriculture (rice and ruminants) is also important in South

East Asia. In China, India and Northern Africa agriculture is the main biogenic source (Saunois et al., 2016). Biomass burning is also an important source in the tropics, especially in Africa. Tropical thermogenic sources include coal in South Africa, natural gas fields in South America and gas and coal fields in Asia (Nisbet et al., 2016). Chapter 3, $\delta^{13}\text{C}$ Tropical Source Signatures, helps constrain some of these isotopic sources. Until now there have been very few measurements of the $\delta^{13}\text{C}$ signature of tropical CH_4 sources so this work has significantly expanded the available isotopic data set.

Turner et al. (2017) have suggested that the most likely solution to the renewed methane growth is due to a decline in the OH sink which is partially offset by a decline in CH_4 emissions. Turner et al. (2017) have also argued that the large uncertainty in isotopic signatures makes it difficult to draw conclusions from CH_4 sources, however predominantly north American isotopic source values are discussed. As isotope source signatures differ in the northern and southern hemispheres as well as regionally it is important to take these differences into account when using them. Rigby et al. (2017) also modelled variations in the OH sink and suggested OH changes may have played a role in the CH_4 growth rate contributing to the more depleted $\delta^{13}\text{C}$ signature. A 1% change of OH in the troposphere is equivalent to around 5 Tg CH_4 yr^{-1} (globally about 2 ppb) emission change and a decrease of the OH sink would also mean $\delta^{13}\text{C}$ values would become more depleted (Nisbet et al., 2016). OH abundance is poorly understood and is not sufficient to explain recent change in source signature as large shifts are needed. There are also no obvious reasons why OH may have varied. Globally, OH change is thought to have varied less than 1% during 2006-2008 and other trace gas measurements oxidised by OH suggest that the 2007 CH_4 increase may only partially be explained by OH (Montzka et al., 2011), thus the

OH sink would not be able to account for the magnitude and consistency of the $\delta^{13}\text{C}$ shift (Nisbet et al., 2016). The Cl sink and methanotrophs are only minor sinks, so it is also unlikely these account for the CH_4 increase as very large changes would be needed, but they may have played a role.

Although sinks may have changed, Schaefer et al. (2016) and Nisbet et al. (2016) interpreted the shift towards more depleted $\delta^{13}\text{C}$ in the records to increased biogenic sources. It has been suggested that these biogenic sources may be from either increased agricultural emissions (Schaefer et al., 2016) or increased emissions from wetlands as a result of meteorological changes, such as strong positive rainfall anomalies (Nisbet et al., 2016).

In Chapter 3 wetland $\delta^{13}\text{C}$ values are around $-57.5 \pm 3.9 \text{ ‰}$, rice paddies values are $-58.7 \pm 0.2 \text{ ‰}$, ruminants with a predominantly C3 diet have values of $-67.6 \pm 3.8 \text{ ‰}$ and ruminants with a predominantly C4 diet have values of $-55.4 \pm 2.5 \text{ ‰}$. Between November 2010 and March 2011 there was a strong southern hemisphere wet season with the following years also being on average wetter, with exceptionally high flood levels in the Amazon wetlands of Bolivia in 2014 (Nisbet et al., 2016; Ovando et al., 2015).

Wetlands respond rapidly to these changes and increased in extent. This may account for the increased CH_4 emissions with more depleted $\delta^{13}\text{C}$ (Nisbet et al., 2016). Schaefer et al. (2016) argues that ruminants predominantly eating a C3 diet fit a more depleted $\delta^{13}\text{C}$ trend better than tropical wetlands, however, many tropical ruminants incorporate C4 plants into their diet meaning they have a slightly more enriched signature. The ranges of $\delta^{13}\text{C}$ values for tropical wetlands, rice agriculture and ruminants overlap so it is also difficult to attribute the CH_4 mole fraction and $\delta^{13}\text{C}$ to one of these sources using only $\delta^{13}\text{C}$ isotopes.

6.3 Growth outside the Tropics

CH₄ emissions outside the tropics are also a contributing factor to the recent global growth rate. It has been suggested that fossil fuel emissions are also a significant factor after tropical emissions for the renewed CH₄ increase (Hausmann et al., 2016; Turner et al., 2016; Peng et al., 2016). Ethane is emitted together with methane from thermogenic sources. At Zugspitze, Germany, a high northern latitude site, ethane emissions increased between 2007-2014, after years of weak decline, with methane to ethane ratios corresponding to oil and gas production sources. This contrasts to a continuing decline in southern high latitudes (Hausmann et al., 2016). In China the main methane source has changed from rice paddies in 1980 to coal exploitation in 2010 (Peng et al., 2016).

Turner et al. (2016) have suggested satellites also show U.S. methane emissions increasing by over 30% between 2002 - 2014. This was attributed to the 20% increase of oil and gas production, however the spatial pattern of CH₄ does not clearly correlate with these sources and isotopes do not support this. Bruhwiler et al. (2017) has demonstrated that North American CH₄ emissions have been flat between 2000 - 2012. The trends in Turner et al. (2016) are not indicative of a trend in the emissions due to the background having increased interannual variability in transport, the seasonal sampling bias used and not being able to account for variation in the seasonal cycle.

6.4 Isotope Source Signatures

Chapter 3 improves constraints on tropical $\delta^{13}\text{C}$ source measurements, which provide strong constraints on methane source apportionment. However, in the

tropical regions $\delta^{13}\text{C}$ measurements are unable to distinguish between biogenic sources. More detailed land use maps may help to distinguish between these sources. Many wetland studies are from chambers and are more variable than mixed atmospheric samples. The results show simple atmospheric grab sampling methods are consistent with chamber studies and are more representative values for regional modelling (Fisher et al., 2017). This sampling technique is easy to teach and equipment can be shipped easily so samples can be taken by external partners, reducing the need for an expensive field campaign. Bag samples can then be shipped back to RHUL and be analysed for $\delta^{13}\text{C}$ using CF-GC/IRMS which has high precision ($\pm 0.05\text{‰}$) allowing observation of small isotopic variations, for example, at Ascension Island.

The EDGAR V4.2 inventory (European Commission, 2011) is useful to characterise total national anthropogenic emissions, however, many tropical regions have large natural sources such as wetlands which are not accounted for in the inventory. Other inventories from the literature, for example Kirschke et al. (2013) and Sanderson (1996) are used in conjunction with the EDGAR database to estimate these gaps. It should also be noted that emissions inventories are not always accurate and there are discrepancies between bottom-up estimates (based on statistics multiplied by specific emissions factors) and top-down (atmospheric observations) estimates (Zazzeri et al., 2017).

Inventories do not separate biomass burning or ruminant emissions into C3 or C4 values so it is difficult to split isotopic values when using models. Termite values are often not considered even though they may contribute up to 4% of total CH_4 global fluxes a year (Sanderson, 1996). In Chapter 3 ruminant and biomass burning sources have been split into C3 and C4 emissions, and termite emissions have been added from the literature. This is not ideal as literature

values are not available for all regions and it is possible, due to the age of the studies, these values may be inaccurate. Chapter 3 also assumes ruminant diets in the tropics are grazing-based and does not account for feed-based diets which vary in C3 and C4 ratios.

Considering the above criteria to split C3 and C4 ruminant and biomass burning emissions, and to include termite emissions, an expected average annual isotopic signature was only calculated for Tropical South America and Africa giving values of $-57 \pm 3 \text{ ‰}$ and $-52 \pm 2 \text{ ‰}$, respectively. This is useful to determine if a region contributes strongly to biogenic, thermogenic or pyrogenic sources and increase the confidence in inventories by comparing calculated values to measured regional plumes. To improve on these expected signatures more regional and seasonal tropical values are needed. It is important to fill in emissions and data gaps especially in South East Asia and India where a yearly $\delta^{13}\text{C}$ emissions value could not be calculated. Improvements include using termite emission values in South East Asia and India, updating older studies and using estimates of ruminants on feed rather than assuming all are grazing.

In regional models it is important to use well constrained values. Table 6.2 uses $\delta^{13}\text{C}$ values from different modelling studies and calculates the yearly $\delta^{13}\text{C}$ signatures for Tropical South America and Africa. These calculated values using $\delta^{13}\text{C}$ from the models vary but are all within error of the RHUL $\delta^{13}\text{C}$ calculated yearly average signatures ($-57.03 \pm 3 \text{ ‰}$ and $-51.56 \pm 2 \text{ ‰}$, respectively) which use tropical observed data.

Rigby et al. (2012) classes source signatures into just 4 categories which may be unrealistic. This gives a yearly value of -58.58 ‰ for Tropical South America and has the largest offset from RHUL (-57.03 ‰), being 1.55 ‰ more depleted, for this region. Bousquet et al. (2006), Mikaloff Fletcher et al. (2004) and Monteil

et al. (2011) also give slightly depleted values compared to the RHUL values. This is likely to be due to the simplified microbial value of -61 ‰ in Rigby et al. (2012) and slightly more depleted wetland values in Bousquet et al. (2006), Mikaloff Fletcher et al. (2004) and Monteil et al. (2011). These studies do not account for the large area of tropical wetlands in this region which have more enriched values (RHUL uses -57.5 ‰) or the split between C3 and C4 ruminants.

For the calculated African value Mikaloff Fletcher et al. (2004) have the largest discrepancy, with a value of -52.85 ‰, depleted by 1.29 ‰, compared to the RHUL value of -51.56 ‰. Bousquet et al. (2006) and Monteil et al. (2011) also have slightly depleted values compared to the RHUL value. This is likely from using more depleted wetland values and oversimplified biomass burning values, which do not account for more enriched C4 burns. Mikaloff Fletcher et al. (2004) used a general value of -25 ‰ compared to RHUL with C3 being -31.2 ‰ and C4 being -17 ‰. Rigby et al. (2012) give a slightly more enriched value which may be due to differences in waste and fossil fuel values between the two studies. Although the values are within error of RHUL, offsets occur if a more general $\delta^{13}\text{C}$ value is used.

Source	Tropical America	South Africa	Reference	RHUL	Bousquet et al. (2006)	Mikaloff Fletcher et al. (2004)	Monteil et al. (2011)	Rigby et al. (2012)
	Tg yr ⁻¹	Tg yr ⁻¹		$\delta^{13}\text{C}$ ‰	$\delta^{13}\text{C}$ ‰	$\delta^{13}\text{C}$ ‰	$\delta^{13}\text{C}$ ‰	$\delta^{13}\text{C}$ ‰
<i>Microbial:</i>								-61
Wetlands	58 [39-92]	24 [22-27]	Kirschke et al. (2013)	-57.5 ± 3.9	-58	-58	-59	
Rice	0.71 ± 0.01	1.04 ± 0.04	European Commission (2011)	-58.8 ± 0.2	-63	-63	-63	
Ruminants:					-60	-60	-62	
Ruminants C3	6.58 ± 0.53	2.44 ± 0.10	European Commission (2011); Osborne et al. (2014)	-67.6 ± 3.8				
Ruminants C4	9.87 ± 0.80	9.75 ± 0.42	European Commission (2011); Osborne et al. (2014)	-55.4 ± 2.5				
Manure	0.39 ± 0.03	0.45 ± 0.02	European Commission (2011)	-55.0 ± 1.2	-55	-55	-62	
Termites	7.20 ± 0.55	8.06 ± 0.61	Sanderson (1996)	-61.6 ± 8.0	-70	-70	-57	
<i>Biomass Burning:</i>					-19	-25	-21.8	-24
Biomass Burning C3	2.07 ± 1.39	6.09 ± 2.42	European Commission (2011); Randerson et al. (2005)	-31.2 ± 2.4				
Biomass Burning C4	0.69 ± 0.46	4.98 ± 1.98	European Commission (2011); Randerson et al. (2005)	-17.0 ± 1.2				
Waste	3.68 ± 0.18	5.07 ± 0.26	European Commission (2011)	-55.0 ± 1.2	-55	-55	-55	-50
Fossil Fuel	3.95 ± 0.26	11.53 ± 0.52	European Commission (2011)	-47.8 ± 6.1	-40.4	-40.5	-42	-40
Average Yearly Signature:	Tropical America	South Africa		-57.03 ± 3	-57.79	-57.97	-57.60	-58.58
				-51.56 ± 2	-51.93	-52.85	-51.89	-51.36

Table 6.2: Emission inventories and calculated regional yearly average source signatures for Tropical South America and Africa (methods are in Chapter 3 SI). The table compares yearly signatures calculated from using $\delta^{13}\text{C}$ values from this thesis (RHUL column) and $\delta^{13}\text{C}$ values used in $\delta^{13}\text{C}$ model studies. Errors are not given for $\delta^{13}\text{C}$ in these studies.

In the tropics biogenic wetland and rice emissions and pyrogenic biomass burning are highly seasonal; the intertropical convergence zone (ITCZ) dominates these seasonal changes between wet and dry seasons (Mitsch et al., 2010). In the wet season wetland emissions increase, therefore $\delta^{13}\text{C}$ becomes more depleted compared to the dry season where biomass burning increases and therefore the $\delta^{13}\text{C}$ becomes more enriched. If the seasonal patterns of the ITCZ change or there is a changing climate, these seasonal wet and dry seasons will change and the seasonal dynamics would be affected. Wetlands in monsoonal climates emit more CH_4 than permanent wet humid wetlands in the tropics. More dry seasons would also increase CH_4 release due to more biomass burning (Mitsch et al., 2010). Continuous monitoring of CH_4 in tropical areas, such as the site at Bachok, along with regular Tedlar bag sampling for $\delta^{13}\text{C}$ data, will show the seasonal cycles and bulk isotopic signatures of tropical regions. Future work will also study the seasonal variability in the isotopic signature of wetland sources which is likely to occur as production and transport processes vary between wet and dry seasons.

The use of hydrogen isotopes, D/H (δD), in further tropical studies could improve characterisation of CH_4 sources. Organic carbon sources (C_3 or C_4 plant), methanogenic pathways (acetate fermentation or CO_2 reduction) and methanotrophy may be inferred by using both $\delta^{13}\text{C}$ and δD . Figure 6.2 suggests how these factors are expected to change these isotope ratios. For example marine or saline environments are generally more enriched than freshwater in deuterium, due to carbonate reduction being the main methanogenic pathway (Whiticar, 1999; Hamilton et al., 2014).

Using ^{14}C could also improve source studies as it allows the distinction of CH_4 from fossil sources (for example natural gas or coal mining), which is ^{14}C free due to it having a half-life of 5730 years, to modern sources (for example wetland or rice

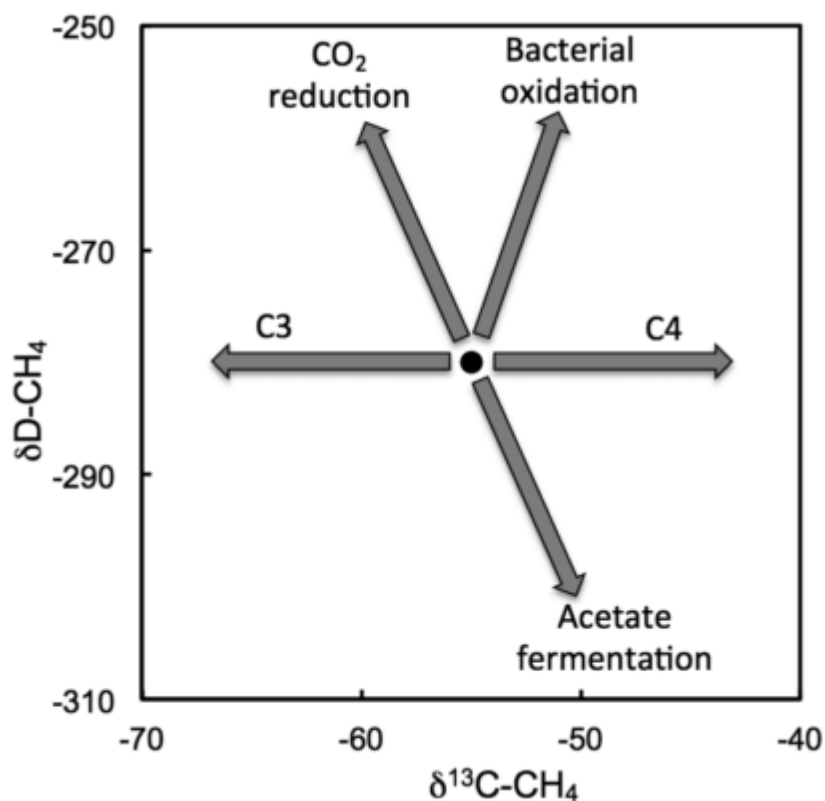


Figure 6.2: Conceptual model of the expected $\delta^{13}\text{C}$ and δH changes with organic carbon sources, methanogenic pathways and bacterial methane oxidation (Hamilton et al., 2014)

paddies)(Quay et al., 1991). There are, however, limited data on ^{14}C of wetland CH_4 sources, especially in the tropics. ^{14}C also gives the residence time of CH_4 from anaerobic sediments (Quay et al., 1991; Nakagawa et al., 2002). Nuclear power facilities release $^{14}\text{CH}_4$ which is poorly quantified meaning using ^{14}C is more difficult in regions where nuclear power stations are present (Lassey et al., 2006).

6.5 Airborne and Mobile Measurements

Airborne measurements are useful for monitoring of multiple air masses, for example chapter 5 using UAS on Ascension Island, or calculating regional fluxes. Ascension Island is an ideal place for UAS measurements up to 2700 masl because it is so remote and isolated. However, other airborne sampling or measurement techniques may be more suited to other areas or in conjunction with the Ascension Island campaigns.

Lightweight CH₄ sensors may be placed on a UAV or UAS to detect changes in mole fractions and are useful for plume mapping, for example from landfills (e.g. Allen et al., 2015) and monitoring inaccessible areas. Current instrumentation is not sufficient to detect the small changes in ambient air as seen on Ascension Island (Khan et al., 2012).

Aircraft measurements may be used to calculate regional net fluxes using a boundary layer mass budget approach (O'Shea et al., 2014) and measure the $\delta^{13}\text{C}$ regional source (Fisher et al., 2017). These measurements would be useful to quantify wetland and biomass burning fluxes in tropical regions and verify the calculated yearly source signatures from Africa and Tropical South America from Chapter 3 and measuring regional sources around Bachok, Malaysia, Chapter 4.

Vertical profile measurements allow for validation of models and tropospheric-stratospheric exchange. AirCore is a technique which drops a long tube with one end open through the atmospheric column. Ambient air is forced into the tube by the positive pressure change. No mixing occurs in the tubing as the molecular diffusion of air is slow. AirCore may be used on multiple platforms such as UAVs (Karion et al., 2010). This could be used alongside the UAS systems on Ascension Island in future campaigns to study mixing between the air masses above and

below the TWI.

Mobile Picarro CRDS measurements installed on a vehicle are also useful for plume mapping and identification of methane sources (Zazzeri et al., 2015). This technique would be useful in Bachok, Malaysia (Chapter 4) to identify biogenic sources around the IOES Bachok marine research station.

6.6 Future locations for tropical measurements

EDGAR V4.2 provides estimates of anthropogenic greenhouse gas emissions on a spatial grid. Figure 6.3 shows the CH₄ EDGAR V 4.2 annual grid map for 2010 (the most recent maps produced). High CH₄ values for 2010 are shown in the red or warmer colours.

Large tropical anthropogenic emissions estimates are highlighted in South America (especially Brazil), across savannah Africa, India, parts of China and Southeast Asia. The NOAA carbon cycle gas measurement sites are shown in purple and highlight the gaps in tropical measurement sites.

Figure 6.4 shows modelled wetland CH₄ emissions trends between 1993 and 2014 from JULES (Joint UK Land Environment Simulator). Long term positive trends, seen in blue, are shown in Southeast Asia, northern Australia, Zambia, Democratic Republic of Congo and seasonally flooded savannas in tropical South America (McNorton et al., 2016) This map shows the high variability of emissions in the tropics and when compared to measurement sites, shown in figure 6.3, measurement gaps are also highlighted.

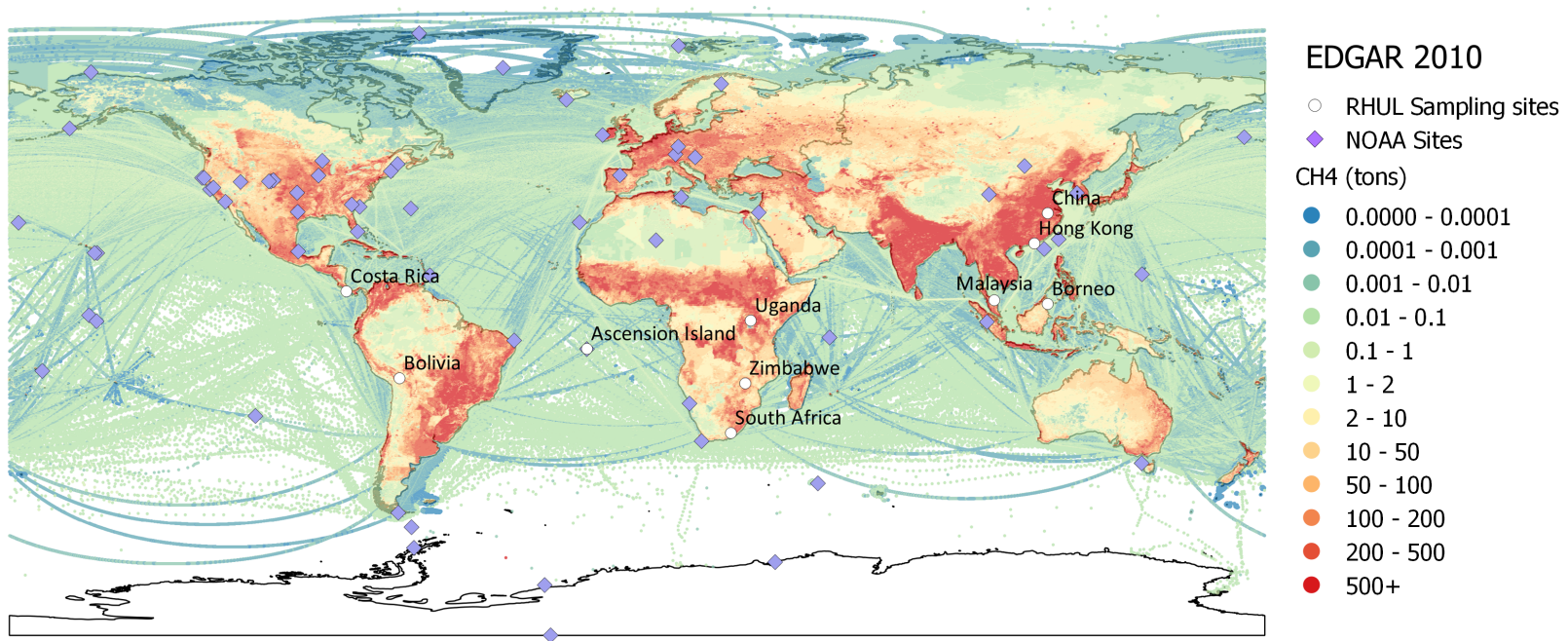


Figure 6.3: EDGAR V4.2 CH₄ emissions (tons) for 2010 (European Commission, 2011) with all active NOAA carbon cycle gas measurement sites (purple diamonds) (from: www.esrl.noaa.gov/gmd/dv/iadv) and RHUL sample locations in this thesis (white circles). Note that $\delta^{13}\text{C}$ for methane is only measured at a small subset of these sites

In the tropics the dominant wetland ecosystems are forested peatlands, swamps and floodplains. It is important to consider these wetland types when studying fluxes, for example, CH_4 fluxes tend to be greater from mineral than organic soils. There are large uncertainties in the distribution of the wetland types which affect CH_4 emissions estimates (Sjögersten et al., 2014). Future measurements should therefore consider a range of wetland types.

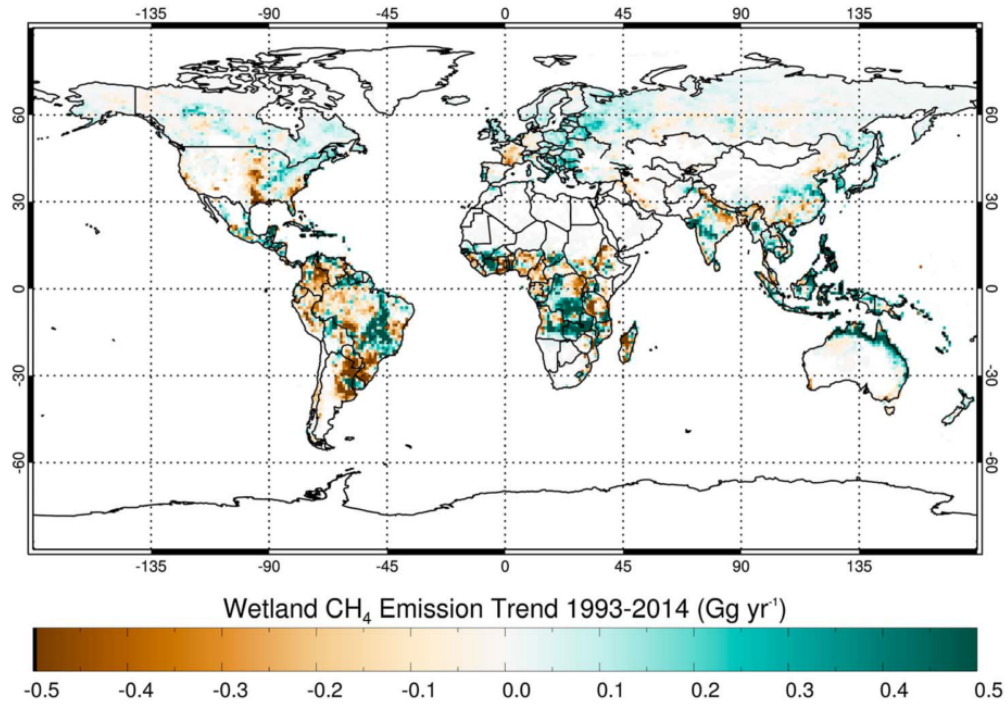


Figure 6.4: Trends in Wetland CH_4 emissions in Gg/yr between 1993 and 2014 from JULES (McNorton et al., 2016).

More continuous CH_4 mole fraction and isotope measurements at sites and sample campaigns, such as obtained done during this thesis (shown as white circles), are needed to cover the tropical gaps and also validate estimates.

6.7 Conclusions

- $\delta^{13}\text{C}$ isotopes provide strong constraints on CH_4 source apportionment although more work is needed to characterise tropical methane source signatures. $\delta^{13}\text{C}$ is unable to distinguish between biogenic sources (wetlands, ruminants, waste etc.) in tropical regions. More detailed regional and seasonal measurements are needed to take into account variations and improve calculated bulk $\delta^{13}\text{C}$ values.
- Monitoring methane isotopes will be important at sites such as IOES Bachok, Malaysia. Isotopic data showed that the CH_4 peaks were not predominantly biomass burning as expected and instead reflected mixing with a biogenic source. The Bachok site has also shown continuous mole fraction measurements are important to monitor CH_4 diurnal cycles. Due to CH_4 mole fraction changes the diurnal cycles allow for Keeling plot analysis and therefore an increased understanding of local sources.
- The Ascension UAS work has shown it is possible to use a comparatively inexpensive method to retrieve air samples from varying heights up to 2700 masl. However, this work has shown it is difficult to separate the $\delta^{13}\text{C}$ isotopes above and below the TWI and pick out varying source signatures.
- In the tropics from 2007 onwards CH_4 mole fraction has increased and $\delta^{13}\text{C}$ shifts become more depleted in ^{13}C . The likely cause is increased biogenic emissions from sources such as natural wetlands, rice or ruminant emis-

sions. Measurements made in this thesis are more representative of source emissions as a whole rather than individual processes, such as those made in chamber measurements. These values may be included in regional models to constrain tropical CH₄ emissions with better source apportionment. Ongoing tropical measurements are being taken as part of the MOYA (Methane Observations and Yearly Assessments) project which will contribute to tropical CH₄ mole fraction and $\delta^{13}\text{C}$ data.

Bibliography

- Akritas, M. G. and Bershad, M. A. (1996), Linear Regression for Astronomical Data with Measurement Errors and Intrinsic Scatter, *The Astrophysical Journal* **470**, 706.
- Allan, W., Manning, M. R., Lassey, K. R., Lowe, D. C. and Gomez, A. J. (2001), Modeling the variation of $\delta^{13}\text{C}$ in atmospheric methane: Phase ellipses and the kinetic isotope effect, *Global Biogeochemical Cycles* **15**(2), 467–481.
- Allan, W., Struthers, H. and Lowe, D. C. (2007), Methane carbon isotope effects caused by atomic chlorine in the marine boundary layer: Global model results compared with Southern Hemisphere measurements, *Journal of Geophysical Research* **112**(D4), D04306.
- Allen, G., Pitt, J., Hollingsworth, P., Mead, I., Kabbabe, K., Roberts, G. and Perciva, C. (2015), *Measuring landfill methane emissions using unmanned aerial systems : field trial and operational guidance*, Environment Agency.
- Aluwong, T., Wuyep, P. and Allam, L. (2013), Livestock-environment interactions: Methane emissions from ruminants, *African Journal of Biotechnology* **10**(8), 1265–1269.
- Archer, D., Eby, M., Brovkin, V., Ridgwell, A., Cao, L., Mikolajewicz, U.,

- Caldeira, K., Matsumoto, K., Munhoven, G., Montenegro, A. and Tokos, K. (2009), Atmospheric Lifetime of Fossil Fuel Carbon Dioxide, *Annual Review of Earth and Planetary Sciences* **37**(1), 117–134.
- Bhullar, G. S., Edwards, P. J. and Olde Venterink, H. (2013), Variation in the plant-mediated methane transport and its importance for methane emission from intact wetland peat mesocosms, *Journal of Plant Ecology* **6**(4), 298–304.
- Bousquet, P., Ciais, P., Miller, J. B., Dlugokencky, E. J., Hauglustaine, D. a., Prigent, C., Van der Werf, G. R., Peylin, P., Brunke, E.-G., Carouge, C., Langenfelds, R. L., Lathière, J., Papa, F., Ramonet, M., Schmidt, M., Steele, L. P., Tyler, S. C. and White, J. (2006), Contribution of anthropogenic and natural sources to atmospheric methane variability, *Nature* **443**(7110), 439–443.
- Bousquet, P., Ringeval, B., Pison, I., Dlugokencky, E. J., Brunke, E. G., Carouge, C., Chevallier, F., Fortems-Cheiney, A., Frankenberg, C., Hauglustaine, D. a., Krummel, P. B., Langenfelds, R. L., Ramonet, M., Schmidt, M., Steele, L. P., Szopa, S., Yver, C., Viovy, N. and Ciais, P. (2011), Source attribution of the changes in atmospheric methane for 2006–2008, *Atmospheric Chemistry and Physics* **11**(8), 3689–3700.
- Brass, M. and Röckmann, T. (2010), Continuous-flow isotope ratio mass spectrometry method for carbon and hydrogen isotope measurements on atmospheric methane, *Atmospheric Measurement Techniques* **3**(6), 1707–1721.
- Bridgham, S. D., Cadillo-Quiroz, H., Keller, J. K. and Zhuang, Q. (2013), Methane emissions from wetlands: biogeochemical, microbial, and modeling

- perspectives from local to global scales, *Global Change Biology* **19**(5), 1325–1346.
- Bruhwyler, L. M., Basu, S., Bergamaschi, P., Bousquet, P., Dlugokencky, E., Houweling, S., Ishizawa, M., Kim, H.-S., Locatelli, R., Maksyutov, S., Montzka, S., Pandey, S., Patra, P. K., Petron, G., Saunio, M., Sweeney, C., Schwietzke, S., Tans, P. and Weatherhead, E. C. (2017), US CH₄ Emissions from Oil and Gas Production: Have Recent Large Increases Been Detected?, *Journal of Geophysical Research: Atmospheres* **122**, 4070–4083.
- Chanton, J. P., Chaser, L., Glasser, P. and Siegel, D. (2005), Carbon and Hydrogen Isotopic Effects in Microbial, Methane from Terrestrial Environments, *in* ‘Stable Isotopes and Biosphere Atmosphere Interactions’, Elsevier, pp. 85–105.
- Chanton, J. P., Rutkowski, C. M., Schwartz, C. C., Ward, D. E. and Borning, L. (2000), Factors influencing the stable carbon isotopic signature of methane from combustion and biomass burning, *Journal of Geophysical Research* **105**(D2), 1867–77.
- Chappellaz, J., Barnola, J. M., Raynaud, D., Korotkevich, Y. S. and Lorius, C. (1990), Ice-core record of atmospheric methane over the past 160,000 years, *Nature* **345**(6271), 127–131.
- Ciais, P., Sabine, C., Bala, G., Bopp, L., Brovkin, V., Canadell, J., Chhabra, A., DeFries, R., Galloway, J., Heimann, M., Jones, C., Le Quéré, C., Myneni, R., Piao, S. and Thornton, P. (2013), *Carbon and Other Biogeochemical Cycles*, Cambridge University Press, Cambridge, United Kingdom and New York, NY, USA, book section 6, pp. 465–570.

- Cicerone, R. J. and Oremland, R. S. (1988), Biogeochemical aspects of atmospheric methane, *Global Biogeochemical Cycles* **2**(4), 299–327.
- Crosson, E. (2008), A cavity ring-down analyzer for measuring atmospheric levels of methane, carbon dioxide, and water vapor, *Applied Physics B* **92**(3), 403–408.
- Crutzen, P. J. and Andreae, M. O. (1990), Biomass burning in the tropics: impact on atmospheric chemistry and biogeochemical cycles., *Science* **250**(4988), 1669–78.
- Dlugokencky, E. J. (2005), Conversion of NOAA atmospheric dry air CH₄ mole fractions to a gravimetrically prepared standard scale, *Journal of Geophysical Research* **110**(18), 1–8.
- Dlugokencky, E. J. (2016), Noaa/esrl (accessed: 28/01/17).
URL: www.esrl.noaa.gov/gmd/ccgg/trends_ch4/
- Dlugokencky, E. J., Bruhwiler, L., White, J. W. C., Emmons, L. K., Novelli, P. C., Montzka, S. a., Masarie, K. a., Lang, P. M., Crotwell, a. M., Miller, J. B. and Gatti, L. V. (2009), Observational constraints on recent increases in the atmospheric CH₄ burden, *Geophysical Research Letters* **36**(18).
- Dlugokencky, E. J., Nisbet, E. G., Fisher, R. and Lowry, D. (2011), Global atmospheric methane: budget, changes and dangers, *Philosophical Transactions of the Royal Society A: Mathematical, Physical and Engineering Sciences* **369**(1943), 2058–2072.
- EPA (2013), Us environmental protection agency, global mitigation of non-co₂ greenhouse gases: 2010-2030.

- Etheridge, D. M., Steele, L. P., Francey, R. J. and Langenfelds, R. L. (1998), Atmospheric methane between 1000 A.D. and present: Evidence of anthropogenic emissions and climatic variability, *Journal of Geophysical Research: Atmospheres* **103**(D13), 15979–15993.
- European Commission, . (2011), Joint research centre/netherlands environmental assessment agency. emission database for global atmospheric research (edgar), release version 4.2.
URL: <http://edgar.jrc.ec.europa.eu>
- FAO (2016), Food and agricultural organisation of the united nations: Faostat emissions database, agriculture, enteric fermentation (accessed: 15/10/16).
URL: <http://faostat3.fao.org/download/G1/GE/E>
- Fisher, R. E., France, J. L., Lowry, D., Lanoisellé, M., Brownlow, R., Pyle, J. A., Cain, M., Warwick, N., Skiba, U. M., Drewer, J., Dinsmore, K. J., Leeson, S. R., Bauguitte, S. J.-B., Wellpott, A., O’Shea, S. J., Allen, G., Gallagher, M. W., Pitt, J., Percival, C. J., Bower, K., George, C., Hayman, G. D., Aalto, T., Lohila, A., Aurela, M., Laurila, T., Crill, P. M., McCalley, C. K. and Nisbet, E. G. (2017), Measurement of the ^{13}C isotopic signature of methane emissions from Northern European wetlands, *Global Biogeochemical Cycles* **31**, 605–623.
- Fisher, R., Lowry, D., Wilkin, O., Sriskantharajah, S. and Nisbet, E. G. (2006), High-precision, automated stable isotope analysis of atmospheric methane and carbon dioxide using continuous-flow isotope-ratio mass spectrometry, *Rapid Communications in Mass Spectrometry* **20**(2), 200–208.
- Green, S. M. (2013), Ebullition of methane from rice paddies: the importance of furthering understanding, *Plant and Soil* **370**(1-2), 31–34.

- Hamilton, S., Sippel, S., Chanton, J. and Melack, J. (2014), Plant-mediated transport and isotopic composition of methane from shallow tropical wetlands, *Inland Waters* **4**(4), 369–376.
- Hartmann, D. J., Klein Tank, A. M. G., Rusticucci, M., Alexander, L. V., Brönnimann, S., Charabi, Y. A. R., Dentener, F. J., Dlugokencky, E. J., Easterling, D. R., Kaplan, A., Soden, B. J., Thorne, P. W., Wild, M. and Zhai, P. (2013), Observations: Atmosphere and Surface, *in* Intergovernmental Panel on Climate Change, ed., ‘Climate Change 2013 - The Physical Science Basis’, Cambridge University Press, Cambridge, pp. 159–254.
- Hausmann, P., Sussmann, R. and Smale, D. (2016), Contribution of oil and natural gas production to renewed increase in atmospheric methane (2007-2014): topdown estimate from ethane and methane column observations, *Atmospheric Chemistry and Physics* **16**(5), 3227–3244.
- Hook, S. E., Wright, A.-D. G. and McBride, B. W. (2010), Methanogens: methane producers of the rumen and mitigation strategies., *Archaea* **2010**.
- Jones, A., Thomson, D., Hort, M. and Devenish, B. (2007), *The U.K. Met Office’s Next-Generation Atmospheric Dispersion Model, NAME III*, Springer US, Boston, MA, pp. 580–589.
- Karion, A., Sweeney, C., Tans, P. and Newberger, T. (2010), AirCore: An Innovative Atmospheric Sampling System, *Journal of Atmospheric and Oceanic Technology* **27**(11), 1839–1853.
- Keeling, C. D. (1960), The Concentration and Isotopic Abundances of Carbon Dioxide in the Atmosphere, *Tellus* **12**(2), 200–203.

- Keppler, F., Hamilton, J. T. G., Braß, M. and Röckmann, T. (2006), Methane emissions from terrestrial plants under aerobic conditions, *Nature* **439**(7073), 187–191.
- Khan, A., Schaefer, D., Tao, L., Miller, D. J., Sun, K., Zondlo, M. A., Harrison, W. A., Roscoe, B. and Lary, D. J. (2012), Low Power Greenhouse Gas Sensors for Unmanned Aerial Vehicles, *Remote Sensing* **4**(12), 1355–1368.
- Kirschke, S., Bousquet, P., Ciais, P., Saunio, M., Canadell, J. G., Dlugokencky, E. J., Bergamaschi, P., Bergmann, D., Blake, D. R., Bruhwiler, L., Cameron-Smith, P., Castaldi, S., Chevallier, F., Feng, L., Fraser, A., Heimann, M., Hodson, E. L., Houweling, S., Josse, B., Fraser, P. J., Krummel, P. B., Lamarque, J.-F., Langenfelds, R. L., Le Quéré, C., Naik, V., O’Doherty, S., Palmer, P. I., Pison, I., Plummer, D., Poulter, B., Prinn, R. G., Rigby, M., Ringeval, B., Santini, M., Schmidt, M., Shindell, D. T., Simpson, I. J., Spahni, R., Steele, L. P., Strode, S. a., Sudo, K., Szopa, S., van der Werf, G. R., Voulgarakis, A., van Weele, M., Weiss, R. F., Williams, J. E. and Zeng, G. (2013), Three decades of global methane sources and sinks, *Nature Geoscience* **6**(10), 813–823.
- Knittel, K. and Boetius, A. (2009), Anaerobic Oxidation of Methane: Progress with an Unknown Process, *Annual Review of Microbiology* **63**(1), 311–334.
- Lai, D. (2009), Methane Dynamics in Northern Peatlands: A Review, *Pedosphere* **19**(4), 409–421.
- Lassey, K. R., Etheridge, D. M., Lowe, D. C., Smith, a. M. and Ferretti, D. F. (2006), Centennial evolution of the atmospheric methane budget: what do the carbon isotopes tell us?, *Atmospheric Chemistry and Physics Discussions* **6**(3), 4995–5038.

- Leng, L., Zhang, T., Kleinman, L. and Zhu, W. (2007), Ordinary least square regression, orthogonal regression, geometric mean regression and their applications in aerosol science, *Journal of Physics: Conference Series* **78**(2007), 012084.
- Lowry, D., Fisher, R., France, J., Lanoisellé, M., Nisbet, E., Brunke, E., Dlugokencky, E., Brough, N. and Jones, A. (2014), Continuous Monitoring Of Greenhouse Gases In The South Atlantic And Southern Ocean: Contributions From The Equianos Network., *GAW Report 213, Geneva* **213**, 109–112.
- Machado, S. L., Carvalho, M. F., Gourc, J.-P., Vilar, O. M. and do Nascimento, J. C. (2009), Methane generation in tropical landfills: Simplified methods and field results, *Waste Management* **29**(1), 153–161.
- McNorton, J., Gloor, E., Wilson, C., Hayman, G. D., Gedney, N., Comyn-Platt, E., Marthews, T., Parker, R. J., Boesch, H. and Chipperfield, M. P. (2016), Role of regional wetland emissions in atmospheric methane variability, *Geophysical Research Letters* **43**(21), 11,433–11,444.
- Mikaloff Fletcher, S. E., Tans, P. P., Bruhwiler, L. M., Miller, J. B. and Heimann, M. (2004), CH₄ sources estimated from atmospheric observations of CH₄ and its ¹³C/ ¹²C isotopic ratios: 2. Inverse modeling of CH₄ fluxes from geographical regions, *Global Biogeochemical Cycles* **18**(4), 1–15.
- Mitsch, W. J., Nahlik, A., Wolski, P., Bernal, B., Zhang, L. and Ramberg, L. (2010), Tropical wetlands: seasonal hydrologic pulsing, carbon sequestration, and methane emissions, *Wetlands Ecology and Management* **18**(5), 573–586.
- Monteil, G., Houweling, S., Dlugokencky, E. J., Maenhout, G., Vaughn, B. H., White, J. W. C. and Rockmann, T. (2011), Interpreting methane variations

- in the past two decades using measurements of CH₄ mixing ratio and isotopic composition, *Atmospheric Chemistry and Physics* **11**(17), 9141–9153.
- Montzka, S. a., Dlugokencky, E. J. and Butler, J. H. (2011), Non-CO₂ greenhouse gases and climate change, *Nature* **476**(7358), 43–50.
- Naik, V., Voulgarakis, A., Fiore, A. M., Horowitz, L. W., Lamarque, J.-F., Lin, M., Prather, M. J., Young, P. J., Bergmann, D., Cameron-Smith, P. J., Cionni, I., Collins, W. J., Dalsøren, S. B., Doherty, R., Eyring, V., Faluvegi, G., Folberth, G. A., Josse, B., Lee, Y. H., MacKenzie, I. A., Nagashima, T., van Noije, T. P. C., Plummer, D. A., Righi, M., Rumbold, S. T., Skeie, R., Shindell, D. T., Stevenson, D. S., Strode, S., Sudo, K., Szopa, S. and Zeng, G. (2013), Preindustrial to present-day changes in tropospheric hydroxyl radical and methane lifetime from the Atmospheric Chemistry and Climate Model Intercomparison Project (ACCMIP), *Atmospheric Chemistry and Physics* **13**(10), 5277–5298.
- Nakagawa, F., Yoshida, N., Sugimoto, A., Wada, E., Yoshioka, T., Ueda, S. and Vijarnsorn, P. (2002), No Title, *Biogeochemistry* **61**(1), 1–19.
- Nisbet, E. G., Dlugokencky, E. J. and Bousquet, P. (2014), Methane on the Rise Again, *Science* **343**(6170), 493–495.
- Nisbet, E. G., Dlugokencky, E. J., Manning, M. R., Lowry, D., Fisher, R. E., France, J. L., Michel, S. E., Miller, J. B., White, J. W. C., Vaughn, B., Bousquet, P., Pyle, J. A., Warwick, N. J., Cain, M., Brownlow, R., Zazzeri, G., Lanoisellé, M., Manning, A. C., Gloor, E., Worthy, D. E. J., Brunke, E. G., Labuschagne, C., Wolff, E. W. and Ganesan, A. L. (2016), Rising atmospheric methane: 2007-2014 growth and isotopic shift, *Global Biogeochemical Cycles* **30**(9), 1356–1370.

- Nisbet, E. and Weiss, R. (2010), Top-Down Versus Bottom-Up, *Science* **328**(5983), 1241–1243.
- Nisbet, R. E. R., Fisher, R., Nimmo, R. H., Bendall, D. S., Crill, P. M., Gallego-Sala, A. V., Hornibrook, E. R. C., López-Juez, E., Lowry, D., Nisbet, P. B. R., Shuckburgh, E. F., Sriskantharajah, S., Howe, C. J. and Nisbet, E. G. (2009), Emission of methane from plants, *Proceedings of the Royal Society of London B: Biological Sciences* **276**(1660), 1347–1354.
- Nowakowski, M., Wojtas, J., Bielecki, Z. and Mikołajczyk, J. (2009), Cavity Enhanced Absorption Spectroscopy Sensor, *Acta Physica Polonica A* **116**(3), 363–367.
- Osborne, C. P., Salomaa, A., Kluyver, T. A., Visser, V., Kellogg, E. A., Morrone, O., Vorontsova, M. S., Clayton, W. D. and Simpson, D. A. (2014), A global database of C 4 photosynthesis in grasses, *New Phytologist* **204**(3), 441–446.
- O’Shea, S. J., Allen, G., Gallagher, M. W., Bower, K., Illingworth, S. M., Muller, J. B. A., Jones, B. T., Percival, C. J., Bauguitte, S. J.-B., Cain, M., Warwick, N., Quiquet, A., Skiba, U., Drewer, J., Dinsmore, K., Nisbet, E. G., Lowry, D., Fisher, R. E., France, J. L., Aurela, M., Lohila, A., Hayman, G., George, C., Clark, D. B., Manning, A. J., Friend, A. D. and Pyle, J. (2014), Methane and carbon dioxide fluxes and their regional scalability for the European Arctic wetlands during the MAMM project in summer 2012, *Atmospheric Chemistry and Physics* **14**(23), 13159–13174.
- Ovando, A., Tomasella, J., Rodriguez, D., Martinez, J., Siqueira-Junior, J., Pinto, G., Passy, P., Vauchel, P., Noriega, L. and von Randow, C. (2015), Extreme

- flood events in the Bolivian Amazon wetlands, *Journal of Hydrology: Regional Studies* **5**(2016), 293–308.
- Pangala, S. R., Hornibrook, E. R., Gowing, D. J. and Gauci, V. (2015), The contribution of trees to ecosystem methane emissions in a temperate forested wetland, *Global Change Biology* **21**(7), 2642–2654.
- Pangala, S. R., Moore, S., Hornibrook, E. R. C. and Gauci, V. (2013), Trees are major conduits for methane egress from tropical forested wetlands, *New Phytologist* **197**(2), 524–531.
- Pataki, D. E., Ehleringer, J. R., Flanagan, L. B., Yakir, D., Bowling, D. R., Still, C. J., Buchmann, N., Kaplan, J. O. and Berry, J. a. (2003), The application and interpretation of Keeling plots in terrestrial carbon cycle research, *Global Biogeochemical Cycles* **17**(1).
- Peng, S., Piao, S., Bousquet, P., Ciais, P., Li, B., Lin, X., Tao, S., Wang, Z., Zhang, Y. and Zhou, F. (2016), Inventory of anthropogenic methane emissions in mainland China from 1980 to 2010, *Atmospheric Chemistry and Physics* **16**(22), 14545–14562.
- Pickers, P. A. and Manning, A. C. (2015), Investigating bias in the application of curve fitting programs to atmospheric time series, *Atmospheric Measurement Techniques* **8**(3), 1469–1489.
- Platt, U., Allan, W. and Lowe, D. (2004), Hemispheric average Cl atom concentration from $^{13}\text{C}/^{12}\text{C}$ ratios in atmospheric methane, *Atmospheric Chemistry and Physics* **4**(9/10), 2393–2399.

- Prather, M. J., Holmes, C. D. and Hsu, J. (2012), Reactive greenhouse gas scenarios: Systematic exploration of uncertainties and the role of atmospheric chemistry, *Geophysical Research Letters* **39**(9).
- Quay, P. D., King, S. L., Stutsman, J., Wilbur, D. O., Steele, L. P., Fung, I., Gammon, R. H., Brown, T. A., Farwell, G. W., Grootes, P. M. and Schmidt, F. H. (1991), Carbon isotopic composition of atmospheric CH₄: Fossil and biomass burning source strengths, *Global Biogeochemical Cycles* **5**(1), 25–47.
- Randerson, J. T., van der Werf, G. R., Collatz, G. J., Giglio, L., Still, C. J., Kasibhatla, P., Miller, J. B., White, J. W. C., DeFries, R. S. and Kasischke, E. S. (2005), Fire emissions from C₃ and C₄ vegetation and their influence on inter-annual variability of atmospheric CO₂ and $\delta^{13}\text{C}$ CO₂, *Global Biogeochemical Cycles* **19**(2), 1–13.
- Reeburgh, W. S. (2003), Global methane biogeochemistry, *Treatise on Geochemistry* **4**, 347.
- Rigby, M., Manning, A. J. and Prinn, R. G. (2012), The value of high-frequency, high-precision methane isotopologue measurements for source and sink estimation, *Journal of Geophysical Research: Atmospheres* **117**(D12).
- Rigby, M., Montzka, S. A., Prinn, R. G., White, J. W. C., Young, D., O’Doherty, S., Lunt, M. F., Ganesan, A. L., Manning, A. J., Simmonds, P. G., Salameh, P. K., Harth, C. M., Mühle, J., Weiss, R. F., Fraser, P. J., Steele, L. P., Krummel, P. B., McCulloch, A. and Park, S. (2017), Role of atmospheric oxidation in recent methane growth, *Proceedings of the National Academy of Sciences* pp. 5373–5377.

- Ringeval, B., de Noblet-Ducoudré, N., Ciais, P., Bousquet, P., Prigent, C., Papa, F. and Rossow, W. B. (2010), An attempt to quantify the impact of changes in wetland extent on methane emissions on the seasonal and interannual time scales, *Global Biogeochemical Cycles* **24**(2).
- Rolph, G. D. (2017), Real-time Environmental Applications and Display sYstem (READY).
- URL:** <http://ready.arl.noaa.gov>
- Sanderson, M. G. (1996), Biomass of termites and their emissions of methane and carbon dioxide: a global database, *Global Biogeochemical Cycles* **10**, 543–557.
- Saunois, M., Bousquet, P., Poulter, B., Peregon, A., Ciais, P., Canadell, J. G., Dlugokencky, E. J., Etiope, G., Bastviken, D., Houweling, S., Janssens-Maenhout, G., Tubiello, F. N., Castaldi, S., Jackson, R. B., Alexe, M., Arora, V. K., Beerling, D. J., Bergamaschi, P., Blake, D. R., Brailsford, G., Brovkin, V., Bruhwiler, L., Crevoisier, C., Crill, P., Curry, C., Frankenberg, C., Gedney, N., Höglund-Isaksson, L., Ishizawa, M., Ito, A., Joos, F., Kim, H.-S., Kleinen, T., Krummel, P., Lamarque, J.-F., Langenfelds, R., Locatelli, R., Machida, T., Maksyutov, S., McDonald, K. C., Marshall, J., Melton, J. R., Morino, I., O'Doherty, S., Parmentier, F.-J. W., Patra, P. K., Peng, C., Peng, S., Peters, G. P., Pison, I., Prigent, C., Prinn, R., Ramonet, M., Riley, W. J., Saito, M., Schroeder, R., Simpson, I. J., Spahni, R., Steele, P., Takizawa, A., Thornton, B. F., Tian, H., Tohjima, Y., Viovy, N., Voulgarakis, A., van Weele, M., van der Werf, G., Weiss, R., Wiedinmyer, C., Wilton, D. J., Wiltshire, A., Worthy, D., Wunch, D. B., Xu, X., Yoshida, Y., Zhang, B., Zhang, Z. and Zhu, Q. (2016), The Global Methane Budget: 2000-2012, *Earth System Science Data* **8**(June), 1–79.

- Schaefer, H., Fletcher, S. E. M., Veidt, C., Lassey, K. R., Brailsford, G. W., Bromley, T. M., Dlugokencky, E. J., Michel, S. E., Miller, J. B., Levin, I., Lowe, D. C., Martin, R. J., Vaughn, B. H. and White, J. W. C. (2016), A 21st-century shift from fossil-fuel to biogenic methane emissions indicated by $^{13}\text{CH}_4$, *Science* **352**(6281), 80–84.
- Seinfeld, J. H. and Pandis, S. N. (2006), *Atmospheric Chemistry and Physics: From Air Pollution to Climate Change*, John Wiley & sons, Hoboken, New Jersey.
- Sjögersten, S., Black, C. R., Evers, S., Hoyos-santillan, J., Wright, E. L. and Turner, B. L. (2014), Tropical wetlands: A missing link in the global carbon cycle?, *Global Biogeochemical Cycles* **28**, 1371–1386.
- Stein, A. F., Draxler, R. R., Rolph, G. D., Stunder, B. J. B., Cohen, M. D. and Ngan, F. (2015), NOAA’s HYSPLIT Atmospheric Transport and Dispersion Modeling System, *Bulletin of the American Meteorological Society* **96**(12), 2059–2077.
- Thorpe, A. (2009), Enteric fermentation and ruminant eructation: the role (and control?) of methane in the climate change debate, *Climatic Change* **93**(3-4), 407–431.
- Tokida, T., Cheng, W., Adachi, M., Matsunami, T., Nakamura, H., Okada, M. and Hasegawa, T. (2013), The contribution of entrapped gas bubbles to the soil methane pool and their role in methane emission from rice paddy soil in free-air $[\text{CO}_2]$ enrichment and soil warming experiments, *Plant and Soil* **364**(1-2), 131–143.

- Turner, A. J., Frankenberg, C., Wennberg, P. O. and Jacob, D. J. (2017), Ambiguity in the causes for decadal trends in atmospheric methane and hydroxyl, *Proceedings of the National Academy of Sciences* **114**, 5367–5372.
- Turner, A. J., Jacob, D. J., Benmergui, J., Wofsy, S. C., Maasakkers, J. D., Butz, A., Hasekamp, O. and Biraud, S. C. (2016), A large increase in U.S. methane emissions over the past decade inferred from satellite data and surface observations, *Geophysical Research Letters* **43**(5), 2218–2224.
- Voulgarakis, A., Naik, V., Lamarque, J.-F., Shindell, D. T., Young, P. J., Prather, M. J., Wild, O., Field, R. D., Bergmann, D., Cameron-Smith, P., Cionni, I., Collins, W. J., Dalsøren, S. B., Doherty, R. M., Eyring, V., Faluvegi, G., Folberth, G. A., Horowitz, L. W., Josse, B., MacKenzie, I. A., Nagashima, T., Plummer, D. A., Righi, M., Rumbold, S. T., Stevenson, D. S., Strode, S. A., Sudo, K., Szopa, S. and Zeng, G. (2013), Analysis of present day and future OH and methane lifetime in the ACCMIP simulations, *Atmospheric Chemistry and Physics* **13**(5), 2563–2587.
- Whiticar, M. (1999), Carbon and hydrogen isotope systematics of bacterial formation and oxidation of methane, *Chemical Geology* **161**(1–3), 693–709.
- Whiticar, M. and Schaefer, H. (2007), Constraining past global tropospheric methane budgets with carbon and hydrogen isotope ratios in ice, *Philosophical Transactions of the Royal Society A: Mathematical, Physical and Engineering Sciences* **365**(1856), 1793–1828.
- WMO (2016), The State of Greenhouse Gases in the Atmosphere Based on Global Observations through 2015.
- URL:** http://library.wmo.int/opac/doc_num.php?explnum_id=3084

Zazzeri, G., Lowry, D., Fisher, R., France, J., Lanoisellé, M., Grimmond, C. and Nisbet, E. (2017), Evaluating methane inventories by isotopic analysis in the London region, *submitted* .

Zazzeri, G., Lowry, D., Fisher, R., France, J., Lanoisellé, M. and Nisbet, E. (2015), Plume mapping and isotopic characterisation of anthropogenic methane sources, *Atmospheric Environment* **110**, 151–162.

Appendix A

Atmospheric Sampling on Ascension Island Using Multirotor UAVs

This paper has been submitted for publication in the journal Sensors and is presented in the paper format. Contributions to this work are listed at the end of the paper. R. Brownlow contributed to the RHUL part of this work, including analysing and interpreting the samples.

Article

Atmospheric Sampling on Ascension Island Using Multirotor UAVs

Colin Greatwood ¹, Thomas Richardson ^{1*}, Jim Freer ^{2 5}, Rick M. Thomas ³, A. Rob MacKenzie ³, Rebecca Brownlow ⁴, David Lowry ⁴, Rebecca E. Fisher ⁴ and Euan G. Nisbet ⁴

¹ Department of Aerospace Engineering, University of Bristol, Bristol, UK, BS8 1TR; colin.greatwood@bristol.ac.uk, thomas.richardson@bristol.ac.uk

² School of Geographical Sciences, University of Bristol, Bristol, UK, BS8 1SS; jim.freer@bristol.ac.uk

³ School of Geography, Earth & Environmental Sciences, University of Birmingham, Birmingham, UK, B15 2TT; r.thomas@bham.ac.uk

⁴ Royal Holloway, University of London, Egham, TW20 0EX; e.nisbet@es.rhul.ac.uk

⁵ Cabot Institute, University of Bristol, Bristol, UK, BS8 1SS

* Correspondence: thomas.richardson@bristol.ac.uk; Tel.: +44-117-33-15532

Academic Editor: name

Version April 7, 2017 submitted to Sensors; Typeset by L^AT_EX using class file mdpi.cls

Abstract: As part of a NERC funded project investigating the southern methane anomaly a team drawn from the Universities of Bristol, Birmingham and Royal Holloway flew small unmanned multirotors from Ascension Island for the purposes of atmospheric sampling. The objective of these flights was to collect air samples from below, within and above a persistent atmospheric feature, the Trade Wind Inversion, in order to characterise methane concentrations and their isotopic composition. These parameters allow the methane in the different air masses to be tied in to different source locations which can be further analysed using back trajectory atmospheric computer modelling. This paper describes the campaigns as a whole including design of the bespoke eight rotor aircraft and the operational requirements that were needed in order to collect targeted multiple air samples up to 2.5km above ground level in under 20 minutes of flight time. Key features of the system described include real time feedback of temperature and humidity as well as system health data. This enabled detailed targeting of the air sampling design to be realised and planned during the flight mission on the downward leg, a capability that is invaluable in the presence of uncertainty in the pre-flight meteorological data. Environmental considerations are also outlined together with the flight plans that were created in order to rapidly fly vertical transects of the atmosphere whilst encountering changing wind conditions. Two sampling campaigns were carried out in September 2014 and July 2015 with over one hundred high altitude sampling missions. Lessons learned are given throughout, including those associated with operating in the testing environment encountered on Ascension Island.

Keywords: Ascension Island; Atmospheric Sampling; Methane; UAV; SUAS; Multirotor; BVLOS

1. Introduction

This study reports the successful development of an important new sampling technique for atmospheric methane in the mid-troposphere. Methane is a major greenhouse gas, which is rising rapidly, particularly in the Tropics [1,2]. The reasons for the rise remain unclear, but tropical wetlands may be a major contributor [3]. These wetlands, many of which are in the Congo and Amazon basins, are relatively inaccessible to integrating studies of emissions: field access is difficult and in some regions of Africa aircraft surveys are both challenging and not favourably viewed by local security

forces. Furthermore such integration of the more global atmospheric signal is problematic where sampling might occur near to a range of source areas and convection processes.

Therefore to obtain a more representative global scale signal, sampling is preferred in zones that are downwind of mixed regional emissions that can then be benchmarked against local background conditions not attributed to the sources being characterised. One such unique place for such a sampling laboratory is Ascension Island in the South Atlantic. In order to sample the atmosphere downwind, a very promising research sampling platform based on a Small Unmanned Air System (SUAS) has a number of benefits. The challenge is to realise safe, repeatable and reliable operations to a significant altitude that is Beyond Visual Line Of Sight (BVLOS). This paper describes the successful demonstration of the use of SUAS to sample equatorial air up to almost 3000 m Above Sea Level (ASL) on Ascension Island, detailing the SUAS used, key operational requirements and lessons learned throughout the build-up and during the field campaigns. Using SUAS, greenhouse gas measurement on Ascension can in principle access both air at ground level from a very wide swathe of the southern oceans, and also sample air from above the Trade Wind Inversion, thereby addressing emissions from a significant part of the global tropical land masses.

SUAS and UAVs are increasingly being developed and deployed for a range of environmental applications [4–9]. In particular significant traction is being realised in the areas of remote sensing [10,11], mapping 2D/3D structures [12–14] and atmospheric sampling [15–25] using a range of emerging sensor technologies [26–29]. However most applications to date that have been used for atmospheric sampling have been at lower altitudes in the 500 m - 1000 m range [15,19] or involve longer range fixed wing platforms that often require considerable resources to deploy [30–32]. This paper critically evaluates the development and deployment of a multirotor-based system to investigate the feasibility of collecting mid-tropospheric air samples from above the Trade Wind Inversion (TWI) layer on Ascension Island for the purposes of identifying methane mole fractions and isotopic composition. The objectives were to capture air samples from below, within and above the inversion layer above Ascension Island in the mid Atlantic. The minimum altitude requirement was to be sufficiently above the TWI inversion layer, which changes altitude seasonally and has some daily fluctuations. This would ensure that the air captured was free of boundary layer air from below the TWI that may have mixed upward; above that minimum altitude. Therefore the higher the sampling altitude achieved, the more confident that we can determine the mixed air back-trajectory [33,34] 'reach' of the method, potentially sampling wide source regions in Africa in the right synoptic conditions.

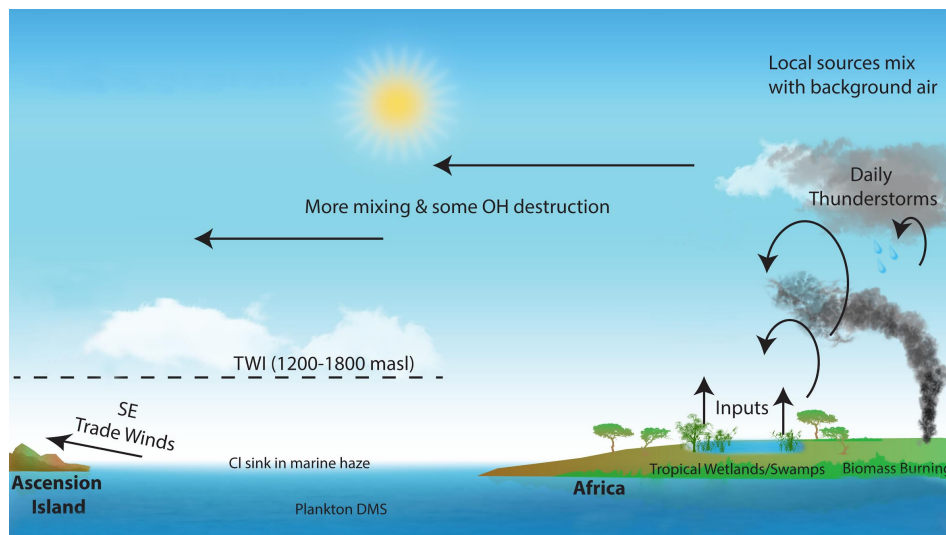


Figure 1. Ascension Atmospheric Sources

2. Campaign Field Site

Ascension Island, situated in the mid-Atlantic just south of the equator (8° South) Figure 2, approximately 1500 km from Africa, is ideally located. At sea level, the SE Trade Winds are in the South Atlantic marine boundary layer. The Trade Winds themselves are almost invariant, derived from the deep South Atlantic and with little contact with Africa. Above the TWI at about 1200 m - 2000 m above sea level (depending on seasonal meteorology and diurnal cycle), the air masses are very different, of equatorial origin, see Figure 1. Dominantly, they have been last in contact with the ground in tropical Africa, but at times from South America. In detail, depending on season, air above the TWI is sourced mainly from tropical and southern Africa with some inputs of air also from southern tropical South America. African and South American methane sources are major contributors to the global methane budget [3,35], but although local campaign studies have been made, these emissions are not well known in bulk. Understanding the changing greenhouse gas burden of the atmosphere demands sustained long-term measurement. Ascension is ideal for this, both in location and in security of access.



Figure 2. Ascension Island location in the mid-Atlantic

The island hosts one of the very few equatorial high precision measurement facilities for CO₂ and CH₄, worldwide [see: 3]. The cavity ring-down greenhouse gas analyser and calibration suite are installed at the UK Met Office base at the Airhead on Ascension, and in normal operation continuously measure CO₂ and CH₄ in the ambient marine boundary air of the Trade Wind. However, the highest point on Ascension is the top of Green Mountain, which is 859 m above sea level and is therefore not high enough to sample air above the TWI. Thus the purpose of this SUAS project, by demonstrating the usefulness of the instrument in measuring air samples from above the TWI, was to show that Ascension potentially becomes a *virtual mountain* with access to air from sea level to nearly 3000 m: it can become the UK equivalent of the US Hawaiian observatory on Mauna Loa, at 3397 m above the Pacific if an effective SUAS sampling platform is fully demonstrated. In addition to being an ideal location for the sample flights from a science perspective; the remote location, military air base and size of the island means it is possible to arrange for segregated airspace. This is a key requirement for allowing current SUAS to operate Beyond Line Of Sight (BLOS).

3. Rationale for the SUAS Platform

Key Targets of the field campaign and the proof of concept system can be identified as:

1. To be able to operate on Ascension Island, with the required associated logistics and support.
2. To be able to operate in a tropical equatorial environment, in close proximity to the sea, at high altitude (for SUAS), and with wind speeds averaging 8 ms^{-1} at ground level.
3. To be able to sample repeatedly at a minimum altitude 100 m or more above the inversion layer, identified on Ascension as varying seasonally between 1200 m and 2000 m ASL through the year.
4. To be able to identify the lower and upper boundaries of the inversion during flight in order to be able to target samples within, above and below.
5. To be able to remotely trigger the air sample collection.
6. To be able to fly multiple times per day, nominally six samples per day at specified altitudes in a safe and reliable manner.

The SUAS approach presented here was chosen because of its inexpensive flexibility. In previous work by the RHUL group, air sampling has been carried out at altitude by using the UK FAAM aircraft facility to fly air sampling equipment at the required altitudes. Sampling with full size aircraft enables greater flexibility than land based measurements offer due to the ability to climb to required altitudes, but incurs very high costs, especially in remote locations. Moreover, the FAAM aircraft barely has the range to reach Ascension with a full load of instruments. The frequency at which samples may be collected would also be very low. Whilst Ascension Island hosts the 3000 m runway of Wideawake Airfield, most flights are large aircraft en route to the Falklands, and not suitable for sustained sampling. No commercial light aircraft or helicopters are based on the island that could be used for the air sampling campaign. In contrast, SUAS have the potential to offer fast turn-around times, remote deployment with small teams and inexpensive sampling [36].

A number of different aerial solutions to the atmospheric sampling problem were considered, including kites, helikites and fixed wing SUAS, however a combination of flexibility, low cost and potential ease of operation led to the choice of a small electric unmanned multirotors. Although other options could have been made to work, the electric multirotor could fly directly to the altitude required, sample and return to base, pausing only for the sample collection at altitude. Key advantages of the multirotor were identified as:

- Potentially low cost.
- Flights could be carried out in a matter of minutes, thereby accounting for rapid changes in conditions, and allowing for multiple samples at specific times throughout the day.
- Flight profiles can be near vertical, allowing for easy airspace integration and de-confliction.
- Transport and ground support for the vehicles is relatively easy to deploy.
- Maintenance has minimal complexity due to a modular design.
- The design allows for flexibility in the payload integration.

There are, however, key challenges to operating a small electric SUAS in this way. These include the requirement to fly what is defined as BVLOS (Beyond Visual Line Of Sight); the requirement to fly through saturated air to allow sampling above the lower cloud layers; the requirement to climb and descend at relatively rapid rates of 5 ms^{-1} continuously; the requirement to continuously monitor temperature and humidity to allow clear identification of the temperature inversion and the requirement to operate in relatively high wind speeds. Throughout this paper however, it is shown that these challenges can be overcome and in the right situations and conditions a SUAS multirotor is an excellent vehicle for sensing applications to over 3000 m. Two sampling campaigns were carried out in September 2014 and July 2015 with over one hundred high altitude sampling missions. Lessons learned are given throughout, including those associated with operating in the harsh environment encountered on Ascension Island.

134 4. System Description

135 The aircraft used for the sampling campaign was an eight motor multirotor (or octocopter) in
 136 an X-8 configuration, as shown in Figure 3(a). The airframe is a custom design from the University
 137 of Bristol that provides enough space for a large battery capacity (typically 533 Wh, but tested with
 138 up to 710 Wh) and air sampling equipment. Situated above the main aircraft, the temperature and
 139 humidity sensors are located towards the centre and away from the body in order to minimise the
 140 effect of the local flow on the sensor readings. The Tedlar bags are held underneath the vehicle to
 141 allow for inflation at the selected altitudes. A summary of the vehicle specifications is given in Table 1
 142 and additional key features are described as in the following section. The ground based element of
 143 the system is shown in Figure 3(b) and is indicative of the operating environment encountered. In
 144 close proximity to the sea and with near constant wind speed this required significant weatherising
 145 of the onboard electronics.



(a) University of Bristol X-8 Multirotor



(b) Ground support on Ascension Island

Figure 3. Unmanned Aircraft System and the Flight Operation Site

146 4.1. Airborne Vehicle

147 **Vehicle Configuration** An eight rotor vehicle was chosen to achieve reasonable redundancy
 148 against loss of a motor or speed controller during flight. The vehicle could theoretically sustain a loss
 149 of four motors, provided that none were on the same arm, and tests on disconnecting three motors
 150 demonstrated that the vehicle retained good control in flight provided there was sufficient overall
 151 thrust. Users of octocopter platforms have also anecdotally suggested that the four arm coaxial
 152 configuration was likely to provide better gust tolerance than a flat eight arm configuration. It was
 153 found that the vehicle did perform well in the wind, but further research is being conducted at the
 154 University of Bristol in order to quantify the differences.

155 **Vehicle Size** The size of the vehicle was driven by three factors: The mass of the payload; the
 156 endurance required to reach high altitudes; and overall vehicle stability in high winds. Tests showed
 157 that the final flight vehicle could operate in wind speeds of up to 20 ms^{-1} . The payload required to
 158 conduct the experiments was designed to be under 0.5 kg and the maximum take off weight given in
 159 the risk assessment and the application for BVLOS operations was 10 kg. This was never exceeded
 160 on Ascension and typical take-off weight was in the region of 8.5-9.5 kg depending on the number of
 161 batteries that were used.

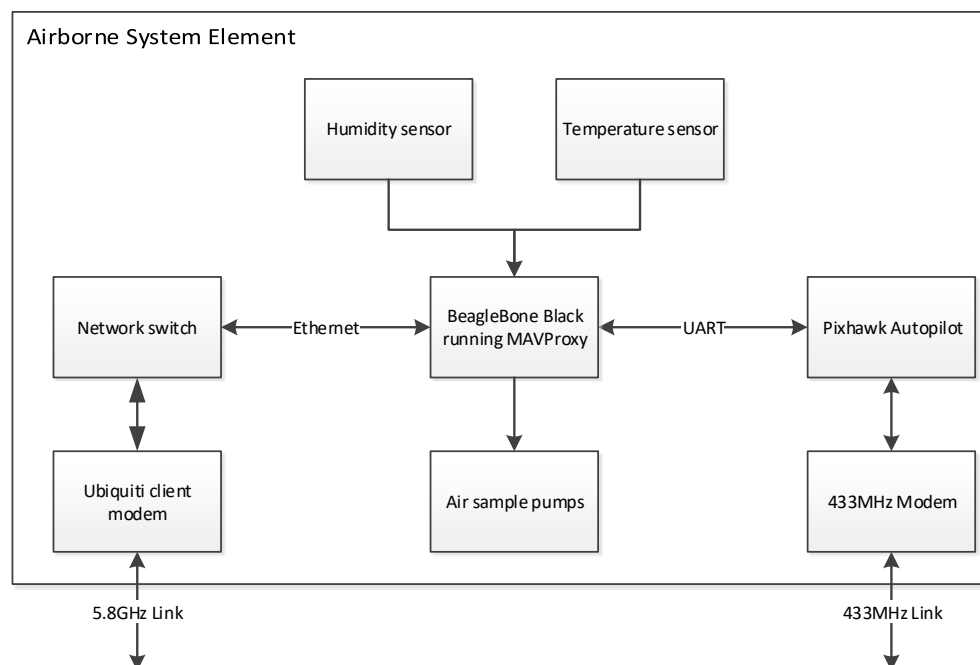
162 **Battery Capacity** The vehicle was configured to be able to operate with either two, three or
 163 four 8 Ah 22.2 V Lithium Polymer (LiPo) batteries in parallel. Fewer installed battery packs would

Table 1. Key UAV Specifications

Maximum Take Off Weight (MTOW) (inc. batteries)	10 kg
Diagonal rotor-rotor distance	1.07 m
Maximum battery capacity	32,000 mAh 6 cell Lithium Polymer
Motors	T-Motor MN3515 400 KV
Propellers	T-Motor 16x5.4"
Electronic Speed Controllers (ESC)	RCTimer NFS ESC 45 A (OPTO)
Autopilot	Pixhawk by 3DRobotics
Autopilot software	ArduCopter v3.1.5
Safety pilot control link	FrSky L9R 2.4 GHz
Ground Control Station (GCS) link	Ubiquiti 5 GHz directional
Onboard computing	BeagleBone Black
Sampling pump	KNF Diaphragm pump (NMP 850 KNDC)

lead to a lighter more agile vehicle, but with reduced endurance. Installing more batteries increases the flight time, but due to the additional mass the additional endurance reduces with each battery. Four batteries was deemed as an acceptable upper limit in terms of endurance achieved and stability of the aircraft. During the campaign the vehicle flew with three batteries as this provided enough endurance to reach beyond the maximum expected TWI altitude of 2.0 km ASL.

Autopilot The ArduCopter autopilot software was selected due to its reliable performance and flexible operation. The telemetry protocol is well documented and enabled integration with a long range telemetry link. Additionally a comprehensive flight dataset is logged for each flight, enabling the analysis presented with this paper. The hardware selected was the Pixhawk by 3D Robotics.

**Figure 4.** Airborne System Diagram

Onboard Computing An onboard computer was required to store and forward the analog and digital data from the onboard sensing as well as control the sample collection pumps. This enables the ground operators to see the sensor data in real time for decision making in flight. MAVProxy

software was installed for forwarding the telemetry data and a custom module was written to allow integrated monitoring and control of the payload. All collected data was stored on-board to allow for dropped packets. The architecture of the on-board system components and how they communicate is shown in Figure 4.

Sensors The payload had three core functions: measure temperature; measure relative humidity; and pump air into sample bags from an external demand signal. Temperature and humidity measurements were used to characterise the boundary layer profile on the ascent and indicate the location and characteristics of the inversion layer. The ascent rates were reasonably fast (5 ms^{-1}) and so it was necessary to select sensors that responded within 20 seconds in order to estimate the boundary layer height to within 100 m. Sensors used in radiosonde measurements were sourced due to having very similar design requirements. The temperature sensor was easy to interface through the onboard computer analog inputs and proved to be reliable, however the relative humidity sensor required more attention to integrate due to the limited I2C address range available and custom addresses had to be programmed ahead of time. The temperature sensor itself was a GE fast-tip FP07 glass bead thermistor (analogue) $< 0.2 \text{ s}$ response time with a spectral response close to 5 Hz (Figure 15 in [37]). Figure 5 shows a three point calibration for this sensor in a standard Weiss WKL 34/40 calibration oven. The calibration was performed at three set points (0°C , 10°C , 20°C) and the reference was a NIST traceable temperature logger combined with a standard thermistor probe (accurate to $\pm 0.2^\circ\text{C}$). Based on this data and in the configuration used these were found to be accurate to $\pm 1^\circ\text{C}$ and therefore suitable for the purposes of this campaign.

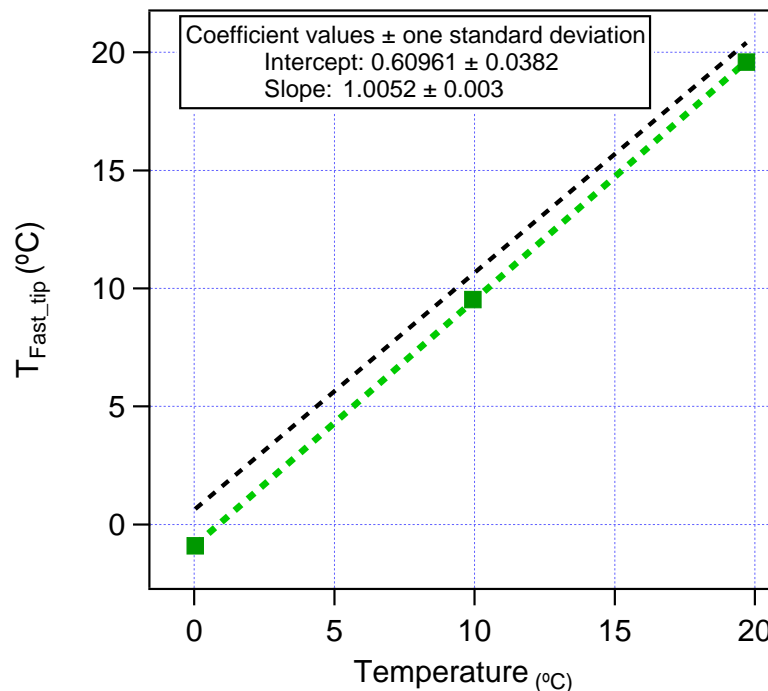


Figure 5. Temperature Sensor Calibration

The relative humidity sensor was significantly more sensitive to general handling and dust ingress than the temperature sensor. Reliability of the sensor was poor, and so it was replaced daily and protected between flights. The humidity sensor used was an IST P-14 Rapid capacitance humidity sensor (I2C) $< 1.5 \text{ s}$ response time, which has been extensively tested for fast-response humidity measurements on UAVs by Wildmann et al. [38]. The manufacturer states that these are calibration

free following their factory calibration to $\pm 3\%$ relative humidity and no changes were made to the sensors themselves prior to flight which would require recalibration.

As mentioned previously, the temperature and humidity sensors were placed toward the centre of the vehicle and above the main chassis. This was done to minimise the effect of the rotor wake on the sensor readings, specifically in the climb to the sample altitudes. Whilst ascending, the air is essentially accelerated vertically downwards, and the sensors themselves are in the relatively smooth air being induced from above (Figure 3 in [39]). It was also found that inspection of the data collected during ascent and descent showed no systematic bias with regards to temperature and pressure. We conclude, therefore, that rotor-induced local air flows have no significant effect on the performance of these sensors when placed in this position. In addition, with the response time of the temperature sensor used at < 0.2 s, the resolution of the data collected at (5 ms^{-1}) ascent rate was higher than required in order to pinpoint the temperature inversion and the sample heights to target during the flight. It was also found that when a second flight was carried out in quick succession to a first flight, the temperature and humidity data followed very closely to the first.

Air Collection The air samples were collected into five litre Tedlar bags by directly pumping in air through NMP 850 KNDC diaphragm pumps, in accordance with internationally agreed best practice [3]. Two pumps were installed, each plumbed directly to a sampling bag. The pumps were controlled via a P-Channel MOSFET load switch circuit triggered from the onboard computer. Whilst the pumps could have been triggered automatically upon the vehicle reaching specific waypoints, it was decided that the triggering should happen remotely - allowing the payload operator the chance to decide during flight on the best sampling locations. A custom box was laser cut out of corrugated correx to house the two bags and was simply attached to the underside of the vehicle. Methane mixing ratios in the Tedlar bag samples were measured within 1-2 days of collection using an in-house Picarro 1301 CRDS (cavity ring-down spectrometer) with a NOAA traceable 6-gas calibration suite (on Ascension Island) giving a precision of ± 0.5 ppb [40]. Samples are measured for 240 s with the last 120 s being used to determine the mixing ratio. For bags containing less air, the bags were run for 120 s with 60 s being used to determine the mixing ratio.

With regards to mixing of the air sample due to the vehicle rotors, the induced velocities at a distance of greater than three rotor diameters are effectively zero (note that this does vary depending on disk loading [39]), and so although the air is mixed locally due to the air vehicle whilst in the hover and when collecting an air sample, the volume over which that sample is collected is actually relatively small, with an outer sample collection diameter (in the absence of wind) of no more than a few metres. With the vertical distances of up to 3 km involved in this campaign, the sample volume itself is relatively very small. With the vehicle itself drawing in air for the sample from only a few metres, the atmospheric conditions themselves will typically have a much greater effect on the mixing of the sample than the vehicle itself.

The air masses under study have been transported several thousand km from interior Africa and have mixed en route. Thus, though on 3000 m scale there are strong vertical changes depending on source inputs, each air mass is generally homogenous on the 10-50 m scale. The UAV causes local mixing on a metre scale, but this scale of mixing is unlikely to be significant in sampling separate air masses, unless there is a sharp laminar boundary present which has survived the transport from Africa and consequent boundary mixing between air masses.

Tedlar bag samples were also taken approximately 1 m above ground level each day from the UAS site and were analyzed together with the samples from the UAS. These samples were then compared with the continuous ground measurements made by RHUL at the Met Office on Ascension Island. The measurements by RHUL are long-standing, both with the in situ continuous system installed on the island, and by regular flask sampling analysed in London. RHUL measurements are subject to ongoing intercomparison with the parallel co-located flask collection by US NOAA, measured in Boulder Colorado. Please see [41] for additional information.

Safety Pilot Link The safety pilot link is used for manual control of the aircraft as well as selecting flight modes such as waypoint following or Return To Home (RTH). The link is required to maintain communication with the vehicle at all times so that the safety pilot could always command a RTH. Two off-the-shelf systems were identified as suitable for the safety pilot link: Immersion RC EzUHF and FrSky L12R systems. The Immersion RC system transmits on 459Mhz (in the UK firmware), whilst the FrSky system uses 2.4Ghz. During testing it was found that the Immersion RC system was sensitive to interference from the onboard systems. The FrSky system proved extremely robust, both during testing as well as the campaign. Ground based tests were conducted before the campaign with a line of sight horizontal separation of 3 km during which the signal strength was consistently strong.

Telemetry Ubiquiti radio modules were selected due to the long range and high bandwidth offered. The primary function of the telemetry link was to enable monitoring of system health data on the ground as well as interaction with the payload. The directional antennas used both on the ground as well as the aircraft were selected to provide a stronger link. A second telemetry link was used for redundancy, transmitting on a separate frequency using a simple omnidirectional antenna. Radio modems by 3D Robotics were used to communicate with the vehicle on 433Mhz, with duplicate vehicle health information being transmitted.

Environmental Protection The motors are able to operate in water and did not require special consideration other than inspection of bearing smoothness prior to flight. Electronics however, required protection and the onboard computer was sprayed with PCB lacquer and both the autopilot and onboard computer were encased within plastic containers with vents on the underside. The vents would enable air in, which would contain moisture from the clouds, but signs of any water deposited within the containers was closely monitored and found to be minimal. Connecting wires were sealed and loops to below the entry points were included to minimise the run down of collected water droplets.

4.2. Ground Station

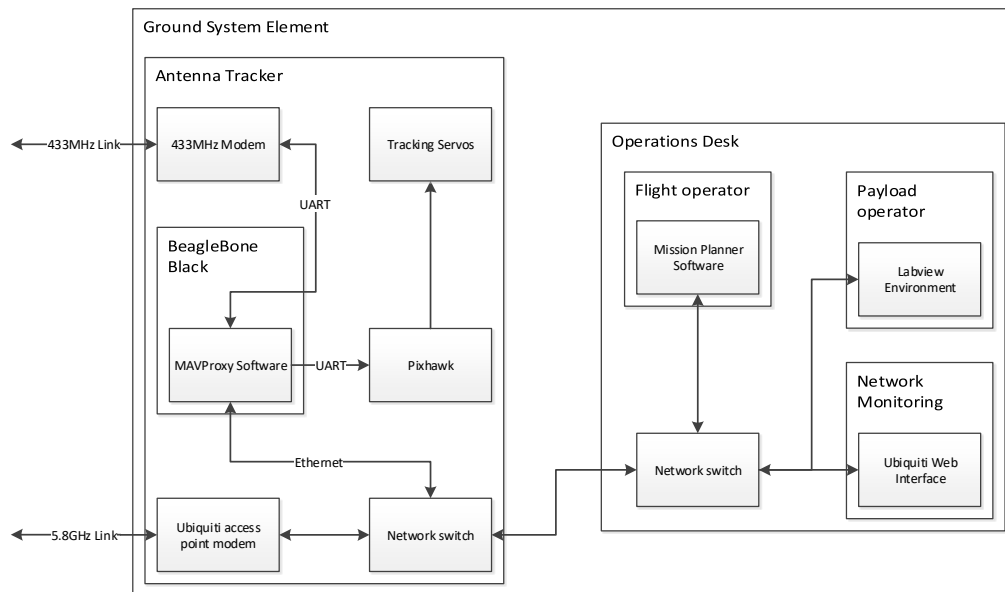


Figure 6. Ground System Diagram

A ground station network was set up as shown in Figure 6. This was designed in order to provide the mission and payload operators with the information required to operate the vehicles safely and reliably. Key elements of this system are as follows.

Antenna Tracker A servo driven pan and tilt system was constructed with both the 433 MHz and 5.8 GHz antennas attached. A pixhawk running the ArduTracker software was installed to control the antenna tracking, which compares the UAV position with the position and attitude of the antennas and sends corrective signals to the pan and tilt servos. The pixhawk obtains information about the position of the UAV from the MAVProxy software, which combines information about the UAV from both telemetry links. The combined information is also shared with the flight and payload operators through a two way data link over the local area network.

Visitor and Road Management Road blocks were setup each day before flight operations commenced as agreed with Ascension Island police force. During operations there was always at least one person ready to handle any external interruptions, allowing the rest of the team to continue focussing on the mission. Typically this would involve answering the radio when road access was requested, but also included talking to visitors that had arranged to watch the flights.

Weather Monitoring A portable weather station was used during the first campaign, primarily to measure wind speed and direction. During the second campaign a Gill Instruments R3 Sonic Anemometer was used, which enabled remote monitoring of the same information.

5. Operational Considerations

5.1. Field Site Operations on Ascension Island

In September 2013 a three person team from Birmingham and Bristol visited Ascension Island for a reconnaissance trip to identify possible operational sites. This proved to be invaluable for the subsequent field campaign, and the authors highly recommend this approach for any significant UAS operations. Three possible sites were initially identified, of which one was selected as the most suitable to operate from. The area found was located by the road leading out to the old NASA site and provides excellent access, isolation and the ability to block the road and control access for third parties. It is approximately 350 m ASL, which reduces the height required to climb compared to a sea level launch and is on the windward side of the island providing clean, unobstructed airflow from the prevailing wind direction - South, South West.

Ideally, all of the equipment including both the vehicles and the ground support equipment would have been shipped to Ascension prior to the field campaign. Due to extended development and early shipping dates however, only the ground equipment and maintenance equipment were sent out ahead of time. This included all the lithium polymer batteries (necessary due to airfreight restrictions) and all the heavy items such as portable shelters. Flights to Ascension Island depart from RAF Brize Norton, with the Air Bridge to Ascension Island and the Falkland Islands.

With the permission of the military personnel and police on Ascension a base was set up as shown in Fig. 7 just off the road to the old NASA site. Given the strong continuous wind speeds on Ascension, two 3.66 m (12 ft) by 3.66 m (12 ft) shelters were shipped from the UK and assembled on site. During the course of the campaign, basic equipment was stored on site throughout, with the aircraft being brought up from Georgetown on a daily basis. Battery charging was carried out both on site and in Georgetown depending on daily usage. Only minor maintenance was required throughout the campaign, and this was carried out in Georgetown.

Safety was the focus of the buildup and operations through the project. Although there is an element of redundancy through the air vehicle configuration chosen there are still multiple single points of failure on the airframe. Because of this, all operations were carried out with the worst safety

case based on a total failure of the onboard power systems. Given the maximum permitted BVLOS altitude of 3048 m (10000 ft) the worse case scenario considered given the conditions encountered throughout the campaign resulted in a safety radius of at least 1.2 km from the flight path. The road was blocked at 1.4 km (straight line) from the point of operation and the nearest inhabited site was 3.0 km from the flight path.

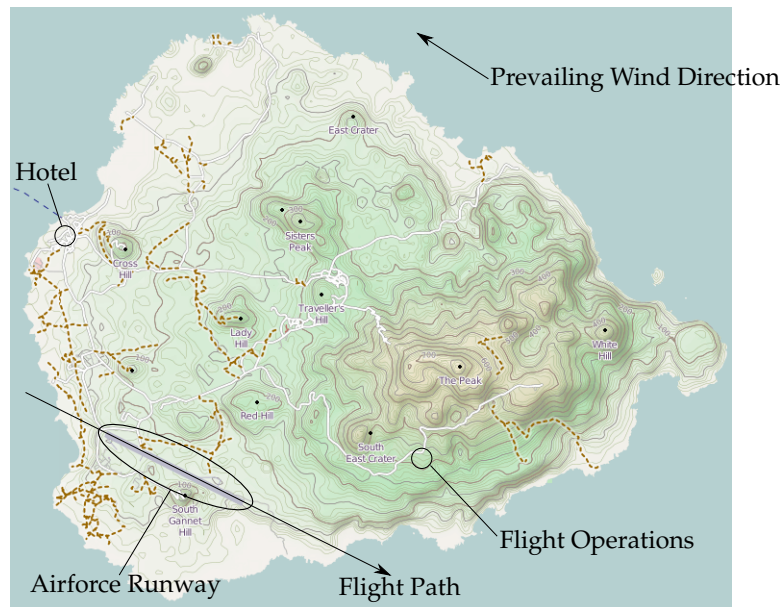


Figure 7. Map of Ascension Island

5.2. Typical Flight Operations

The objectives required the multirotor to climb to a commanded altitude and loiter in position whilst an air sample was taken, pausing for ten seconds prior to the sample collection. This air sample was collected using a diaphragm pump that inflated a bag in just under one minute. The vehicle would then return to base and the air sample would be removed for analysis. Throughout the flights the temperature and Relative Humidity (RH) were measured and transmitted to the ground station at a rate of 10 Hz and it was possible to ascertain the location of the trade wind inversion and the different air masses from the temperature and humidity readings during the ascent. The real-time measurement of the atmospheric profile is a significant capability of the system and enabled the atmospheric scientists to accurately target key parts of the profile to collect the samples.

For both campaigns, the flights on Ascension Island were carried out under Beyond Visual Line Of Sight (BVLOS) conditions. This required an exemption to the Air Navigation Order which was granted by Air Safety Support International (ASSI) for the period of both campaigns. The exemption itself was based on a safety case which the University of Bristol put together and was granted subject to a number of conditions including; contact with Wideawake Airport would be maintained at all times; all flights would be operated in accordance with the permission/procedures agreed with the Royal Air Force and the United States Air Force. These measures put in, both prior to the campaigns and during flight operations, were designed to ensure complete separation from other air traffic. For example, no flights were carried out during a given window encompassing an aircraft arriving or departing from the island. Whilst this approach to BVLOS operations requires airspace separation and close communication with all other airspace operators and users, it allows small SUAS vehicles to be operated safely in challenging environments. Ongoing improvements with communications, sensors and computing will allow more closely integrated BVLOS operations in the future, however

for the present, the use of segregated airspace for these types of operational flights is likely to be required.



Figure 8. Sample Flight Path over Ascension Island

The flight operations themselves followed a pattern, established over the course of the first week. This was based on the following tasks:

1. Preparation of the flight vehicle including physical and system checks and preparation of the air sample bags including air evacuation.
2. Preparation of the flight plan - including alternative routes for descent depending on the upper wind conditions. See Figure 8 for a visual depiction of a typical mission.
3. Pre-flight checks, arm the vehicle and manually take-off to 20 m AGL undergoing manual flight checks by the safety pilot.
4. Switch the vehicle into automatic mode and carry out the ascent to the pre-determined altitude at 5 ms^{-1} ascent speed.
5. Monitor temperature and relative humidity profiles throughout the climb, confirming the location and thickness of the trade wind inversion. The sensor operator at this time would confirm the predetermined sample heights or adjust depending on the altitude at which the trade wind inversion was encountered.
6. On agreement with the ground station and sensor operators the air samples were triggered at the required altitudes. Pump times varied between 40 s and 60 s depending on the target altitudes for the samples.
7. The descent was carried out automatically at -5 ms^{-1} , reverting to manual at 20m Above Ground Level (AGL).
8. Post flight checks were then carried out, battery voltages recorded, flight data stored and the air sample(s) retrieved.

For all flights on Ascension Island, the aircraft was taken off and landed manually, under the direct control of the safety pilot. Although the system is fully capable of an automatic take-off and landing, a manual approach allowed for the safety pilot to carry out flight checks prior to initializing the mission. The take-off point itself was situated across and downwind from the operations tent, allowing the ground crew to remain upwind, and yet control full access to the site. One of the benefits of operating on Ascension Island is that the prevailing wind direction and strength at ground level is consistent and predictable, allowing the flight operations to be consistent and refined over time.

379 6. Lessons Learned

380 All anomalies with any part of the system were fully investigated prior to any operations. The
381 following is a list of the key problems encountered during the field campaign and the actions taken
382 as a result.

- 383 1. Ground station power was lost during one of the initial flights. The power sources taken to
384 support operations malfunctioned and a return to launch was triggered by the safety pilot. All
385 subsequent operations in the first campaign were powered from two inverters. For the second
386 field campaign a generator was sourced to provide power on site.
- 387 2. One of the ESCs (Electronic Speed Controller) failed as the aircraft was prepared for flight. This
388 was identified by the safety pilot and replaced before further operations continued.
- 389 3. Difficulties were identified at one point with the telemetry downlink – this was traced to a file
390 size limit being reached on the onboard computer. Once identified this was corrected and flights
391 continued.
- 392 4. High wind speeds above the inversion were identified in the second half of the first field camp
393 again. These are outlined in detail together with mitigation strategies in the subsequent section.
- 394 5. One of the GPS batteries became loose during flight and was identified in the pre-flight checks
395 prior to the following operation. This was triggered as a magnetometer error and the unit was
396 replaced and checked before the subsequent flight.
- 397 6. One of the commercially purchased battery connections failed during flight, which was identified
398 from the flight director observing an unusually high voltage drop on the initial climb out,
399 therefore a return to home was triggered by the safety pilot. All additional battery connections
400 were checked and modified prior to resumption of flight operations.

401 7. Flight Envelope

402 7.1. Achieving Maximum Altitude and On-board Power Management

403 At the start of the campaign the maximum commanded altitude of the UAV was increased
404 gradually as knowledge and confidence in the system grew. The maximum altitude achieved was
405 2500 m AGL, which surpassed the required altitude (typical of the local TWI) by approximately 1000
406 m. Figure 9 shows some of the recorded data for a 2500 m AGL flight. The current drawn from the
407 flight battery illustrates that, as one might expect, the majority of the energy is expended during the
408 ascent. The UAV drew 45 A in the hover at 20 m AGL (370 m ASL) and peaked at 90 A at the top of
409 the ascent, before dropping to just under 70 A whilst hovering at 2500 m AGL. The increase in motor
410 speeds required to hover at 2500 m AGL is also apparent from the bottom of the plots, where the
411 speed to hover at 20 m AGL is 50% compared to 66% at 2500 m. On this particular flight, the UAV
412 landed with 23% of the battery capacity remaining.

413 7.2. Performance in Wind

414 The trade wind conditions were found to be very consistent from day to day at ground level. The
415 winds above the TWI, however, were seen to change over the course of the campaign. The different
416 wind conditions therefore enabled the team to test the UAV performance in conditions ranging from
417 light wind to prohibitively strong winds. It is possible to estimate the speed and direction of the
418 wind from the aircraft orientation after estimating some key parameters found by performing a slow
419 orbit manoeuvre such as that shown in Figure 10(b). Making some assumptions about steady wind
420 conditions, and resolving free body diagram forces a simple mapping function can be created between
421 attitude angles reported by the autopilot and the estimated wind conditions. Full details on the
422 procedure are outlined in Ref. [42].

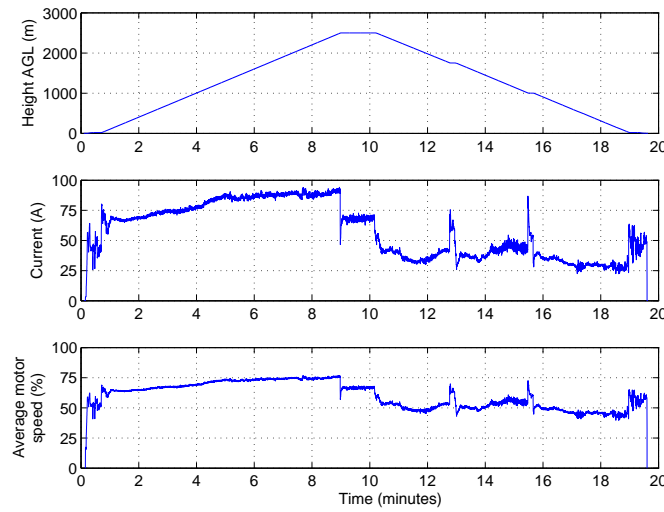


Figure 9. Altitude, Battery Voltage and Motor Speeds for a Sample Flight to 2500 m AGL

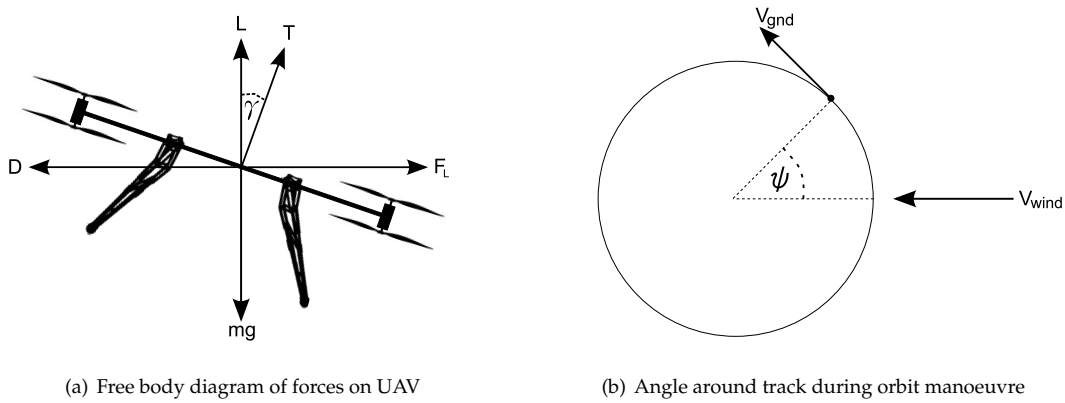


Figure 10. Forces, Angles and Velocities used for Wind Estimation

7.3. Flight Through Still Air

The ideal flight path for the UAV from a mission scripting perspective would be to ascend vertically to the required altitude and then descend back along the same path to the take-off site. Rapid descent through still air for rotary wing aircraft however can lead to instability. The wind speeds on Ascension Island were typically around 7 ms^{-1} to 8 ms^{-1} at ground level, which is equivalent to the UAV travelling at a reasonable forward velocity in still air conditions. As previously mentioned, the wind conditions varied above the TWI and over the course of a few days of the first campaign the wind speeds were found to be extremely low. Conditions varied significantly reaching less than 2.5 ms^{-1} at times, such as in the flight shown in Figure 11 where aircraft bank angles and estimated wind speeds have been plotted against height above ground.

Figure 12(a) shows the roll and pitch angles during the same flight, overlaid on the altitude. The windspeed on the ground was approximately 8 ms^{-1} , meaning that the vehicle had to roll and pitch in order to maintain position during the loiter and vertical climb-out. An interesting result can be seen around the four to seven minute mark (*i.e.* between 600 m and 1500 m) where the roll and pitch angles change significantly during the ascent. During this stage of the ascent, the angle of the vehicle

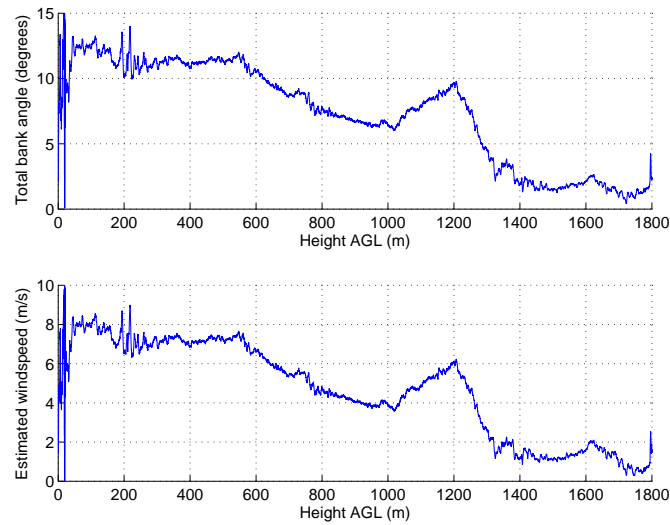
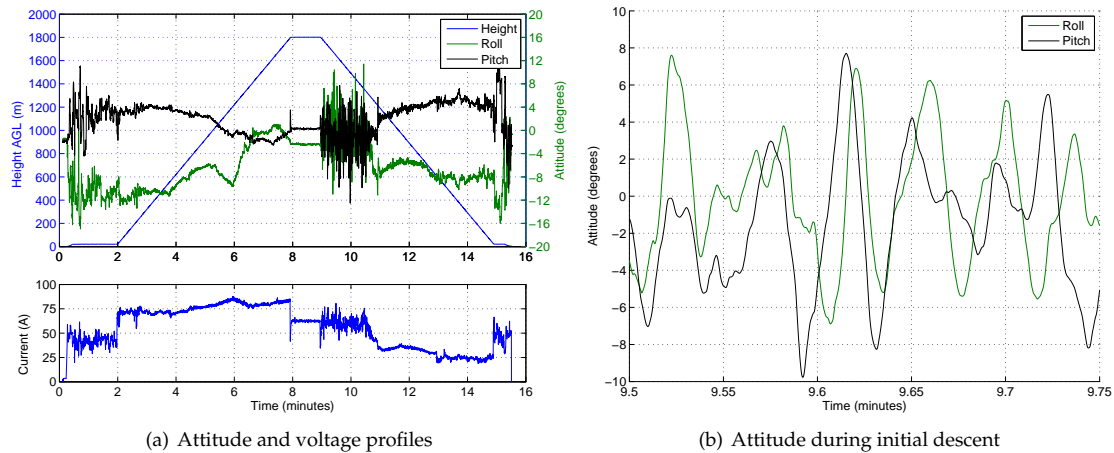


Figure 11. Estimated Windspeeds from the Aircraft Attitude during a Flight up to 1800 m AGL



(a) Attitude and voltage profiles

(b) Attitude during initial descent

Figure 12. Sample at 1800 m AGL, with Low Wind Speeds above the TWI

438 has rotated from around -10° roll and 4° pitch to approximately 0° roll and -2° pitch. The change in
 439 attitude is attributed to a dramatic reduction in wind speed as the vehicle enters a different air mass.

440 During the ascent, the reduction in wind speed poses no problems. Descending through still
 441 air, however, requires the vehicle to constantly make corrective actions and it has to work harder
 442 to maintain a level attitude. The attitude is shown in Figure 12(b) for a 15 second period half way
 443 through the still-air descent phase (at around 1600 m). Although the magnitude of the attitude
 444 variations is manageable, the persistent rate of change in attitude undesirable. The constant sharp
 445 changes in attitude observed in the still-air descent will lower the vehicle's endurance. Figure 12(a)
 446 also shows the current being drawn by the UAV, which during the initial descent through still air is
 447 roughly the same as that required to hover at 1800 m. Upon descending into the different airmass
 448 with higher wind speeds the current drops to nearly half as the motors do not have to work as hard
 449 to maintain stability of the aircraft. The current only increases again at the end of the flight when the
 450 UAV hovers briefly prior to touch down.

7.4. Trajectory Design for Descent in Still Air Conditions

It is well known by helicopter pilots that one should not descend vertically as this would entail entering the helicopter's own wake and lead to instabilities as described in [43]. The descent through still air described in Section 7.3 is undesirable as it reduces the endurance of the vehicle, which in turn reduces the altitudes attainable. To provide the rotors with clean airflow the mission script was modified to include a lateral manoeuvre during the descent. This lateral manoeuvre, referred to here as a dog-leg, typically consisted of translating away from the launch site whilst descending, pausing and then translating back towards the launch location. This can be seen clearly in Figure 8 with a climb to the sample altitude, followed by a descent to the waypoint identified then a return to the original trajectory. The profile shown is to the same scale as Ascension Island.

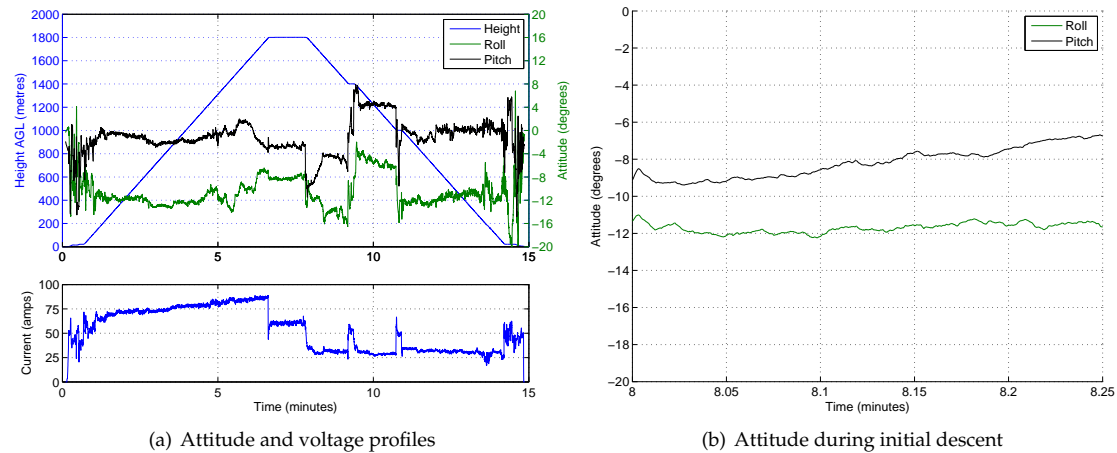


Figure 13. Sample Flight to 1800 m AGL, with a Translation Manoeuvre through Low Wind Speeds above the Trade Wind Inversion

The current consumption shown in Figure 13(a) suggests that the inclusion of a dog-leg reduced the power consumed, as the current drops significantly once the descent has initiated and apart from two brief sections of hovering stays low. The pauses at the additional waypoints required the UAV to arrest its movement and draw additional power, but this is believed to have significantly less impact on the endurance than omitting the dog-leg and descending vertically in still air. It should be noted that the dog-leg does not increase the time taken to descend as the vertical velocity is unchanged. The key reason for including this manoeuvre however is the reduction in the roll rates that are experienced during the descent in the low speed air mass. This reduction in rolling and pitching during the initial descent can be observed by comparing those angles previously shown in Figure 12(b) and those found by including a dog-leg in Figure 13(b).

The improvements observed by updating the flight plan with knowledge of the wind conditions suggests that some form of automatic trajectory generation would be highly beneficial. The wind direction and magnitude can be estimated using the attitude of the vehicle during the ascent and, as previously observed, the still air masses can clearly be spotted by the dramatic reduction in roll and pitch angles. An automatic trajectory planner could therefore introduce flight paths to ensure a stable descent. Furthermore, the planner should be constrained to guarantee that the trajectory does not pass into prohibited airspace and that the trajectory brings the vehicle back to the launch site.

7.5. Upper Windspeed Limits

The wind speeds above the TWI were, on some of the days during the campaign, observed to increase rather than decrease as discussed in Section 7.3. Figure 14 shows flight data collected on such a day, where the wind speed increases significantly at around 1350 m AGL.

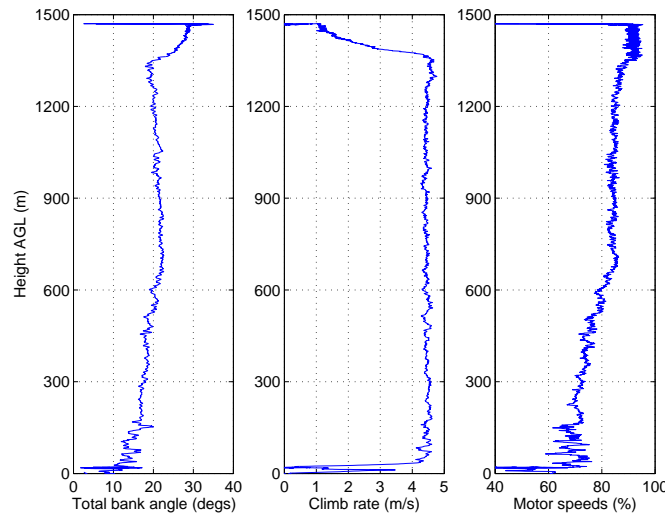


Figure 14. Sample Flight during High Wind Speeds above the TWI

Figure 14 shows how the climb rate remained constant at 4.5 ms^{-1} until around 1350 m AGL when it was seen to decrease to just 1 ms^{-1} . The decrease in climb rate was a direct result of the increase in wind speed, which caused the vehicle to pitch and roll to maintain the commanded ground course. The figure also shows the total bank angle of the vehicle during the ascent by taking the magnitude of the roll and pitch angles. The low level strong winds required the aircraft to bank by an average of 20° during the main portion of the climb. At around 1350 m AGL, however, the attitude required to maintain ground course increased to nearer 30° from level, dramatically reducing the available thrust to maintain the desired climb rate. Upon inspection of the motor speeds in the bottom of the figure, it could be reasonably assumed that the flight controller has saturated the motor outputs within the requirements for stability, *i.e.* the motors are spinning at their maximum speeds. Throughout these high winds the UAV was still able to maintain an ascent, albeit at a reduced 1 ms^{-1} .

8. Payload

8.1. Meteorological Sensor Assessment

The fast-response temperature and humidity sensors, generally performed well during the field campaigns and we assess their performance in terms of targets 3 and 4. However, the normally robust capacitance RH sensors were adversely affected by volcanic wind-blown dust during the first campaign. For the second campaign, an improved shielding cap (with sufficient holes for rapid air ingress, but not allowing large dust particles to enter) was designed. The shield was constructed from white correx with an extended circular plate over a perforated tube. There is no evidence - *e.g.* from a discrepancy between the upward and downward legs - to suggest the shield had a significant effect on the time response of the temperature and humidity sensor system. In addition, the high wind speeds encountered during most flights aspirates the sensor to make solar heating effects unlikely [44].

Figure 15 shows a typical flight profile of temperature (red) and humidity (light blue), and also the pitch (green) and roll (dark blue) angles during a flight made on the 14th September 2014. A

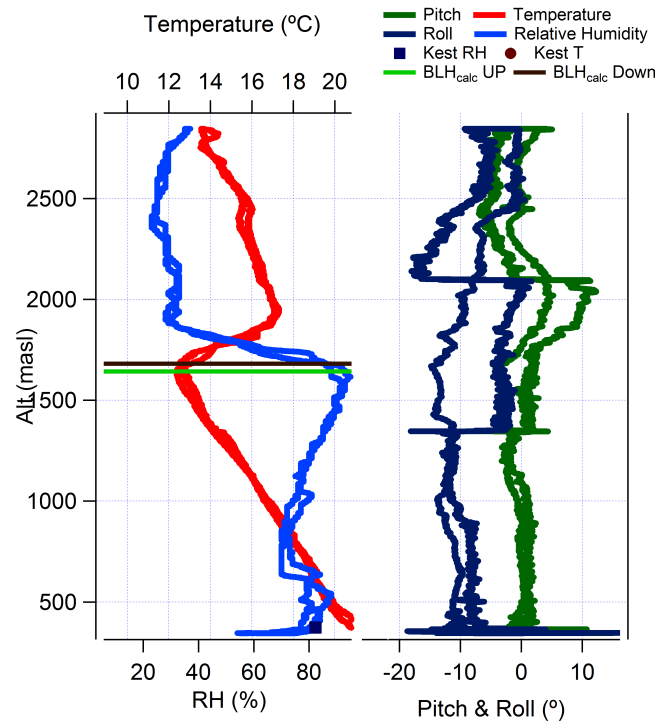


Figure 15. Meteorological data: Temperature (red), Relative Humidity (light blue), Pitch (green) and Roll (dark blue) angles for a Sample Flight made at 16:54 pm on the 14th September 2014.

kestrel 4500 weather station under manufacturer's calibration was operated at the measurement site during each flight day and these baseline measurements are shown for reference and comparison with the onboard sensors. Pitch and roll angles are included in 15 to enable the reader to identify where the samples are being taken; which in this case corresponds to the two altitudes where there are rapid variations in roll and pitch angles. In this example, the base of the TWI, where temperature begins to rise with altitude, is apparent at 1,670 m ASL and marks the top of the turbulently mixed atmospheric boundary layer below. The inversion zone acts as a cap on the upward motions of the boundary layer. Fig 15 shows the temperature increasing from 12°C to 17°C over this transition to the unmixed free-troposphere above, and correspondingly, humidity drops from near saturation in the boundary layer to 30 percent at at 1,880 m ASL, the top of the TWI. This thickness of 210 m for the inversion (entrainment) zone is at the larger end of inversion thickness observations during both campaigns, with 50 m - 70 m being more typical.

The temperature and humidity traces show both the upward and downward data and clearly demonstrate the suitability of the sensors for this task with a temperature difference of less than a degree and a minimal relative humidity difference for most - some of the larger differences most likely represent real variability, e.g. the proximity to clouds/proto-clouds in the lower boundary layer at about 600 m ASL. Given the narrow inversion layer thickness, this campaign clearly demonstrates the ability of small UAVs to measure small scale atmospheric features (<200 m) with minimal disturbance. With such a system, there is potential for new insights into such features which may have implications for numerical weather prediction and global pollutant transport models.

With the data shown in Figure 15 relayed to the ground station in real-time, it was possible during the ascent to identify the exact location of the inversion in terms of the lower and upper limits. Based on these, the sample positions were then chosen, allowing the air samples to be taken in the upper air mass and clear of the inversion, within the inversion itself or below it. This capability,

in the presence of uncertainty in the meteorological data prior to the flight, provided the required confidence for selection of the air sample collection points relative to the TWI.

To target a minimum of 100 m above the trade wind inversion when ascending at 5 m/s the sensors need to be fast enough to respond to a step change in temperature within 20 seconds for this to be the case. Ideally this is within 10 seconds to account for uncertainty in the down leg measurement when assessing the sample height post-flight (we do not profile up and down and then choose a sampling height). To demonstrate the performance of this system, the inversion height for the up and down legs of flights from September 2014 have been calculated and compared. Sensor lag time will manifest as a systematic difference in calculated boundary layer height when two profiles are compared; up-leg BLH will be higher than down legs. This will give an indication of BLH accuracy based on sensor lag time.

A potential temperature method was used to identify the start of the potential temperature gradient maximum, similar to Hennemuth and Lammert [45]. Methods to calculate the inversion height are varied [46], and beyond the scope of this paper to resolve - however, using the same algorithm and thresholds to calculate the up- and down-leg boundary layer heights offer directly comparable results in this test. The result of this analysis for 25 flights which crossed the TWI in the Sept 2014 campaign demonstrate a positive bias; 2 out of 25 flights analysed demonstrating a negative difference between BLH-UP minus BLH-Down. The mean vertical difference was 30.7 m with a standard deviation of 21.1 m (Maximum 76.5 m, Minimum 2.3 m), which is well within the stated aim of targeting 100 m above the TWI.

To assess the influence of propeller interference in the sensor response we contrast power spectra for two periods - one when the Octocopter was stationary on the surface, and one when in a hover at 300 m above ground level. Figure 16 shows the raw and smoothed power spectra for each period a -5/3 line is shown for comparison. Propeller rotation rate for the motors and propellers used, Table 1, was between 4050 (50 % throttle) and 6250 (100 % throttle) rpm, or 67.5 - 104 Hz. These fundamental frequencies and associated harmonics are not seen in the temperature sensor, which from the spectra in Figure 16 responds up to 2 Hz in our system. There is also no indication that the propellers, or the aircraft's movement during hover influence the temperature signal.

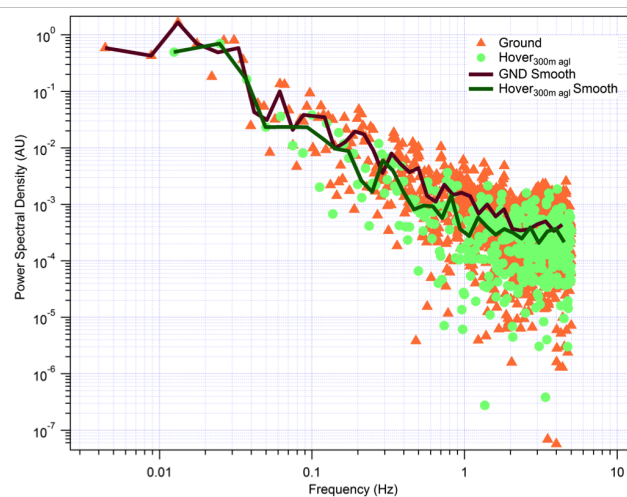


Figure 16. Power spectral density (arbitrary units) for the Fast Tip Temperature sensor when stationary on the ground (motors off) and at a level hover at 300m. Averaging periods were 226 and 80 seconds respectively. Propellers rotate at 67.5 - 104 Hz, and this fundamental frequency is greater than the approximately 2Hz response time seen here. Agreement between the spectra indicate no influence of either the propellers or the aircraft movement on the measured temperature.

8.2. Methane Sample Results

Figure 17 demonstrates the good agreement, within expected variability and vertical profile, between the ground bag samples and the continuous values measured by the permanent cavity-ringdown system installed on the ground at the Airhead. It also shows that there is good consistency between the ground bag samples and the bag samples taken below the TWI with the r^2 values for the two plots greater than the critical value showing significant correlation. Details for each campaign are:

17(a) September 2014 campaign: Correlation between the ground bag samples and CRDS samples: $r^2 = 0.558$ where critical $r^2 = 0.247$ at 0.05 significance. Correlation between ground samples and samples taken below the TWI: $r^2 = 0.329$ where critical $r^2 = 0.283$ at 0.05 significance.

17(b) July 2015 campaign: correlation between the ground bag samples and CRDS samples: $r^2 = 0.77$ where critical $r^2 = 0.171$ at a 0.05 significance. Correlation between ground samples and samples taken below the TWI: $r^2 = 0.493$ where critical $r^2 = 0.305$ at 0.05 significance.

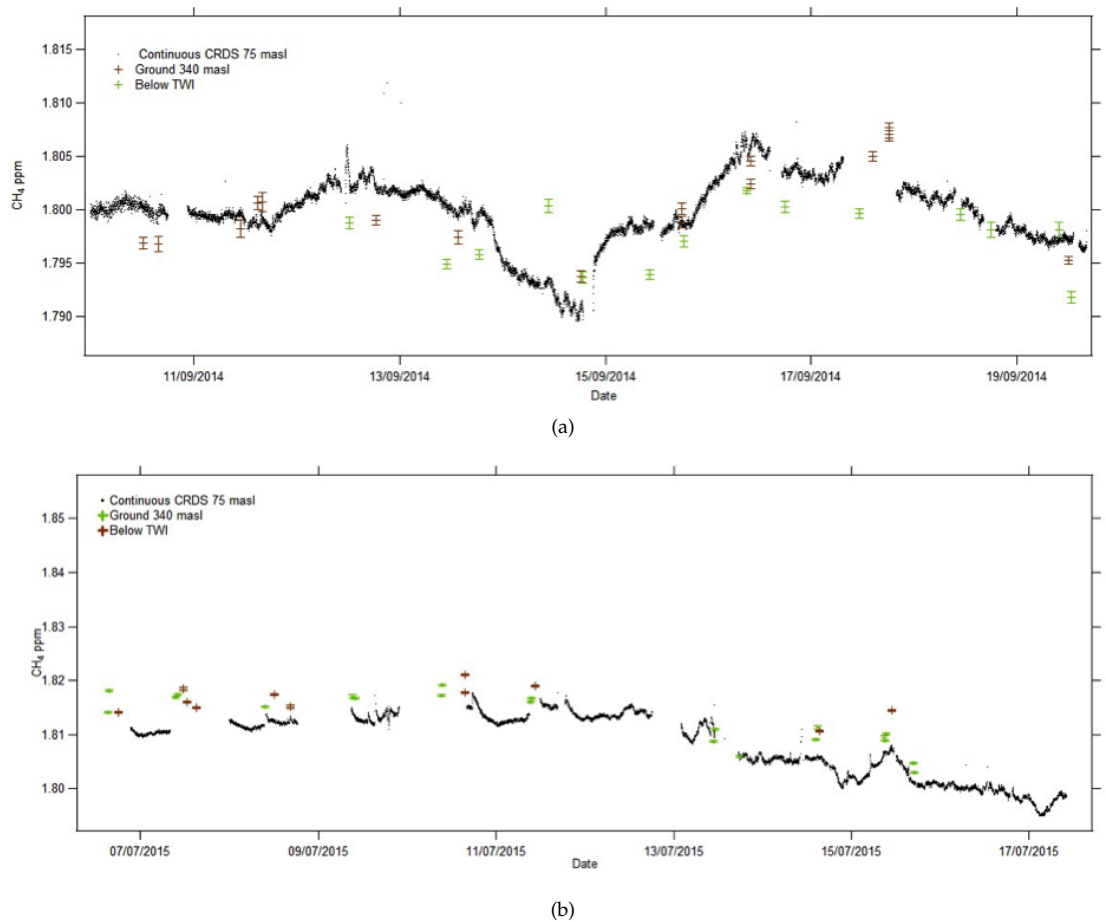


Figure 17. Continuous Cavity Ring-Down Spectroscopy (CRDS) CH₄ ground level (75m ASL) compared with bag samples taken from the ground (340 m ASL) and below the TWI. Date markers are 00:00 UTC.

Figure 18 shows the CH₄ mole fraction (ppm) variation with both altitude ASL and relative to the boundary layer for both campaigns. Both the September 2014 and July 2015 campaigns show consistently higher CH₄ mole fractions above the TWI, Figure 18, with increments up to 31 ppb. Mixed source emissions (e.g. wetlands, agriculture and biomass burning) from north of the

intertropical convergence zone and Africa may be influencing the air masses. Samples from July 2015 have higher CH_4 mole fractions and ranges compared to September 2014 which is likely to reflect the year on year growth and seasonality [47]. Different mixing ratios across the TWI may also be inferred when comparing the continuous ground level monitoring and samples with CH_4 mole fractions above the TWI [47].

Green mountain on Ascension Island is not high enough to enable samples to be taken above the TWI without the use of an air vehicle. With the increased levels of CH_4 shown in Figure 18, there is strong evidence a system is required in order to collect additional high altitude air samples. SUAS offer the potential for a low cost, repeatable and flexible sample system which in the longer term could be used routinely by a non-specialist for air sample collections of this type.

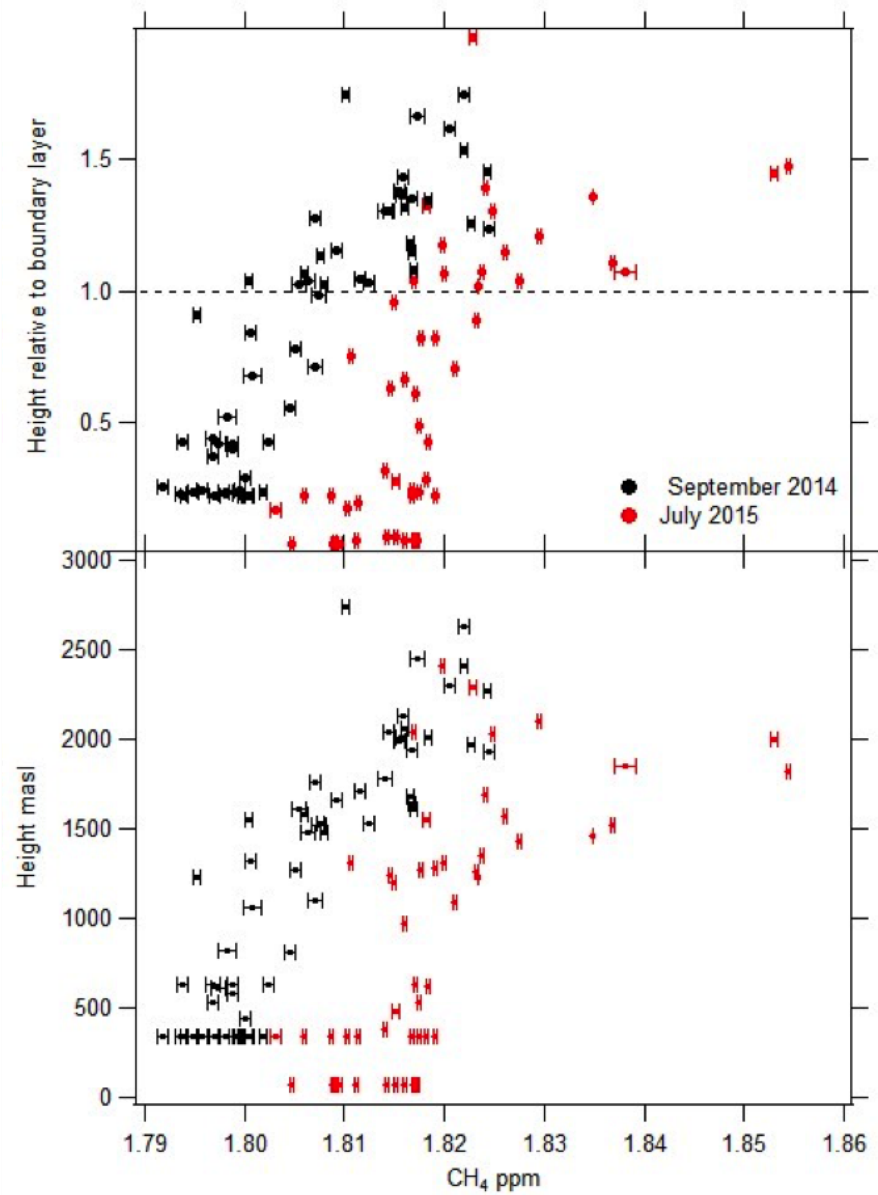


Figure 18. CH_4 Mole Fraction (ppm) with Altitude during the two campaigns (bottom). CH_4 Mole Fraction normalised to the Boundary Layer Height for the Two Campaigns [47].

9. Conclusions and Future Work

A multirotor has been successfully flown on Ascension Island up to 2500 m above ground level collecting air samples for analysis over the course of two campaigns in September 2014 and July 2015. The system was shown to operate reliably, amassing over one hundred flights without incidence. This paper has highlighted key aspects of the system from the vehicle specification through to flight performance data and lessons learned. Recommendations have been made for using the system to identify wind conditions at the edge of the vehicle's flight envelope as well as a flight profile that can alleviate issues encountered with still air.

Throughout the flights the temperature and relative humidity were measured and transmitted to the ground station making it possible to identify the location of the trade wind inversion and the different air masses during the ascent. This real-time measurement of the atmospheric profile is a significant capability of the system and enabled the atmospheric scientists to accurately target key parts of the profile during the flights in order to collect the samples required.

Using SUAS, it has been shown that in principle greenhouse gas measurement on Ascension can access both air at ground level from a very wide swathe of the southern oceans, and also sample air from above the Trade Wind Inversion, thereby addressing emissions from a significant part of the global tropical land masses. These air samples can be used for the purposes of identifying methane mole fractions and isotopic composition.

Whilst the campaigns in September 2014 and July 2015 required a highly specialised team of engineers and scientists for successful operations, it is expected that a fully automatic atmospheric sampling SUAS could be developed for long term sampling requirements. This could also include the development of more capable vehicles for sampling in higher wind conditions and in more challenging environments.

One of the key requirements for the campaigns to be successful was to be able to operate the platforms Beyond Line of Sight (BLOS). The approach taken in this work was to manage the question of BLOS operations through operational strategy, procedures and flight within restricted airspace. BLOS operations in unrestricted airspace would significantly expand the potential applications of SUAS including air sampling, however this integration will take time and will require significant research and development effort into platform reliability, autonomous operations, sense and avoid, and the legal framework. As each of these is addressed, the range of applications for which SUAS are applicable will increase, including air sampling, together with the range of airspace that is open for operations.

Acknowledgments: This work is supported by the Natural Environment Research Council Grant NE/K005979/1. We would also like to say thank-you for the huge amount of support we gained from the RAF and USAF base commanders, and also the Ascension Police, Government, CAA, ASSI, Met Office, Ascension Conservation and the people of Ascension Island

Author Contributions: Colin Greatwood, Thomas Richardson, Jim Freer, Rick Thomas and Rob MacKenzie designed, built and operated the SUAS platforms and sensors in Ascension. Rebecca Brownlow, David Lowry, Rebecca Fisher devised the sampling strategy and analysed the air samples. Euan Nisbet created and led the Investigation of the Southern Methane Anomaly project.

Conflicts of Interest: The authors declare no conflict of interest. The founding sponsors had no role in the design of the study; in the collection, analyses, or interpretation of data; in the writing of the manuscript, and in the decision to publish the results.

Abbreviations

The following abbreviations are used in this manuscript:

AGL	Above Ground Level
ASL	Above Sea Level
BBB	Beagle Bone Black
BVLOS	Beyond Visual Line of Sight
DOAJ	Directory of open access journals
ESC	Electronic Speed Controller
MDPI	Multidisciplinary Digital Publishing Institute
RH	Relative Humidity
RTH	Return To Home
SUAS	Small Unmanned Air System
TWI	Trade Wind Inversion
UAV	Unmanned Air Vehicle

References

- Nisbet, E.G.; Dlugokencky, E.J.; Bousquet, P. Methane on the Rise-Again. *Science* **2014**, *343*, 493–495.
- Dlugokencky, E.J.; Nisbet, E.G.; Fisher, R.; Lowry, D. Global atmospheric methane: budget, changes and dangers. *Philosophical Transactions of the Royal Society a-Mathematical Physical and Engineering Sciences* **2011**, *369*, 2058–2072.
- Nisbet, E.G.; Dlugokencky, E.J.; Manning, M.R.; Lowry, D.; Fisher, R.E.; France, J.L.; Michel, S.E.; Miller, J.B.; White, J.W.C.; Vaughn, B.; Bousquet, P.; Pyle, J.A.; Warwick, N.J.; Cain, M.; Brownlow, R.; Zazzeri, G.; Lanoisellé, M.; Manning, A.C.; Gloor, E.; Worthy, D.E.J.; Brunke, E.G.; Labuschagne, C.; Wolff, E.W.; Ganesan, A.L. Rising atmospheric methane: 2007–2014 growth and isotopic shift. *Global Biogeochemical Cycles* **2016**, *30*, 1356–1370. 2016GB005406.
- Bhardwaj, A.; Sam, L.; Akanksha.; Martin-Torres, F.J.; Kumar, R. UAVs as remote sensing platform in glaciology: Present applications and future prospects. *Remote Sensing of Environment* **2016**, *175*, 196–204.
- Pajares, G. Overview and Current Status of Remote Sensing Applications Based on Unmanned Aerial Vehicles (UAVs). *Photogrammetric Engineering and Remote Sensing* **2015**, *81*, 281–329.
- Klemas, V.V. Coastal and Environmental Remote Sensing from Unmanned Aerial Vehicles: An Overview. *Journal of Coastal Research* **2015**, *31*, 1260–1267.
- Detweiler, C.; Ore, J.P.; Anthony, D.; Elbaum, S.; Burgin, A.; Lorenz, A. Bringing Unmanned Aerial Systems Closer to the Environment. *Environmental Practice* **2015**, *17*, 188–200.
- Vivoni, E.R.; Rango, A.; Anderson, C.A.; Pierini, N.A.; Schreiner-McGraw, A.P.; Saripalli, S.; Laliberte, A.S. Ecohydrology with unmanned aerial vehicles. *Ecosphere* **2014**, *5*.
- Fladeland, M.; Sumich, M.; Lobitz, B.; Kolyer, R.; Herlth, D.; Berthold, R.; McKinnon, D.; Monforton, L.; Brass, J.; Bland, G. The NASA SIERRA science demonstration programme and the role of small-medium unmanned aircraft for earth science investigations. *Geocarto International* **2011**, *26*, 157–163.
- Tamminga, A.D.; Eaton, B.C.; Hugenholtz, C.H. UAS-based remote sensing of fluvial change following an extreme flood event. *Earth Surface Processes and Landforms* **2015**, *40*, 1464–1476.
- Immerzeel, W.W.; Kraaijenbrink, P.D.A.; Shea, J.M.; Shrestha, A.B.; Pellicciotti, F.; Bierkens, M.F.P.; de Jong, S.M. High-resolution monitoring of Himalayan glacier dynamics using unmanned aerial vehicles. *Remote Sensing of Environment* **2014**, *150*, 93–103.
- Zweig, C.L.; Burgess, M.A.; Percival, H.F.; Kitchens, W.M. Use of Unmanned Aircraft Systems to Delineate Fine-Scale Wetland Vegetation Communities. *Wetlands* **2015**, *35*, 303–309.
- Stocker, C.; Eltner, A.; Karrasch, P. Measuring gullies by synergetic application of UAV and close range photogrammetry - A case study from Andalusia, Spain. *Catena* **2015**, *132*, 1–11.
- Nagai, M.; Chen, T.; Shibasaki, R.; Kumagai, H.; Ahmed, A. UAV-Borne 3-D Mapping System by Multisensor Integration. *Ieee Transactions on Geoscience and Remote Sensing* **2009**, *47*, 701–708.

- Peng, Z.R.; Wang, D.S.; Wang, Z.Y.; Gao, Y.; Lu, S.J. A study of vertical distribution patterns of PM_{2.5} concentrations based on ambient monitoring with unmanned aerial vehicles: A case in Hangzhou, China. *Atmospheric Environment* **2015**, *123*, 357–369.
- Diaz, J.A.; Pieri, D.; Wright, K.; Sorensen, P.; Kline-Shoder, R.; Arkin, C.R.; Fladeland, M.; Bland, G.; Buongiorno, M.F.; Ramirez, C.; Corrales, E.; Alan, A.; Alegria, O.; Diaz, D.; Linick, J. Unmanned Aerial Mass Spectrometer Systems for In-Situ Volcanic Plume Analysis. *Journal of the American Society for Mass Spectrometry* **2015**, *26*, 292–304.
- Alvarado, M.; Gonzalez, F.; Fletcher, A.; Doshi, A. Towards the Development of a Low Cost Airborne Sensing System to Monitor Dust Particles after Blasting at Open-Pit Mine Sites. *Sensors* **2015**, *15*, 19667–19687.
- Martin, S.; Beyrich, F.; Bange, J. Observing Entrainment Processes Using a Small Unmanned Aerial Vehicle: A Feasibility Study. *Boundary-Layer Meteorology* **2014**, *150*, 449–467.
- Cassano, J.J. Observations of atmospheric boundary layer temperature profiles with a small unmanned aerial vehicle. *Antarctic Science* **2014**, *26*, 205–213.
- Bates, T.S.; Quinn, P.K.; Johnson, J.E.; Corless, A.; Brechtel, F.J.; Stalin, S.E.; Meinig, C.; Burkhardt, J.F. Measurements of atmospheric aerosol vertical distributions above Svalbard, Norway, using unmanned aerial systems (UAS). *Atmospheric Measurement Techniques* **2013**, *6*, 2115–2120.
- Reuder, J.; Jonassen, M.O.; Olafsson, H. The Small Unmanned Meteorological Observer SUMO: Recent Developments and Applications of a Micro-UAS for Atmospheric Boundary Layer Research. *Acta Geophysica* **2012**, *60*, 1454–1473.
- Karion, A.; Sweeney, C.; Tans, P.; Newberger, T. AirCore: An Innovative Atmospheric Sampling System. *Journal of Atmospheric and Oceanic Technology* **2010**, *27*, 1839–1853.
- Villa, T.; Gonzalez, F.; Miljevic, B.; Ristovski, Z.; Morawska, L. An Overview of Small Unmanned Aerial Vehicles for Air Quality Measurements: Present Applications and Future Prospectives. *Sensors* **2016**, *16*.
- Brady, J.; Stokes, M.; Bonnardel, J.; Bertram, T. Characterization of a Quadrotor Unmanned Aircraft System for Aerosol-Particle-Concentration Measurements. *Environmental Science and Technology* **2016**, *50*, 1376–1383.
- Roldan, J.; Joossen, G.; Sanz, D.; Cerro, J.; Barrientos, A. Mini-UAV Based Sensory System for Measuring Environmental Variables in Greenhouses. *Sensors* **2015**, *15*, 3334–3350.
- Detert, M.; Weitbrecht, V. A low-cost airborne velocimetry system: proof of concept. *Journal of Hydraulic Research* **2015**, *53*, 532–539.
- Hill, S.L.; Clemens, P. Miniaturization of High-Spectral-Spatial Resolution Hyperspectral Imagers on Unmanned Aerial Systems. In *Next-Generation Spectroscopic Technologies VIII*; Druy, M.A.; Crocombe, R.A.; Bannon, D.P., Eds.; 2015; Vol. 9482, *Proceedings of SPIE*.
- Wildmann, N.; Mauz, M.; Bange, J. Two fast temperature sensors for probing of the atmospheric boundary layer using small remotely piloted aircraft (RPA). *Atmospheric Measurement Techniques* **2013**, *6*, 2101–2113.
- Thornberry, T.D.; Rollins, A.W.; Gao, R.S.; Watts, L.A.; Ciciora, S.J.; McLaughlin, R.J.; Fahey, D.W. A two-channel, tunable diode laser-based hygrometer for measurement of water vapor and cirrus cloud ice water content in the upper troposphere and lower stratosphere. *Atmospheric Measurement Techniques* **2015**, *8*, 211–224.
- Corrigan, C.E.; Roberts, G.C.; Ramana, M.V.; Kim, D.; Ramanathan, V. Capturing vertical profiles of aerosols and black carbon over the Indian Ocean using autonomous unmanned aerial vehicles. *Atmospheric Chemistry and Physics* **2008**, *8*, 737–747.
- Ramana, M.V.; Ramanathan, V.; Kim, D.; Roberts, G.C.; Corrigan, C.E. Albedo, atmospheric solar absorption and heating rate measurements with stacked UAVs. *Quarterly Journal of the Royal Meteorological Society* **2007**, *133*, 1913–1931.
- de Boer, G.; Palo, S.; Argrow, B.; LoDolce, G.; Mack, J.; Gao, R.S.; Telg, H.; Trussel, C.; Fromm, J.; Long, C.N.; Bland, G.; Maslanik, J.; Schmid, B.; Hock, T. The Pilatus unmanned aircraft system for lower atmospheric research. *Atmospheric Measurement Techniques* **2016**, *9*, 1845–1857.

- Freitag, S.; Clarke, A.D.; Howell, S.G.; Kapustin, V.N.; Campos, T.; Brekhovskikh, V.L.; Zhou, J. Combining airborne gas and aerosol measurements with HYSPLIT: a visualization tool for simultaneous evaluation of air mass history and back trajectory consistency. *Atmospheric Measurement Techniques* **2014**, *7*, 107–128.
- Chambers, S.D.; Zahorowski, W.; Williams, A.G.; Crawford, J.; Griffiths, A.D. Identifying tropospheric baseline air masses at Mauna Loa Observatory between 2004 and 2010 using Radon-222 and back trajectories. *Journal of Geophysical Research-Atmospheres* **2013**, *118*, 992–1004.
- Saunois, M.; Bousquet, P.; Poulter, B.; Peregon, A.; Ciais, P.; Canadell, J.G.; Dlugokencky, E.J.; Etiope, G.; Bastviken, D.; Houweling, S.; Janssens-Maenhout, G.; Tubiello, F.N.; Castaldi, S.; Jackson, R.B.; Alexe, M.; Arora, V.K.; Beerling, D.J.; Bergamaschi, P.; Blake, D.R.; Brailsford, G.; Brovkin, V.; Bruhwiler, L.; Crevoisier, C.; Crill, P.; Curry, C.; Frankenberg, C.; Gedney, N.; Höglund-Isaksson, L.; Ishizawa, M.; Ito, A.; Joos, F.; Kim, H.S.; Kleinen, T.; Krummel, P.; Lamarque, J.F.; Langenfelds, R.; Locatelli, R.; Machida, T.; Maksyutov, S.; McDonald, K.C.; Marshall, J.; Melton, J.R.; Morino, I.; O'Doherty, S.; Parmentier, F.J.W.; Patra, P.K.; Peng, C.; Peng, S.; Peters, G.P.; Pison, I.; Prigent, C.; Prinn, R.; Ramonet, M.; Riley, W.J.; Saito, M.; Schroeder, R.; Simpson, I.J.; Spahni, R.; Steele, P.; Takizawa, A.; Thornton, B.F.; Tian, H.; Tohjima, Y.; Viovy, N.; Voulgarakis, A.; van Weele, M.; van der Werf, G.; Weiss, R.; Wiedinmyer, C.; Wilton, D.J.; Wiltshire, A.; Worthy, D.; Wunch, D.B.; Xu, X.; Yoshida, Y.; Zhang, B.; Zhang, Z.; Zhu, Q. The Global Methane Budget: 2000–2012. *Earth System Science Data Discussions* **2016**, *2016*, 1–79.
- Watai, T.; Machida, T.; Ishizaki, N.; Inoue, G. A Lightweight Observation System for Atmospheric Carbon Dioxide Concentration Using a Small Unmanned Aerial Vehicle. *J. Atmos. Oceanic Technol.* **2006**, *23*, 700–710.
- Katsaros, K.B.; Decosmo, J.; Lind, R.J.; Anderson, R.J.; Smith, S.D.; Kraan, R.; Oost, W.; Uhlig, K.; Mestayer, P.G.; Larsen, S.E.; Smith, M.H.; de Leeuw, G. Measurements of Humidity and Temperature in the Marine Environment during the HEXOS Main Experiment. *Atmospheric and Oceanic Technology*, **1994**, *11*, 964.
- Wildmann, N.; Kaufmann, F.; Bange, J. An inverse-modelling approach for frequency response correction of capacitive humidity sensors in ABL research with small remotely piloted aircraft (RPA). *Atmospheric Measurement Techniques* **2014**, *7*, 3059–3069.
- Chen, R. *A Survey of Nonuniform Inflow Models for Rotorcraft Flight Dynamics and Control Applications*; 1989.
- Lowry, D.; Fisher, R.; France, J.; Lanoiselle, M.; Nisbet, E.; Brunke, E.; Dlugokencky, E.; N., B.; Jones, A. Continuous monitoring of greenhouse gases in the South Atlantic And Southern Ocean: Contributions from the equianos network. *17th WMO/IAEA Meeting of Experts on Carbon Dioxide, Other Greenhouse Gases and related Tracers Measurement Techniques* **2013**, *213*, 109–112.
- Nisbet, E.G.; Dlugokencky, E.; Manning, M.; Lowry, D.; Fisher, R.; France, J.; Michel, S.; Miller, J.; White, J.; Vaughn, B.; Bousquet, P.; Pyle, J.; Warwick, N.; Cain, M.; Brownlow, R.; Zazzeri, G.; Lanoiselle, M.; Manning, A.; Gloor, E.; Worthy, D.; Brunke, E.; Labuschagne, C.; Wolff, E.; Ganesan, A. Rising Atmospheric Methane: 2007–2014 Growth and Isotopic Shift. *Global Biogeochemical Cycles* **2016**, *30*.
- Greatwood, C.; Richardson, T.; Freer, J.; Thomas, R.; Brownlow, R.; Lowry, D.; Fisher, R.E.; Nisbet, E. Automatic Path Generation for Multirotor Descents Through Varying Air Masses above Ascension Island. *AIAA SciTech Forum* **2016**.
- Padfield, G.D. *Helicopter flight dynamics*; John Wiley & Sons, 2008.
- Anderson, S.; Baumgartner, M. Radiative Heating Errors in Naturally Ventilated Air Temperature Measurements Made from Buoys. *Journal of Atmospheric and Oceanic Technology* **1998**, *15*, 157–173.
- Hennemuth, B.; Lammert, A. Determination of the Atmospheric Boundary Layer Height from Radiosonde and Lidar Backscatter. *Boundary-Layer Meteorology* **2006**, *120*, 181–200.
- Dai, C.; Wang, Q.; Kalogiros, J.A.; Lenschow, D.H.; Gao, Z.; Zhou, M. Determining Boundary-Layer Height from Aircraft Measurements. *Boundary-Layer Meteorology* **2014**, *152*, 277–302.
- Brownlow, R.; Lowry, D.; Thomas, R.M.; Fisher, R.E.; France, J.L.; Cain, M.; Richardson, T.S.; Greatwood, C.; Freer, J.; Pyle, J.A.; MacKenzie, A.R.; Nisbet, E.G. Methane mole fraction and

Appendix B

Rising atmospheric methane: 2007-2014 growth and isotopic shift

Contributions to this work are listed in the SI section 17. R. Brownlow contributed to the RHUL part of this work, including plotting and calculating the year on year growth to the Ascension data.

RESEARCH ARTICLE

10.1002/2016GB005406

Key Points:

- Atmospheric methane is growing rapidly
- Isotopic evidence implies that the growth is driven by biogenic sources
- Growth is dominated by tropical sources

Supporting Information:

- Supporting Information S1

Correspondence to:

E. G. Nisbet,
e.nisbet@rhul.ac.uk

Citation:

Nisbet, E. G., et al. (2016), Rising atmospheric methane: 2007–2014 growth and isotopic shift, *Global Biogeochem. Cycles*, 30, 1356–1370, doi:10.1002/2016GB005406.

Received 3 MAR 2016

Accepted 2 SEP 2016

Accepted article online 26 SEP 2016

Published online 27 SEP 2016

Rising atmospheric methane: 2007–2014 growth and isotopic shift

E. G. Nisbet¹, E. J. Dlugokencky², M. R. Manning³, D. Lowry¹, R. E. Fisher¹, J. L. France^{1,4}, S. E. Michel⁵, J. B. Miller^{5,6}, J. W. C. White⁵, B. Vaughn⁵, P. Bousquet⁷, J. A. Pyle^{8,9}, N. J. Warwick^{8,9}, M. Cain^{8,9}, R. Brownlow¹, G. Zazzeri¹, M. Lanoisellé¹, A. C. Manning⁴, E. Gloor¹⁰, D. E. J. Worthy¹¹, E.-G. Brunke¹², C. Labuschagne^{12,13}, E. W. Wolff¹⁴, and A. L. Ganesan¹⁵
¹Department of Earth Sciences, Royal Holloway, University of London, Egham, UK, ²US National Oceanic and Atmospheric Administration, Earth System Research Laboratory, Boulder, Colorado, USA, ³Climate Change Research Institute, School of Geography Environment and Earth Sciences, Victoria University of Wellington, Wellington, New Zealand, ⁴Centre for Ocean and Atmospheric Sciences, School of Environmental Sciences, University of East Anglia, Norwich, UK, ⁵Institute of Arctic and Alpine Research, University of Colorado Boulder, Boulder, Colorado, USA, ⁶Cooperative Institute for Research in Environmental Sciences, University of Colorado Boulder, Boulder, Colorado, USA, ⁷Laboratoire des Sciences du Climat et de l'Environnement, Gif-sur-Yvette, France, ⁸Department of Chemistry, University of Cambridge, Cambridge, UK, ⁹National Centre for Atmospheric Science, Cambridge, UK, ¹⁰School of Geography, University of Leeds, Leeds, UK, ¹¹Environment Canada, Downsview, Ontario, Canada, ¹²South African Weather Service, Stellenbosch, South Africa, ¹³School of Physical and Chemical Sciences, North-West University, Potchefstroom, South Africa, ¹⁴Department of Earth Sciences, University of Cambridge, Cambridge, UK, ¹⁵School of Geographical Sciences, University of Bristol, Bristol, UK

Abstract From 2007 to 2013, the globally averaged mole fraction of methane in the atmosphere increased by 5.7 ± 1.2 ppb yr⁻¹. Simultaneously, $\delta^{13}\text{C}_{\text{CH}_4}$ (a measure of the ¹³C/¹²C isotope ratio in methane) has shifted to significantly more negative values since 2007. Growth was extreme in 2014, at 12.5 ± 0.4 ppb, with a further shift to more negative values being observed at most latitudes. The isotopic evidence presented here suggests that the methane rise was dominated by significant increases in biogenic methane emissions, particularly in the tropics, for example, from expansion of tropical wetlands in years with strongly positive rainfall anomalies or emissions from increased agricultural sources such as ruminants and rice paddies. Changes in the removal rate of methane by the OH radical have not been seen in other tracers of atmospheric chemistry and do not appear to explain short-term variations in methane. Fossil fuel emissions may also have grown, but the sustained shift to more ¹³C-depleted values and its significant interannual variability, and the tropical and Southern Hemisphere loci of post-2007 growth, both indicate that fossil fuel emissions have not been the dominant factor driving the increase. A major cause of increased tropical wetland and tropical agricultural methane emissions, the likely major contributors to growth, may be their responses to meteorological change.

1. Introduction

The methane content of the atmosphere began rising again in 2007 after a growth slowdown that had first become apparent in the late 1990s [Dlugokencky et al., 1998; Nisbet et al., 2014]. The mole fraction of Southern Hemisphere atmospheric methane varied little for 7 years up to 2006 but then started to increase in early 2007. Since 2007, sustained increases in atmospheric methane mole fraction have occurred in most latitudinal zones of the planet but with major local short-term excursions from the overall spatial pattern of growth (Figure 1). In the Northern Hemisphere autumn of 2007, rapid growth was measured in the Arctic and boreal zone (Figure 1). However, both in 2007 and thereafter, global growth has dominantly been driven by the latitudes south of the Arctic/boreal zone, for example, both north and south of the equator in 2008 and in the southern tropics in 2010–2011. Even compared to the increases of preceding years, 2014 was exceptional, with extremely strong annual (1 January 2014 to 1 January 2015) growth at all latitudes, especially in the equatorial belt (Figure 1).

CH₄ mole fractions provide insufficient information to determine definitively the causes of the recent rise [Kirschke et al., 2013]. Isotopic measurements [Dlugokencky et al., 2011] provide powerful constraints that can help to identify specific source contributions. Atmospheric methane is also becoming more depleted in the isotope ¹³C. At any individual location, local meteorological factors such as shifting prevailing wind directions may influence measurements; however, the sustained nature of the increase and isotopic shift, and the regional and global distribution of the methane growth, implies that major ongoing changes in methane budgets are occurring.

©2016. The Authors. This article has been contributed to by U.S. Government employees and their work is in the public domain in the U.S.A. This is an open access article under the terms of the Creative Commons Attribution License, which permits use, distribution and reproduction in any medium, provided the original work is properly cited.

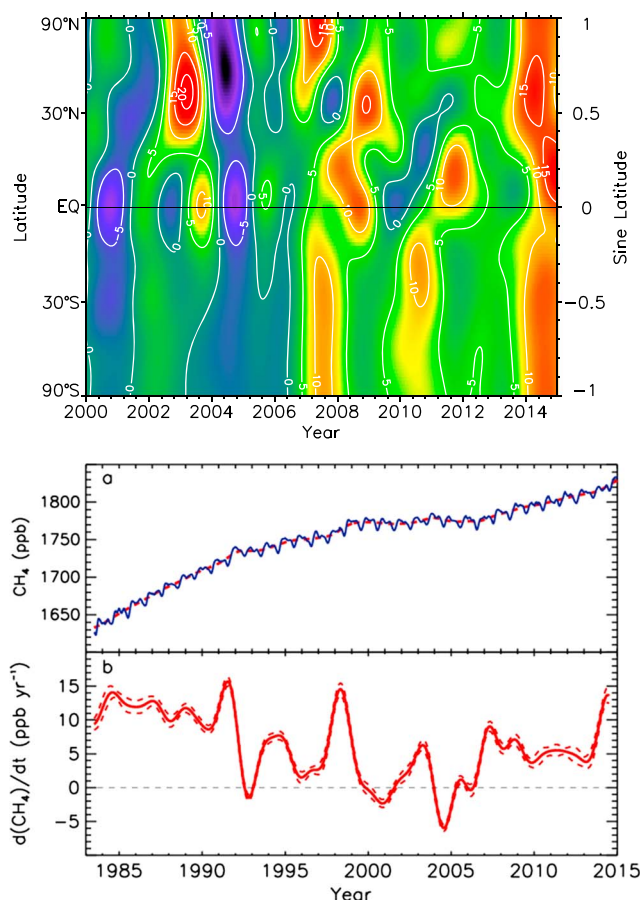


Figure 1. Global trends in CH_4 from 2000 to the end of 2014. (top) Global sine latitude versus time plot of CH_4 growth rate. Green, yellow, and red colors show increases; blue, dark blue, and violet show declines, contoured in increments of 5 ppb yr^{-1} . (bottom) Globally averaged methane and growth rates in 1983–2014. Plot a shows atmospheric mole fraction. Red dashed line is a deseasonalized trend curve fitted to the global averages. Plot b shows instantaneous growth rate from the time derivative of the red dashed line in plot a. Thin dashed lines are ± 1 standard deviation.

Figure 1 illustrates the CH_4 record over the three decades since the start of detailed global monitoring by NOAA (http://www.esrl.noaa.gov/gmd/ccgg/trends_ch4/). The very high growth rates in the 1980s (~ 14 ppb in 1984 and >10 ppb yr^{-1} through 1983–1991) [Dlugokencky *et al.*, 1998; Dlugokencky *et al.*, 2011] were driven by the strong increase in anthropogenic emissions in the post-War years, for example, from the Soviet gas industry [Dlugokencky *et al.*, 1998]. In 1992 the eruption of Mt. Pinatubo and the major El Niño event had important impacts on sources and sinks. Following this, growth rates declined. Major reductions in leaks from the gas industry may have contributed to the reduction in growth rates [Dlugokencky *et al.*, 1998]. Strong growth resumed briefly during the strong El Niño event of 1997–1998, but apart from this single event, methane growth rates were subdued in the period 1992–2007. The overall trend from 1983 to 2007 is consistent with an approach to equilibrium [Dlugokencky *et al.*, 2011], implying no trend in total global emissions and an atmospheric lifetime of approximately 9 years.

2. Methods

Observations reported here are from measurements made by the USA National Oceanic and Atmospheric Administration (NOAA) Cooperative Global Air Sampling Network, for whom the Institute of Arctic and Alpine Research (INSTAAR) carry out $\delta^{13}\text{C}_{\text{CH}_4}$ measurement on a subset of the same air samples analyzed for CH_4 , by Royal Holloway, University of London (RHUL, UK), and by the University of Heidelberg (UHEI). Details are

Recently, Schaefer *et al.* [2016] used a one-box model of CH_4 mole fraction and $\delta^{13}\text{C}_{\text{CH}_4}$ isotopic data to reconstruct the global history of CH_4 emissions to the atmosphere. They concluded that the isotopic evidence demonstrates that emissions of thermogenic methane (e.g., from fossil fuels and biomass burning) were not the dominant cause of the post-2007 growth and pointed out that this contradicts emission inventories. In contrast, Schaefer *et al.* [2016] concluded that the cause of the post-2007 rise was primarily an increase in biogenic emissions and that these emissions were located outside the Arctic. Furthermore, they inferred that the increased emissions were probably more from agricultural sources than from wetlands.

The evidence reported here includes new Atlantic and Arctic methane mole fraction and isotopic data and develops the analysis by using a running budget analysis (see supporting information S1, section 16) of monthly averages over four latitude zones instead of annual averages and a one-box model. This detailed analysis permits latitudinal differentiation of changes in CH_4 emission sources, which our isotopic data show have significant interannual variability in the overall trend to more negative values since 2007.

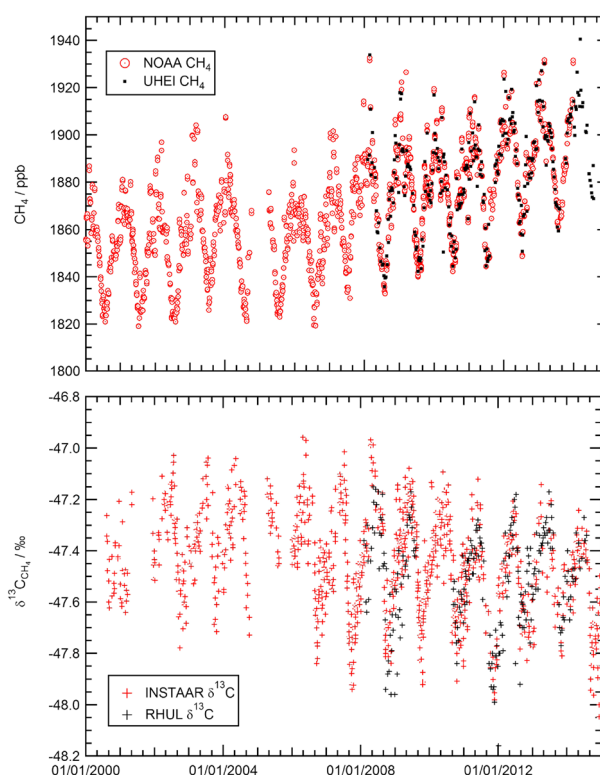


Figure 2. (top) Methane mole fraction and (bottom) $\delta^{13}\text{C}_{\text{CH}_4}$ isotope measurements in discrete air samples collected from Alert, Canada. Mole fraction data from NOAA and University of Heidelberg (UHEI) samples; isotopic measurements from NOAA-INSTAAR and RHUL.

by $5.7 \pm 1.2 \text{ ppb yr}^{-1}$ (parts per billion, or nmol mol^{-1} , dry air, ± 1 standard deviation of annual increases; uncertainty of each annual increase is $\sim \pm 0.5 \text{ ppb yr}^{-1}$). Growth has continued strongly with an increase of $12.5 \pm 0.4 \text{ ppb}$ in 2014. Simultaneously, results presented here show that $\delta^{13}\text{C}_{\text{CH}_4}$ (a measure of the $^{13}\text{C}/^{12}\text{C}$ isotope ratio in methane) has recently shifted significantly to more negative values. For example, prior to 2007, as monitored in remote equatorial Southern Hemisphere air at Ascension Island, $\delta^{13}\text{C}_{\text{CH}_4}$ was stable or increased slightly, with $\delta^{13}\text{C}_{\text{CH}_4}$ changing by less than $+0.01\text{‰ yr}^{-1}$. Post 2007, $\delta^{13}\text{C}_{\text{CH}_4}$ started to decrease. The shift has been in excess of -0.03‰ yr^{-1} , with a total shift of $-0.24 \pm 0.02\text{‰}$ by 2014. Similar patterns to those observed at Ascension have been observed globally, though with regional variation (Figure S10).

3.1. Methane $\delta^{13}\text{C}_{\text{CH}_4}$ in High Northern Latitudes: Alert, Canada ($82^\circ 27' \text{N}$, $62^\circ 31' \text{W}$)

Methane mole fractions (Figure 2, top and Figure S1) in NOAA air samples from Alert, Nunavut, Canada, which are representative of the western Arctic, show a sharp increase in summer 2007. In September 2007, methane measured at Alert was 16 ppb higher than in the previous September, although note that single-month comparisons can depend heavily on sustained local meteorological conditions. That year, the annual increase averaged over 53°N to 90°N was $13.3 \pm 1.3 \text{ ppb}$. But this was not sustained. In 2008, 2010, and markedly so in 2011–2012, Arctic growth was below global means. As fast horizontal mixing at high latitudes efficiently links Arctic emission zones with Alert [Bousquet *et al.*, 2011], this indicates that from 2008 to 2013 no major sustained new methane emission increase occurred in the wider Arctic. In 2014, year-on-year strong Arctic increases began anew (Figure S1) but at a rate comparable with the global increase that year.

In the NOAA air samples from Alert, an overall isotopic trend to more depleted $\delta^{13}\text{C}_{\text{CH}_4}$ is apparent, beginning in about 2006 (Figure 2, bottom). Since 2008, $\delta^{13}\text{C}_{\text{CH}_4}$ measurements made by RHUL and NOAA on Alert air samples show that this overall negative trend has been maintained through 2013, with a slight positive relaxation since (Figure 2, bottom, and Figure S10).

given in the supporting information S1, sections 6–8. Mole fraction measurements are reported on the World Meteorological Organization X2004A scale [Dlugokencky *et al.*, 2005 updated at http://www.esrl.noaa.gov/gmd/ccl/ch4_scale.html].

By comparing data from different laboratories, we have checked for systematic bias among the measurement programs. Further details on RHUL-INSTAAR intercomparison are in the supporting information S1, sections 8–10.

3. Measurements

To understand the factors driving global methane trends in the past decade, we focus on key background stations in regions where significant methane events have occurred: (1) the Arctic and boreal zone, (2) the Atlantic equatorial tropics, and (3) the Southern Hemisphere.

From 2007 to 2013, we report that the globally averaged mole fraction of methane in the atmosphere increased

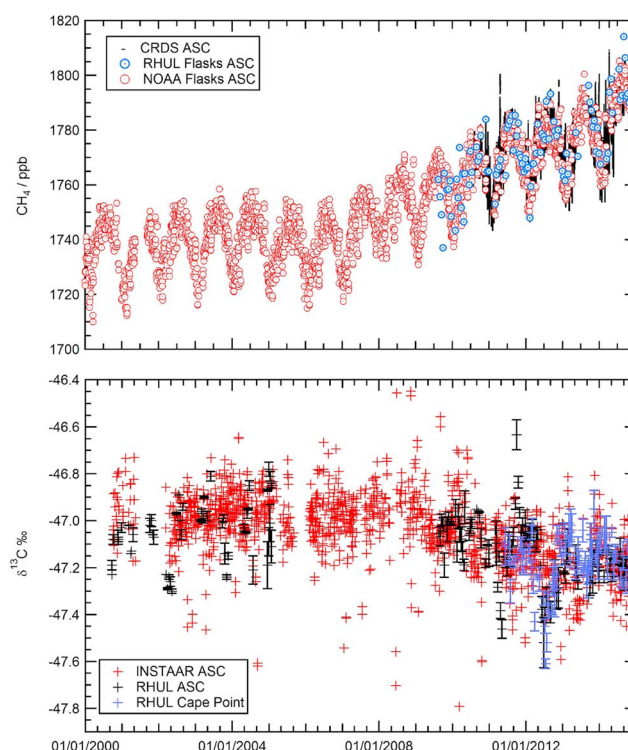


Figure 3. (top) Methane mole fraction from Airhead, Ascension Island. Red circles are NOAA discrete air samples from 2000. The black line shows RHUL continuous observations, and blue squares show RHUL flask air samples from the same site. (bottom) South Atlantic $\delta^{13}\text{C}_{\text{CH}_4}$ data, 2000–2015. The graph shows both NOAA-INSTAAR (red crosses) and RHUL measurements (black crosses, showing error bars) from Ascension (ASC) and RHUL data from Cape Point, South Africa (CPT; purple crosses and error bars). See Figure S4 for trend analysis: Change in $\delta^{13}\text{C}_{\text{CH}_4}$ pre-2007 was less than $+0.01\text{‰ yr}^{-1}$; post-2007, the shift has been in excess of -0.03‰ yr^{-1} .

impact on year-on-year comparison). Further details of growth are given in the supporting information S1, section 4 and Figure S3.

In low latitudes of the Southern Hemisphere, between the equator and 30°S (i.e., southern tropics and extratropical winter rainfall belts), smoothed annual (January to January) growth trends in the NOAA network show similar behavior. In this latitudinal zone there was near-zero growth from 2001 to 2006 (including a decline in 2004 and 2005) followed by growth of 7.9 ± 0.5 ppb in 2007, 7.0 ± 0.5 ppb in 2008, 2.6 ± 0.5 ppb in 2009, 8.1 ± 0.4 ppb in 2010, 4.8 ± 0.3 ppb in 2011, 4.3 ± 0.3 ppb in 2012, 5.8 ± 0.5 ppb in 2013, and 11.2 ± 0.4 ppb in 2014.

The $\delta^{13}\text{C}_{\text{CH}_4}$ record of marine boundary air sampled at Ascension Island is shown in Figure 3 (bottom). In general, methane in the Southern Hemisphere, much of which has passed through the OH-rich region in the midtroposphere around the brightly lit and humid Intertropical Convergence Zone (ITCZ), is slightly “heavier,” that is, richer in ^{13}C , than north of the equator, where the dominant sources are located. Error bars in individual measurements are also shown in the figure. The data show poorly defined $\delta^{13}\text{C}_{\text{CH}_4}$ isotopic seasonality and from 2001 to 2005 show no significant trend. Both NOAA and RHUL datasets independently show a shift ($>0.2\text{‰}$) to more ^{13}C -depleted values from 2009, becoming more marked with excursions to much more negative values in early 2011 and 2012. Values have since recovered to slightly less negative values by the end of 2014, but Ascension $\delta^{13}\text{C}_{\text{CH}_4}$ values through into 2015 have stabilized around 0.2‰ , more negative than in 2007–2008. This shift is far greater than experimental uncertainty (see error bars on figure). If the trends are assumed to be linear, the shift pre-2007 was less than $+0.01\text{‰ yr}^{-1}$; post 2007, the shift has been in excess of -0.03‰ yr^{-1} (see Figure S4). Ongoing 2015 $\delta^{13}\text{C}_{\text{CH}_4}$ measurements suggest continuing decline. The assumption of a linear change in $\delta^{13}\text{C}_{\text{CH}_4}$ is, however, a broad simplification.

3.2. Atlantic Equatorial Air—Methane and $\delta^{13}\text{C}_{\text{CH}_4}$ at Ascension Island ($7^\circ 58'\text{S}$, $14^\circ 24'\text{W}$)

At Ascension Island, strong growth in methane has been sustained from 2007 to 2014 (Figure 3, top; see also Figures S3 and S4). Taking all RHUL and NOAA measurements together, in 2010–2011 year-on-year (January to January) growth, calculated from a smoothed spline, was 10.1 ± 2.9 ppb, in contrast to the global growth rate of 5.0 ± 0.7 ppb in the NOAA data that year. In 2011–2012, an HPspline curve fit [Pickers and Manning, 2015] of the Ascension record shows moderate growth compared to other years (3.4 ± 1.1 ppb) and again in 2012–2013 (3.0 ± 0.9 ppb) followed by stronger growth in 2013–2014 (8.9 ± 2.7 ppb, compared to a global growth of 5.9 ± 0.5 ppb). Following 2014, very strong growth has resumed, with the year-on-year growth in monthly averages well over 10 ppb yr^{-1} . In 2014–2015, RHUL measurements show extreme growth of 12.7 ± 2.3 ppb, especially toward the end of the year (but note that at a single location, short timescale meteorological variability can have a large

3.3. Comparison With Other Southern Latitude Sites: Cape Point, South Africa (34°21'S, 18°30'E), and South Pole

Hybrid Single Particle Lagrangian Integrated Trajectory model (HYSPLIT) (http://www.arl.noaa.gov/HYSPLIT_info.php) [Stein *et al.*, 2015] air mass backward trajectories indicate that much of the air reaching Ascension in early to mid-2012 was from the southwestern South Atlantic, including prior inputs of air from south of the equator in South America (see Figure S2), and from the Southern Ocean. From Cape Point, the RHUL flask sampling record of methane mole fraction and $\delta^{13}\text{C}_{\text{CH}_4}$ (Figure 3; see also Figure S5) begins in 2011 and the NOAA record in 2009. There was moderate annual growth in mole fraction (5 ppb in 2011–2012, 3 ppb in 2012–2013) until 2013–2014, when a strong (>10 ppb) year-on-year rise took place. The RHUL $\delta^{13}\text{C}_{\text{CH}_4}$ record shows a sharp shift to isotopically more negative values in 2012, reverting to previous levels in early 2013 and then perhaps becoming slightly more negative again in 2014. These Cape Point values are similar to those observed in RHUL air samples from Ascension over the same time.

Southern Hemisphere background trends are represented by NOAA samples from the South Pole (Figures S6 and S7). These measurements record strong and sustained methane growth from 2007 onward. In the polar Southern Hemisphere (60–90°S), zonal average annual means were 1726 ± 0.1 ppb in 2006, rising to 1774 ± 0.1 ppb in 2014. Concurrent with this growth is a sustained shift to more negative $\delta^{13}\text{C}_{\text{CH}_4}$, also beginning around 2006 (see Figures S6 and S8). The pronounced negative dip observed at the South Pole in late 2011 is comparable to the Ascension dip in 2011 and 2012. At the South Pole, as for Ascension, if the $\delta^{13}\text{C}_{\text{CH}_4}$ trends are assumed to be linear, the shift pre-2007 was negligible; post-2007, the shift has been about -0.03‰ yr^{-1} (see Figure S8).

4. Global Evolution of Trends in Methane Mole Fraction and Isotopic Values

What hypotheses can be proposed to account for these observations? In this section, possible explanations are proposed, both for the Arctic trends and for the trends observed in the savanna and equatorial tropics; then in section 5 a running budget analysis is used to investigate the hypotheses for plausibility in matching the mole fraction and isotopic records.

4.1. Possible Explanations of the Observed Growth and Isotopic Shift, Arctic and Tropical Zones

Bousquet *et al.* [2006] found that declining growth rates in anthropogenic emissions were the cause of the decreasing atmospheric methane growth rates during the 1990s but that after 1999 anthropogenic emissions of methane rose again. The effect of this increase was initially masked by a decrease in wetland emissions, but remote sensing data show that surface water extent started to increase again in 2002 [Prigent *et al.*, 2012]. Recent widening of the Hadley Cell [Min and Son, 2013; Tselioudis *et al.*, 2016] would have extended the high rainfall zone under the ITCZ, increasing both natural wetland and agricultural emissions in the tropics. Thus, these sources are discussed in detail, by region.

4.1.1. Arctic

The most obvious explanation of the increase in Arctic methane in 2007 is an increase in emissions. If so, isotopic and time-of-season constraints both point to increased late summer Arctic and boreal wetland emissions. Methane emitted from Arctic and boreal wetlands is markedly depleted isotopically: in Fennoscandia, atmospheric sampling and Keeling plot studies [Fisher *et al.*, 2011; Sriskantharajah *et al.*, 2012] showed that the emissions had $\delta^{13}\text{C}_{\text{CH}_4}$ values of $-70 \pm 5\text{‰}$, while Canadian boreal wetland emissions are around $-67 \pm 2\text{‰}$ (unpublished RHUL studies). These values are close to the $\delta^{13}\text{C}_{\text{CH}_4}$ value of around -68‰ of the regional Arctic summer methane increment over Atlantic background, indicating that the summer source is mainly from wetlands [Sriskantharajah *et al.*, 2012; Fisher *et al.*, 2011]. In contrast, gas field and hydrate sources are too enriched in ^{13}C to produce the observed shift. Siberian gas fields are very large but typically have $\delta^{13}\text{C}_{\text{CH}_4}$ around $-50 \pm 3\text{‰}$ [Dlugokencky *et al.*, 2011], which is close to bulk atmospheric values and after dilution in regional air masses would be unlikely to produce the shift observed in the Alert values. Similarly, Fisher *et al.* [2011] and Berchet *et al.* [2016] found no evidence for large hydrate emissions.

Thus, the most likely explanation of the sharp growth in Arctic methane in late 2007, and the concurrent trend to more negative $\delta^{13}\text{C}_{\text{CH}_4}$ values in ambient Arctic methane, is an increase in wetland emissions. The year 2007 was an exceptional year in the Arctic, when the North American Arctic wetlands experienced unusually sunny skies and large temperature increases compared to past records, with warm southerly winds

[Kay *et al.*, 2007]. The anomalous temperatures and southerly winds [Comiso *et al.*, 2008] likely drove very strong growth of summer and autumn emissions from Arctic and boreal wetlands. Bergamaschi *et al.* [2013] reported an increase in emissions of 2–3 Tg CH₄ in 2007, then below average emissions from 2008 to 2010. Similarly, Bruhwiler *et al.* [2014] estimated that in 2007, the emissions were 4.4 Tg CH₄ higher than the decadal average. The very depleted $\delta^{13}\text{C}_{\text{CH}_4}$ values from Alert in autumn 2007 thus most probably record the presence of methane-rich boreal and Arctic wetland air.

From 2008 to 2013, growth of methane and isotopic shifts in the Arctic were unexceptional compared to the global record; in 2014 very strong growth occurred, but similar growth occurred elsewhere worldwide. Overall, although Arctic emissions contributed to the Arctic methane shift in 2007, they do not seem to have been major contributors since then.

4.1.2. Tropics and Southern Hemisphere: Isotopic Signatures of Sources South of 30°N

Most of the strongest growth in methane since 2007 has been led by the wider tropics, here taken as the zone between the Tropics of Cancer and Capricorn (23°26') and also including the region experiencing passage of the Intertropical Convergence Zone (ITCZ) in South and East Asia. Saunio *et al.* [2016] found from top-down studies that almost two thirds (~64%) of the global methane emissions are from south of 30°N, while latitudes north of 60°N contribute only 4%. In the tropics, the main biogenic methane emissions are in subequatorial and savanna wetlands, from rice paddies and ruminants in southern and Southeast Asia and from ruminants in India, South America, and savanna Africa [Kirschke *et al.*, 2013; Dlugokencky *et al.*, 2011]; on grasslands dominated by grasses using the C4 pathway; and widespread biomass burning, especially in Africa's C4 savannas. The main anthropogenic sources in the region are not well quantified but include large ruminant populations, especially in India but also in China, Southeast Asia, South America, and Africa, in addition to dry season (winter) biomass burning. Thermogenic fossil fuel sources in the region include South Africa's coal industry, subequatorial gas fields in South America, and widespread large gas fields and coal fields in Asia and Australia.

The $\delta^{13}\text{C}_{\text{CH}_4}$ values of tropical wetland methane emissions to the air (as opposed to methane within the water/vegetation/mud columns) are poorly constrained but appear typically to be around $-54 \pm 5\text{‰}$ (unpublished RHUL results in Uganda, Southeast Asia, Peru, and Ascension; and from Dlugokencky *et al.* [2011]). This contrasts with values of around -68‰ for Arctic wetlands [Fisher *et al.*, 2011]. In the northern tropics, wetland flooding from runoff is typically in the late rainy season (August–September onward) or later in river-fed swamps. Conversely, in the southern tropics (e.g., Bolivia and Zambia) wetlands fill in February–March onward. Tropical seasonal wetland emissions are readily distinguishable from dry season biomass burning emissions that come a few months later from the same general regions. Methane in smoke from grass fires in tropical C4 grasslands in winter (NH: November–February; SH: May–August) has $\delta^{13}\text{C}_{\text{CH}_4}$ values around -20‰ to -10‰ (unpublished RHUL results and see supporting information S1, section 1 and Dlugokencky *et al.* [2011]). Thus, biomass burning injects methane with $\delta^{13}\text{C}_{\text{CH}_4}$ that is more positive than the atmosphere: in this context, the continuing shift to negative values in 2014, an El Niño year, is of interest as such events are usually associated with biomass burning [Duncan *et al.*, 2003].

The $\delta^{13}\text{C}_{\text{CH}_4}$ values of tropical ruminant methane emissions have been very little studied in the field. Schaefer *et al.* [2016] assumed that ruminants are C3-fed and emit methane with $\delta^{13}\text{C}_{\text{CH}_4}$ of -60‰ , but grasslands and ruminant fodder crops in the tropics tend to be C4 rather than C3 dominated. Dlugokencky *et al.* [2011] considered C4 ruminant methane emissions to be $-49 \pm 4\text{‰}$, and thus tropical ruminant emissions are likely more enriched in $\delta^{13}\text{C}_{\text{CH}_4}$ than the 60‰ value assumed by Schaefer *et al.* [2016]. Many free-grazing tropical ruminants live in C4 savanna grasslands, and supplemental fodder may be maize, millet, sorghum crop waste, or sugar cane tops, all $\delta^{13}\text{C}_{\text{CH}_4}$ -enriched C4 plants. Thus, it is likely that methane from such cows is substantially more enriched than the -60‰ C3 value and more likely to have $\delta^{13}\text{C}_{\text{CH}_4}$ values around -50‰ or less [Dlugokencky *et al.*, 2011]. But tropical data are very sparse.

Fossil fuel emissions in the region south of 30°N are typically isotopically enriched in $\delta^{13}\text{C}_{\text{CH}_4}$, although published isotopic measurements are few. For example, Bolivian gas in La Paz is -35‰ (unpublished RHUL results), while the very large Pars gas field in Qatar/Iran is -40‰ [Galimov and Rabbani, 2001]. Methane from Chinese coal is also isotopically enriched and likely to be in the -35 to -45‰ range (own observations and see Thompson *et al.* [2015]). Southern Hemisphere Gondwana coalfield methane from Australia is close to bulk atmospheric values [Hamilton *et al.*, 2014], but some mines can be isotopically depleted compared to

the atmosphere [Zazzeri *et al.*, 2016]. In the Hunter coalfield of Australia (typical of large coal mines in the Southern Hemisphere), Zazzeri *et al.* [2016] report $\delta^{13}\text{C}_{\text{CH}_4}$ of $-66.4 \pm 1.3\text{‰}$ from surveys around bituminous coal mines and -60.8 ± 0.3 around a ventilation shaft. Some of the more negative values may reflect the input of secondary biogenic methane into the coalfield emissions. Worldwide, open cast coal mining may be associated with the production of some isotopically lighter microbial methane.

To summarize overall, although much better site-by-site information is needed, and while emissions from a few fossil sources are isotopically relatively depleted compared to the atmosphere, methane emissions from the majority of large gas and coal fields are characteristically ^{13}C -enriched relative to the atmosphere and thus *not* the cause of the observed isotopic shifts. However, some Southern Hemisphere coalfield emissions from open cast bituminous mines may have contributed to the observed isotopic shift.

4.1.3. Ascension—The Remote Marine Tropics

Ascension lies in the heart of the southern tropics, remote from any landmass, and thus interpretation of its methane record must take note of events in the remote source regions of winds reaching the island, especially in South America (see Figure S2). The Ascension $\delta^{13}\text{C}_{\text{CH}_4}$ record shows a marked change beginning in late 2010, when strong growth was accompanied by a sharp isotopic shift to more depleted $\delta^{13}\text{C}_{\text{CH}_4}$, in parallel with a comparatively subdued CO cycle, albeit with excursions. The Cape Point and South Pole records are similar to the Ascension pattern (Figures 3, S5, and S6). A distant source of air reaching Ascension is Amazonia south of the ITCZ. In 2010, Amazonia experienced a major drought and biomass burning. It is possible that the early 2010 rise in methane at Ascension (Figure 3) may have been driven by biomass burning [Crevoisier *et al.*, 2013], consistent with the observed enrichment of $\delta^{13}\text{C}_{\text{CH}_4}$ in early to mid-2010, both typical results of C4 savanna grassland fires. However, the seasonal timing is perplexingly early in the southern winter. Trajectory studies suggest that such emissions would take some time to mix to Ascension, south of the ITCZ.

The Ascension observational record during this southern summer of 2010–2011 is most simply interpreted as the result of the very strong regional Southern Hemisphere wet season in November 2010 to March 2011, with subsequent very high Amazon flood levels in the first half of 2011 (Figure S12). Precipitation and perhaps also warmth in the wetlands may have driven a major emission pulse of isotopically strongly depleted methane during the later (wetland-filling) part of the Southern Hemisphere wet season, in March–June. This was a period so wet across the equatorial and southern tropics that ocean levels dropped [Boening *et al.*, 2012]. Subsequent years were also wetter than average: record Amazon flood levels were repeatedly observed in 2012, 2013, and again in 2014, when there was heavy precipitation in the eastern flanks of the Andes in Bolivia and Peru, with exceptional flood levels in the Amazon wetlands of Bolivia in 2007, 2008, and 2014 [Ovando *et al.*, 2015] (see also supporting information S1, section 12 and Figure S12). The South American tropics have experienced rising temperatures and increased wet-season precipitation post-2000 [Gloor *et al.*, 2013, 2015], which would further drive increasing emissions of methane, particularly in the very hot year of 2014 [Gedney *et al.*, 2004]. Wetlands in Angola, Zambia, and Botswana likely experienced also high precipitation, as evidenced by flood levels in Lake Kariba and the Okavango River in Botswana (supporting information S1, section 15).

4.1.4. Wetlands and Agriculture

Dlugokencky *et al.* [2009] found that the most likely drivers of methane growth in 2007–2008 were high temperatures in the Arctic and high precipitation in the tropics. In the years since then, much of the growth has a tropical geographic locus, while the isotopic evidence implies that fossil fuel emissions were not the dominant driver. This suggests that tropical wetland or agricultural emissions or a combination of both are the likely dominant causes of the global methane rise from 2008 to 2014. There is much evidence that the variations in the global methane budget are strongly dependent on tropical wetland extents and temperatures [Bousquet *et al.*, 2006].

Tropical wetlands produce around 20–25% of global methane emissions: taking the mean of many models of emissions in 1993–2004 Melton *et al.* [2013] found that wetlands in the 30°N–30°S latitude belt produced $126 \pm 31 \text{ Tg CH}_4 \text{ yr}^{-1}$. Wetland methane emissions respond quickly to meteorological changes in temperature as emission has an exponential dependence on temperature [Gedney *et al.*, 2004; Westerman and Ahiring, 1987] and precipitation (expanding wetland area at the end of the rainy season). Methane emission responds rapidly to flooding and warmth [Bridgman *et al.*, 2013], with lags of a few days between flooding and emission [Chamberlain *et al.*, 2016], and methanogenic consortia have high resilience to drought periods.

Bousquet et al. [2016] found that variation in wetland extent could contribute 30–40% of the range of wetland emissions. Emissions show strong seasonality, following the passage of the ITCZ. Savanna wetlands fill in the late rainy seasons, after groundwater has been replenished, typically in February to April in the Southern tropics and August to October in the Northern Hemisphere tropics.

Hodson et al. [2011] showed that a large fraction of global variability in wetland emissions can be correlated with the El Niño–Southern Oscillation (ENSO) index. For example, in the La Niña years of 2007 and 2008, there is evidence that methane emissions from some Amazonian wetland regions may have increased by as much as 50% [*Dlugokencky et al.*, 2009] compared to 2000–2006. Amazon flood levels (see Figure S12) were very high in 2009. In the La Niña of early 2011 [*Boening et al.*, 2012], many southern tropical regions were unusually wet and equatorial Amazon flood levels were again high. Amazon flooding also took place in 2012–2014. In early 2014 (before the onset of the 2014 El Niño), extreme flood events occurred in the Amazon wetlands of Bolivia [*Ovando et al.*, 2015]. Thus, summarizing, southern summer wetland (February–April) or ruminant (November–April) emissions can lead to isotopically depleted excursions, while winter (NH December–March; SH June–September) biomass burning of C4 grasslands produces CO-rich air masses with isotopically enriched methane [*Dlugokencky et al.*, 2011]. The response of emissions to temperature and the lag in wetland drying may in part account for methane growth in some El Niño events (e.g., 1997), but this remains unexplained. In the moderate El Niño event of 2006, *Worden et al.* [2013] showed that methane from Indonesian fires could have compensated for an expected decrease in tropical wetland methane emissions from reduced rainfall.

Agricultural emissions also respond to high rainfall, which supports rice agriculture and fodder growth for ruminants, though widespread water storage and irrigation in the seasonal tropics is now smoothing out the impact of year-to-year fluctuations. There is no evidence for a sudden sharp increase in rice fields in 2007. Rice-harvested area in Asia is increasing but fluctuates: in 1999 (an above-trend year) the area was 140.4 million hectares and 141.0 million hectares in 2009 (a below-trend year). By 2013 Asian rice field area harvested had risen to 146.9 million hectares (<http://ricestat.irri.org:8080/wrs2/entrypoint.htm>). In China, as an example, it is possible that rice agriculture may have contributed to increased emissions, but there is no evidence for a step change in rice fields under cultivation: indeed, paddy field area harvested is relatively stable and declined from 2006 to 2007 (<http://faostat.fao.org>). Tropical agricultural emissions from ruminants are indeed likely to have increased in highly rainy seasons, but if so, these increases were probably mainly in South America and Africa. This is because in India, the nation with the world's largest ruminant population, recent monsoons have mostly been average to poor, and cattle populations have declined (see supporting information S1, section 11).

4.2. Methane Sink Variation?

A possible explanation for global methane growth is that destruction rates reduced over this time period. The global atmospheric burden of methane corresponding to 1 ppb is about 2.77 Tg of methane. Reaction with tropospheric OH is the main methane sink: for example, a 1% change in OH abundance, equivalent to a $\sim 5 \text{ Tg CH}_4 \text{ yr}^{-1}$ change in methane emissions, or roughly 2 ppb globally, could contribute significantly to an apparent “source shift” over several years. OH abundance is greatest in the bright sunlight of the moist tropical troposphere and thus can vary significantly with short-term changes in tropical meteorology and pollution. For example, the major global wildfires during the intense El Niño event of 1997–1999 coincided with, and likely caused, an OH minimum [see *Prinn et al.*, 2005; *Duncan et al.*, 2003].

The long-term trend, if any, in OH abundances is not well understood [*Prinn et al.*, 2005; *Patra et al.*, 2014], but there is evidence for OH having small interannual variations [*Montzka et al.*, 2011]. OH is well buffered in the tropical upper troposphere [*Gao et al.*, 2014], and globally OH appears to have been stable within $\pm 3\%$ over 1985–2008: this result is more reliable from 1997 onward [*Rigby et al.*, 2008]. *Rigby et al.* [2008] inferred a large, but uncertain, decrease in OH in 2007 ($-4 \pm 14\%$), implying that part of the growth in methane mole fraction in 2007 may have been driven by a smaller sink; however, that work had not considered the isotopic CH_4 data. During 2006–2008, OH may have only varied by less than 1% globally, although larger regional changes may have occurred, with some evidence for low OH over the western Pacific warm pool [*Rex et al.*, 2014]. Thus, there is little *prima facie* evidence that a major change in OH has driven methane's rise and isotopic shift. Methane removal by the atomic Cl sink, discussed in supporting information S1, section 16, is also unlikely to explain the observed changes.

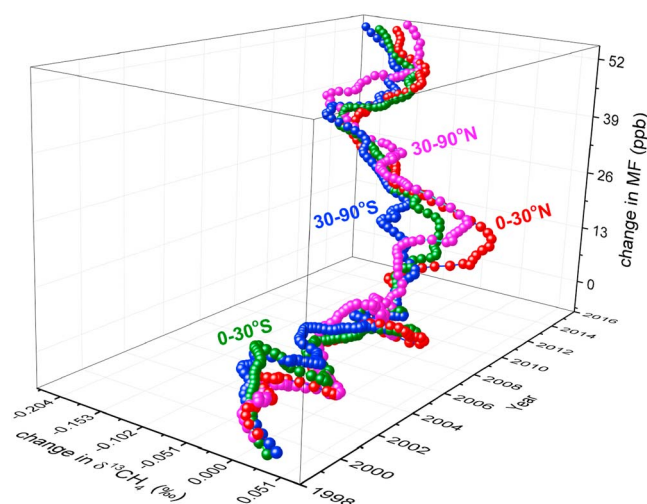


Figure 4. Three-dimensional graphic for changes in $\delta^{13}\text{C}_{\text{CH}_4}$ and mole fraction with time, showing midpoints for the years marked. MF = mole fraction. Color code: blue = 30–90°S, green = 0–30°S, red = 0–30°N, mauve = 30–90°N.

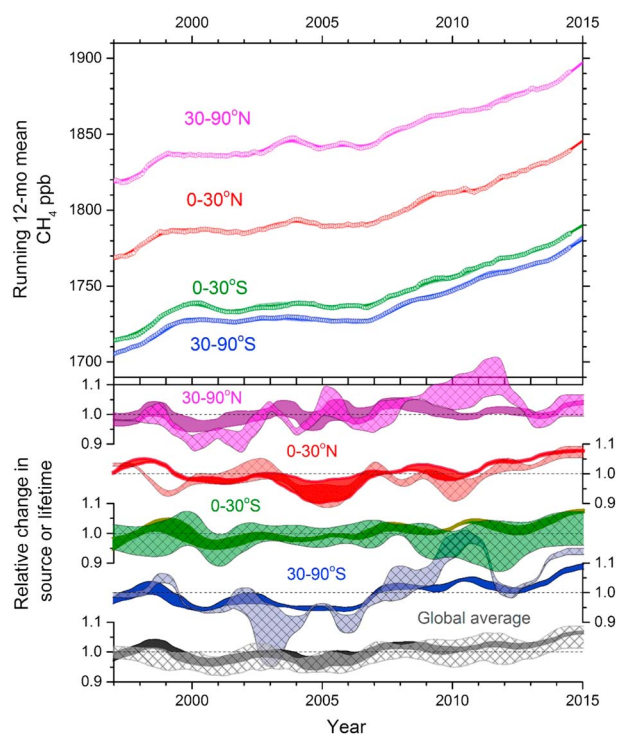


Figure 5. (top) Running 12 month means of methane mole fractions from the NOAA Cooperative Global Air Sampling Network averaged over 0–30° and 30–90° latitude regions in each hemisphere (see supporting information S1, section 16). Uncertainty bands around these running means show the range of mole fraction values that remain after correcting for average site differences. Ranges for fits to the data are shown using changes either in CH_4 source emissions (darker) or in removal rates (lighter); however, as each gives good fits to the mole fractions these are hard to distinguish. (bottom) The corresponding ranges for relative changes in zonal CH_4 source emissions (darker) or lifetimes, i.e., the inverse of removal rates (lighter and crosshatched) for each region and for the global average. See text for source emission and removal rate ranges.

5. Running Budget Analysis and Interpretation of Shifts in the $\delta^{13}\text{C}_{\text{CH}_4}$ Record

An objective analysis of the cause for the recent rise in methane requires a balanced consideration of changes in sources or removal rates. Figure 4 summarizes the changes with time of mole fraction and $\delta^{13}\text{C}_{\text{CH}_4}$ over the period since 1998. The importance of $\delta^{13}\text{C}_{\text{CH}_4}$ data for identifying such changes in CH_4 sources or removal rates is becoming increasingly clear [Monteil *et al.*, 2011; Ghosh *et al.*, 2015].

To consider how the most recent data can clarify explanations for the increase in mole fraction together with the striking concurrent reversal of the long-term trend for increasing $\delta^{13}\text{C}_{\text{CH}_4}$ over the last hundred years, a latitudinally zoned monthly budget analysis is carried out here. Two hypotheses to explain the recent changes in the methane mole fraction and isotopic records are considered: (a) “changes in emissions” or (b) “changes in removal rates.” The second option also considers whether a spatial redistribution of removal rates can explain the recent changes in atmospheric CH_4 .

There are still significant uncertainties in the CH_4 budget, as shown by the bottom-up estimates for emissions from natural sources over 2000–2009 being 50% larger than their top-down estimates and the range of estimates for anthropogenic emissions being 100% larger for top-down estimates than for bottom-up estimates [Ciais *et al.*, 2013]. However, the focus here is to consider how recent changes in the budget can cause a transition from the relatively stable period over 1999–2006 to significant increases in mole fraction together with decreases in $\delta^{13}\text{C}_{\text{CH}_4}$ over 2007–2014. This is done by considering the magnitudes and timings of changes to a central estimate for the top-down budget [Kirschke *et al.*, 2013; Ciais *et al.*, 2013] which can explain the observations. This is not designed to improve our understanding of the total budget

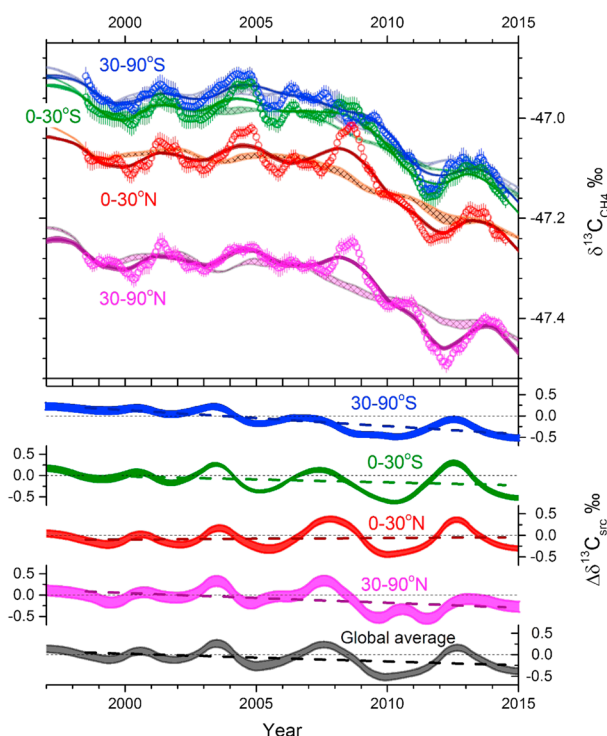


Figure 6. (top) Running 12 month means for $\delta^{13}\text{C}_{\text{CH}_4}$ from the NOAA and RHUL sites that have also been combined to represent averages over the four regions. Results from the budget analysis are shown for changes in source emissions (darker) or removal rates (lighter and crosshatched) as in Figure 5. (bottom) The corresponding variations in source $\delta^{13}\text{C}$ (‰) for the four regions and for the global average source $\delta^{13}\text{C}$.

but rather to assess how much it has to change to explain recent data.

A simple running budget analysis is used here to compare how variations in CH_4 emissions or in its removal rate can explain the observed changes in mole fraction and $\delta^{13}\text{C}_{\text{CH}_4}$ data. The focus is on 1998–2014. However, NOAA mole fraction data from 1983, together with ice core and firn air data [Ferretti *et al.*, 2005], and earlier NIWA (New Zealand National Institute of Water and Atmospheric Research) $\delta^{13}\text{C}_{\text{CH}_4}$ data over 1992–1997 [Lassey *et al.*, 2000] have also been used to carry out a spin-up phase for this analysis.

Monthly average mole fraction and $\delta^{13}\text{C}_{\text{CH}_4}$ data are used to determine the total emissions and their $\delta^{13}\text{C}$ values for four semihemisphere regions (30–90°S, 0–30°S, 0–30°N, and 30–90°N) but with the focus being on long-term trends and major year-to-year variations around these, rather than specific regional effects. CH_4 mixes within each hemisphere over periods of a few months and between hemispheres over about 1 year. As shown in Figures S13 and S14, this

leads to a fairly stable spatial distribution modulated by seasonal cycles that depend on location but have relatively small interannual variations [Dlugokencky *et al.*, 1994]. Cubic spline fits to the CH_4 data for the four regions are then used to compare how monthly variations in emissions or in removal rates can reproduce the data over 1998–2014.

Interannual variations are shown by using running 12 month means to remove the seasonal cycle for the observed mole fraction data in Figure 5 and for $\delta^{13}\text{C}_{\text{CH}_4}$ in Figure 6. However, the budget analysis is fitted to monthly data, as shown in supporting information S1, section 16, in order to cover seasonal cycles in emissions and removal rates that have nonlinear effects on isotope ratios.

The differential equations used here to relate mole fractions to emissions and removal rates are

$$\frac{d}{dt}C_i = S_i - K_i C_i - \sum_j X_{ij}(C_i - C_j) \quad (1)$$

where i denotes a region, C_i are mole fractions in units of ppb, S_i are emission rates in units of ppb/yr, K_i are removal rates (1/yr), and X_{ij} are exchange rates between the one or two adjacent regions. The differential equations used for $\delta^{13}\text{C}_{\text{CH}_4}$ are similar to Lassey *et al.* [2000] where simpler differential equations for $^{13}\text{C}/^{12}\text{C}$, are treated by using systematic differences between $^{13}\text{C}/^{12}\text{C}$ and $^{13}\text{C}/^{12}\text{C}$ ratios as

$$[^{13}\text{CH}_4] = (1 + \delta)R_{\text{PDB}}[^{12}\text{CH}_4] = \frac{(1 + \delta)R_{\text{PDB}}}{[1 + (1 + \delta)R_{\text{PDB}}]}C_i = (1 + \delta')R_{\text{PDB}}C_i \quad (2)$$

where $R_{\text{PDB}} = 0.0112372$ for the VPDB (Vienna Pee Dee Belemnite) standard, and δ' applies to the $^{13}\text{C}/^{12}\text{C}$ ratios. The differential equations for $^{13}\text{CH}_4$ mole fractions, now written as F_i , are then

$$\frac{d}{dt}F_i = (1 + \delta'_i)R_{\text{PDB}}S_i - (1 + \varepsilon)K_i(1 + \delta'_i)R_{\text{PDB}}C_i - \sum_j X_{ij}(F_i - F_j) \quad (3)$$

Table 1. The Range of Options Considered in Determining Fits of Sources or of Removal Rates to the Regional Mole Fraction and $\delta^{13}\text{C}_{\text{CH}_4}$ Data

Process	Option 1	Option 2
<i>Seasonal Cycles</i>		
OH removal	<i>Spivakovsky et al. [2000]</i>	
Cl removal	Constant	Same as OH
Soil removal	Constant	Same as OH
Cross tropopause transport	Constant	
Source	Fitted to data for each region, no interannual variability	
Source $\delta^{13}\text{C}$	Fitted to data for each region, no interannual variability	
<i>Spatial Distributions</i>		
OH removal	<i>Spivakovsky et al. [2000]</i>	
Cl removal	Uniform	SH only
Soil removal	Proportional to land area	
Cross tropopause transport	Uniform	Low latitudes only
<i>Interannual Variations</i>		
Removal rates	Source fits	Removal rate fits
Source	No change	Vary over 1992–2014
Source $\delta^{13}\text{C}_\text{S}$	Vary over 1990–2014	Vary over 1990–1998
Exchange rates 1990–2014	Vary over 1998–2014	Vary over 1990–1998
	Fixed varying	Fixed varying

where δ'_{Si} are for the source $^{13}\text{C}/\text{C}$ ratios, and ε is the Kinetic Isotope Effect for the removal rate. This can then be simplified to

$$\frac{d}{dt}\delta'_i = (\delta'_{\text{Si}} - \delta'_i)(S_i/C_i) - \varepsilon K_i - \sum_j X_{ij}(\delta'_i - \delta'_j)(C_j/C_i) \quad (4)$$

While equation (1) and its equivalent for $^{13}\text{CH}_4$ used in some analyses [Schaefer et al., 2016] are linear equations, (4) makes it clear that the δ'_i have nonlinear relationships with the S_i and C_i .

Mole fraction data from 51 NOAA sites together with $\delta^{13}\text{C}_{\text{CH}_4}$ data from 20 NOAA sites and 2 RHUL sites are used, but because of limited spatial coverage for $\delta^{13}\text{C}_{\text{CH}_4}$ data, monthly averages over four semihemispheres, covering 0–30° and 30–90° zonal regions, are used to determine corresponding emissions, removal, and transport. The CH_4 emissions and their $\delta^{13}\text{C}$ values are fitted to the observed mole fraction and $\delta^{13}\text{C}_{\text{CH}_4}$ data using a range of estimates for removal rates consistent with the last IPCC (Intergovernmental Panel on Climate Change) assessment report [Ciais et al., 2013] but covering options for spatial and seasonal distributions of the removal by soils, tropospheric Cl, and cross tropopause transport which are less well defined than they are for removal by OH. Interannual variations in exchange rates between the regions are also considered as another option. Then for comparison an alternative set of model runs allows interannual variations in the removal rate over 1998–2014 while keeping the emissions fixed after 1999. In both cases this is a simple form of inverse modeling that avoids prior estimates of the source budget and treats interannual variations in either source emissions or in removal rates equally. More details of the data averaging and running budget analysis are provided in Table 1 and in supporting information S1, section 16.

5.1. Mole Fraction Constraints

Most of the variation in mole fraction data can be explained by either of the two hypotheses: “changes in source emissions,” or “changes in removal rates”, or a combination of both. Models assuming changes in emissions only and “changes in removals” only are shown in Figure 5. While there are some systematic differences between data and fits, the residuals are only slightly larger for the changes in removal option.

The changes in source emissions model shown in Figure 5 has emissions in the range 560–580 Tg $\text{CH}_4 \text{ yr}^{-1}$ when averaged over 1998–2014, similar to values of Kirschke et al. [2013], with 11% in the 30–90°S region, 27% in 0–30°S, 32% in 0–30°N, and 30% in 30–90°N. There is a source trend of 0.8 to 1.5% yr^{-1} in the 0–30°N region over 2005 to 2014 in contrast to the 30–90°N that has a trend of –0.5 to +0.1% yr^{-1} over this period. In the 0–30°S region this trend is 0.4 to 0.5% yr^{-1} , and in the 30–90°S region it is 0.8 to 0.9% yr^{-1} . The larger relative variations for 30–90°S may reflect this zone’s emissions being small relative to the global total

making it more sensitive to variations in transport such as an increasing extent of Hadley circulation [Tselioudis *et al.*, 2016]. Total source increases over this period are in the range of 3 to 6% and predominantly in the 0–30°S and 0–30°N regions. These source changes are described in more detail in supporting information S1, section 16 and are consistent with other estimates [Dlugokencky *et al.*, 2009; Bousquet *et al.*, 2011] but have now been continuing for 9 years.

If, alternatively, changes in removal rates (or lifetimes) are used to explain the CH₄ mole fraction data, then significantly larger relative variations are needed than for source variations; however, this is partly due to the constraints also being imposed by the $\delta^{13}\text{C}_{\text{CH}_4}$ data as shown below. Over 1998–2014, variations of 7%–10% are used in the low latitudes and 15%–25% in the high latitudes. In particular, the slowdown in CH₄ growth rate over 2009–2011 requires very large increases in the lifetimes in high latitudes and some compensating reduction in lifetimes in the low latitudes. Relative changes in the global mean lifetime are smaller because of these compensating effects, but it still requires an increase of ~10% over 2000–2014. This is much larger than expected fluctuations of OH radicals [Montzka *et al.* 2011]. Furthermore, because cross tropopause transport is expected to remove ~8% of CH₄ while reaction with Cl and the soil sink each account for 4–5% [Ciais *et al.*, 2013], variations in removal rate that are required to explain the observed mole fraction data cannot be explained without some significant changes in OH.

5.2. Isotopic Constraints

An even clearer distinction between the two modeled hypotheses is shown when isotopes are considered (Figure 6). The shift in the bulk $\delta^{13}\text{C}_{\text{CH}_4}$ value of the global source is about -0.17‰ . The changes in source emissions option follows the interannual variations in $\delta^{13}\text{C}_{\text{CH}_4}$ much better than the changes in removal rates option and this is more obvious in the Northern Hemisphere where these variations are large. Furthermore, variations in removal rates cannot explain the large positive anomalies in 2004 and 2008 or the large negative anomaly over 2011–2012.

Source $\delta^{13}\text{C}$ values averaged over 1998–2014 for the regions are in the following ranges: $-57.8 \pm 0.05\text{‰}$ for 30–90°S; $-53.9 \pm 0.04\text{‰}$ for 0–30°S; $-51.9 \pm 0.07\text{‰}$ for 0–30°N; and $-53.4 \pm 0.13\text{‰}$ for 30–90°N. In addition to significant interannual variations mentioned above there is also clearly a longer-term trend of decreasing $\delta^{13}\text{C}_{\text{CH}_4}$ values. Figure 6 shows that this corresponds to a decrease in source $\delta^{13}\text{C}$ values that started 5 to 10 years earlier as would be expected because of the significant lag in the $\delta^{13}\text{C}_{\text{CH}_4}$ response to change [Tans, 1997]. The most obvious trends in source $\delta^{13}\text{C}$ are in the 30–90°S and 30–90°N regions, but there is also a negative trend in the 0–30°S region (see also Figure S4). This spatial pattern for trends in source isotopic signatures may relate to the long-term decrease in biomass burning over this period [Le Quéré *et al.*, 2014] at the same time as an increase in wetland emissions [Bousquet *et al.*, 2011]. Also, the timing for this change in source $\delta^{13}\text{C}$ values is consistent with satellite data showing trends in land surface open water areas that decreased from 1993 to 2002 but then started to increase [Prigent *et al.*, 2012].

While an increase in lifetimes, i.e., decrease in removal rates by OH and other sinks, could reproduce the long-term decrease in $\delta^{13}\text{C}_{\text{CH}_4}$, this analysis shows that it requires major changes in the global average removal rate as well as large fluctuations in the four semihemispheres, while still not accounting for much of the year-to-year interannual variations. The extent to which reversal of the long-term trend in $\delta^{13}\text{C}_{\text{CH}_4}$ could be caused by a decrease in OH is heavily constrained by the more direct tracers of OH which suggest that it has no long-term trend [Montzka *et al.*, 2011]. However, a much larger fractionation occurs in removal by soil methanotrophy, and this can be anticorrelated with methanogenesis [Bridgman *et al.*, 2013] so that changes in wetlands could be having a larger relative effect on the seasonal cycle for $\delta^{13}\text{C}_{\text{CH}_4}$ than for the mole fraction. Furthermore, the large isotopic fractionation due to reaction with Cl in the marine boundary layer is sensitive to temperature, and this may lead to interannual variability that may have been recognized in some data not included here [Allan *et al.*, 2001].

6. Conclusions

The $\delta^{13}\text{C}_{\text{CH}_4}$ isotopic shifts reported here and the likelihood that changes in the OH methane sink are not consistent with the observed trends suggest that from 2007 growth in atmospheric methane has been largely driven by increased biogenic emissions of methane, which is depleted in ^{13}C . Both the majority of this methane increase and the isotopic shift are biogenic. This growth has been global but, apart from 2007, has

been led from emissions in the tropics and Southern Hemisphere, where the isotopically depleted biogenic sources are primarily microbial emissions from wetlands and ruminants, with the trend in source $\delta^{13}\text{C}_{\text{CH}_4}$ in the 0–30°S zone being particularly interesting.

While significant uncertainties in the global methane budget still remain, our top-down analysis has shown that relative increases in the global average emissions of 3–6% together with a shift of about -0.17‰ in the bulk $\delta^{13}\text{C}_{\text{CH}_4}$ value of the global source over the last 12 years can explain much of the observed trends in methane's mole fraction and $\delta^{13}\text{C}_{\text{CH}_4}$ values. Alternative explanations, such as increases in the global average atmospheric lifetime of methane, would have to have been an unrealistic 5–8% over this period and cannot explain the interannual variations observed in $\delta^{13}\text{C}_{\text{CH}_4}$.

Although fossil fuel emissions have declined as a proportion of the total methane budget, our data and results cannot rule out an increase in absolute terms, especially if the source gas were isotopically strongly depleted in ^{13}C : however, both the latitudinal analysis and isotopic constraints rule out Siberian gas, which is around -50‰ [Dlugokencky *et al.*, 2011], as a cause of the methane rise, and emissions from other fossil fuel sources such as Chinese coal, US fracking, or most liquefied natural gas are typically more enriched in ^{13}C and thus also do not fit the isotopic constraints.

The evidence presented here, and in the supporting information, is that the growth, isotopic shift, and geographic location coincide with the unusual meteorological conditions of the past 9 years, especially in the tropics. These events included the extremely warm summer and autumn in 2007 in the Arctic, the intense wet seasons in the Southern Hemisphere tropics under the ITCZ in late 2010–2011 and subsequent years, and also the very warm year of 2014. The monsoonal 0°–30°N Northern Hemisphere, probably especially in South and East Asia [Nisbet *et al.*, 2014; Patra *et al.*, 2016], also contributed to post-2011 growth.

Schaefer *et al.* [2016], using a one-box model, considered but rejected the hypothesis that wetland emissions have been the primary cause of methane growth. This was on the basis of remote sensing data that suggested that growth was led from the Northern Hemisphere and also isotopic arguments, as they assumed that tropical ruminants were C3-fed. They preferred the hypothesis that growth has been driven by agricultural emissions but commented that the evidence was “not strong.” The evidence presented here for the latitudinal distribution of growth suggests that Southern Hemisphere wetland emissions may have been more important than thought by Schaefer *et al.* [2016].

Our study concurs with Schaefer *et al.* [2016] that the methane rise is a result of increased emissions from biogenic sources. The location and strong interannual variability of the methane growth suggest that a fluctuating natural source is predominant rather than an anthropogenic one. Rice field and ruminant emissions have likely contributed significantly to the rise in tropical methane emissions, but rice-harvested areas and animal populations change slowly and there is little evidence for a step change in 2007 that is capable of explaining the trend change in the methane record. Consequently, while agricultural emissions are likely to be increasing, as postulated by Schaefer *et al.* [2016], and probably have been an important component in the recent increase, we find that tropical wetlands are likely the dominant contributor to recent growth.

Schaefer *et al.* [2016] raised the troubling concern that the need to control methane emissions may conflict with food production. They warned that, “if so, mitigating CH_4 emissions must be balanced with the need for food production.” This is a valid concern, but we believe that changes in tropical precipitation and temperature may be the major factors now driving methane growth, both in natural wetlands and in agriculture.

Renewed growth in atmospheric methane has now persisted for 9 years. The methane record from 1983 to 2006 (Figure 1) shows a clear trend to steady state [Dlugokencky *et al.*, 2009; Dlugokencky *et al.*, 2011], apart from “one-off” events, such as the impact of the Pinatubo eruption in 1991–1992 and the intense El Niño of 1997–1998. But the current growth is different and has been sustained since 2007, although the modeling work presented above suggests that the present trend to more isotopically depleted values may have started in the last years of the previous century. The abrupt timing of the change in growth trend in 2007 is consistent with a hypothesis that the growth change was primarily in response to meteorological driving factors. Changes in emissions from anthropogenic sources, such as fossil fuels, agricultural ruminant populations, and area of rice fields under cultivation, would be more gradual. The strong isotopic shifts measured in late

2010–2011 are consistent with a response to the intense La Niña. The exceptional global methane increase in 2014 (Figure 1) was accompanied by a continuation of the recent isotopic pattern (Figures 2, 3, and S10).

The scale and pace of the present methane rise (roughly 60 ppb in 9 years since the start of 2007), and the concurrent isotopic shift showing that the increase is dominantly from biogenic sources, imply that methane emission (both from natural wetlands and agriculture) is responding to sustained changes in precipitation and temperature in the tropics. If so, is this merely a decadal-length weather oscillation, or is it a troubling harbinger of more severe climatic change? Is the current sustained event in the normal range of meteorological fluctuation? Or is a shift occurring that is becoming comparable in scale to events recorded in ice cores [Wolff and Spahni, 2007; Möller et al., 2013; Sperlich et al., 2015]? In the past millennium between 1000 and 1700 C.E., methane mole fraction varied by no more than about 55 ppb [Ferretti et al., 2005]. Methane in past global climate events has been both a “first indicator” and a “first responder” to climatic change [Severinghaus and Brook, 1999; Möller et al., 2013; Etheridge et al., 1998]. Comparison with these historic events suggests that if methane growth continues, and is indeed driven by biogenic emissions, the present increase is already becoming exceptional, beyond the largest events in the last millennium.

Acknowledgments

This work was supported by the UK NERC projects NE/N016211/1 The Global Methane Budget, NE/M005836/1 Methane at the edge, NE/K006045/1 The Southern Methane Anomaly and NE/I028874/1 MAMM. We thank the UK Meteorological Office for flask collection and hosting the continuous measurement at Ascension, the Ascension Island Government for essential support, and Thumeka Mkololo for flask collection in Cape Town. Data sources and archiving are listed in the supporting information S1, section 2. RHUL data are being stored with the UK Centre for Environmental Data Analysis. NOAA data are accessible from ftp://afftp.cmdl.noaa.gov/data/greenhouse_gases/ch4/flask/surface/. For figures, see the U.S. NOAA ESRL website and <http://www.esrl.noaa.gov/gmd/ccgg/figures/>. INSTAAR data found in the readme file are available from ftp://afftp.cmdl.noaa.gov/data/trace_gases/ch4c13/flask/surface/ and ftp://afftp.cmdl.noaa.gov/data/trace_gases/ch4c13/flask/surface/README_surface_flask_ch4c13.html

References

- Allan, W., M. R. Manning, K. R. Lassey, D. C. Lowe, and A. J. Gomez (2001), Modelling the variation of $\delta^{13}\text{C}$ in atmospheric methane: Phase ellipses and the kinetic isotope effect, *Global Biogeochem. Cycles*, 15(2), 467–481, doi:10.1029/2000GB001282.
- Berchet, A., et al. (2016), Atmospheric constraints on the methane emissions from the East Siberian Shelf, *Atmos. Chem. Phys.*, 16, 4147–4157.
- Bergamaschi, P., et al. (2013), Atmospheric CH_4 in the first decade of the 21st century: Inverse modeling analysis using SCIAMCHY satellite retrievals and NOAA surface measurements, *J. Geophys. Res. Atmos.*, 118, 7350–7369, doi:10.1002/jgrd.50480.
- Boening, C., J. K. Willis, F. W. Landerer, R. S. Nerem, and J. Fasullo (2012), The 2011 La Niña: So strong the oceans fell, *Geophys. Res. Lett.*, 39, L19602, doi:10.1029/2012GL053055.
- Bousquet, P., et al. (2006), Contribution of anthropogenic and natural sources to atmospheric methane variability, *Nature*, 443, 439–443.
- Bousquet, P., et al. (2011), Source attribution of the changes in atmospheric methane for 2006–2008, *Atmos. Chem. Phys.*, 11, 3689–3700.
- Bridgman, S. D., H. Cadillo-Quiroz, J. K. Keller, and Q. Zhuang (2013), Methane emissions from wetlands: Biogeochemical, microbial, and modeling perspectives from local to global scales, *Global Change Biol.*, 19, 1325–1346.
- Bruhwyler, L. M., E. Dlugokencky, K. Masarie, M. Ishizawa, A. Andrews, J. Miller, C. Sweeney, P. Tans, and D. Worthy (2014), CarbonTracker- CH_4 : An assimilation system for estimating emissions of atmospheric methane, *Atmos. Chem. Phys.*, 14, 8269–8293.
- Chamberlain, S. D., N. Gomez-Casanovas, M. T. Walter, E. H. Boughton, C. J. Bernacchi, E. H. DeLucia, P. M. Groffman, E. W. Keel, and J. P. Sparks (2016), Influence of transient flooding on methane fluxes from sub-tropical pastures, *J. Geophys. Res. Biogeosci.*, 121, 965–977, doi:10.1002/2015JG003283.
- Ciais, P., et al. (2013), Chapter 6: Carbon and other biogeochemical cycles, in *Working Group I Contribution to the IPCC Fifth Assessment Report (AR5), Climate Change 2013: The Physical Science Basis*, edited by T. Stocker et al., Cambridge University Press, Cambridge.
- Comiso, J. C., C. L. Parkinson, R. Gersten, and L. Stock (2008), Accelerated decline in the Arctic sea ice cover, *Geophys. Res. Lett.*, 35, L01703, doi:10.1029/2007GL031972.
- Crevoisier, C., et al. (2013), The 2007–2011 evolution of tropical methane in the mid-troposphere as seen from space by MetOp-A/IASI, *Atmos. Chem. Phys.*, 13, 4279–4289.
- Dlugokencky, E. J., K. A. Masarie, P. M. Lang, P. P. Tans, L. P. Steele, and E. G. Nisbet (1994), A dramatic decrease in the growth rate of atmospheric methane in the northern hemisphere during 1992, *Geophys. Res. Lett.*, 21, 45–8.
- Dlugokencky, E. J., K. A. Masarie, P. M. Lang, and P. P. Tans (1998), Continuing decline in the growth rate of atmospheric methane, *Nature*, 393, 447–450.
- Dlugokencky, E. J., R. C. Myers, P. M. Lang, K. A. Masarie, A. M. Crotwell, K. W. Thoning, B. D. Hall, J. W. Elkins, and L. P. Steele (2005), Conversion of NOAA atmospheric dry air CH_4 mole fractions to a gravimetrically prepared standard scale, *J. Geophys. Res.*, 110, D18306, doi:10.1029/2005JD006035.
- Dlugokencky, E. J., et al. (2009), Observational constraints on recent increases in the atmospheric CH_4 burden, *Geophys. Res. Lett.*, 36, L18803, doi:10.1029/2009GL039780.
- Dlugokencky, E. J., E. G. Nisbet, R. E. Fisher, and D. Lowry (2011), Global atmospheric methane: Budget, changes, and dangers, *Philos. Trans. R. Soc. London, Ser. A*, 369, 2058–2072.
- Duncan, B. N., R. V. Martin, A. C. Staudt, R. Yevich, and J. A. Logan (2003), Interannual and seasonal variability of biomass burning emissions constrained by satellite observations, *J. Geophys. Res.*, 108(D2), 4040, doi:10.1029/2002JD002378.
- Etheridge, D. M., L. P. Steele, R. J. Francey, and R. L. Langenfelds (1998), Atmospheric methane between 1000 A.D. and present: Evidence of anthropogenic emissions and climatic variability, *J. Geophys. Res.*, 103, 15,979–15,993, doi:10.1029/98JD00923.
- Ferretti, D. F., et al. (2005), Unexpected changes to the global methane budget over the past 2000 years, *Science*, 309, 1714.
- Fisher, R. E., et al. (2011), Arctic methane sources: Isotopic evidence for atmospheric inputs, *Geophys. Res. Lett.*, 38, L21803, doi:10.1029/2011GL049319.
- Galimov, E. M., and A. R. Rabbani (2001), Geochemical characteristics and origin of natural gas in southern Iran, *Geochem. Int.*, 39, 780–792.
- Gao, R. S., K. H. Rosenlof, D. W. Fahey, P. O. Wennberg, E. J. Hintsa, and T. F. Hanisco (2014), OH in the tropical upper troposphere and its relationships to solar radiation and reactive nitrogen, *J. Atmos. Chem.*, 71, 55–64.
- Gedney, N., P. M. Cox, and C. Huntingford (2004), Climate feedback from wetland methane emissions, *Geophys. Res. Lett.*, 31, L20503, doi:10.1029/2004GL020919.
- Ghosh, A., et al. (2015), Variations in global methane sources and sinks during 1910–2010, *Atmos. Chem. Phys.*, 15, 2595–2612.
- Gloor, M., R. J. W. Brien, D. Galbraith, T. R. Feldpausch, J. Schöngart, J.-L. Guyot, J. C. Espinoza, J. Lloyd, and O. L. Phillips (2013), Intensification of the Amazonian hydrological cycle over the last two decades, *Geophys. Res. Lett.*, 40, 1729–1733, doi:10.1002/grl.50377.

- Gloor, M., J. Barichivich, G. Ziv, R. Brien, J. Schöngart, P. Peylin, B. B. Ladvat Cintra, T. Feldpausch, O. Phillips, and J. Baker (2015), Recent Amazon climate as background for possible ongoing and future changes of Amazon humid forests, *Global Biogeochem. Cycles*, **29**, 1384–1399, doi:10.1002/2014GB005080.
- Hamilton, S. K., S. D. Golding, K. A. Baublys, and J. S. Esterle (2014), Stable isotopic and molecular composition of desorbed coal seam gases from the Walloon Subgroup, eastern Surat Basin, Australia, *Int. J. Coal Geol.*, **122**, 21–36.
- Hodson, E. L., B. Poulter, N. E. Zimmermann, C. Prigent, and J. O. Kaplan (2011), The El Niño–Southern Oscillation and wetland methane interannual variability, *Geophys. Res. Lett.*, **38**, L08810, doi:10.1029/2011GL046861.
- Kay, J. E., T. L'Ecuyer, A. Gettelman, G. Stephens, and C. O'Dell (2007), The contribution of cloud and radiation anomalies to the 2007 Arctic Sea Ice minimum, *Geophys. Res. Lett.*, **35**, L08503, doi:10.1029/2008GL033451.
- Kirschke, S., et al. (2013), Three decades of global methane sources and sinks, *Nat. Geosci.*, **6**, 813–823.
- Lassey, K. R., D. C. Lowe, and M. R. Manning (2000), The trend in atmospheric methane $\delta^{13}\text{C}$ and implications for isotopic constraints on the global methane budget, *Global Biogeochem. Cycles*, **14**, 41–49.
- Le Quééré, C., et al. (2014), Global carbon budget 2013, *Earth Syst. Sci. Data*, **6**, 235–263.
- Melton, J. R., et al. (2013), Present state of global wetland extent and wetland methane modeling: Conclusions from a model intercomparison project (WETCHIMP), *Biogeosciences*, **10**, 753–788.
- Min, S.-K., and S.-W. Son (2013), Multimodal attribution of the Southern Hemisphere Hadley cell widening: Major role of ozone depletion, *J. Geophys. Res. Atmos.*, **118**, 3007–3015, doi:10.1002/jgrd.50232.
- Möller, L., T. Sowers, M. Bock, R. Spahni, M. Behrens, J. Schmitt, H. Miller, and H. Fischer (2013), Independent variations of CH_4 emissions and isotopic composition over the past 160,000 years, *Nat. Geosci.*, **6**, 885–890.
- Monteil, G., S. Houweling, E. J. Dlugokencky, G. Maenhout, B. H. Vaughn, J. W. C. White, and T. Rockmann (2011), Interpreting methane variations in the past two decades using measurements of CH_4 mixing ratio and isotopic composition, *Atmos. Chem. Phys.*, **11**, 9141–9153.
- Montzka, S. A., M. Krol, E. Dlugokencky, B. Hall, P. Jöckel, and J. Lelieveld (2011), Small interannual variability of global atmospheric hydroxyl, *Science*, **331**, 67–69.
- Nisbet, E. G., E. J. Dlugokencky, and P. Bousquet (2014), Methane on the rise – Again, *Science*, **343**, 493–5.
- Ovando, J., J. Tomasella, D. A. Rodriguez, J. M. Martinez, J. L. Siqueira-Junior, G. L. N. Pinto, P. Passy, P. Vauchel, L. Noriega, and C. von Randow (2015), Extreme flood events in the Bolivian Amazon wetlands, *J. Hydrol. Reg. Stud.*, **5**, 293–308.
- Patra, P. K., et al. (2014), Observational evidence for inter-hemispheric hydroxyl-radical parity, *Nature*, **513**, 219–223.
- Patra, P. K., et al. (2016), Regional methane emission estimation based on observed atmospheric concentrations (2002–2012), *J. Met. Soc. Jpn.*, **94**, 91–113.
- Pickers, P. A., and A. C. Manning (2015), Investigating bias in the application of curve fitting programs to atmospheric time series, *Atmos. Meas. Tech.*, **8**, 1469–1489.
- Prigent, C., F. Papa, F. Aires, C. Jiménez, W. B. Rossow, and E. Matthews (2012), Changes in land surface water dynamics since the 1990s and relation to population pressure, *Geophys. Res. Lett.*, **39**, L08403, doi:10.1029/2012GL051276.
- Prinn, R. G., et al. (2005), Evidence for variability of atmospheric hydroxyl radicals over the past quarter century, *Geophys. Res. Lett.*, **32**, L07809, doi:10.1029/2004GL022228.
- Rex, M., et al. (2014), A tropical West Pacific OH minimum and implications for stratospheric composition, *Atmos. Chem. Phys.*, **14**, 4827–4841.
- Rigby, M., et al. (2008), Renewed growth of atmospheric methane, *Geophys. Res. Lett.*, **35**, L22805, doi:10.1029/2008GL036037.
- Saunio, M., et al. (2016), The Global Methane budget: 2000–2012, *Earth Syst. Sci. Data Discuss.*, doi:10.5194/essd-2016-25.
- Schaefer, H., et al. (2016), A 21st century shift from fossil-fuel to biogenic methane emissions indicated by $^{13}\text{CH}_4$, *Science*, **352**, 80–84.
- Severinghaus, J. P., and E. J. Brook (1999), Abrupt climate change at the end of the last glacial period inferred from trapped air in polar ice, *Science*, **286**, 930–934.
- Sperlich, P., H. Schaefer, S. E. Mikaloff Fletcher, M. Guillevis, K. Lassey, C. J. Sapart, T. Röckmann, and T. Blunier (2015), Carbon isotope ratios suggest no additional methane from boreal wetlands during the rapid Greenland Interstadial 21.2, *Global Biogeochem. Cycles*, **29**, 1962–1976, doi:10.1002/2014GB005007.
- Spivakovskiy, C. M., et al. (2000), Three dimensional climatological distribution of tropospheric OH: Update and evaluation, *J. Geophys. Res.*, **105**, 8931–8980, doi:10.1029/1999JD901006.
- Srisankharajah, S., R. E. Fisher, D. Lowry, T. Aalto, J. Hatakka, M. Aurela, T. Laurila, A. Lohila, E. Kuitunen, and E. G. Nisbet (2012), Stable carbon isotope signatures of methane from a Finnish subarctic wetland, *Tellus B*, **64**, 18818.
- Stein, A. F., R. R. Draxler, G. D. Rolph, B. J. B. Stunder, M. D. Cohen, and F. Ngan (2015), NOAA'S HYSPLIT Atmospheric Transport and Dispersion Modeling System, *Bull. Am. Meteorol. Soc.*, **96**, 2059–2077, doi:10.1175/bams-d-14-00110.1.
- Tans, P. P. (1997), A note on isotopic ratios and the global atmospheric methane budget, *Global Biogeochem. Cycles*, **11**, 77–81, doi:10.1029/96GB03940.
- Thompson, R. L., et al. (2015), Methane emissions in East Asia for 2000–2011 estimated using an estimated Bayesian inversion, *J. Geophys. Res. Atmos.*, **120**, 4352–4369, doi:10.1002/2014JD022394.
- Tselioudis, G., B. R. Lipat, D. Konsta, K. M. Grise, and L. M. Polvani (2016), Midlatitude cloud shifts, their primary link to the Hadley cell, and their diverse radiative effects, *Geophys. Res. Lett.*, **43**, 4594–4601, doi:10.1002/2016GL068242.
- Westerman, P., and B. K. Ahring (1987), Dynamic of methane production, sulfate reduction and denitrification in a permanently waterlogged alder swamp, *Appl. Environ. Microbiol.*, **53**, 2554–2559.
- Wolff, E., and R. Spahni (2007), Methane and nitrous oxide in the ice core record, *Philos. Trans. R. Soc. London, Ser. A*, **365**, 1775–1792.
- Worden, J., et al. (2013), El Niño, the 2006 Indonesian peat fires, and the distribution of atmospheric methane, *Geophys. Res. Lett.*, **40**, 4938–4943, doi:10.1002/grl.50937.
- Zazzeri, G., et al. (2016), Carbon isotopic signature of coal-derived methane emissions to atmosphere: From coalification to alteration, *Atmos. Chem. Phys. Discuss.*, doi:10.5194/acp-2016-235.

Global Biogeochemical Cycles

Supporting Information for

Rising atmospheric methane: 2007-14 growth and isotopic shift.

E.G. Nisbet¹, E.J. Dlugokencky², M.R. Manning³, D. Lowry¹, R.E. Fisher¹, J.L. France^{1,4}, S. E. Michel⁵, J.B. Miller^{5,6}, J.W.C. White⁵, B. Vaughn⁵, P. Bousquet⁷, J.A. Pyle⁸, N.J. Warwick⁸, M. Cain⁸, R. Brownlow¹, G. Zazzeri¹, M. Lanoisellé¹, A.C. Manning⁴, E. Gloor⁹, D.E.J. Worthy¹⁰, E.-G. Brunke¹¹, C. Labuschagne^{11,12}, E.W. Wolff¹³, A.L. Ganesan¹⁴

Contents of this file

1. Methane Budget: Sources, Sinks, Controls on Carbon Isotopic Ratios
2. Data sources and archiving
3. Alert, Nunavut, Canada (82°27'N, 62°31'W)
4. Ascension Island (7°58'S, 14°24'W)
5. Cape Point Observatory (34°21'S, 18°30'E)
6. NOAA's South Pole Station (90°S)
7. Global growth by zone
8. Mole fraction: Intercomparison between RHUL and NOAA
9. Methane isotope measurement at RHUL and INSTAAR
10. Isotopic measurement: $\delta^{13}\text{C}_{\text{CH}_4}$ Intercomparison between RHUL, INSTAAR and NIWA-New Zealand
11. Ruminant emissions
12. Coal and Gas emissions
13. Methane inventory emissions inventories
14. Variability of methane production from Tropical Wetland
15. Isotopic Trends
16. Methane Budget Variations
17. Contributions to the Work.
- References for Supporting Information

Figure SI1 Alert – Methane mole fraction as measured in NOAA flask-air

Figure SI2 Sources of air arriving in the marine boundary layer at Ascension in 2010

Figure SI3 Ascension Island – Methane mole fraction as measured in NOAA flask-air

Figure SI4 Ascension Island: $\delta^{13}\text{C}_{\text{CH}_4}$ growth rates 2000-2014

Figure SI5 Cape Point: RHUL CH_4 and RHUL $\delta^{13}\text{C}_{\text{CH}_4}$ record, 2011-2014

Figure SI6 South Pole NOAA CH_4 and NOAA-INSTAAR $\delta^{13}\text{C}_{\text{CH}_4}$ record, 2000-2014

Figure SI7 *South Pole – Methane mole fraction in NOAA flask-air*
 Figure SI8 *South Pole Observatory: $\delta^{13}C_{CH_4}$ linear growth rates*
 Figure SI9 *Geographic distribution of methane annual increase in NOAA zonal average*
 Figure SI10 *Annual mean trends in $\delta^{13}C_{CH_4}$*
 Figure SI11 *World and Indian ruminant populations*
 Figure SI12 *Discharge of the Amazon River at São Paulo de Olivença no Amazonas, in Brazil*
 Figure SI 13 *CH_4 mole fraction latitudinal distribution and interannual variations*
 Figure SI 14 *Latitudinal distribution and interannual variations for $\delta^{13}C_{CH_4}$*
 Figure SI 15 *Global average $\delta^{13}C_{CH_4}$ values*
 Figure SI16 *Model monthly values for CH_4 mole fractions in the four regions together with the range of fits*

Introduction

- This Supporting Information provides further detail on the points listed in the main text. The Information gives information about data sources and archiving, specific figures on methane growth from Alert, Ascension, Cape Point, and South Pole, and a zonal growth plot. Details are given about the intercomparability of RHUL and NOAA measurements. There is a supporting discussion of the isotopic impact of ruminant and fossil fuel (coal and gas) emissions, and emission inventories. Information is given on the recent histories of major Tropical Wetlands and isotopic trends. The final sections of the Supporting Information give more detail on the analysis of budget variations. In the final section, the contributions by individual authors to this work are listed.

Supporting Information

1. Methane Budget: Sources, Sinks, Controls on Carbon Isotopic Ratios

Methane emissions are about one-third from natural sources such as wetlands and other fresh-water systems, lightning-lit fires, geological leaks, termites, and wild ruminants, and about two-thirds from anthropogenic sources, including fossil fuel exploitation, ruminants and rice paddies, waste, sewage, and biomass burning (Dlugokencky et al., 2011). Many natural and agricultural emissions and their distributions respond strongly to precipitation and temperature changes, but climate-change feedbacks remain poorly quantified.

A pulse of 2.77 Tg adds 1 ppb to the atmospheric methane burden of roughly 5 Pg, which will then decay over the ~9 yr lifetime of the methane. Thus a year-on-year growth of 10 ppb implies addition of about 28 Tg. Assuming ‘top down’ emissions for 2000-2009 estimated by Kirschke et al., came from a single source, a 10 ppb addition in a single year would imply 16% growth in global wetland emissions (if they were the sole source), or 13% growth in global agricultural emissions, or 29% growth in fossil fuel emissions, or 92% growth in methane from biomass burning.

The main methane sink is destruction by reaction with atmospheric hydroxyl (OH), particularly in the moist tropical troposphere. Destruction by OH imposes a kinetic isotope shift on $\delta^{13}\text{C}_{\text{CH}_4}$, by roughly 4 to 6‰ when the budget is in equilibrium: thus, globally, sources averaging about -52 to -53‰ produce ambient atmospheric $\delta^{13}\text{C}_{\text{CH}_4}$ values around -47‰ (Allan et al., 2001). The temporal response to changes in sources over the decadal atmospheric lifetime means that $\delta^{13}\text{C}_{\text{CH}_4}$ takes longer to reach equilibrium than the methane mole fraction (Tans, 1997), though emission pulses have immediate impact. Emission of a strong short-lived pulse of isotopically very negative (light) methane would, by mass balance, produce depleted bulk atmospheric values for a few years, but then as the methane pulse was destroyed by OH and the kinetic isotope shift took effect, the atmosphere would regress towards earlier equilibrium values prior to the pulse. Soil methanotrophy in aerobic soils both in boreal and tropical environments is also an important and widespread sink (Dlugokencky et al., 2011, Cicerone and Oremland, 1988), enriching the residual CH_4 in ^{13}C . Tropospheric methane is also destroyed by atomic chlorine in the marine boundary layer and is lost upwards to the stratosphere (Allan et al., 2010).

Atmospheric methane has a lifetime of about 9 years, and mixes globally over about a year (Dlugokencky et al., 2011; Prather et al., 2012). Atmospheric transport and mixing affect the geographic distribution of rises and declines in methane mole fraction. If a local emission spurt occurs, and the next year returns to the multi-year average, the regional methane record may show a decline, simply as a result of mixing. At any individual location, sustained local meteorological conditions that occur as normal meteorological fluctuations may influence seasonal averages. However, long-term increases seen over many stations in various regions, and the global distribution of the observed methane growth, imply that significant changes in methane budgets are taking place. The sources can be apportioned using isotopic source signatures and geographic location. By using atmospheric transport models to simulate the backward trajectory of the wind that brought an air mass to the measurement point, we can then infer the regions where the air mass was recently in prolonged contact with the surface and use measured methane mole fractions to identify likely source locations. Combining this source location information with isotopic data can allow us to locate and identify the source type (e.g., gasfield, wetland, and cattle population).

Carbon Isotope Ratios – source inputs and sink fractionation

Carbon isotopes offer a powerful tool in tracking methane emissions. Biogenic methane, made by anaerobic archaea in wetlands or ruminant stomachs, is strongly depleted in ^{13}C relative to atmospheric values (isotopically "light"). In contrast, thermogenic methane generated by combustion or geothermal maturation of organic-rich sediment, is enriched in ^{13}C (isotopically "heavy") (Kirschke et al., 2013, Dlugokencky et al., 2011). Typical isotopic signatures (expressed by the notation $\delta^{13}\text{C}_{\text{CH}_4}$, in per mil, ‰) of emissions vary greatly. Characteristic values from boreal and Arctic wetlands can range around -70‰ to -60‰, while tropical wetland emissions are typically less depleted in ^{13}C (-60 to -50‰). In contrast, gas leaks can range from -25‰ to -50‰, but are characteristically tightly clustered for any specific gasfield, depending on the thermal history of the source;

coalfield emissions also range from -20‰ to -50‰, also depending on thermal history; methane from ruminants typically ranges from around -50‰ for C4 diets to -70‰ for ruminants on C3 feed; and methane from biomass burning can be much less negative, around -30‰ to -20‰ for C3 vegetation and -20‰ to -10‰ for tropical C4 grasses (data summarised in Dlugokencky et al. (2011) and also from unpublished RHUL results). Note that the major sources that are significantly more depleted than -50‰ are wetlands (including rice paddies) and C3-fed ruminants.

There is evidence that past OH changes have influenced methane budgets. For example, although other powerful factors were likely important (especially significant reductions in leaks of Russian natural gas, which is relatively light isotopically), OH changes may have contributed to the major $\delta^{13}\text{C}_{\text{CH}_4}$ excursion event in 1991-1993 (Mak et al. 2000; Lowe et al., 1997). Indeed, Pacific and Southern Ocean measurements showed a marked enrichment of $\delta^{13}\text{C}_{\text{CH}_4}$ in 1991. This took place in a year of a major El Niño event and prolonged drought in Africa. This was likely partly driven by the impact on OH abundance of the eruption of sulphate aerosols from Mt Pinatubo, and also in part by biomass burning in 1990-1991 (Mak et al., 2000; Lowe et al., 1997). There was then a pronounced negative $\delta^{13}\text{C}_{\text{CH}_4}$ anomaly in 1992-1993 after wetland recovery and inter-hemispheric mixing. More generally, if this past El Niño produced isotopic enrichment followed by depletion during recovery, conversely, a La Niña event might be expected to drive a reverse pattern: a depletion spike, followed by enrichment in the recovery period. A recent reduction in OH sink would drive ambient $\delta^{13}\text{C}_{\text{CH}_4}$ values to be more depleted, but would not on its own be able to account for the magnitude of the observed shift (Montzka et al., 2011) and lack of recovery to earlier norms.

From 1983 through 2006, methane was on a pathway approaching and then close to equilibrium between total global emissions and removal, but there are still major questions about how emissions from each specific source may be changing. Inverse modelling has also raised questions about the accuracy of estimates for anthropogenic emissions (such as the EDGAR database) and the extent to which interannual variations in the distribution of both sources and removal are being treated (Bergamaschi et al., 2013, Kirschke et al. 2013). Changes in sources or removal differently affect $^{13}\text{CH}_4$ and $^{12}\text{CH}_4$, leading to nonlinear responses in $\delta^{13}\text{C}_{\text{CH}_4}$ with both short term and long term effects (Tans, 1997; Lassey et al., 2000). Furthermore, large seasonal cycles in CH_4 emissions and removal mean that $\delta^{13}\text{C}_{\text{CH}_4}$ never reaches equilibrium, that the mole fraction and $\delta^{13}\text{C}_{\text{CH}_4}$ values can have different seasonal cycles, and that $\delta^{13}\text{C}_{\text{CH}_4}$ responses to a perturbation are sensitive to the time of year when that occurs.

2. Data sources, measurement support, archiving, and Uncertainties

Observations reported here are from measurements by US NOAA, for whom INSTAAR carry out $\delta^{13}\text{C}_{\text{CH}_4}$ measurement, and by Royal Holloway, University of London (RHUL). By combining and comparing data from different laboratories, we check for systematic bias in the measurement programs. Further details on RHUL-INSTAAR comparison are in the supplementary online sections 8, 9, and 10. Mole fraction measurements are to the WMO X2004A scale for both NOAA and RHUL.

Observations reported here are from measurements by NOAA, for whom INSTAAR carry out $\delta^{13}\text{C}_{\text{CH}_4}$ measurement on the same air samples measured for CH_4 , and by Royal Holloway, University of London (RHUL).

All discrete air samples from remote sites are analysed in the supporting laboratories in Boulder (NOAA and INSTAAR) and London (RHUL).

RHUL data will be deposited in CEDA, the UK "Centre for Environmental Data Analysis" which has succeeded the British Atmospheric Data Centre.

NOAA data are on the WMO X2004A scale and reported by:

Dlugokencky, E.J., P.M. Lang, A.M. Crotwell, K.A. Masarie, and M.J. Crotwell (2014), Atmospheric Methane Dry Air Mole Fractions from the NOAA ESRL Carbon Cycle Cooperative Global Air Sampling Network, 1983-2013, at ftp://ftp.cmdl.noaa.gov/data/trace_gases/. For figures, *US NOAA ESRL website and* <http://www.esrl.noaa.gov/gmd/ccgg/figures/>

INSTAAR data are found in the readme file are available from: ftp://aftp.cmdl.noaa.gov/data/trace_gases/ch4c13/flask/surface/:

ftp://aftp.cmdl.noaa.gov/data/trace_gases/ch4c13/flask/surface/README_surface_flask_ch4c13.html

RHUL data will be deposited in CEDA, the UK "Centre for Environmental Data Analysis" which has succeeded the British Atmospheric Data Centre.

Uncertainties

Uncertainties in NOAA measurements are about 1 to 1.5 ppb relative to the WMO CH_4 mole fraction standard scale (in other words, excluding the absolute uncertainty in the scale, but including a term for propagation of the scale over time). However it is difficult to state uncertainties for several reasons; several factors are important. First, there is natural variability caused by short-term meteorological events, which can affect daily, monthly or even seasonal averages but do not necessarily show long-term change is occurring. For monthly means, NOAA assessed uncertainties at MLO and BRW with "fake flask" records. Weekly samples that met NOAA sampling criteria were randomly selected, to produce 100 time series, and the standard deviation of the monthly means was examined from these 100 time series. At MLO, the uncertainty in monthly means was ± 6 ppb. Uncertainty determined by this method would be less at ASC, because CH_4 is less variable there. Uncertainties for zonal averages were also estimated with a Monte Carlo method.

3. Alert, Nunavut, Canada (82°27'N, 62°31'W)

In conjunction with Environment Canada, NOAA have a long-standing discrete sampling program for marine boundary layer air at Alert, at a coastal site on Ellesmere Is. in the Arctic Ocean. Samples are measured by NOAA for methane mole fractions, and by the INSTAAR for $\delta^{13}\text{C}_{\text{CH}_4}$. Since 2008, RHUL measurements have also been made on flask air samples from Alert collected by Environment Canada. Methane mole fraction is measured continuously by Environment Canada, while $\delta^{13}\text{C}_{\text{CH}_4}$ is measured by RHUL from glass flasks supplied via the Institut für Umweltphysik, Univ. of Heidelberg (thanks

to Prof. I. Levin). In partnership with the Norwegian Institute for Atmospheric Research (NILU), RHUL also maintain daily $\delta^{13}\text{C}_{\text{CH}_4}$ sampling at Zeppelin, Spitsbergen, to be reported elsewhere.

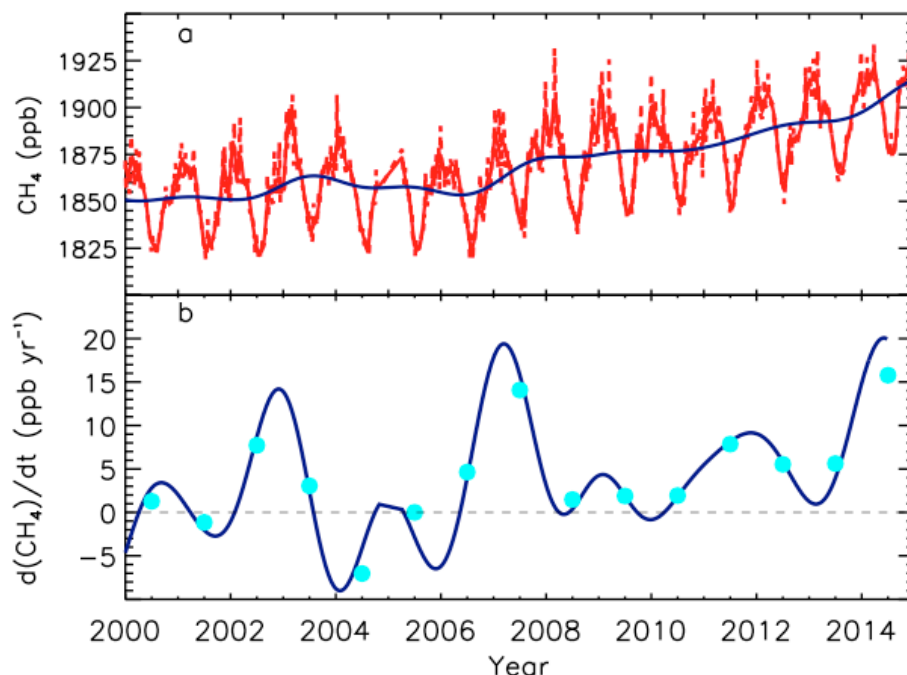


Figure SI 1 Alert – Methane mole fraction as measured in NOAA flask-air during the period considered in this report.

a – mole fraction (red) and deseasonalized trend (blue line). b – solid line is instantaneous growth rate and symbols are annual increase determined from deseasonalized trend line. For smoothing procedures, see http://www.esrl.noaa.gov/gmd/ccgg/about/global_means.html

4. Ascension Island (7°58'S, 14°24'W).

On *Ascension Island*, in collaboration with the UK Meteorological Office and co-located with NOAA collection of discrete air samples, Royal Holloway (RHUL) sustains continuous greenhouse gas measurement at the UK Met Office at the Airhead (7°58'S, 14°24'W), with rooftop air intake, about 90 m asl, at the NW end of the 3 km long runway. The wind is an almost invariant SE Trade wind, typically a fresh breeze around 20-30 km hr^{-1} (Force 4 to 6), but ranging up to 90 km hr^{-1} . There is no population upwind of the runway. The site samples the marine boundary layer. Measurement for continuous high-precision CH_4 and CO_2 mole fractions, using a cavity ring-down Picarro Inc. 1301 analyser, has continued since 2010, with a 6-gas calibration suite including target and long-term target gases. For $\delta^{13}\text{C}_{\text{CH}_4}$, air is regularly sampled in steel flasks for analysis in the RHUL lab for $\delta^{13}\text{C}_{\text{CH}_4}$, as part of the *Equianos* network (equianos.com). Flask-air sampling is on the surface at the edge of the apron, near the UK Met Office building. RHUL $\delta^{13}\text{C}_{\text{CH}_4}$ flask-air sampling began in 2000 but was interrupted in 2006-10 as funding was unavailable. In addition, there have been a number of RHUL sampling campaigns on the island using Tedlar bag collection (at surface and also up to 3000 m

using an unmanned aerial vehicle). NOAA $\delta^{13}\text{C}_{\text{CH}_4}$ sampling at Ascension dates from 2000, initially on the apron at USAF Ascension and currently co-located with RHUL sampling at the UK Met Office, at the Airhead, about 200 m away from the earlier site. Both at Alert and Ascension, the co-location of NOAA and RHUL sampling is invaluable. The two wholly independent measurement sets allow factors such as instrument drift, calibration bias, or systematic lab changes to be ruled out, and thus the trends can be accepted with confidence.

Air in the marine boundary layer arriving at Ascension is almost invariant SE trade wind, with back trajectories along the Coriolis curve from the remote South Atlantic around and east of Tristan da Cunha (Fig. SI 2). More distantly the air is derived both from the Falklands and previously from interior S. America (including the wetlands of Paraguay, Bolivia and southern Amazonia), and also from wide areas of the Southern Ocean. Peaks in methane mole fraction typically occur in June and July, and low values in January. Under the trade wind inversion at about 1.5 km, the SE trades move along forward trajectories from Ascension across the Atlantic Ocean to provide the incoming background air for southern Amazonia. Above Ascension, higher than the inversion, back trajectory analyses undertaken in this study show the air has tropical sources, mainly from Africa. Thus Ascension is well located to sample a wide tract of the Southern Hemisphere.

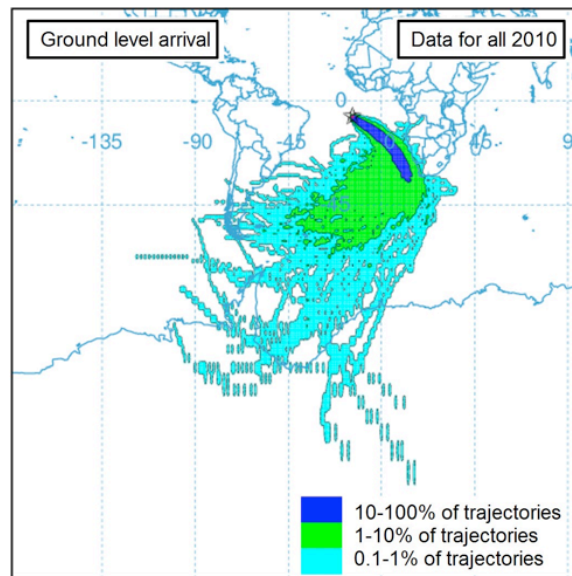


Figure SI 2 Sources of air arriving in the marine boundary layer at Ascension in 2010. NOAA Hysplit (Hybrid Single Particle Lagrangian Integrated Trajectory Model) back trajectories.

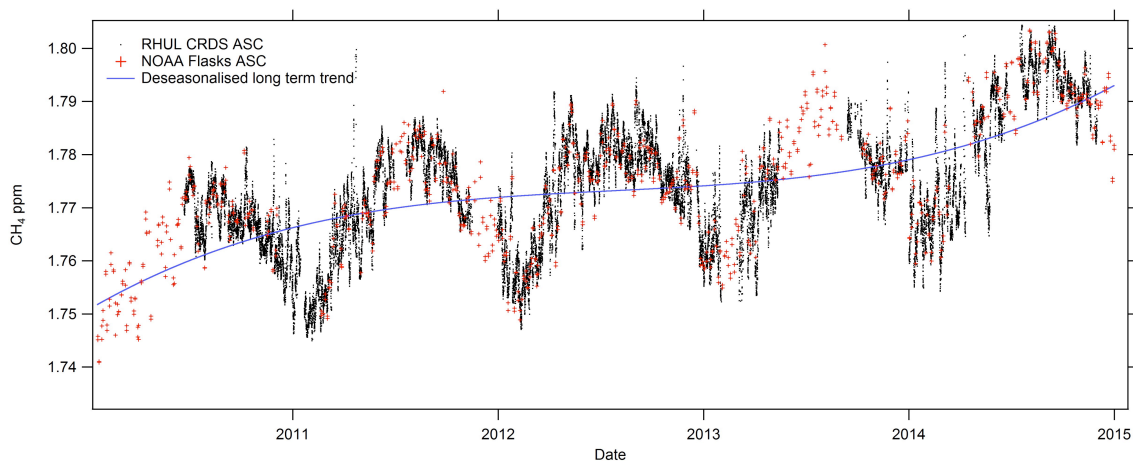
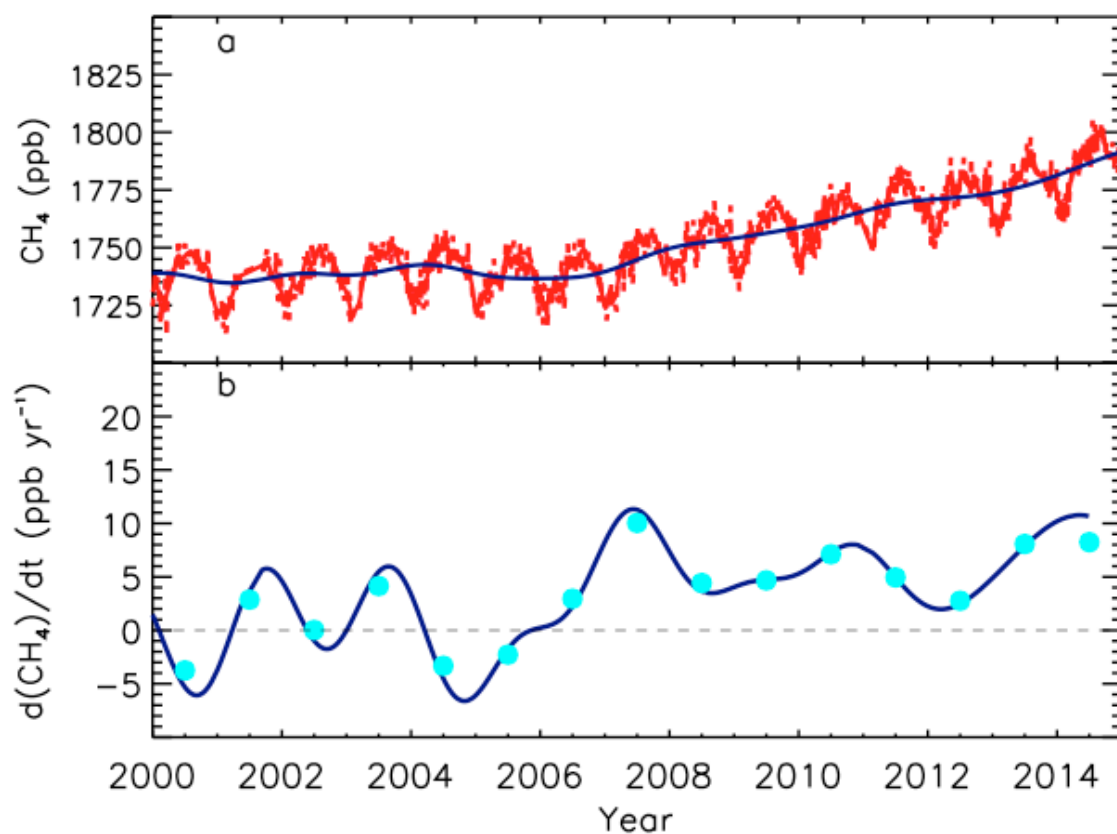


Figure SI 3 Ascension Island – Growth in Methane mole fraction as measured in NOAA flask-air samples and in RHUL continuous measurements.

Upper figure: Top panel – mole fraction. Lower panel – solid line is instantaneous growth rate and symbols are annual increases determined from a deseasonalized trend. For smoothing procedures, see

http://www.esrl.noaa.gov/gmd/ccgg/about/global_means.html

Lower figure: Growth in RHUL continuous record and NOAA flask-air samples, 2010-2015. To fit the curve the program HPspline was used with the parameters suggested in

Pickers & Manning, (2015). This curve is from hourly averaged RHUL Picarro data, RHUL flasks and NOAA flask-air. To get the annual growth the deseasonalised monthly averages were subtracted from the previous year's deseasonalised monthly average to give the growth rate of each month. The average was taken for each month's growth rate in a year giving the yearly growth and the standard deviation of this applies to the yearly growth rates.

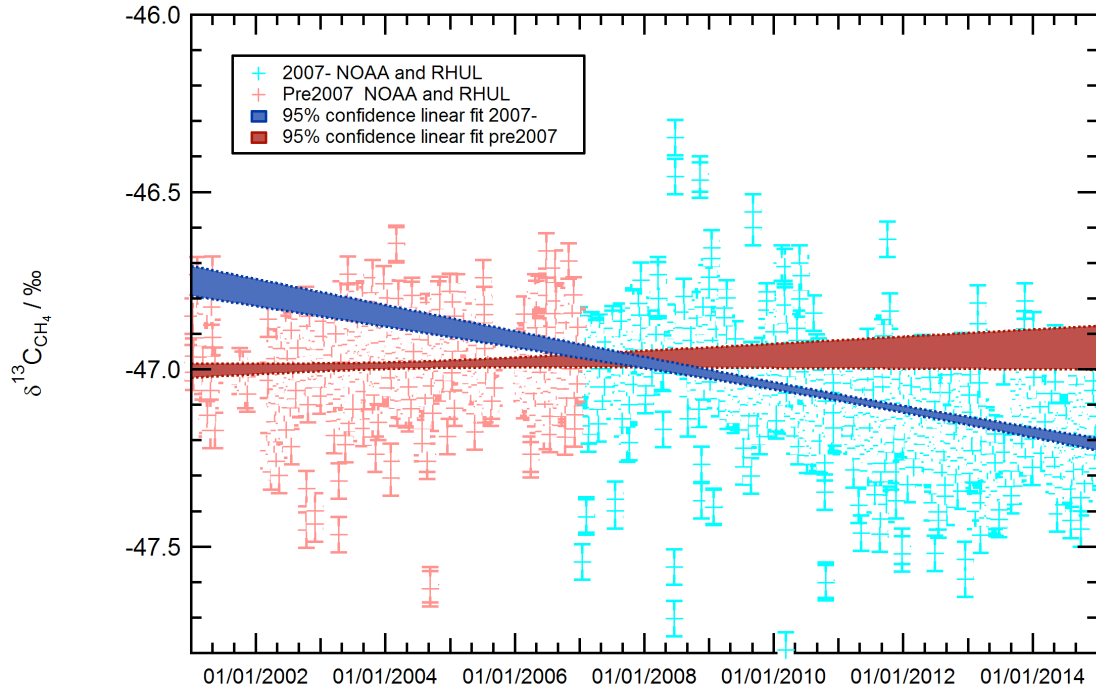


Figure SI 4 Ascension Island: $\delta^{13}C_{CH_4}$ growth rates, assuming linear growth rates from pre-2007 and 2007 onwards. 95% confidence bands for the growth rates are calculated for both pre-2007 and 2007 onwards: Growth rates are projected for the duration to display the clear step change in growth. 2007 is chosen as the step change year due to the clear change in actual CH_4 growth rates as seen in Figure SI3. $\delta^{13}C_{CH_4}$ growth: Pre 2007: $+0.002 \pm 0.008$ ‰ / year; 2007 onwards: -0.035 - -0.031 ‰ / year

5. Cape Point Observatory (34°21'S, 18°30'E)

Thumeka Mkololo of the South African Weather Service (SAWS) collects discrete air samples for NOAA and Univ. East Anglia in collaboration with RHUL. The sampling program has been run by EB and CL. SAWS also maintain continuous measurement of CH_4 .

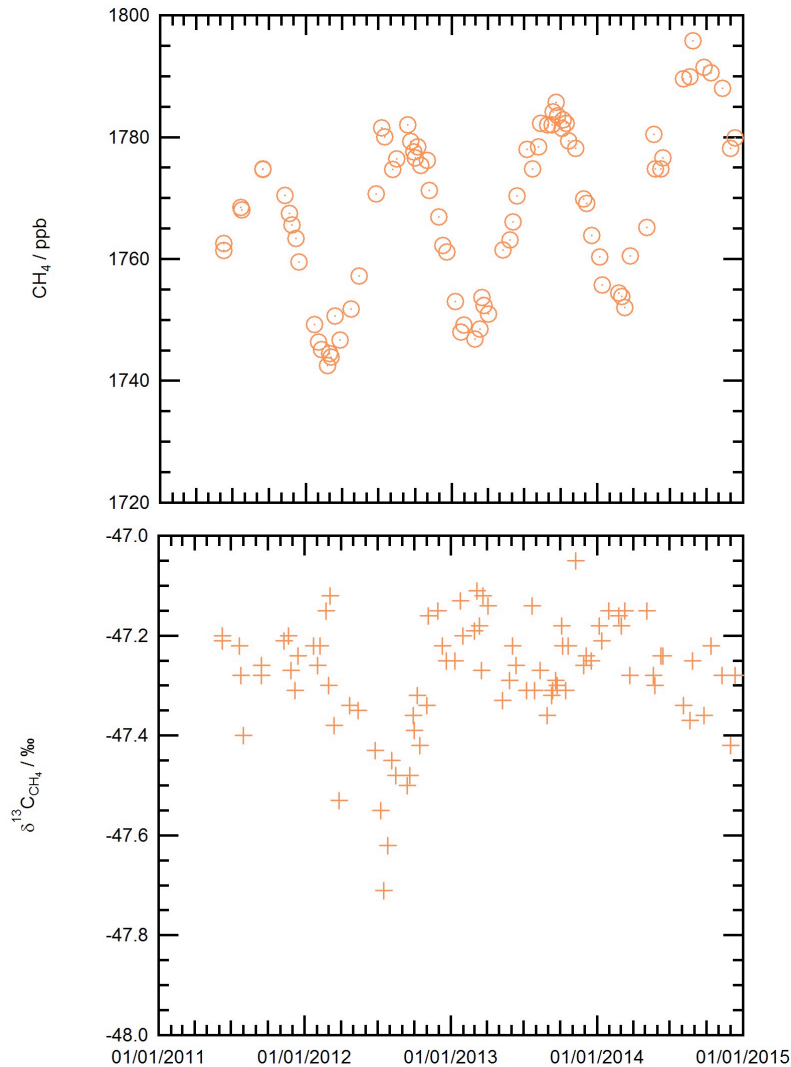
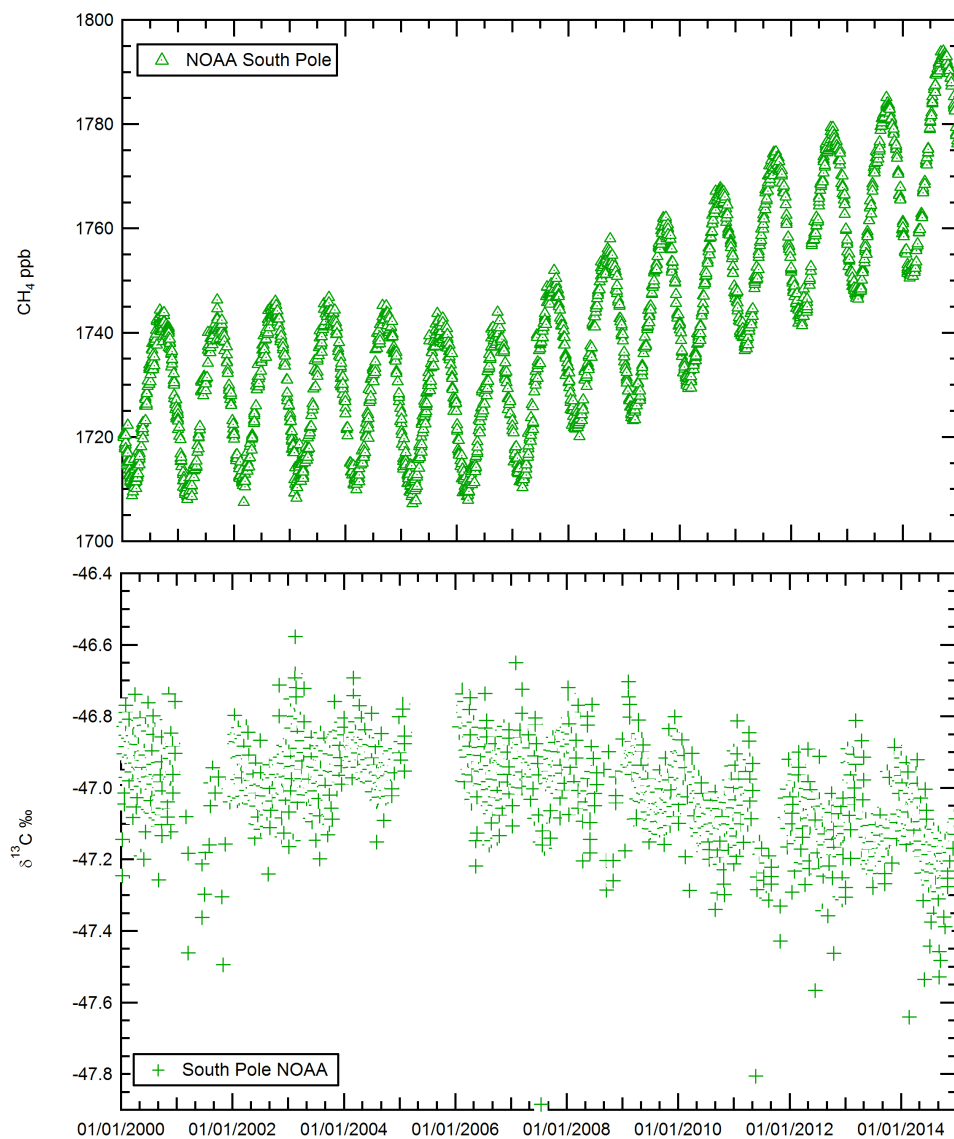


Figure SI 5 – Cape Point: RHUL CH_4 and RHUL $\delta^{13}\text{C}_{\text{CH}_4}$ record, 2011-2014. Note very negative $\delta^{13}\text{C}_{\text{CH}_4}$ values in mid-2012, possibly indicating mixing of major end-of rainy season emissions from Southern Hemisphere wetlands into regional Southern Ocean air.

6. South Pole Station (90°S)

Here discrete air samples are collected for both CH_4 mole fraction and $\delta^{13}\text{C}_{\text{CH}_4}$ measurement. South Pole is very remote from methane sources, though Fiebig et al. (*Geophys. Res. Lett.*, **36**, L038531, 2009) traced biomass burning products from Brazil as far south as the Pole. The South Pole record (Figs. SI 6, 7 & 8) thus should follow the integrated global trends established in the north; much of the overall rise in deep Southern Hemisphere methane, as well as the isotopic shift, should parallel overall global patterns with a lag of up to 12 months. Methane mixes zonally in the Northern Hemisphere, and then over a year mixes south to the ocean-dominated temperate Southern Hemisphere and then to ice-covered Antarctica; in addition, the polar vortex

324 contributes air that has relatively low mole fraction, isotopically heavy methane.
325



326
327
328 *Figure SI 6 South Pole NOAA CH_4 and NOAA-INSTAAR $\delta^{13}\text{C}_{\text{CH}_4}$ record, 2000-2014.*
329 *Note very negative $\delta^{13}\text{C}_{\text{CH}_4}$ values in 2012-2013.*

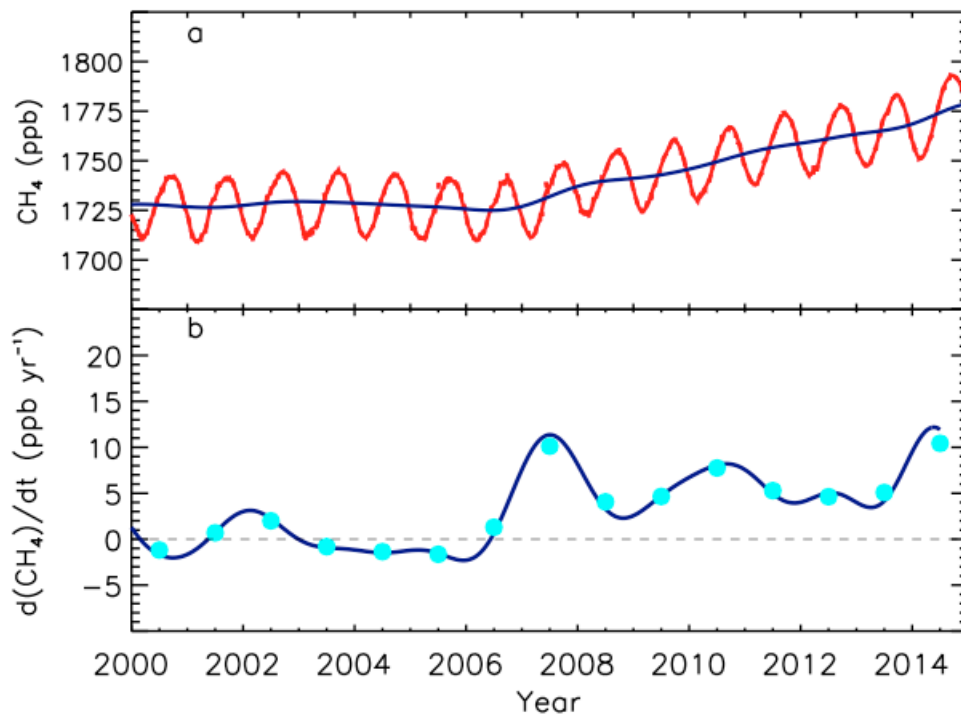


Figure SI 7 South Pole – Methane mole fraction as measured in NOAA flask-air. Panels as Fig. SI 4 above. For smoothing procedures, see http://www.esrl.noaa.gov/gmd/ccgg/about/global_means.html

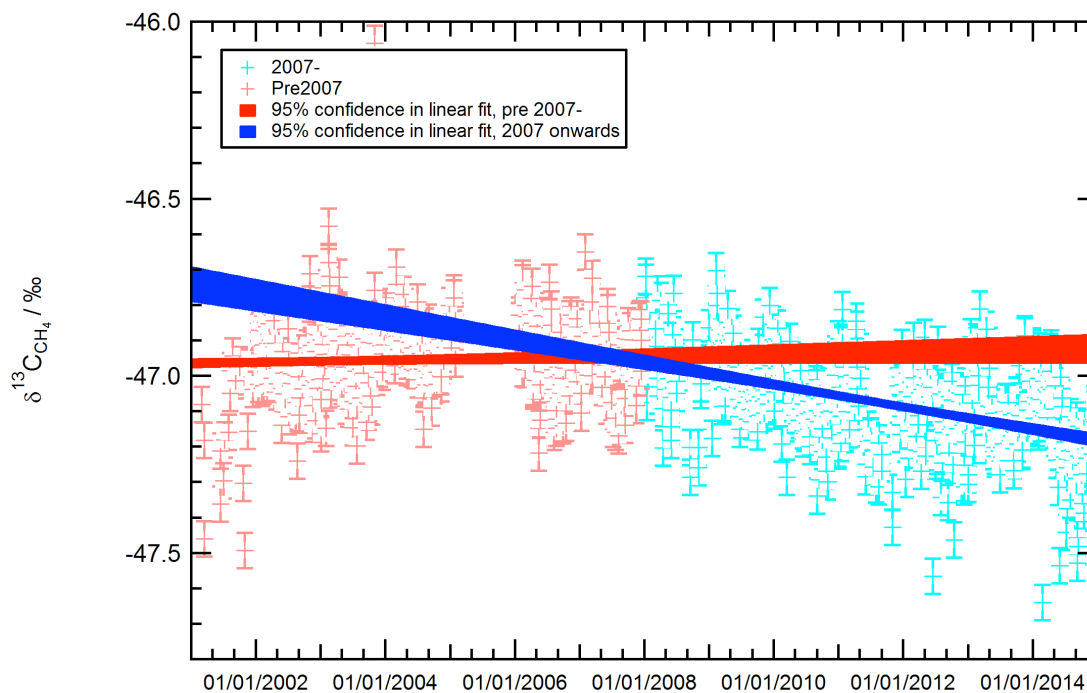


Figure SI 8 South Pole Observatory: $\delta^{13}C_{CH_4}$ linear calculation of growth rates, as for Ascension Is. data (see Fig. SI4):
 $\delta^{13}C_{CH_4}$ growth: Pre 2007 = $+0.0001 \pm 0.005\%/year$. 2007 onwards = $-0.036 - 0.026\%/year$

7. Annual increase by zone

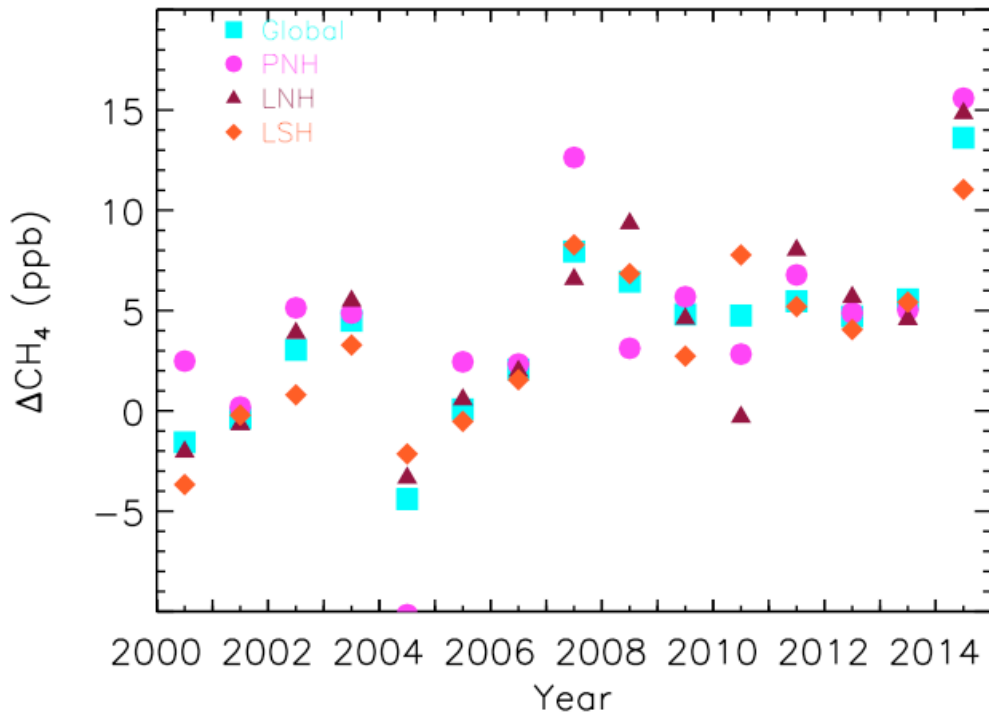


Fig. SI 9. Geographic distribution of methane annual increase in NOAA zonal averages. PNH: Polar and Boreal Northern Hemisphere, ($90^\circ - 53^\circ N$); LNH: Low latitude Northern Hemisphere ($30^\circ - 0^\circ N$); LSH: Low latitude Southern Hemisphere ($0^\circ - 30^\circ S$).

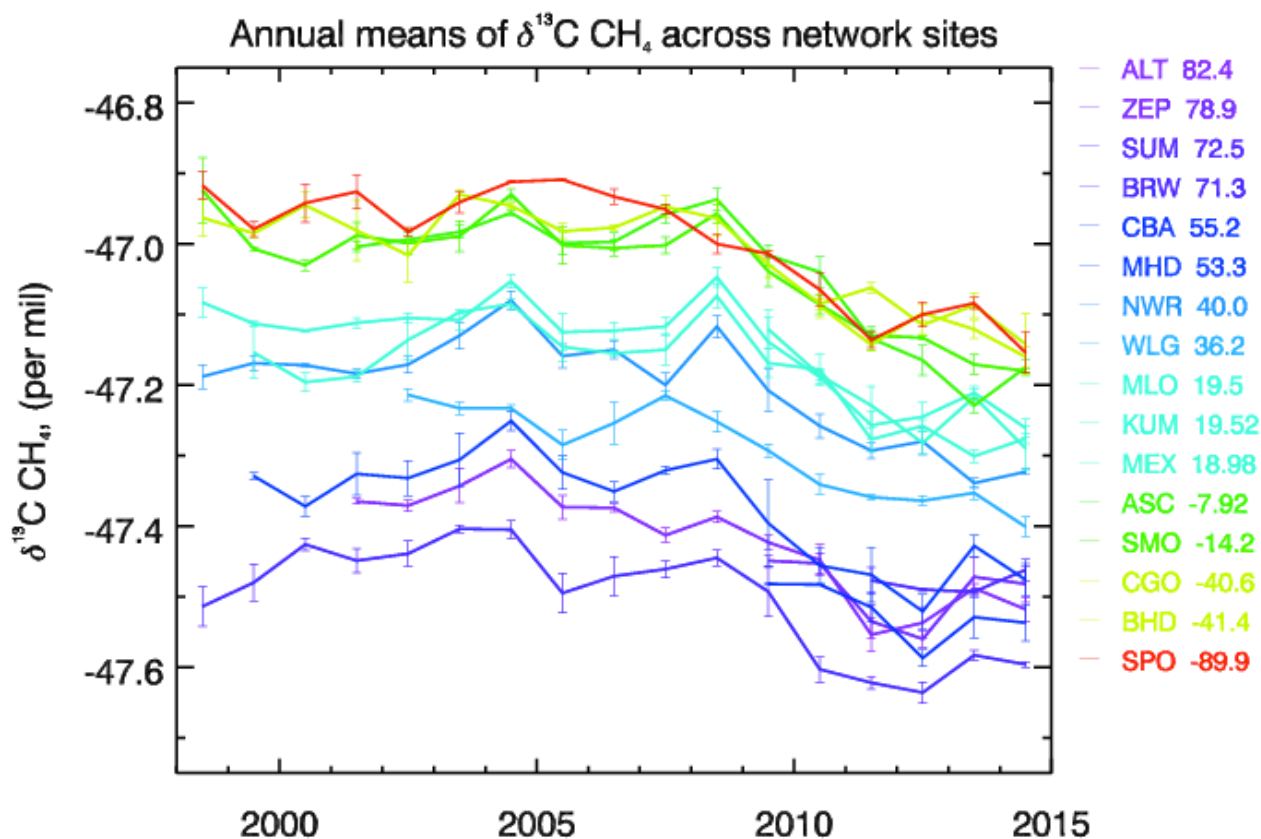


Fig. SI 10. Annual mean trends in $\delta^{13}\text{C CH}_4$, at NOAA stations (right side column gives latitude). Error bars show standard deviations of deseasonalized smoothed curve.

8. Mole fraction: Comparison between RHUL and NOAA

In the 2013 global multi-lab WMO international comparison of CH_4 standards, the difference between air measured in RHUL by the laboratory Picarro 1301 system and NOAA (RHUL – NOAA r.m.s.) was -0.14 ppb. The Ascension Island 1301 system is closely comparable to the RHUL lab system, and has a six-gas calibration suite including NOAA WMO standards on the X2004 scale, target, long-term target, and working gas.

9. Methane isotope measurement at RHUL and INSTAAR.

$\delta^{13}\text{C CH}_4$ was analysed at RHUL using a modified GC-IRMS system (Trace Gas and Isoprime mass spectrometer, Isoprime Ltd.) as described in detail by Fisher et al. (2006). Analyses were carried out to 0.05‰ repeatability with all measurements made in triplicate. $\delta^{13}\text{C CH}_4$ measurement at INSTAAR was also by GC-IRMS, following Miller et al. (2002) on pairs of flask-air samples, the averages of which are reported here. Repeatability is at or better than 0.07‰ based on repeated analysis from a high pressure cylinder of ambient air. Isotope ratios are given in δ -notation on the VPDB (Vienna Pee Dee Belemnite) scale.

10. Isotopic measurement: $\delta^{13}\text{C}_{\text{CH}_4}$ comparison between RHUL, INSTAAR and NIWA-New Zealand

In 2014, comparison by two-way tank exchange shows that RHUL's continuous flow system (CF) has a positive ^{13}C offset of 0.3‰ compared to NIWA. The prior intercomparison was in 2004, when for a tank with air containing methane near -47‰, the RHUL (CF)-NIWA offset was about 0.1‰ and RHUL(CF) and NOAA were within uncertainty. RHUL and INSTAAR intercompared again in 2014.

11. Ruminant emissions

Ruminant emissions typically have $\delta^{13}\text{C}_{\text{CH}_4}$ $-55 \pm 5\text{‰}$, depending on the dietary mix (circa -49‰ for C4 grasses; -70 for C3 fodder) (Dlugokencky et al., 2011). Eructation from tropical savanna cows fed on isotopically enriched C4 grasses may be somewhat more positive than -55‰.

The global ruminant population has grown by 16% from 2000-2013, with the most rapid rise between 2002-2007, mostly in the tropics (Food and Agriculture Organization of the United Nations, FAOSTAT database (FAOSTAT, 2015), available at <http://faostat3.fao.org>, accessed 3 Sept 2015).

IPCC AR5 (2013) estimates ruminant emissions in 2009 as 89 Tg, (bottom-up, in a range of 87-94 Tg), while Bergamaschi et al. (2013) use EDGAR inventories (91.3-100.2 Tg). Slightly over 1% growth in this number translates to about an increase of 1 Tg per year due to higher ruminant numbers, or about 0.37 ppb addition to the global burden. There is no strong evidence for a particularly sharp year-to-year step-change in population in 2007. Thus the 16% increase in global ruminants in 2000 - 2013, or, say, slightly over 1% per year in ruminant numbers, does not suggest that ruminants dominate the recent growth, though they may have contributed. However, over the period of 8 years from the start of 2007, 1% annual growth in ruminant emissions would input 7-8 Tg more methane per year, or about 2.5 to 3 ppb per year. For comparison, a 10 ppb year-on-year rise in methane (27.7 Tg), if solely a result of increased ruminant exhalation, would imply a one-quarter to one-third increase in total global ruminant emission that year.

Moreover, tropical ruminant population growth (for example in Brazil and Bolivia) is in part linked to conversion by drainage of wetland, which reduces natural methane emissions. Methane emissions are also linked to ruminant productivity, which is largely controlled by the type and supply of fodder. The feed supply can be influenced by year-to-year changes in temperature and precipitation, but bovine population and fodder changes are buffered by carry-over in stock and feed from one year to the next (Dikshi and BIRTHAL, 2010), and also by the smoothing impact of irrigation. Thus, while ruminant emissions have likely contributed significantly to the rise in tropical methane emissions, there is little evidence for a step-change in 2007 that is capable of explaining the trend-change in the methane record. Perhaps increased ruminant emissions help sustain the continued increase, but they did not solely initiate the change.

India is a special case as it is the nation with by far the largest population of ruminants, with roughly a third of the global total population and thus a dominant contributor to bovine emissions in the northern subtropics. (US Dept. of Agriculture http://apps.fas.usda.gov/psdonline/circulars/livestock_poultry.pdf). Indian monsoon precipitation records are accessible from the India Meteorological Department at

http://www.imd.gov.in/section/nhac/dynamic/Monsoon_frame.htm. Figure SI11 shows the year-to-year variability in monsoon rainfall along with annual milk production from dairy cattle. The fluctuations in annual rainfall are not reflected in the milk yield, suggesting that other factors are also important for maintaining ruminant productivity. To first order, we assume that milk production is indicative of dairy cattle feed.

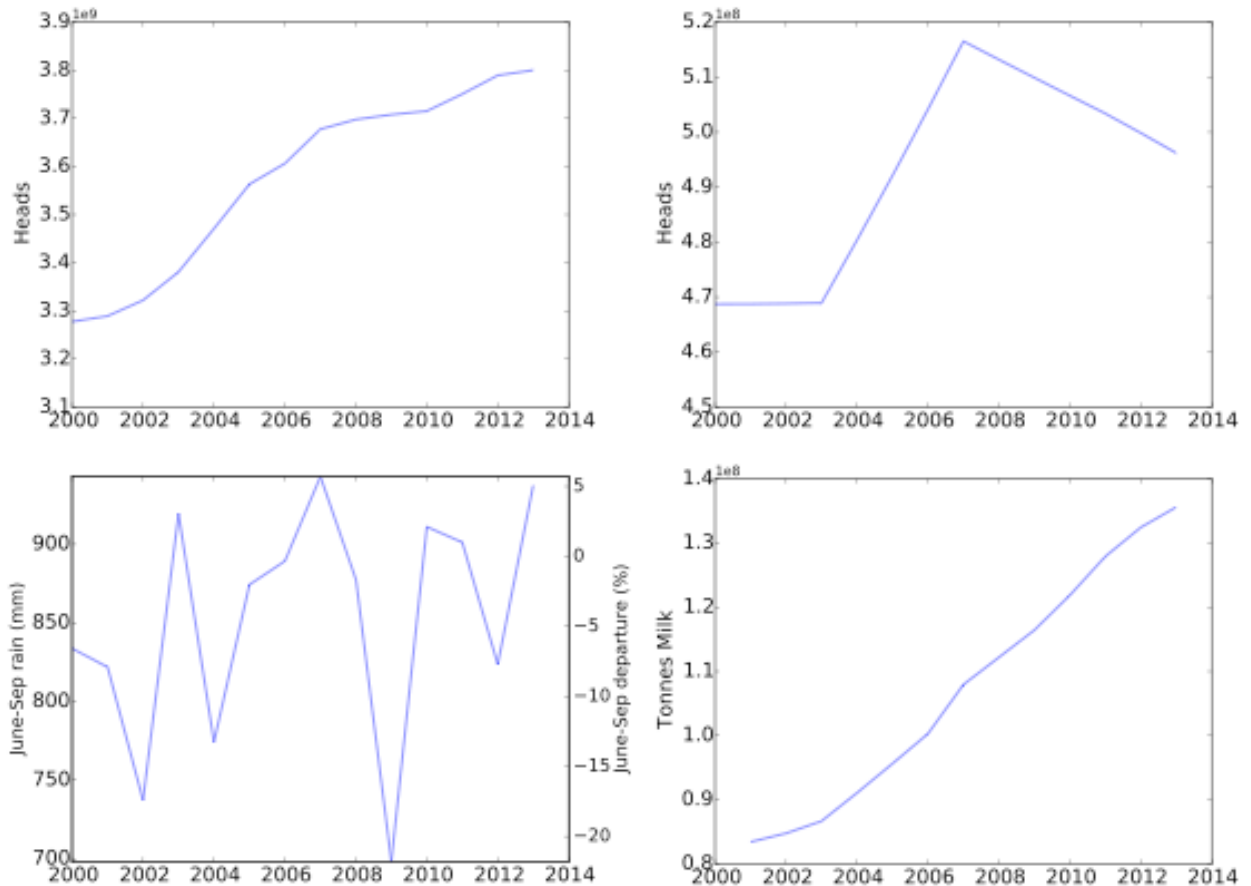


Fig. SI 11 (top left) World ruminant population (cattle, buffalo, sheep and goat $\times 10^9$) and (top right) India's ruminant population ($\times 10^8$). (bottom left) Monsoon rainfall between June-September of each year in mm and the % departure. (bottom right) India's total milk production in tonnes. Agricultural data are from the Food and Agricultural Organization of the United Nations.

Thus, given the poor or average recent Indian monsoons, ruminant emissions from the Indian sub-continent may not have been a significant factor in methane growth in the latitudinal zone around 30°N in 2008-9 (Fig. 1), nor in the rapid tropical methane growth starting in 2007. Indeed, cattle populations may have peaked around 2007.

However, ruminant emissions in other countries, especially China, Brazil, Argentina, Uruguay and sub-Saharan Africa may have increased significantly, both from total numbers and from good feed in the *La Niña* years. The geographic foci of growth have been in the tropics (see Fig. 1 in main text). Thus if ruminant emissions are a major factor

driving the methane growth, then this is likely to be primarily sourced in the tropical countries. Better isotopic constraints on these sources are needed along with improved emission factors for ruminants in these regions.

12. Gas and Coal industry emissions.

Fossil fuel sources are found to be increasing in emissions inventories (see SI section 11), and thought to contribute to the atmospheric growth since 2007, though to what extent is not clear (Kirschke et al., 2011). Fossil fuel emissions are roughly 100 Tg globally (Kirschke et al., 2013). If for example fossil fuel emissions were the sole cause of a year-on-year rise in the global methane burden, a sudden one-year injection of 10 ppb to the atmospheric methane burden would need about 28 Tg of new source. That would require a jump of a quarter to a third in total fossil fuel methane emissions.

Fossil fuel sources are characteristically though not exclusively isotopically enriched in ^{13}C relative to atmosphere (note that natural gas varies widely in $\delta^{13}\text{C}_{\text{CH}_4}$). Natural gas is mostly methane, and this methane is typically enriched in ^{13}C compared to the atmosphere, but varies greatly globally. Although some important sources, especially Russian gas, have $\delta^{13}\text{C}_{\text{CH}_4}$ that is slightly depleted compared to methane in the atmosphere, elsewhere much of the methane released by increasing fossil fuel production is enriched, around -40‰. Russian natural gas, the main supplier for continental northern Europe, is $-51 \pm 2\text{‰}$ (Fisher et al., 2011). This is close to global average methane emissions from all sources of -53‰, and thus over a decadal period, allowing for the kinetic isotope effect on methane oxidation, changes in the Russian gas industry's leak rates would not cause marked shifts in $\delta^{13}\text{C}_{\text{CH}_4}$. In contrast, North Sea gas is around -35‰ ('around' in this context is roughly $\pm 5\text{‰}$, varying from well to well)(RHUL unpublished), and North Sea gas delivered to the UK typically has $\delta^{13}\text{C}_{\text{CH}_4} - 36 \pm 2\text{‰}$ (Zazzeri et al., 2015). Gas from the giant Gulf fields between Arabia and Iran (the world's largest) is around -35‰ to -40‰ (e.g. Galimov and Rabbani, 2001). Values of $\delta^{13}\text{C}_{\text{CH}_4}$ in North American gasfields are variable, depending on thermal history. For example, the conventional gas in mid-continent Kansas has $\delta^{13}\text{C}_{\text{CH}_4}$ ranging from -48‰ to -39‰ (Jenden, et al., 1988).

Northern mid-latitude ($\sim 30^\circ\text{N}$) emission growth has occurred since 2008 (Fig. 1). This region includes the US gasfields, the Mediterranean, the gas and oilfields of the Middle East, and the coal-dependent economies of China and India. As noted above, a postulated increase in the proportion of fossil fuel emissions in the global budget is difficult to reconcile with our bi-hemispheric observation that $\delta^{13}\text{C}_{\text{CH}_4}$ has trended more negative. Leak reduction may be occurring in the gas industry (Worthy et al., 2009; Peischl et al., 2015). For example, loss rates from gas extraction in the volumetrically important US Haynesville (1.0-2.1%), Fayetteville (1.0–2.8%) and Marcellus shales (0.18-0.41%), representing over half of US gas production in 2013, are smaller than those reported in other regions (Peischl et al., 2015).

Coal methane emissions may be declining given the recent decline in global coal production.

<http://www.bp.com/content/dam/bp/pdf/energy-economics/statistical-review-2015/bp-statistical-review-of-world-energy-2015-coal-section.pdf>

Methane from coal has $\delta^{13}\text{C}_{\text{CH}_4}$ that varies widely, according to the diagenetic and metamorphic history of the coal. High temperature thermogenic coal-associated methane is typically more positive (e.g. -20 to -40‰) than global atmospheric sources, while some coals with a gentle thermal history can have more negative $\delta^{13}\text{C}_{\text{CH}_4}$. For example, RHUL group work by Zazzeri et al (2016) found a range of values, some as depleted as $\delta^{13}\text{C}_{\text{CH}_4}$ -66.4±1.3‰ in the Hunter coalfield of Australia (discussed in the main text Sect. 4.1). Other measurements of Australian coals reported by Zazzeri et al. are around -60‰, while UK coals are -30 to -51‰. Chinese coal is very diverse, reflecting the great range of geological sources, but perhaps typically around -40‰ with wide ranges (see also Thompson et al. (2015)).

13. Methane emission inventories

Kirschke et al. (2013) pointed out: “*trends in natural and anthropogenic emissions are still very uncertain and limit our ability to definitively attribute changes in emissions from specific sources*”. Links to global methane inventories are given below:

EDGAR http://edgar.jrc.ec.europa.eu/download.php?edgar_dst=28065

GFED http://www.falw.vu/~gwerf/GFED/GFED4/tables/GFED4_BETA_CH4.txt)

World Bank

<http://data.worldbank.org/indicator/EN.ATM.METH.KT.CE/countries/1W?display=default>

14. Variability of methane production from Tropical Wetland.

Given the negative direction of the observed global isotopic shift reported in this study, fossil fuels are unlikely to be the cause. An alternative hypothesis for the northern mid-latitude growth is increased emissions from the intense monsoonal agriculture (rice, ruminants, wetlands etc.) under the Inter-Tropical Convergence Zone in northern India, Bangladesh, and S.E. and E. Asia.

Interannual variability of wetland area is known to produce major year-to-year anomalies in regional methane fluxes from both tropical and boreal wetlands (Melton et al., 2013). Nearly half the year-to-year variability in global wetland CH_4 emissions may be from tropical wetlands (Hodson et al., 2011), whose methane productivity depends on the intensity of precipitation and geographic position and width of the Inter-Tropical Convergence Zone. The difference in water transfer from ocean to land between tropical drought and tropical flood years is very large indeed, as illustrated by the sea level drop recorded by Boening et al. (2012) in the 2010-2011 La Niña.

High rainfall expands wetlands, provides strong grass growth and may increase wetland ambient temperatures under cloudy nights. Methane emissions from central Amazonia have been estimated as about 22 Tg yr⁻¹ (Melack et al., 2004), and Ringeval et al., 2014 found that Amazonia as a whole may emit as much as 44 ± 5 Tg yr⁻¹. A 50% increase in this number would add about 8 ppb to atmospheric methane.

In the seasonal outer tropics, with heavy summer rainfall under the Inter-Tropical Convergence Zone, and long winter droughts, good wet season savanna rains provide

grass fuel for dry season biomass burning. Temperature is also important as methane emission from wetlands has an exponential relationship to temperature (Gedney et al., 2004; Westerman and Ahring, 1987), thus warmer years would be expected to produce exponentially more methane than cooler years, all other variables being equal.

Tropical wetlands typically flood in the late rainy season and early winter, first in localized wetlands under heavy rain, and then in wide wetlands such as the Bolivian Pantanal and the Zambesian wetlands of central Africa, as river systems deliver water. However in many regions precipitation data are very scarce or absent (e.g. in the Congo, Angola, South Sudan, etc.) As a proxy for rainfall, river flows are a good indicator of precipitation. Also remote sensing data have shown a decrease in land surface open water areas over 1993 to 2002 followed by an increase over 2003 to 2007 (Prigent et al., 2012).

Amazon and Paraguay flood levels

The Amazon and Paraguay basins include several of the most methane-productive wetlands in the global tropics. Flood levels in these rivers are proxies for wetland flooding. Information on Amazon flood levels (Fig. SI 12) is accessible from the Brazilian hydrological service ANA (Agencia Nacional de Aguas, Brasilia/ National Agency for Water, Brazil). Data are available from <http://hidroweb.ana.gov.br/> - station codes can be found on http://www2.ana.gov.br/Paginas/servicos/informacoes_hidrologicas/redehidro.aspx; to retrieve data click on 'Series Historias' and follow from there. See also Espinoza et al. (2014). For Paraguay, information is accessible from:

Dirección de Meteorología e Hidrología DMH/DINAC, Gerencia de Navegación e Hidrografía GNH/ANNP (2014) BOLETIN HIDRO/ METEOROLÓGICO DEL RÍO PARAGUAY. See for example, for October 2014 <http://www.annp.gov.py/seccion/34-boletin-hidrometeorologico.html>.

Amazon Discharge 1973–2014 at Sao Paulo de Olivenca (68.8 W, 3.5 S)

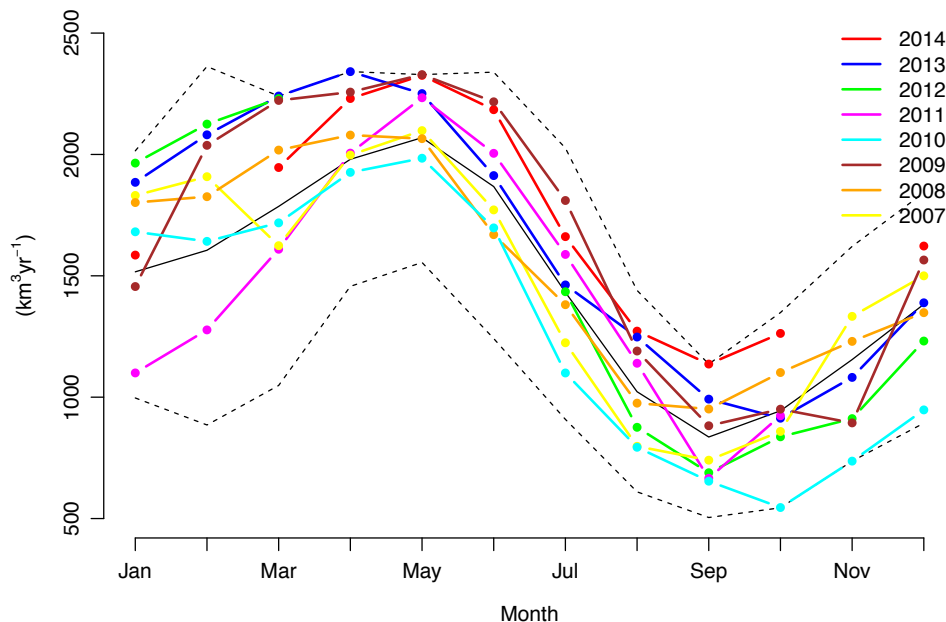


Fig. SI 12. Discharge of the Amazon River at São Paulo de Olivença no Amazonas, in Brazil near the tri-country border with Peru and Bolivia. Dashed lines show maximum and minimum flood levels from 1973-2014, and solid black line is the mean. Note extreme flood volumes in March-June (after the Southern Hemisphere rains) in the years since 2011.

There are very few public domain records of precipitation in the major wetlands of the Congo basin and Angola, which have very widespread wetlands but very few sites with routine measurement of precipitation. However the Okavango river flood, regularly reported by the Botswanan tourist industry, is a good proxy for intensity of precipitation in southern Angola. Record flood levels were recorded in 2010 and 2011 in the Okavango swamps of Botswana.

<http://www.eyesonafrica.net/updates/flood-update.htm>

Similarly, the end-of-season lake levels of the Kariba reservoir (Earth's largest freshwater impoundment at 185 km³ when filled), although subject to variable hydropower usage, are a rough public domain proxy for Zambezi river flow, and thus rainfall in NW Zambia, E Angola and Southern DR Congo. These show very low levels in 2007/8 changing to very high levels in 2011-onwards. In late 2015, after a prolonged drop in 2014, Kariba lake levels were at among the lowest recorded since the lake was filled in the early 1960s.

<http://www.zaraho.org.zm/hydrology/lake-levels>

15. Earlier debate on Isotopic Trends

Global trends in $\delta^{13}\text{C}_{\text{CH}_4}$ and $\delta^{13}\text{D}_{\text{CH}_4}$ were evaluated by Kai et al. (2011). They found the inter-hemispheric difference in $\delta^{13}\text{C}_{\text{CH}_4}$ decreased from $-0.24 \pm 0.11\text{‰}$ during 1989–1993 to $-0.10 \pm 0.04\text{‰}$ during 2001–2005. They attributed this change to decreasing rice emissions during the last two decades. However, Levin et al. (2012) disputed this finding on the grounds that Kai et al. used only one continental mountain station (Niwot Ridge, Colorado, USA) to represent the entire Northern Hemisphere. In contrast, Levin et al.'s data set from background air in both hemispheres showed that the inter-hemispheric difference in $\delta^{13}\text{C}_{\text{CH}_4}$ changed by less than 0.05‰ since 1990. They thus did not support the conclusion drawn by Kai et al. that there was evidence of a significant reduction of microbial sources in the Northern Hemisphere in the period.

16. Running budget analysis of methane source and sink variations: supplementary information

Atmospheric data used in the analysis (C_i , δ_i , δ_i')

Monthly CH₄ mole fraction data are used from 51 NOAA background sites and $\delta^{13}\text{C}_{\text{CH}_4}$ data from 20 INSTAAR time series together with the 2 RHUL sites as discussed in the main text. The NOAA INSTAAR $\delta^{13}\text{C}_{\text{CH}_4}$ data were updated from ftp://ftp.cmdl.noaa.gov/data/trace_gases/ in August 2015.

The spatial pattern of mole fraction data has a clear seasonal cycle, around the global average value, that has remained quite stable. This is constructed by treating the monthly data for all sites as:

$$MF_{i,m,y} = G_{m,y} + S_{i,m} + E_{i,m,y}$$

where $MF_{i,m,y}$ is the mole fraction value for site i in month m and year y ; $G_{m,y}$ is a global average for month m and year y ; $S_{i,m}$ is a seasonal cycle for site i that is treated as the same for all years, and $E_{i,m,y}$ is a residual. Values for $G_{m,y}$ and $S_{i,m}$ are determined by minimizing the sum of squares for the $E_{i,m,y}$ values. This method is also used to fill in missing data for some sites by setting the $E_{i,m,y}$ to zero.

Fig SI 13 shows the $S_{i,m}$ and $E_{i,m,y}$ values for most of the sites being used here and for the months January and July. Interannual variations $E_{i,m,y}$ are small relative to the latitudinal profile, however, changes over the 31 years are seen as trends in those variations. In particular, several high northern latitude sites such as Alert (alt) and Barrow (brw), show a decrease relative to the global averages, while Ascension (asc) is showing an increase in the amplitude of its seasonal cycle. The most likely explanation is that this is evidence of emissions increasing faster in the tropics than in the north, although changes in transport and sink factors could be significant also. The spline fits similar to those shown here are used for each month to determine averages over each semi-hemisphere while also following these small changes in the latitudinal variation.

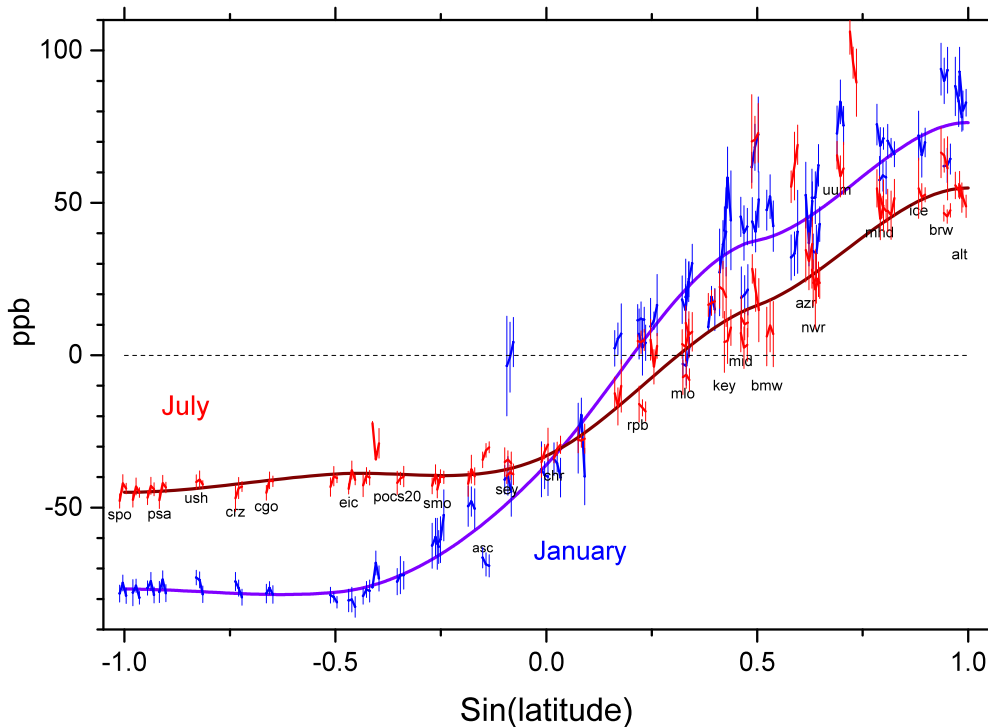


Fig. SI 13. CH_4 mole fraction latitudinal distribution and interannual variations defined by $S_{i,m} + e_{i,m,y}$ values that give ranges for differences from the global mean at most of the

sites used in this analysis. Blue symbols show values for January and red are for July. For each of three periods (1984 – 1998, 1999 – 2006 and 2007 – 2014) and for each site this shows the average and a one standard deviation range around that for each period, together with lines connecting those averages. The smooth curves are spline fits in four segments fitted to the averages for all years and this excludes 10% of the outliers in order to produce a more robust fit. For example, the northernmost site shown in the Southern Hemisphere is at Seychelles and has a very different seasonal cycle because it is affected by variations in the position of the inter-tropical convergence zone.

Regional average values for $\delta^{13}\text{C}_{\text{CH}_4}$ are based on fewer measurement sites and interannual variations in the isotopic differences between sites are relatively more significant than they are for methane mole fractions. The standard deviations of differences between pairs of sites within the same region from 1998 to 2014 range from 0.029‰ to 0.047‰ for the NOAA sites, but differences between the NOAA and RHUL sites in the 0-30°S region have a standard deviation of 0.065‰. However, this should be compared with the interannual changes occurring within each region of ~0.1‰ and the decrease from 2007 to 2014 of 0.2 – 0.25‰ in each region.

Monthly averages for $\delta^{13}\text{C}_{\text{CH}_4}$ over the four regions are estimated in the same way as for mole fraction averages. However, because there are fewer sites, and for a shorter period, this only uses a single spline to determine the latitudinal profile and much more of the variations in the data are covered by the global average in this case. Fig SI 14 shows the $\delta^{13}\text{C}_{\text{CH}_4}$ latitudinal profiles for January and July.

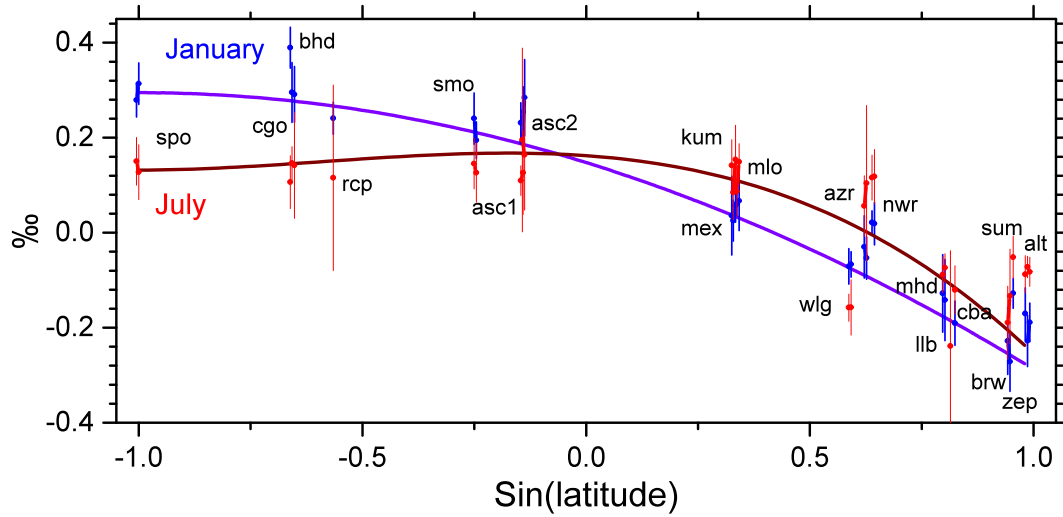


Fig. SI 14. Latitudinal distribution and interannual variations around the $G_{m,y}$ global average for $\delta^{13}\text{C}_{\text{CH}_4}$ values at 20 sites for Januarys and Julys together with a spline fit to these.

The global average $G_{m,y}$ values for $\delta^{13}\text{C}_{\text{CH}_4}$ constructed here include much more of the seasonal cycle for data at all sites and its interannual variability than is the case for mole fraction data. This occurs because the seasonal cycles in 30-90°N are significantly larger relative to those in 30-90°S than occurs for MF data. As a result the $G_{m,y}$ values also have

a seasonal cycle and the values shown in Fig SI 14 are additional variations around this. For completeness, the running global average $\delta^{13}\text{C}_{\text{CH}_4}$ values extracted in this process are shown in Fig SI 15., and for convenience recent changes in mole fraction and isotopes are summarized in Fig. SI 16.

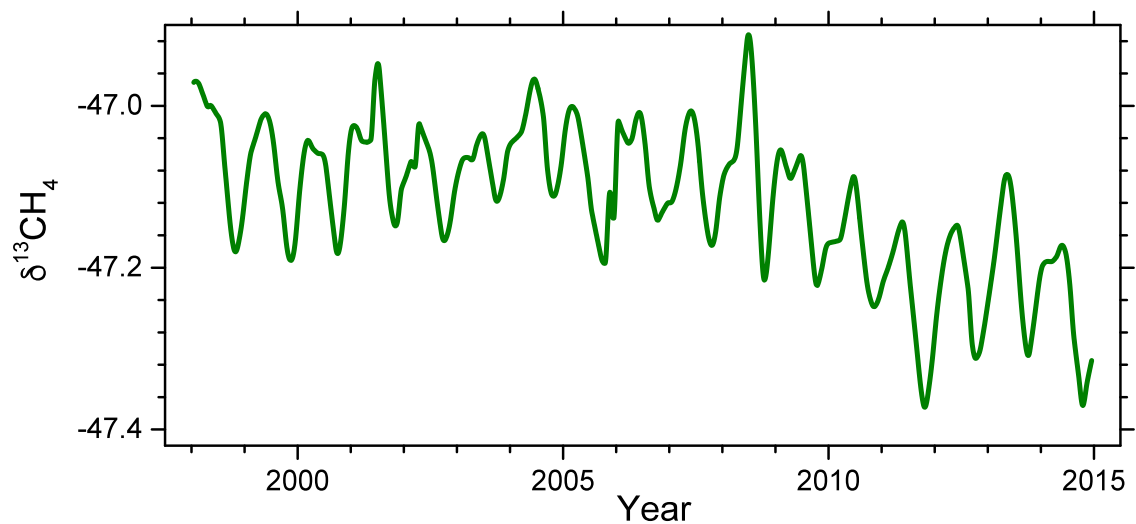


Fig. SI 15. Global average $\delta^{13}\text{C}_{\text{CH}_4}$ values derived here when separating this from a fixed seasonal cycle for site differences from the global average.














































Region	Time period	[CH ₄]	$\delta^{13}\text{C}_{\text{CH}_4}$
Global	1983-1991		-
	1992-1996		
	1997-1998		
	1999-2006		
	2007-2013		
	2014		
Arctic	2001-2005		
	2006-2007		
	2008-2009		
	2010-2013		
	2014		
Northern Temperate Latitudes	2003		
	2004-2008		
	2009-2013		
	2014		
Tropics	2001-2006		
	2007-2011		
	2012-2013		
	2014		
Southern Temperate and Antarctic	2001-2006		
	2007-2012		
	2013		
	2014		

Fig. SI 16. Qualitative summary of changes in methane mole fraction and $\delta^{13}\text{C}_{\text{CH}_4}$ values, over recent decades. Arrow sizes reflect broad trends. See Fig. 4 of main text for 3D view.

Removal rates (K_i)

Seasonal cycles in removal are based on estimates for the effects of OH, tropospheric Cl, soil uptake, and cross tropopause transport followed by oxidation in the stratosphere. The total removal rate is based on Ciais et al. (2013). Tropospheric OH is the predominant sink, but additional removal is by tropospheric reaction with atmospheric Cl, by soil uptake, and also by transport into the stratosphere and then oxidation in the stratosphere. Table 6.8 of Ciais et al (2013) shows systematic discrepancies between top-down and bottom up estimates for the removal rate. For consistency with a top-down approach this analysis is using a total removal rate corresponding to an average methane lifetime of ~9 years while also using relative contributions from the different removal processes that come from the bottom-up approach. . As the aim in this analysis is to consider changes that can explain the recent increase in mole fractions at the same time as a decrease in $\delta^{13}\text{C}_{\text{CH}_4}$, the uncertainties of up to 25% in source magnitude given in the literature are not being considered here. Rather the focus is on using a best estimate for the budget and then considering relative changes to that which explain the trends for increasing MF values and decreasing $\delta^{13}\text{C}_{\text{CH}_4}$ values. However, to check the sensitivity to estimates of the removal rate, the analysis described here has also been done with an average removal rate of ~8 years to consider more rapid responses in atmospheric CH_4 . That makes only very minor changes to the results shown in Figs 4 and 5 (in main text) and does not affect the systematic differences seen between fits to the data that vary the sources or that vary the removal rates.

The latitudinal distribution and seasonal cycles for removal by OH are based on Spivakovsky *et al.* (2000), which has recently been found more consistent with atmospheric chemistry data than other estimates (Patra et al., 2011). Isotopic fractionation by OH removal uses the Saueressig *et al.* (2001) estimates for the kinetic isotope effect (KIE). However, recent reviews of atmospheric chemistry data (Sander et al., 2011) still include earlier estimates by Cantrell et al. (1990) and this is considered below.

Latitudinal distributions of the other removal processes are less well defined and bring in much larger fractionation effects. A regional distribution for the soil sink is taken as being proportional to the land areas in each region, but because removal by Cl in the troposphere is expected to be related to marine boundary layer chemistry and has only been determined in detail for the Southern Hemisphere (Allan et al., 2007; Allan et al., 2010) its distribution is taken as either being proportional to ocean areas in each region or that restricted just to the Southern Hemisphere.

Similarly removal by transport into the stratosphere is taken as either being evenly distributed across the four regions or else only occurring in the two mid-latitude regions consistent with studies of cross tropopause transport (Fueglistaler et al., 2004). Mixing of CH_4 back from the stratosphere is being treated implicitly as part of the total source into the troposphere.

Seasonal variations in removal due to soil uptake and reaction with Cl are not as well defined as that for OH. Consequently the range of options for removal rates covers cases

where these do not have any seasonal cycle or that it is the same as that for OH. Transport into the stratosphere is taken as having no seasonal variation.

This range of options that is being considered for different seasonal variations in the different removal processes leads to seasonal cycles in the isotopic fractionation effects. In the 30-90°S region the net fractionation effect is as high as -15‰ for some months in one of the options being considered, however, this is not inconsistent with ship data in the Pacific Ocean (Lowe et al., 1999).

Atmospheric exchange between regions (X_{ij})

Transport between the four regions is simulated by comparing constant and varying exchange rates between the adjacent regions. Prior values are based on an interhemispheric exchange rate of 1.2 years similar to that determined by considering its relationship with Hadley circulation (Bowman & Cohen, 1997); to values used in other treatments of transport in box models for analysing the budget of methane (Rigby et al., 2008) and SF₆ (Maiss and Levin, 1994); and for considering differences in mole fraction and $\delta^{13}\text{C}_{\text{CH}_4}$ response times for perturbations to the CH₄ budget (Tans, 1997). Exchange between downwelling in the Hadley circulation at the mid-latitudes and that in the mid-latitude circulation Ferrel cell has more short term variability and so exchange rates between the two regions within each hemisphere are initially set to be 60% larger. However, to ensure that these estimates do not bias the results these exchange rates are only weakly constrained when carrying out fits to the MF and $\delta^{13}\text{C}_{\text{CH}_4}$ data. These fits change them by up to 23% for exchange between the 00-30°S and 00-30°N regions and the 00-30°N and 30-90°N regions, but by up to 40% for exchange between the 30-90°S and 00-30°S regions.

These temporal variations in transport are implemented as being piecewise linear over the 12-month periods, rather than as step changes, and when fitted to the CH₄ data they show similar patterns of change over 1998 – 2014 when different regional distributions are used for the removal processes. While this suggests that variation in transport can be playing a role in determining variations in the MF and $\delta^{13}\text{C}_{\text{CH}_4}$ data, the effect is not large. For example, using fixed exchange rates only increases the root mean square residuals in fits to the MF and $\delta^{13}\text{C}_{\text{CH}_4}$ data by < 1%.

Fitting Methane emissions (S_i , δ_{S_i} , δ_{S_i}') to data

Time varying emissions are constructed by fitting solutions to the differential equations given above to the observed CH₄ mole fractions and $\delta^{13}\text{C}_{\text{CH}_4}$ values for each region. Because changes in sources result in different long term responses for mole fraction and $\delta^{13}\text{C}_{\text{CH}_4}$ (Tans, 1997) a spin up phase starts in 1950 with the sources set to follow the Antarctic firn and ice core records (Etheridge et al., 1998; Ferretti et al., 2005) together with earlier NIWA $\delta^{13}\text{C}_{\text{CH}_4}$ data for 30-90°S (Lassey, et al., 2000). For this early period, differences in mole fractions between the four regions are treated as increasing in proportion the total source, while the differences in $\delta^{13}\text{C}_{\text{CH}_4}$ between the regions is assumed to have been constant from 1950 – 1985.

Variations in the emissions treat these as only changing linearly over 1950 – 1985 and then at a different rate over 1985 – 1992, but changing annually from 1990 to 2014. More specifically, S_i and δ'_{Si} values for 1950, 1985, 1992, 1999, 2006, 2007 and 2014 are initially fitted to all the data while using linear interpolations for source values between these times. Use of adjacent years 2006 and 2007 is done here to consider the potential for a more abrupt change at this point. Seasonal cycles that modulate the sources in each semi-hemisphere are treated as repeating each year and are fitted to the monthly C_i and δ'_i data by using sinusoidal 12-month and 6-month cycles. Interannual variations in the source S_i and δ'_{Si} values are then used to adjust each year from 1990 to 2014, using linear interpolations between the mid-point of each year, to follow short term variations.

Fits to the data also use a Bayesian approach by first optimising fits for the sources and their $\delta^{13}\text{C}$ values for 1985, 1992, 1999, 2006, 2007 and 2014 with linear interpolations between these years as a prior estimate. That is then extended to include interannual variations in the sources and this improves fits to the data significantly, typically reducing the RMS residual for MF data by 25% and that for the $\delta^{13}\text{C}_{\text{CH}_4}$ data by 20%. Also while selection of the adjacent years 2006 and 2007 was done initially to allow for a transition occurring at about this time adding interannual variations in the sources leads to the prior estimates for source changes becoming spread out over several years and extending back to about 2004.

Despite these features, the current approach excludes very short term source variations as well as any long term trends in the seasonal cycles for S_i and δ'_{Si} . Furthermore this treatment of $\delta^{13}\text{C}_{\text{CH}_4}$ is also limited by the lack of Northern Hemisphere data prior to 1998. For this reason interannual variations in the δ'_{Si} values are not considered prior to 1998. However, to avoid side effects of an abrupt change in δ'_{Si} values a linear trend is used from initial values in 1992 to fitted values in 1998.

The distribution of sources across the four regions obtained this way varies slightly depending on what is used for the distribution of removal rates as described above, but the relative contributions of: 30-90°S, 0-30°S, 0-30°N, and 30-90°N are: 11%, 27%, 32% and 31% of the global total source and this has a range 560 – 580 Tg CH_4/yr when averaged over 1998 - 2014. Source $\delta^{13}\text{C}$ values are sensitive to what is used for the removal rate and particularly to the distribution of high fractionation removal by Cl across the four regions. Over 1998 – 2014 the long term global average source $\delta^{13}\text{C}$ is in the range -53.6‰ to -53.4‰ and the short term changes shown in Fig 5 vary by $\pm 0.5\text{‰}$ around this. However, this reflects only the effect of different spatial distributions for removal processes and does not include the uncertainties in fractionation rates noted above. The Cantrell *et al.* (1990) estimate for the KIE in the reaction of CH_4 with OH was 5.4‰ which is slightly more than the Saueressig value of 3.9‰ used here, and using this would change the average source $\delta^{13}\text{C}$ values fitted to the data by $\sim 1.5\text{‰}$.

Comparing changes in removal rate or emissions

The approach used to consider trends or variation in removal rates is similar to that for variations in sources, but for the period 1999 – 2014 sources do not change and interannual variations in removal rate are used to fit the data instead. Again this is

initially done for the years 1999, 2006, 2007 and 2014 with linear interpolations between these years, as well as from 1992 to 1999 to cover the longer term effects of change in removal rate. Interannual variations in removal rates are then added to improve fits to the data.

Initial values for the sources in 1950 are set to match the earlier MF and $\delta^{13}\text{C}_{\text{CH}_4}$ data (Etheridge et al., 1998; Ferretti et al., 2005) and then adjustments are made to the source values for 1985 and for all years from 1990 on. In addition, seasonal cycles in the sources are fitted with two sinusoid components that have periods of 12 months and 6 months. This is done separately for each of the four semi-hemispheres and leads to 124 source parameters. Similarly, there are also 124 parameters determining the $\delta^{13}\text{C}$ values for these source emissions. In addition, the three exchange rates between the four semi-hemispheres are allowed to vary over 1991 to 2014 adding another 69 parameters and leading to a total of 317 parameters. These are being fitted to 2269 data values, 33% of which are $\delta^{13}\text{C}_{\text{CH}_4}$ values because these start later and have some gaps during 2001 – 2002 and 2005 - 2006.

Fits to the data using changes in removal rates affect the mole fraction and $\delta^{13}\text{C}_{\text{CH}_4}$ values over different timescales and so this is restricted to years 1998 to 2014 when both types of data are available. However, linear trends in the removal rate from the a priori values in 1992 to fitted values in 1998 are used to avoid any side effects of an abrupt change. This leads to 68 scaling factors being fitted to the data. Also in this case, source variations are stopped in 1999, but variations in exchange rates still cover the full period of 1991 to 2104. And there is a total of 241 parameters being fitted to the data.

Results

Fig SI 17 compares the seasonal variations resulting from this analysis with data for January 2005 – June 2009. As in Figs 4 and 5 (in main text), this shows that $\delta^{13}\text{C}_{\text{CH}_4}$ values are relatively more sensitive to small changes in the sources than removal rate and that source variations are better at reproducing large relative changes in $\delta^{13}\text{C}_{\text{CH}_4}$ such as the negative anomaly in 2007 followed by a positive anomaly in 2008. However, this also shows that such sharp variations in $\delta^{13}\text{C}_{\text{CH}_4}$ cannot be fully explained by this simple running budget analysis. Also there are larger interannual variations in the $\delta^{13}\text{C}_{\text{CH}_4}$ seasonal cycle than in the MF seasonal cycle and this indicates that the net source $\delta^{13}\text{C}$ value is quite variable.

Fig 5 (in main text) shows that short term changes in total source $\delta^{13}\text{C}$ values of $\pm 1\text{‰}$ are able to reproduce much of the observed variation in $\delta^{13}\text{C}_{\text{CH}_4}$, but that this requires a strong correlation in sources across all four semi-hemispheres, particularly in 2008. Also, as shown in Fig SI 17, this analysis does not explain a rapid switch from an anomalous decrease in $\delta^{13}\text{C}_{\text{CH}_4}$ to a very large increase seen in the 30–90°N region during 2007 – 2008.

Because there is no clear correlation between changes in the magnitude of sources and their $\delta^{13}\text{C}$ values, particularly in 2007 - 2008, this analysis is allowing for competing effects; such as climate variations leading to a decrease in isotopically light wetland

emissions, at the same time as an increase in isotopically heavy emissions from biomass burning. However, to explain the atmospheric data, net changes in source $\delta^{13}\text{C}$ of $\sim 1\text{‰}$ would require a 20-30% annual increase in biomass burning together with a 5% reduction in wetland emissions. The focus here is to compare overall variations in sources and removal rates, but a more detailed analysis should also consider how short term source changes can modify the seasonal cycle for source $\delta^{13}\text{C}$ values.

The source variations considered here have been done as year to year scaling of their average value and the amplitude of their seasonal cycle because the emphasis has been to compare these with variations in removal rates. When variations in both sources and removal rates are fitted to the data the result is similar to that shown here for variations just in the sources. However, this analysis suggests that better fits to the data will require source variations that also modify the seasonal cycle. Furthermore because the normal seasonal cycle for $0\text{--}30^\circ\text{S}$ was completely overridden by the $\delta^{13}\text{C}_{\text{CH}_4}$ variations seen in 2007 – 2008, this suggests that transport anomalies may also be more significant than is treated here.

Overall, the analysis shows that the growth of long-term $\delta^{13}\text{C}_{\text{CH}_4}$ time series datasets is now placing important constraints on the CH_4 budget. The discriminatory power of isotopic data in turn demonstrates the need for better information on $\delta\text{D}_{\text{CH}_4}$, for better knowledge of the geographic distribution and the characterization of isotopic signatures of specific sources. More isotopic data are also needed for a better understanding of both trends and interannual variability in the minor removal processes such as Cl and methanotrophy, that have large fractionation effects.

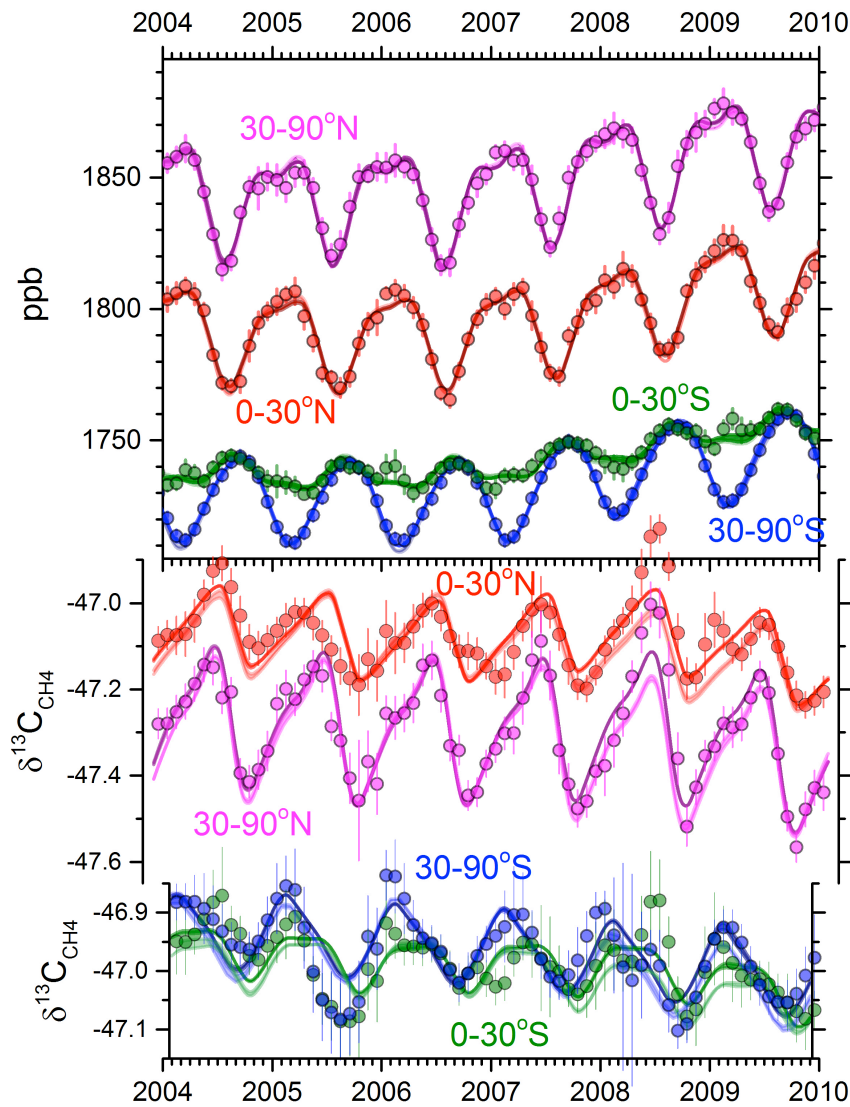


Figure SI 17. The upper panel shows monthly values for CH_4 mole fractions in the four regions together with the range of fits discussed here. The darker lines are for variations in the sources and the paler lines for variations in removal rates. Interannual variations are larger when source variations are used and give a slightly better fit to the data. The lower panel shows similar results for $\delta^{13}\text{C}_{\text{CH}_4}$ but has much larger differences between the two types of fit based on variations in sources or in removal rates. Discrepancies with data are larger in the $0\text{--}30^\circ\text{S}$ region than in the other regions and the anomaly observed over 2007 – 2008 is not being fully explained by this analysis, particularly in the $0\text{--}30^\circ\text{S}$ region.

17. Contributions to the work.

At NOAA, EJD is responsible for all methane measurements. The $\delta^{13}\text{C}_{\text{CH}_4}$ measurement on NOAA flask-air from ALT, ASC and SPO was carried out by SEM, with JBM and the INSTAAR team led by JWCW and BV. RHUL (EGN,DL,RF,JLF,ML,GZ,RB) maintain continuous measurement at ASC and $\delta^{13}\text{C}_{\text{CH}_4}$ analysis on flasks from ASC, CPT and ALT, in a project jointly with JAP, NW and MC. RHUL also carried out field studies in Uganda, Bolivia, S. Africa, Zimbabwe, Ascension, Hong Kong to determine tropical

source $\delta^{13}\text{C}_{\text{CH}_4}$ signatures. E-GB and CL, with ACM, provided CPT flasks for analysis at RHUL, and ALT flasks were supplied by DEJW, via Prof. Ingeborg Levin (Univ. of Heidelberg), whose generosity we gratefully thank.

Methane Budget analysis was carried out by MRM, with advisory inputs from several other authors, including EGN, EJD, JBM, PB, and MG, who also contributed on Amazonian precipitation. EWW and JWCW advised on ice core methane. The manuscript was written by EGN, MRM, and EJD, with inputs and corrections from all authors.

Funding for RHUL long-term time series measurement came from various sources: internal Royal Holloway laboratory funds, a succession of projects funded by the UK Natural Environment Research Council, most recently in the NERC Global Methane consortium ‘MOYA’, and the European Union's InGOS, IMECC and GeoMON projects. NOAA is an agency of the US Federal Government, and also supports work with the Univ. of Colorado Institute for Arctic and Alpine Research (INSTAAR). UK NERC supported the Cambridge and UEA groups. Other authors were funded in this work by their institutions.